University of Strathclyde Engineering

Investigation of Novel Mg-Li-Y Alloys for Bioresorbable Vascular Scaffolds

Kenneth John MacLeod

Department of Mechanical & Aerospace Engineering, University of Strathclyde, Glasgow

July 2023

Submitted to the Department of Mechanical & Aerospace Engineering in partial fulfilment of the requirements of Doctor of Philosophy

Abstract

Magnesium alloys are promising candidates for application in the development of new bioresorbable medical devices. Magnesium alloys are known to be safe in *vivo* and degrade within suitable time frames for a range of bioresorbable medical devices. Through selective alloying and processing the mechanical properties of magnesium can be tailored to suit specific device requirements. Bioresorbable vascular scaffolds (BVS) are one such device where magnesium alloys are being applied. BVS offer the potential to revolutionise the treatment of arterial disease through the removal of the long-term risks associated with current treatments. Recent developments in BVS technology have considered the use of a range of materials with magnesium alloys being one of the most promising material candidates for use in this new technology. One of the limiting factors of magnesium alloys for application in BVS technology is their relative lack of ductility, meaning new alloys must be developed.

In this work two Mg-4Li-xY (x = 0.5 and 2%) alloy wires are investigated for application in a new wire form balloon expandable BVS device. The two alloys are supplied cold drawn to a diameter of 125µm. Firstly, a series of thermal treatments are applied to maximise the ductility of each alloy wire. It is found that ductility is maximised soon after complete recrystallisation and deteriorates during prolonged annealing through grain coarsening in the Mg-4Li-0.5Y alloy wire and increased precipitation of a $Mg_{24}Y_5$ phase in both alloys. Both alloy wires are shown to be capable of achieving tensile elongation to failure of ≈20% and survive high idealised bending strains (>40%). Microstructural investigation revealed that recrystallisation is initiated, first, from regions closest to the surface of the wire and progresses inwards as the annealing time is prolonged. Following annealing for maximum elongation to failure both alloy wires developed a transverse basal texture. However, the increased Y content in the Mg-4Li-2Y alloy wire resulted in a weaker basal texture developing during annealing. Both alloy wires were shown to exhibit relatively high ductility, indicating they are both suitable candidates for application in BVS technology.

Both alloy wires were applied in the design of the novel wire form BVS under investigation and the processing routes applied during manufacture were investigated to optimise the mechanical performance of the device. Devices manufactured from the Mg-4Li-0.5Y alloy wire could survive over expansion of 1mm beyond its nominal diameter of 3mm and had a radial force at its nominal diameter >1N/mm. Devices manufactured from the Mg-4Li-2Y alloy wire had a radial

force >1N/mm at its nominal diameter but inconsistent failure of the device occurred during 1mm over expansion. These failures initiate from the internal diameter of the new device's novel wave form geometry. An increase in number of secondary phase particles in the Mg-4Li-2Y device is expected to contribute to these fractures with evidence found of cracks initiating adjacent to these particles. Further, the forming route and subsequent annealing process applied during the manufacture of the novel device, results in a split in texture developing through the device. Along the inner diameter of the wave form, deformation is dominated by tensile twinning, resulting in the recrystallised microstructure being dominated by new grains nucleated from these twins. Consequently, along the inner diameter of the wave form, the grains are aligned with their c-axis parallel to the expected loading direction during device expansion. This will limit the activation of prismatic slip which likely contributes to the failure of the devices investigated.

Application of the processing routes developed within this work have resulted in enhanced mechanical performance of the novel BVS device under investigation. Devices manufactured from the Mg-4Li-0.5Y alloy exhibited high radial force (>1N/mm) and repeatable over expansion, up to 1mm beyond its nominal diameter. These advancements have resulted in the device having comparable performance to competitors, allowing it to progress to the next stages of development.

The methodologies developed as part of this work to characterise and investigate the devices identified several potential avenues for continued device/alloy development. Consequently, several routes for continued research are identified that will aid in improving the performance of the Mg-4Li-0.5Y devices. Further, routes to address the sources of failure in the Mg-4Li-2Y are identified. If resolved, it may lead to these devices outperforming the Mg-4Li-0.5Y devices, further advancing this technology towards being applied in the clinical setting to improve the quality of life of patients.

Declaration of Authenticity and Author's / Companies' Rights

Signed:

Date:

Acknowledgements

I would first like to thank my supervisor, Professor David Nash, without whom this project would not have been possible. His continued support, guidance, and encouragement throughout the work from supporting equipment/travel costs to technical guidance has been invaluable.

I am grateful to all of those based at the sponsoring company of this project, MedAlliance. From project start those at MedAlliance have provided continued support in supplying all materials and assisted with testing and manufacture of the devices. In particular thanks must go to my industrial supervisor Dr David Bow, whose technical expertise and enthusiasm helped greatly in all aspects of this project.

I would also like to thank my secondary academic supervisor Dr Athanasios Toumpis, who always offered support and had an open door when needed.

Finally, to all the staff to the Advanced Materials Research Laboratory at the University of Strathclyde I will be forever grateful for the help and support provided whilst working in their labs. In particular to James Kelly whose patience, support and technical knowledge made working in his lab a very valuable and enjoyable experience throughout.

Contents

List of Figures

List of Tables

Abbreviations

ATK	Above the Knee
BMS	Bare Metal Stent
BSE	Backscattered Electron
BTK	Below the Knee
BVS	Bioresorbable Vascular Scaffolds
CAD	Coronary Artery Disease
CRSS	Critically Resolved Shear Stress
CVD	Cardiovascular Disease
DCB	Drug Coated Balloons
DD	Drawing Direction
DES	Drug Eluting Stents
DRX	Dynamic Recrystallisation
EBSD	Electron Backscattered Diffraction
EDS	Energy Dispersive X-ray Spectroscopy
FDA	Food and Drug Administration
HCP	Hexagonal Close Packed
ID	Internal Diameter
IMP	Inter Metallic Particle
IPF	Inverse Pole Figure
ISR	In-stent Restenosis
KAM	Kernel Average Misorientation
LST	Late Stent Thrombosis
MACE	Major Adverse Cardiovascular Events
MBD	Minimum Bend Diameter
ND	Normal Direction
OCT	Optical Coherence Tomography
OD	Outer Diameter
PAD	Peripheral Artery Disease
PCI	Percutaneous Coronary Intervention

PLLA	Poly-l-lactic acid
POBA	Plain Old Balloon Angioplasty
PSN	Particle Stimulated Nucleation
RD	Rolling Direction
RE	Rare Earth
REE	Rare Earth Element
SCC	Stress Corrosion Cracking
SEM	Scanning Electron Microscope
SRX	Static Recrystallisation
ST	Stent Thrombosis
TD	Transverse Direction
TLF	Target Lesion Failure
UTS	Ultimate Tensile Stress
XRD	X-ray Diffraction
YS	Yield Stress

Chapter 1: Introduction

1.1 Arterial Disease and Current Treatments

Cardiovascular diseases (CVD) are the leading cause of death globally with 18.6 million CVD deaths reported in 2019. The global burden of CVD is growing, particularly in developing countries where the rates of smoking and obesity are increasing, with the global number of CVD cases almost doubling from 1990 (271 million) to 2019 (523 million).[1] A more recent study, from 2022, demonstrates this trend is expected to continue with rates of ischemic heart disease, heart failure and stroke predicted to increase by over 30% from 2025 to 2060 with the rates of myocardial infraction expected to increase by 16.9% over the same period in the USA.[2] Not only is CVD the leading cause of death globally, it also severely limits patients' quality of life and puts significant economic pressure on governments worldwide. In 2015, the USA spent approximately $126 billion on treatments for atherosclerosis related CVD and this is expected to rise to over $300 billion by 2035.[3] Preventative measures combined with new and improved treatments are vital in reducing deaths, improving patients' quality of life, and reducing the economic burden on governments.

CVD is a broad term that is used to describe all diseases that affect the vascular system and include coronary artery disease (CAD), cerebrovascular disease, and peripheral artery disease (PAD). Atherosclerosis is the most common underlying cause of all CVD.[4] Atherosclerosis is a chronic inflammatory disease that progresses overtime and the earliest, visible, stage of atherosclerosis, the "fatty streak", can present as early as childhood. The fatty streak is commonly referred to as the first stage of atherosclerosis and is caused by the buildup of lipid laden foam cells in the intima.[5-7] Fatty streaks can develop in any artery however, it is known that these lesions develop more frequently in areas of the arterial system with non-uniform blood flow such as at bifurcation points. Sites that induce non-uniform blood flow reduce the shear stress acting on the arterial walls and increase turbulence which can increase the inflammation response of the arteries. Constant exposure of the endothelium to uniform shear flow is anti-inflammatory as the constant mechanical forces detected by the cells can be converted into biochemical signals that prevent inflammation.[8, 9] Fatty streaks have been identified in the aorta in the first decade of life, coronary arteries in the second and cerebral arteries in the third, though these very rarely result in significant clinical events. Some fatty streaks developed in children can regress whilst some can progress overtime into more

complicated lesions that can pose significant clinical risk in later life.[7, 10] Overtime the fatty streak can develop into a "fibrous lesion" through the progressive deposition of lipids and smooth muscle cells. These fibrous lesions tend to form with a "fibrous cap" of smooth muscle cells that encapsulates a core made up of necrotic tissue and lipids. Fibrous lesions pose a significant risk as they can grow into the lumen of the artery, restricting blood flow, and can begin to damage the arterial wall. It is possible for these lesions to grow so large that they fully occlude the artery, blocking blood flow to the major organs and tissue. However, it is more likely that they rupture causing a blood clot, or thrombus, to form that can fully occlude the artery.[11]

Early intervention is preferable in the case of atherosclerosis with treatment options varying from improving diet, exercise, and non-invasive use of drugs to slow progression of the disease, or even reverse it. If a patient exhibits more severe symptoms, or has suffered a blockage, often non-invasive treatments are not sufficient and, in these cases, the most common treatment protocol is percutaneous coronary intervention (PCI).[12, 13] PCI widens the narrowed or blocked artery using a balloon catheter that is fed through the artery to the site of blockage (stenosis) and inflated against the arterial wall, widening the artery. Commonly a metallic stent is placed on the balloon and is expanded against the artery wall to provide support to the diseased artery once the balloon is removed. The development of PCI treatments has resulted in improved patient outcomes for those suffering from CVD but development of current technologies are still required to further improve long-term patient outcomes.[13]

1.1.1 Treatment of CVD

The treatment of CVD was transformed by the development of PCI in 1977 and since has undergone three key revolutions over the past 40 years. In 1977 Dr Andreas Grüntzig performed the first balloon angioplasty (now referred to as plain old balloon angioplasty or POBA) on a coronary artery by using a pressurised balloon fixed to a catheter tip to widen the stenosed artery.[14] POBA revolutionised the treatment of CVD, however was not without its limitations, largely caused by elastic recoil (whereby the artery recoils to its stenosed diameter or fully collapses). In 5-10% of patients elastic recoil of the artery occurred immediately (within hours) after the procedure, resulting in acute myocardial infraction that requires immediate intervention through bypass surgery.[13, 15] 6 months post treatment with POBA, restenosis (renarrowing of the artery) occurred in approximately 30% of patients. In the case of restenosis, repeat POBA could be used to widen the artery.[13] The issues associated with POBA led to the

second revolution in the treatment of CVD through development of the bare metal stent (BMS). These devices were introduced to reduce the rates of elastic recoil and restenosis through implanting a metallic mesh that would provide continued support to the artery, opposing vessel recoil.[15]

The self-expanding Wallstent (Schneider AG) was the first BMS developed and was first implanted in a coronary artery in 1986 by Sigwart et al.[16] The stent was manufactured from stainless steel and used a "catheter sheath" type deployment system. The device was placed on an inner shaft and constrained by an outer sheath. Once the outer sheath was removed the stent self-expanded against the artery wall. The Wallstent stent provided, continued, support to the artery and reduced complications caused by immediate elastic recoil however restenosis of the stented region remained an issue with this device.[16, 17] The self-expanding design of the Wallstent meant the complex nature of its deployment procedure restricted its application in the clinical setting, and it 1991 it was pulled from the market. Despite this, the self-expanding stent design has since been refined and today many self-expanding devices are available on the market (including a new and refined Wallstent design).[15, 18] The issues with deployment of self-expanding stents meant that balloon expandable stents were developed, with the first balloon expandable stent, the Palmaz Schatz, being approved by the FDA in 1987.[13] Deployment of balloon expandable stents involves first mounting the device on a balloon tipped catheter, which is then delivered through the artery to the site of stenosis. The balloon and stent system are then expanded against the artery wall widening the artery. Finally, the balloon is deflated and removed from the artery, leaving behind the expanded stent supporting the vessel wall. Following the development of Palmaz-Schatz BMS several other BMS were brought to market, however the Palmaz-Schatz remained one of the most widely used BMS in the 1990's. The introduction of BMS devices did reduce the rates of acute elastic recoil associated with POBA, however they introduced other limitations. The interaction between the permanent metallic device and the vessel walls saw relatively high rates stent thrombosis (ST) and in-stent restenosis (ISR). Despite the complications of ISR and ST, BMS began to replace POBA in the treatment of lesions in the coronary arteries. The third and final revolution in the treatment of atherosclerosis came in the development of drug eluting stents (DES) designed to reduce the rates of ST and ISR.[13]

DES were first introduced with the aim of reducing the rates of ISR seen in patients treated with BMS, through incorporating anti-inflammatory, anti-proliferative, and anti-restenosis drugs to tackle the foreign body response seen when implanting BMS. The Cypher (Cordis/Johnson &

Johnson) was the first DES introduced in 2002. The Cypher device was manufactured from stainless steel, with 132µm thick struts and had 12.6µm thick layer of permanent polymer coating that controlled the release of Sirolimus drug with anti-proliferation and immunosuppressant properties.[19] Following the approval of the Cypher device the Taxus (Boston Scientific) DES was approved for use, also manufactured from stainless steel. These devices are generally referred to as first-generation DES. The introduction of these first-generation DES reduced the risk of restenosis as shown by the 5-year rate of target vessel revascularisation decreasing from 30.1% to 15.2% in a pooled analysis of 4 randomised trials of coronary arteries treated with BMS and cypher DES respectively.[20] Despite the improved rates of target vessel revascularisation in first-generation DES they introduced the risk of late stent thrombosis (LST), defined as thrombosis occurring 30 days post procedure. Once the anti-proliferation drug coating was depleted, the interaction between the permanent polymer coating and vessel walls increased the risk of LST through increased inflammation and late stent mallapositon. Therefore, first-generation DES did decrease rates of ISR associated with BMS, however they introduced the risk of more long term complications owing to their permanent polymer coating.[21] This led to the development of second-generation DES which sought to combine the benefits of BMS and first-generation DES.

Second-generation DES improved upon first-generation devices through updated geometry, reduced strut thickness, new drugs and improved polymer coatings. First-generation devices were manufactured from stainless steel and had strut thicknesses of 130–140µm. Second-generation DES began to use stronger, cobalt-chromium and platinum-chromium alloys, meaning the strut size could be reduced whilst maintaining similar radial force to first-generation DES. Today, DES are available with strut thicknesses <70µm, which improves device deliverability and reduces vessel injury.[22] Further, current DES use bioresorbable polymers to incorporate the anti-proliferative drugs on the devices, meaning that once the drugs have been fully released into the system the polymer coating is fully absorbed by the body, removing any adverse effects associated with the permanent coating of first-generation DES. The design improvements of second-generation DES led to vast improvements in patient outcomes compared to BMS and first-generation DES.[15, 19, 23] Early second-generation DES reduced the rates of restenosis, ST and death compared to first-generation devices in the treatment of CAD, with a large scale study showing a reduction of 38%, 43% and 23% in the above risk factors respectively over a two year period.[24] The success in patient outcomes from the development of DES is clear, however the success of DES in the treatment of CAD has not been carried over

to the entire arterial system. One such indication is the treatment of PAD where the complex lesions coupled with increased biomechanical loading make treatment with DES challenging.[25, 26]

1.1.2 Treatment of Peripheral Artery Disease

PAD most commonly refers to atherosclerotic lesions developing in the legs. After CAD and stroke, lower extremity PAD is the third most prevalent cause of atherosclerotic morbidity and affects more than 230 million people worldwide.[27, 28] Lower extremity PAD is most commonly caused by atherosclerotic lesions developing and occluding the arteries. PAD is therefore a progressive disease and at first patients may be asymptomatic. Progression of the disease can lead to intermittent claudication (pain during exercise that subsides with rest), rest pain and in severe cases necrosis and gangrene (tissue loss) which may result in limb loss if not treated appropriately.[29]

Though current treatments, such as DES, are effective for treating CAD there is still a clinically unmet need in treating PAD, particularly treating arteries “below the knee” (BTK). The arteries in the legs can be defined as BTK or “above the knee” (ATK). The femoral arteries (common, superficial and deep femoral arteries) ATK are generally larger in diameter (approximately 7-9mm in healthy patients) compared to the arteries (peroneal, anterior tibial and posterior tibial arteries) BTK which are approximately 3-5mm in diameter in healthy patients.[30, 31] Artery size, however, is patient specific and depends on age, sex and health, whilst measuring the diameter of arteries is complex and results can vary depending on the measurement techniques used.[32] The size of the arteries BTK are similar to that of the coronary system, however the lesions that develop BTK are often more challenging to treat as they are generally longer, more calcified and are exposed to increased biomechanical loading.[25] Owing to these challenges the success of treating coronary artery disease with DES has not been replicated in arteries BTK, with the permanent devices causing increased inflammation and risk of late stent thrombosis.[33] Use of DES for the treatment of arteries BTK has been shown to have improved patient outcomes over alternative interventions up to 12 months but no superiority beyond 12 months.[26] The long-term effects of this were revealed in a long-term randomised control trial (PADI) which showed very high 10-year mortality rates for patients treated with DES and alternative catheter-based interventions BTK (80.8% and 78.1% respectively).[34]

1.1.3 Future Treatment Perspectives for PAD

With PAD disease remaining the third most common cause of atherosclerotic morbidity, the need to develop suitable treatments to improve patients' quality of life is clear. As with all CVD, the best treatment for PAD is early diagnosis and changes in lifestyle to slow, and in some cases reverse, progression of the disease. However, in many cases intervention is required. As mentioned previously DES have shown appropriate short-term outcomes but are associated with long-term complications, owing to the complex lesions, and increased biomechanical loading leading to failure of the devices. Consequently, there are no DES approved for use in arteries BTK, although off label usage of coronary devices BTK is common in the treatment of short lessions.[25]

In many instances where the use of DES to treat arteries BTK is not possible, PCI is performed with POBA or drug coated balloons (DCB). POBA of BTK arteries has been commonly applied as it allows for revasularisation of the artery without the need for implantation of a permanent DES, that can lead to long-term complications. However, high rates of restenosis (up to 70%) have been reported in the treatment of BTK arteries with POBA.[35] DCB were developed with the aim of reducing late restenosis. DCB are balloon catheters that are coated with antiproliferative drugs that are delivered to the artery walls during expansion. DCB aim to reduce the rates of restenosis through the delivery of these drugs.[36] DCB have shown promising results, in particular more recent DCBs that incorporate alternative drug coatings to those used in early devices.[37] However, limitations persist with both POBA and DCB, associated with the lack of continued vessel support post revascularisation. Another additional complication is that during POBA and DCB procedures, dissection of the artery wall is common. A dissection is effectively a tear in the vessel wall. Some level of dissection is unavoidable during balloon angioplasty. However, the severity of dissections varies and in some cases the tear can protrude into the vessel lumen and impede blood flow. In these cases, "bailout stenting" (where a stent is implanted to restore regular blood flow) is commonly required. The rate of bailout stenting varies across studies but is not insignificant, with one study showing the rate of bailout stenting being as high as 32%.[38] Currently no FDA approved permanent stents are approved for use in BTK arteries however, off-label use of coronary stents in the treatment of BTK arteries is common.[39]

The Phillips, Tack Endovascular System is a stent like device that has been approved by the FDA for treatment of dissections in arteries BTK.[40] Manufactured from Nitinol, the Tack Endovascular System is a short (6mm), self-expanding the device that is deployed at the site of a dissection following angioplasty to provide continued support to the vessel. The device was granted FDA

approval following the TOBA II study which investigated the use of the Tack device to treat dissections in the superficial femoral or proximal popliteal arteries following angioplasty. The Tack device has been shown to have promising outcomes in the treatment of dissections, however risk will still remain with a permanent foreign body in the treatment of arteries BTK.[39, 40] Therefore, there remains a clinical need to provide continued vessel support post angioplasty of longer more complex lesions in BTK arteries. One such solution proposed is bioresorbable vascular scaffolds (BVS).

BVS are temporary devices that seek to provide effective support to the artery for the first 6-12 months post deployment before being fully absorbed. In order to develop suitable BVS devices new materials must be considered for their manufacture. These materials include bioresorbable polymers and metals, greater detail will be provided on these in Chapter 2. As DES have been shown to have improved outcomes over the first 12 months post implantation to other interventions it is thought that successful development of BVS devices will mimic these improved outcomes over the first 12 months, and remove the long-term complication post 12 months.[26, 41]

As well as improving the outcomes for patients with PAD, BVS technology offers the potential to revolutionise the treatment of all CVD. Firstly, long-term complications persist with the implantation of DES in all arteries. Although the treatment of CAD with DES has greatly improved with the development of DES, long-term complications persist owing to the foreign body response associated with permanent implants. BVS devices offer the potential to eradicate these complications in the treatment of all arteries with stent/scaffold technology.[41, 42] Further, paediatric patients who suffer from congenital heart disease are often treated with small DES. As the patients age, they outgrow these devices and invasive follow-up surgery is required to remove these devices. BVS technology offers the potential to treat paediatric patients with a device that will be fully absorbed before their arteries begin to outgrow the device, removing the need for repeat intervention in the early stages of life.[43, 44] A needs analysis survey in 2016 of 68 cardiologists in 8 countries found that 41% ranked BVS devices as their first choice of new devices for use in congenital interventions.[45] The advantages of BVS technology are clear and successful development of a BVS device offers the potential to revolutionise the treatment of CVD. The primary challenge of BVS development centres around material selection. As the devices must be safely absorbed by the body the range of suitable materials is limited. This work investigates the suitability of two new Mg-Li-Y alloy wires for the application in BVS technology from the perspective of their mechanical properties.

1.2 Project Scope

BVS offer the potential to improve clinical outcomes when treating arterial disease relative to current DES due to elimination of permanent implantation of a foreign body. However, there remains several challenges facing the development of these devices. The primary challenge is the selection of a biocompatible material that can be safely absorbed by the body over an appropriate timeframe that also has sufficient mechanical properties to allow the BVS device to be capable of safely being deployed in the artery and provide sufficient support to the diseased vessel.

The focus of this thesis is to investigate the suitability of two Mg–4Li–xY (x = 0.5 and 2.0wt%) alloy wires in the manufacture of a novel wire form BVS device. The BVS device under investigation is initially planned to target the treatment of PAD, meaning it is designed with a nominal diameter of 3mm. The primary purpose for targeting this indication is the current lack of appropriate treatment options available. The benefits of BVS devices compared to current technologies in the treatment of PAD are clear, meaning successful development of a BVS device will have a great impact on the quality of life of millions of patients globally. However, owing to the similar size of arteries BTK and in the coronary system these devices have the potential to be applied in the treatment of additional indications. With one of the major limitations of the materials available for application in BVS technology being their relative lack of ductility the focus will be on, first, optimising a thermal processing route for the two alloys in order to maximise ductility. The microstructure of both alloys is investigated to understand how the increased Y content affects the texture, grain size and secondary phase particle distribution. The two alloys are thereafter applied in the manufacture of a new wire form BVS device, where the processing parameters will be optimised to maximise the expansion range of the device. Conclusions are drawn on how varying the Y content influences the microstructure and mechanical properties of the alloy wires and how both alloys behave when applied in the final device. Final recommendations are summarised on future device design modifications based on both alloying content and device processing.

Chapter 2: Literature Review

2.1 Current Status of BVS Devices

There are currently no BVS devices widely applied in the clinical setting, though there is a growing level of research into BVS devices as the potential benefits are clear. BVS devices are generally manufactured from bioresorbable polymers or metals and as such can be categorised as polymeric or metallic based BVS devices.[46] The bulk of the research on BVS devices has centred on polymeric devices, with the first FDA approved device being the polymer based Absorb (Abbott Vascular).[47] However, owing to many deficiencies associated with polymeric devices, metallic based devices, primarily manufactured from Mg alloys, have gained increased attention, such as the Magmaris/Dreams (Biotronik) device(s), manufactured from Mg alloys.[48] This section briefly summarises the most relevant bioresorbable materials being applied in BVS technology and discusses their application in devices currently under development.

2.1.1 Polymer BVS

The major body of research into BVS devices has centred on the use of bioresorbable polymers, as they have been applied in resorbable medical devices since the end of the 1960s, in the development of resorbable sutures and as such are known to be safe *in vivo*.[49] [50] There are a range of bioresorbable polymers available with varying mechanical and corrosion properties. The properties of the most widely used bioresorbable polymers are summarised in Table 2-1 alongside the properties for the Mg alloy, WE43, stainless steel (SS 316L) and cobalt chromium (Co-Cr).[51] As can be seen from Table 2-1 the majority of the polymers have relatively low strength and ductility relative to the comparative metals. Considering the application of polymers in BVS technology, their low strength results in thick strut geometries being required to provide sufficient strength to the device, whilst their low ductility limits the expansion range of devices. Table 2-1 does show that high ductility polymers are available (e.g. PCL), however these polymers do not have the required strength to be considered for application in BVS technologies.[51-53] Currently the main polymer being applied in BVS devices under development is poly-l-lactic acid (PLLA). PLLA is a semi crystalline polymer that degrades into water and carbon dioxide within approximately 2-3 years in *vivo*.[53]

Table 2-1: Summary of most widely applied bioresorbable polymers with reference to metals used in stent technology[51]

Polymer	*T_g (°C)*	*T_m (°C)*	*Modulus (GPa)*	*Strength (MPa)*	*Elongation at break (%)*	*Degradation (months)*
PLA	60	180–190	2–4	65	2–6	18–30
PDLLA	55	Amorph.	1–3.5	40	1–2	3–4
PLLA	60–65	175	2–4	60–70	2–6	> 24
PDLGA (50/50)	45	Amorph.	1–4.3	45	1–4	1–2
PLGA (82/12)	50	135–145	3.3–3.5	65	2–6	12–18
PCL	− 54	55–60	0.34–0.36	23	> 4000	24–36
PLA/PCL (70/30)	20	100–125	0.02–0.04	2–4.5	> 100	12–24
WE43 (Mg alloy)	N.A	540–640	40–50	220–330	2–20	~ 12
SS 316L	N.A	1371–1399	193	668	40	Biostable
Co-Cr	N.A	~ 1454	210–235	> 1000	40	Biostable

The polymer based Absorb scaffold, manufactured by *Abbott Vascular* from PLLA, was approved for use by the FDA in 2016.[54] The Absorb device had a strut thickness of 156µm and was designed to treat arteries between 2.5 and 3.75mm in diameter. Early, controlled, studies (Absorb I, cohort A and B) of the Absorb device showed promising results where scaffold thrombosis did not occur in any patient after 5 years and the rate of major adverse cardiac events (MACE) were low.[55, 56] However, as increased clinical data became available, the rates of target lesion failure (TLF) in patients treated with the Absorb device were considerably higher than in patients treated with DES. TLF encompasses patients who suffered cardiac death, myocardial infraction or required revascularisation of the target lesion.[53] A meta-analysis of seven randomised trials (5583 patients in total) revealed that the rates of device thrombosis was increased in those

treated with the Absorb device compared to DES (2.3 vs 0.7%).[57] Results from these more long term follow up trials caused Abbot to pull the Absorb device from the market in 2017.[58]

A five-year follow up study of the Absorb III trial did however provide an indication of the benefits of BVS technology.[59] This study revealed that the rates of adverse events between the Absorb scaffold were increased over the full five-year follow up period compared to the DES group. However, following complete resorption of the Absorb device (after 3 years) the rates of adverse events were reduced compared to those treated with DES.[59] This finding provides an indication that should a BVS be developed that can mimic (or exceed) the performance of DES until complete degradation, the long-term risks associated with permanent DES can be lessened or potentially removed completely.

The poor performance of the Absorb scaffold was attributed to limitations in both mechanical performance and degradation rate.[60] In order to match the radial strength of comparable DES at the time of development the Absorb scaffold was required to have significantly increased strut thickness (156µm compared to the Xience DES which had 88µm thick struts).[51] Further the poor ductility of PLLA resulted in limited expansion capabilities of the Absorb device meaning device failure and mallaposition occurred during deployment. Despite the poor performance of the Absorb device, there remains a number of polymer based (primarily manufactured from a PLLA backbone) devices currently under development, all of which are attempting to develop BVS devices with reduced strut thickness compared to the Absorb device.[51, 60]

2.1.2 Metallic BVS

BVS devices manufactured from bioresorbable metals are being developed as, compared to polymers, their mechanical properties are more similar to that of permanent metallic stents.[61] The three main metals being considered for use in bioresorbable medical implants are, Fe, Zn, and Mg.[62] Fe alloys were one of the first bioresorbable metals to be investigated for use in resorbable devices. The main attraction of Fe alloys is their high strength (similar to that of stainless steels) however the limiting factor of Fe alloys is their slow degradation rate.[62] Peuster et al.[63] revealed that the in *vivo* degradation rate of a pure Fe scaffold with 100-120µm thick struts was much slower in *vivo* compared to in *vitro* tests. The authors concluded that further work was required to accelerate the degradation rate of Fe based devices in *vivo*.[63] A long-term in *vivo* study by Zheng et al.[64] investigated the performance of a nitrided Fe scaffold with 70µm thick struts over several time points over the first year as well as at 7-years post implantation in

a porcine model. The authors found that the device had acceptable biocompatibility and that the struts were nearly completely absorbed after 7 years but some degradation product remained 7 years post implantation.[64] Researchers have investigated improving the degradation rate through alloying (primarily with Mn) and developing new porous Fe alloys, for a range of bioresorbable devices.[65, 66] Research into Fe based biomaterials continues but there remains questions over how to best improve the issues associated with the slow degradation rate.[67]

Mg alloys are perhaps the most researched biomaterial owing to their more appropriate degradation rates (compared to Fe) and suitable mechanical properties. As such the only metallic BVS that has gained CE approval (Magmaris) is manufactured from an Mg alloy (WE43). Pure Mg wires were first used as a biomaterial in 1878 when Dr Edward C. Huse used Mg wires as ligatures to stop the bleeding of vessels. Huse's early success led to the application of Mg (and Mg alloys) in a range of procedures over the proceeding years. However, the rapid degradation of Mg alloys coupled with their relatively limited ductility meant these developments had limited success.[68] However, in recent years interest in Mg as potential biomaterial has had a resurgence with a range of Mg based devices being proposed, including BVS.[68, 69] In order to improve the corrosion rate and mechanical properties, appropriate alloys must be developed. Much research has gone into developing such alloys, including alloying with Al, Zn, Ca, Li, and rare earth (RE) elements.[70, 71] Several new alloys have been developed that improve the properties of Mg alloys, though perhaps the most significant (in terms of bioresorbable alloys) is WE43 that was originally developed for use in high strength and high temperature applications. More recently, however, WE43 was used in the design and manufacture of the Magmaris device.[72] More detail on this device is provided in Section 2.1.3 but it is the only metallic based BVS to gain CE approval. Despite some success in the application of Mg alloys in BVS technology challenges persist in developing new alloys and processing routes to unlock the full potential of Mg based BVS devices.

Zn based biomaterials are an alternative to the more widely researched Fe and Mg alloys, as they have more moderate corrosion rates. Compared to Fe and Mg the literature concerning Zn as a biomaterial is somewhat limited though various reviews have summarised its application in detail.[73-77] Zn has a faster corrosion rate than Fe but slower rate than Mg. Zn alloys also offer relatively impressive mechanical properties with similar strength and increased ductility compared to Mg alloys. One concerning factor is the aging effect observed in various Zn alloys, resulting in strengthening and a reduction in ductility overtime.[75, 78] Jin et al.[79] Demonstrated

this aging effect in a ZnMg alloy wire with a diameter of 250µm developed for application in bioresorbable devices. The authors performed tensile tests on the alloy wire within 2-3hours of drawing to its final diameter and then following storage for 1, 9 and 365days at room temperature. The results from this study are shown in Figure 2.1. After 9days the wires elongation to failure was reduced by ≈50%, whilst the yield strength (YS) was increased by ≈50%. The authors suggest this aging effect may be caused by the precipitation of Mg_2Zn_{11} particles overtime.[79] Although aging has been observed in Zn alloys, much of the research has been conducted on industrial alloys, meaning new Zn based alloys developed for bioresorbable application may not suffer from room temperature aging. However, considerable attention should be given to this effect when designing new alloys for application in BVS technology as the shelf life of products must be considered.[78]

Drelich et al.[80] investigated the suitability of Zn for use in BVS technology through implanting 250µm diameter pure Zn wires into the abdominal aorta of rats. The results showed that the wires exhibited uniform corrosion and a reduction in cross-sectional area of 65% at 20 months with no local toxicity. Consequently the authors proposed that Zn is a suitable candidate material for use in BVS technology as it can degrade safely and uniformly within 1-2years.[80] Though Zn offers more moderate corrosion rates it generally has lower strength compared to Fe and Mg alloys. As cast pure Zn has both low strength and ductility (tensile strength 18MPa and elongation to failure of 0.32%). Alloying with Cu, Ag, Mg, Al, Li, Sr and Ca can be used to improve the mechanical properties of pure Zn, making Zn alloys more suitable for use in bioresorbable

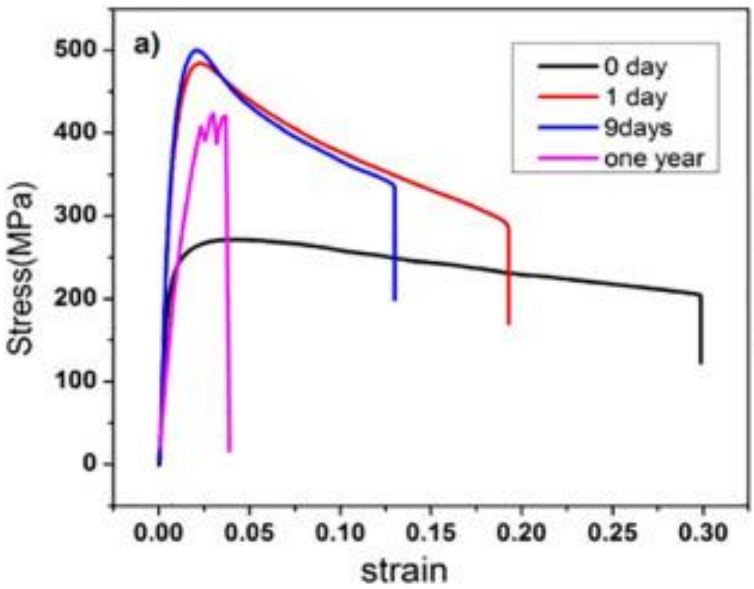

Figure 2.1: Aging response of ZnMg alloy wires[79]

devices.[81] Hehrlein et al.[82] deployed BVS devices with a nominal diameter of 6mm manufactured from a Zn-3Ag alloy in a porcine model. The authors compared the mechanical properties of the Zn-3Ag alloy (YS of 130–145MPa, ultimate tensile stress, UTS, of 240–260MPa and elongation to failure of 70–135%) to alternative Mg based biomaterial, WE43. Compared to WE43 the Zn-3Ag alloy had slightly decreased strength (≈20-40MPa, lower UTS) but improved ductility, which may offer great advantages in BVS designs.[82] The research of Zn based alloys is promising but further research is required to characterise the alloys response in *vivo* and to investigate the aging of new bioresorbable Zn alloys at room temperature.

Fe, Mg and Zn alloys all have potential for application in bioresorbable medical device technology, but the current trend in metallic BVS development is focussed most on Mg alloys. Mg alloys exhibit impressive mechanical properties, are safe in *vivo* and offer appropriate degradation rates that can be tailored through alloying and the incorporation of protective coatings.

2.1.3 Magmaris

In 2005 Biotronik began testing the first iteration of their Mg based BVS device, the AMS1, for the treatment of PAD.[83] Their device was manufactured from the Mg alloy WE43, without a polymer or drug coating. They also tested the device in the treatment of paediatric patients with aortic and pulmonary artery disease.[84, 85] These, controlled, trials demonstrated promising results and identified several limitations that required further device refinement to address. The device underwent several iterations, where the alloy was refined along with the geometry of the device and a drug eluting polymer coating added. Through these iterations the device finally evolved into the Magmaris device, which was the first Mg based BVS to gain CE approval.[86]

The Magmaris device was manufactured through the laser cutting of a WE43 hypotube followed by electropolishing. The electropolished struts had a thickness of 150x150µm (for devices with a nominal diameter of 3 and 3.5mm) and incorporated a 7µm thick sirolimus eluting PLLA coating. The device was designed to have a scaffolding time of 12 months and could be safely expanded up to a maximum of 0.6mm above the nominal diameter.[86, 87] The first-in-man clinical trial, Biosolve-II, saw 125 Magmaris devices implanted in 121 patients with stable or unstable angina. 6 month follow up results of the patient cohort were promising, with no definite or probable scaffold thrombosis observed, whilst the rate of TLF was low (3%). The study did note that as a first-in-man study the patients were selected based on having “straightforward de-

novo lesions". Consequently, the promising 6 month results in this study could not be extrapolated to more complex lesions.[88] A secondary controlled study on the Magmaris device, Biosolve-III, also output favourable results for the Magmaris device when compared to competing polymer based devices where the rates of TLF were reduced.[48] Despite the promise of the Magmaris device in these trials, limitations in device performance begun to emerge as continued clinical data was gathered.

One of the first issues identified with the Magmaris device was the that it was not being completely absorbed. After the initial 12 months, up to 95% of the Mg was resorbed however, a calcium phosphate corrosion product remained. The presence of this calcium phosphate corrosion product was not shown to cause adverse effects, but the long-term biological response is unknown.[86, 89, 90] However, more concerning issues associated with unexpected, early scaffold collapse became apparent as the Magamris device was more widely applied in the clinical setting. Gutiérrez-Barrios et al.[91] investigated the outcome of 90 patients with acute coronary syndrome treated with the Magmaris device at 18 and 24 months. 30% of patients imaged with optical coherence tomography (OCT) from this study (14/46) had suffered from ISR which was attributed to early scaffold collapse in the majority of cases (10/14). The cause of this early scaffold collapse was attributed to rapid loss of radial force of the device.[91] Consequently, the Magmaris device was only recommended in patients with simple lesions with low calcification. As result of these findings Biotronik refined their device and developed a new iteration, the Dreams 3G scaffold. Detailed design information is limited, but the new device has increased radial strength and reduced strut thickness (117x150µm for devices with a nominal diameter of 3 and 3.5mm). This is achieved, in part, through application of their new BIOMag alloy (6.25wt% Al with the balance Mg). A pre-clinical study showed the device provided support to the vessel walls in a porcine model for 3-6 months.[92-94] 6 and 12 month data is currently available from the first-in-man study of the new Dreams 3G device.[93, 94] A total of 116 patients with coronary artery lesions were selected for the study. The early (6 and 12 month) data have shown that the rates of TLF remain low, as in the Magmaris device, whilst the rates of late lumen loss are much improved. From this controlled trial it suggests hope that the new design with new alloy composition has improved the device's performance, allowing it to compete with current DES.[93, 94] However, much more testing is required to truly assess the efficacy of this new device, though early results suggest that the improved alloy composition has allowed this new device to more appropriately treat CVD, providing future hope to the industry as a whole.

2.2 Deformation of Magnesium

One of the key limitations of applying Mg alloys in BVS technology is their relatively poor mechanical properties which is primarily attributed to the lack of easily activated deformation modes at room temperature.

2.2.1 Slip

Pure Mg often exhibits relatively poor ductility and anisotropic properties, which is largely caused by its hexagonal close packed (HCP) crystal structure limiting the number of easily activated slip systems at room temperature. In HCP materials slip activates along the basal ⟨a⟩, prismatic ⟨a⟩, first-order pyramidal ⟨a⟩, and second-order pyramidal ⟨c+a⟩ slip planes as shown in Figure 2.2.[95] Slip is activated on these planes when the stress acting on them in the slip direction reaches some critical value, defined as the critically resolved shear stress (CRSS).[96] Basal slip is the most easily activated slip system in Mg as it has a CRSS at room temperature (0.5-1MPa). Prismatic and pyramidal slip have higher CRSS (≈40 and 80MPa respectively) at room temperature.[97] The high CRSS of prismatic and pyramidal slip means basal slip dominates during deformation of Mg. Basal slip only provides two independent slip systems both acting in the ⟨a⟩ direction, meaning it alone does not satisfy the von-Mises criterion for a ductile material.[96] The von-Mises criterion states that at least five independent slip systems are required for a material to undergo arbitrary deformation. The basis behind the requirements of this criterion is that arbitrary deformation involves 6 strains. However, during deformation, the total volume remains constant, meaning that a constraint is applied, resulting in 5 independent strains being required to accommodate arbitrary deformation. These can be accommodated through 5 independent slip systems.[98] The large difference in CRSS of the slip systems meant it was originally thought that only basal slip would be active during deformation. However, elongations to failure of 5-30% (depending on grain size and texture) are achievable in Mg and its alloys which would not be possible if only basal slip were active.[96] Despite the high CRSS of

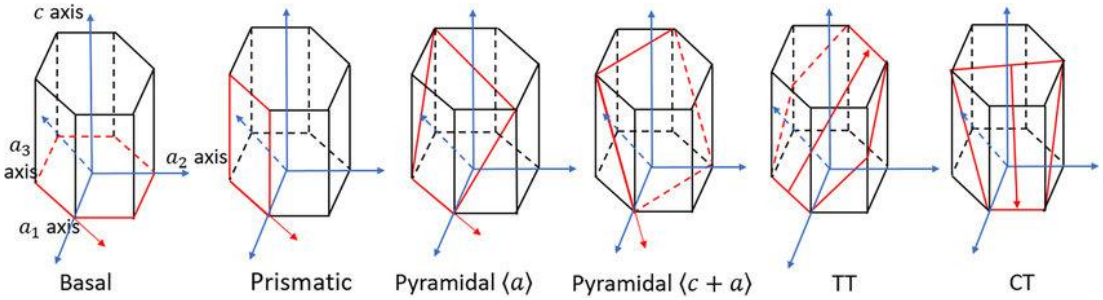

Figure 2.2: Slip and twinning systems in Mg[95]

prismatic and pyramidal slip determined through single crystal studies, in order to explain the, relatively, high ductility of Mg polycrystals these slip systems must be active. During deformation of Mg, grains well aligned for basal slip can be constrained by surrounding grains, that are not well aligned for basal slip, leading to the build-up of high, incompatibility stresses at the grain boundaries. These incompatibility stresses can be sufficient to activate non-basal slip as they can be up to five times that of the applied stress.[99, 100 101]

The dominate slip system can also be affected by the inter planar spacing. In HCP metals, such as Zr and Ti, prismatic slip is the dominate slip system. The Peierls-Nabarro stress defines the minimum shear stress required for dislocation motion and decreases with increased planar spacing. In Zr and Ti, the c/a axis ratio is reduced, compared to Mg, meaning the spacing between the basal planes is reduced relative to the spacing of the prismatic planes. This reduction of the c/a axis ratio results in prismatic slip becoming the dominate slip system in these metals.[102] Reducing the c/a axis ratio of the Mg HCP crystal structure through appropriate alloying can be used to improve ductility through increasing activation of prismatic slip. One example of this is seen in MgLi alloys. When low levels (<5.5wt%) of Li are alloyed with Mg the Li remains in solution and reduces the interplanar spacing of the basal planes, causing the c/a axis to reduce. This results in improved ductility of these alloys through increased activation of prismatic slip.[103] When alloyed above 5.5wt% a Li rich phase forms with a BCC structure which further improves the ductility of the alloy though at the expense of strength and corrosion resistance which both decrease with the formation of this phase.[48] Experimentally alloying with Li has been shown to also increase the activation of pyramidal slip which is vital in accommodating strains along the c-axis. The mechanisms behind the increased activation of pyramidal slip are unclear and cannot be explained by the reduced c/a axis ratio.[104, 105]

2.2.2 Twinning

Due to the lack of easily activated slip systems at room temperature, twinning plays an important role in the deformation of Mg alloys, particularly tensile twinning. Deformation twins form when a crystal shears along a plane (mirror plane), resulting in “twinned” and “un-twinned” regions forming. The twinned region is a mirror image of the un-twinned region, sheared at a specific angle (defined by the twinning mode) about the mirror plane. Twinning, unlike slip, only operates in one direction meaning its activation depends upon the straining direction of the grain. In Mg alloys, tension and compression twins are activated when the c-axis of the HCP crystal structure is strained in tension and compression respectively. Tensile twinning commonly

occurs on the $\{10\bar{1}2\}$ plane and compression twinning on the $\{10\bar{1}1\}$ plane.[106] Tension twinning is the dominant twinning mode in Mg and after basal slip it is the second most readily activated deformation mode with a CRSS of approximately 2MPa in single crystal studies. Compression twinning has a much higher CRSS (100MPa) and as such is less readily activated.[107] Both tensile and compressive twinning result in a reorientation of the grain about the twin plane, the angle of this reorientation is consistent for each twin mode. $\{10\bar{1}2\}$ twins result in a reorientation of the basal pole by 86° whereas $\{10\bar{1}1\}$ twins result in a reorientation of 56°.[108]

As mentioned, twinning is directional, however if a heavily twinned microstructure is deformed through reverse loading, tensile and compressive twins have been shown to reverse, termed detwinning. Jäger et al.[109] investigated the detwinning effect during bending of pure Mg wires with a diameter of 250µm. The nature of deformation through bending results in a varying stress state developing through the sample with compression along the inner diameter (ID) and tension on the outer diameter (OD) of the bend, this stress state is of course reversed if the wire is straightened and bent in the opposite direction. Owing to the typical basal texture developed in Mg wires the majority of grains were aligned with their c-axis perpendicular to the drawing direction (DD). Therefore, during compressive loading (in the DD), tensile twinning is preferred and vice versa. Jäger et al.[109] first showed that during progressive bending around smaller diameters tensile twining was activated along the ID of the bend and the activation of tensile twinning was increased as the bend diameter decreased. The authors also investigated the deformation during a single cycle of reverse loading through bending the wire around a 1.5mm radius, straightening and reverse bending around a 1.5mm radius. During this loading cycle tensile twinning was observed along the ID of the bend, upon straightening "detwinning" was observed in this region and upon reverse bending tensile twins were developed on other side of the wire as it underwent compressive loading, Figure 2.3. In order to accommodate the deformation twins during bending, slip is activated resulting in a build-up of dislocations that do not exhibit the same reversibility as the twins upon reverse loading. Thus, during repeated bending there is a build-up of dislocations and residual twins (though detwinning can occur, not all deformation twins will de-twin and as such can be termed residual twins) during repeated bending cycles that contributes to a loss of mechanical integrity. To demonstrate this Jäger et al.[109] performed repeated bending (5 cycles) on the wire and visualised the microstructure with kernel average miss orientation (KAM) mapping, Figure 2.4. From Figure 2.4 it can be seen that following the 5 cycles of loading a clear band of stress concentration develops through the wire that is caused through the progressive build-up of dislocations and residual twins. The build-up

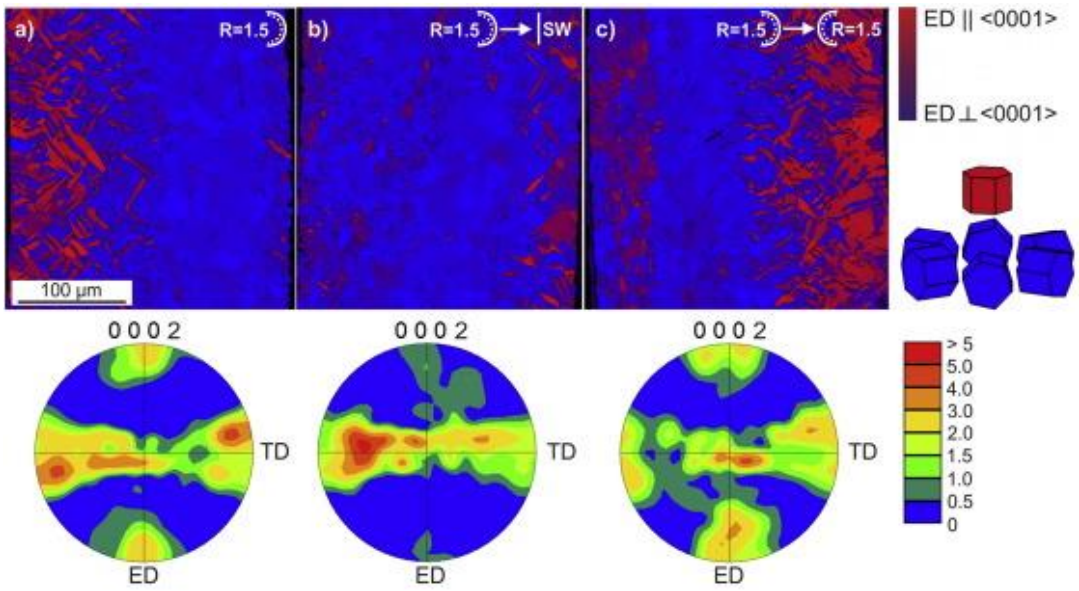

Figure 2.3: A wire bent around a radius of 1.5 mm (a), then straightened (SW) (b) and consequently bent again around a radius of 1.5 mm in the opposite direction (c). Colour schemes on the right depict orientation of the c-axis with respect to the ED (ED is vertical); original as-extruded orientation is in blue, and twinned reorientation is in red. Scale bar in a) is valid for all micrographs. Corresponding (0002) pole figures below are calculated from OIM maps and show texture evolution during bending due to {1012} twinning[109]

of dislocations and residual twins will act as potential sites for crack initiation during fatigue testing.[109]

2.2.3 Shear Band Formation

Shear bands are bands of high localised strain that are often developed during forming. Shear bands are typically associated with strain localisation initiating along compression and double twins. Compression and double twins result in a reorientation of the grain that offers a softer orientation for basal slip. Consequently, basal slip can be readily activated resulting in a build-up of internal strain within the shear band that, unlike the twin boundary, can extend through multiple grains. [108, 110] Owing to the high concentration of internal strain within shear bands they

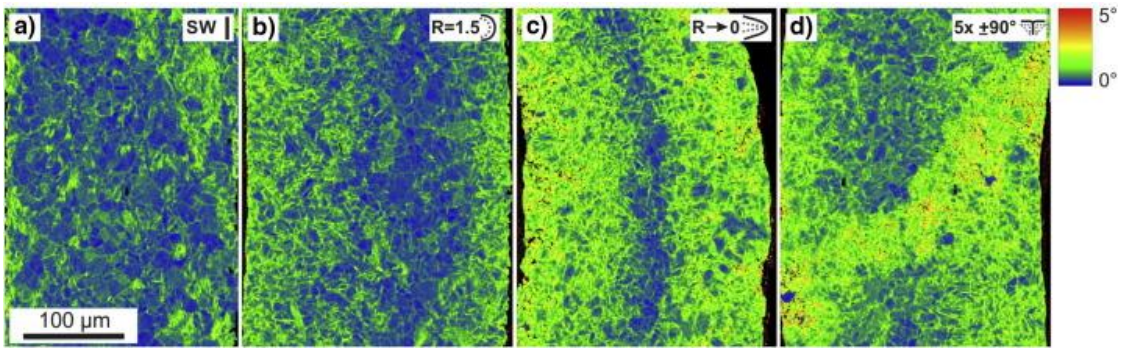

Figure 2.4: Stress concentrations of the wires visualized via KAM; a) as-extruded straight wire; b) after bending around a radius of 1.5 mm; c) after bending around a sharp edge; d) after repeated bending (5 × ±90°) around a right angle. Note that a band of strain[109]

are often pre cursers for failure, whilst they also act as nucleation sites during recrystallisation.[108, 110] In Mg alloys typically few shear bands are formed but those that do are often large and traverse through multiple grains. This was shown by Sandlöbes et al.[111] when the authors observed large shear bands within the microstructure of a rolled pure Mg plate that begun to crack around the edges after 10% thickness reduction. However, the authors compared this to a Mg-3Y alloy plate. In the Mg-3Y plate, cracking was only observed after a 40-50% area reduction. The microstructure of the Mg-3Y alloy contained a high number of small shear bands evenly distributed through the microstructure. The authors attributed this to increased activation of pyramidal slip, contraction, and double twinning in the Mg-3Y alloy compared to the pure Mg sheet. Instead of initiating early failure the formation of a homogeneous distribution of small shear bands improved ductility through allowing an additional path for internal strain to be stored during continued deformation.[111]

2.2.4 Deformation Texture

Mg and its alloys typically develop a basal texture during forming via standard rolling, extrusion and drawing routes.[107] Following forming, the basal planes of the grains are aligned parallel to the forming direction, this is termed the basal texture. The basal texture developed in Mg alloys during rolling and extrusion are described in the work of Nie et al.[107] Figure 2.5 and Figure 2.6 reproduce figures from this work that aid in the understanding of the deformed texture developed in rolled and extruded Mg alloys respectively.[107] The texture shown in Figure 2.6 for the extruded alloy is similar to that which is typically developed in drawn Mg alloys.[112] Typically the basal texture developed during forming of Mg alloys is maintained during recrystallisation. Although through selective alloying and tailoring of thermal processing routes the texture can be weakened during recrystallisation.

The basal texture is developed due to the dominance of basal slip during deformation. Activation of basal slip during forming, causes grains to reorientate with their basal planes parallel to the forming direction. Further, in grains aligned with their c-axis parallel to the forming direction, where the activation of basal slip will be most suppressed, tensile twinning can be readily activated. This results in the reorientation of the grains by 86°, which further promotes the formation of the basal texture.[107] This strong texture coupled with the dominance of basal slip, low activity of the non-basal slip systems and directionality of deformation twinning explain the anisotropic properties associated with Mg alloys. Much work has been conducted on characterising the anisotropic properties of Mg alloys as it severely limits the application of these

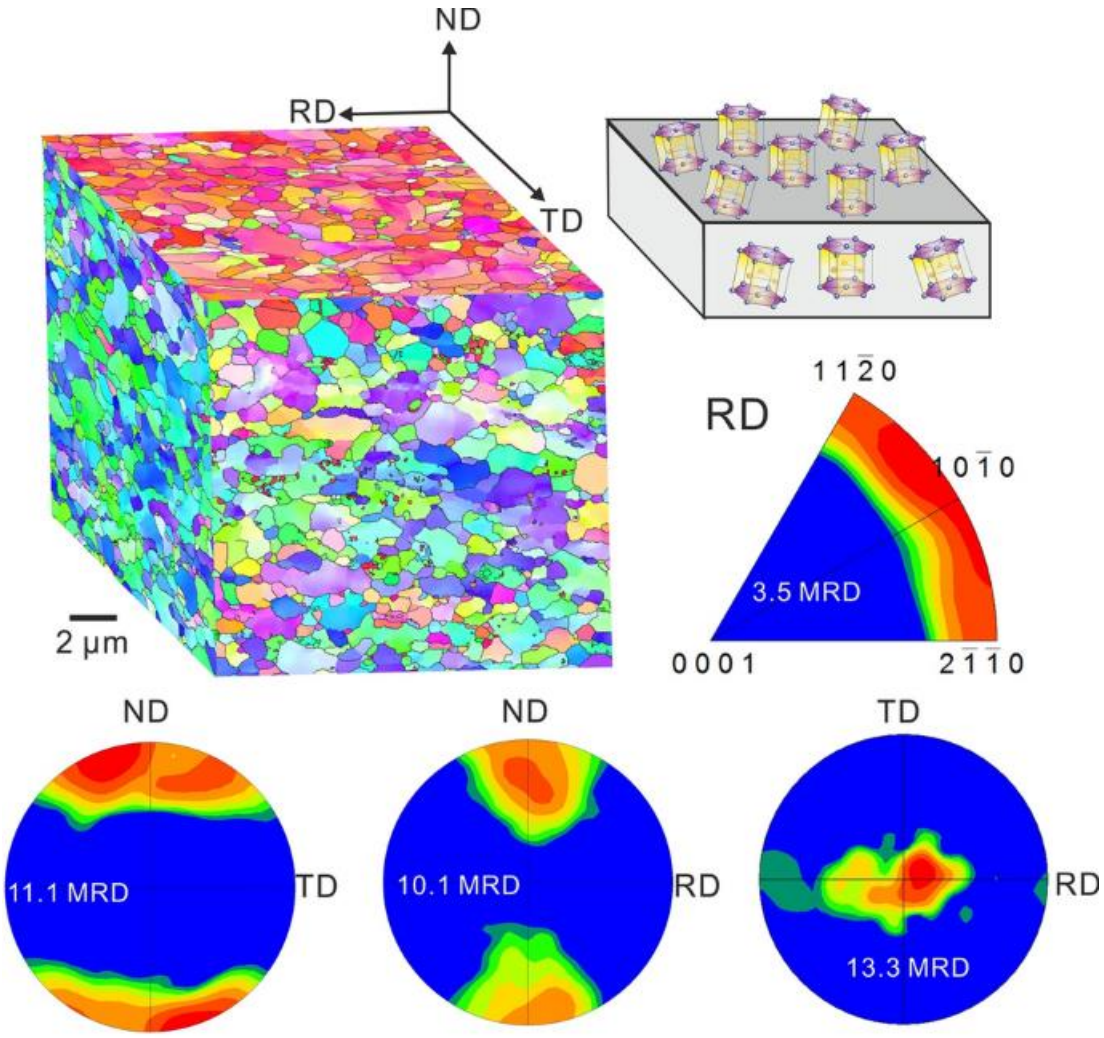

Figure 2.5: Cube of EBSD orientation maps of TD–ND, RD–ND, and RD–TD surfaces of a cold-rolled pure Mg sheet. TD is the abbreviation of transverse direction. Schematic illustration showing a basal texture, i.e., [0001]//ND. EBSD (0002) pole figures of TD–ND, RD–ND[107]

alloys in the design of components/devices that will experience multi axial loading. Wu et al.[113] demonstrated this anisotropy through tensile and compression testing of a rolled AZ31B alloy, (that exhibited a strong basal texture) along the rolling (RD), normal (ND) and transverse directions (TD). Figure 2.7 shows the results from this study where the anisotropic properties of the alloy are clearly shown. In all the loading directions the grains are not well aligned for basal slip meaning the influence of additional deformation mechanisms will play a key role in the deformation of the samples. Samples loaded in tension along the TD and RD exhibited the highest ductility as, the grains are well aligned for the activation of prismatic slip. Whilst compression along the TD and RD will result in c-axis extension, resulting in activation of tensile twinning. This results in the stress-strain curves following the typical trend associated with twinning dominated deformation, low YS followed by an initial low hardening rate before a rapid increase in hardening. Similarly, when loaded in tension along the ND the grains will be well

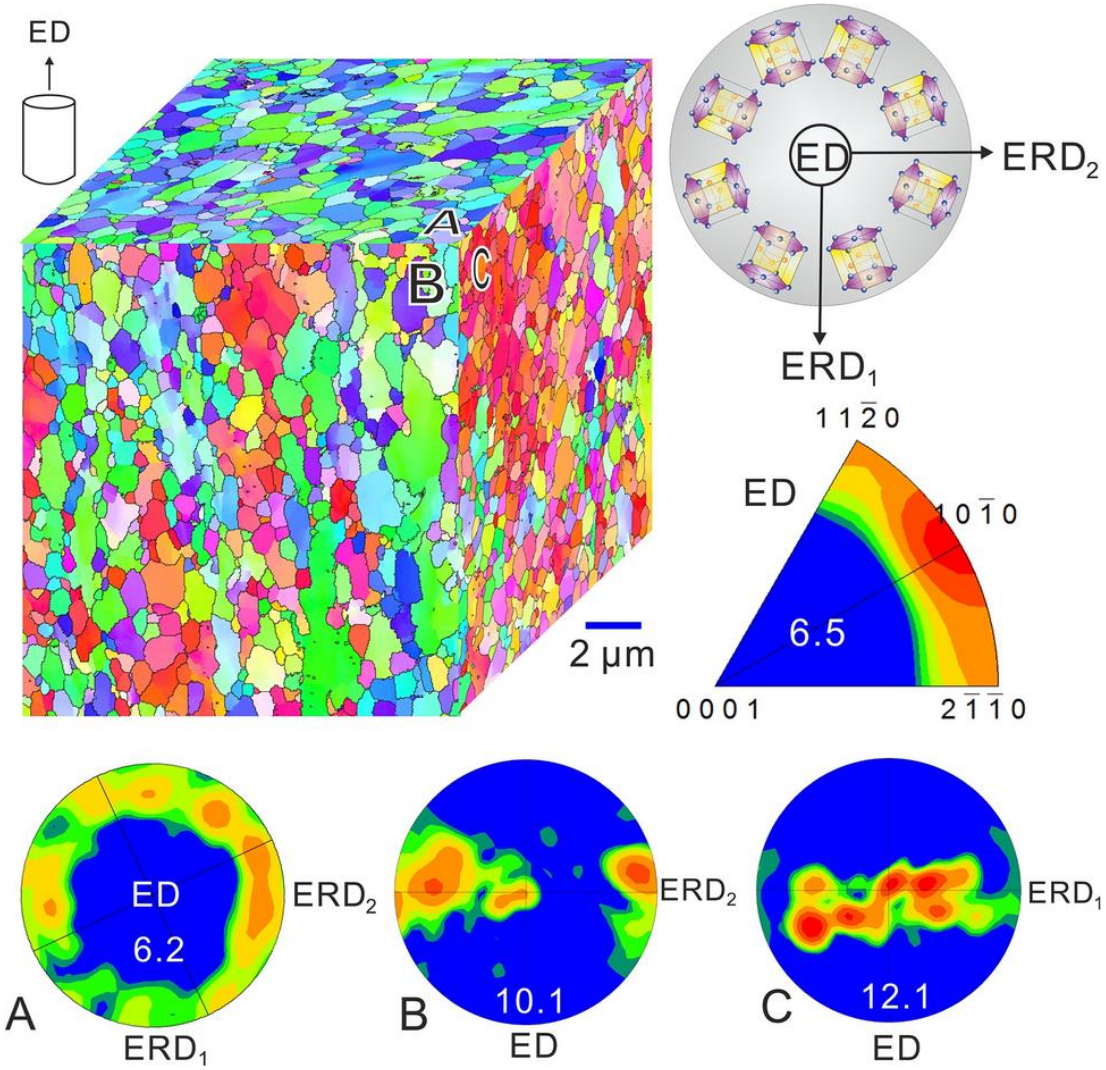

Figure 2.6: Cube of EBSD orientation maps of pure Mg extruded at 80 °C with a ram speed of 0.1 mm s−1 and an extrusion ratio of 19:1. EBSD basal pole figures of three surfaces of the cube, and inverse pole figure along the ED. The average grain size is ~1.2µm[107]

aligned for tensile twinning and the stress-strain curve is similar to the curves seen for the compressive loading along the TD and RD. Finally, when loaded in compression in the ND the grains are poorly aligned for both basal and prismatic slip as well as tensile twinning. This results in reduced ductility of the alloy when loaded in compression along the ND.[113] The anisotropic properties of Mg alloys can be reduced through alloying additions to increase the activation of non-basal slip at room temperature and weakening of the strong basal texture.

2.3 Recrystallisation

Recrystallisation occurs in deformed metals when heated above a specific temperature, termed the recrystallisation temperature, and results in the deformed grains being replaced by new, strain-free grains. The recrystallisation temperature depends on the alloy composition and prior

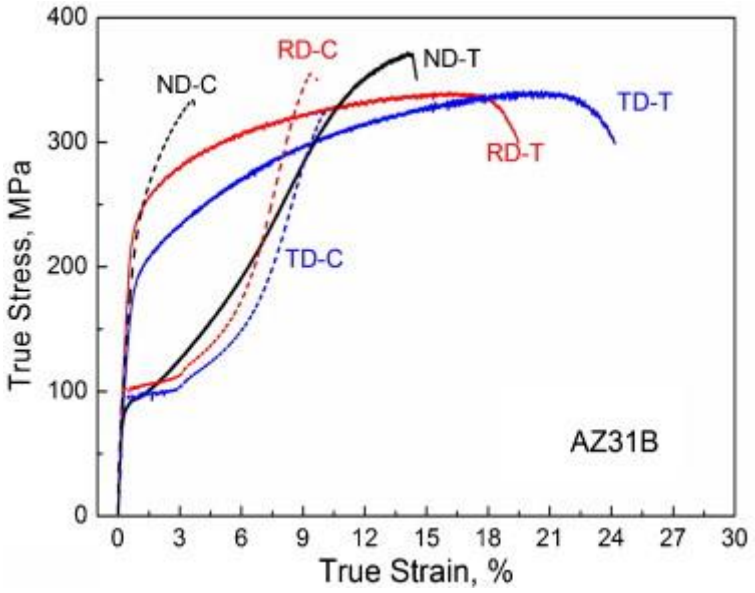

Figure 2.7: The monotonic mechanical responses loaded, respectively, along the RD, TD and ND directions both under compression (C) and tension (T) of AZ31B alloy. Solid lines for tension, and dashed lines for compression[113]

deformation. Recrystallisation can occur during deformation, termed dynamic recrystallisation (DRX), or statically during annealing treatments post deformation, termed static recrystallisation (SRX). DRX plays an important role in the hot forming of Mg alloys and much work has been conducted to control the DRX processes activated during hot forming of Mg alloys.[114] However, as this work focuses on the annealing of cold drawn Mg alloy wires only SRX mechanisms will be discussed here.

The recrystallisation of a strain free microstructure is a complex process that can be broken down into 3 key stages. Firstly, recovery of the deformed microstructure takes place, where the internal strains of the deformed microstructure are slowly relieved, and the dislocation density of the deformed material lessens. Next, nucleation of new, strain free, grains initiates, first at the regions of highest internal strain (or greatest deformation). Following nucleation, these new grains begin to grow and consume adjacent deformed regions eventually leading to a fully recrystallised microstructure of new strain-free grains. In Mg alloys typically the recrystallised microstructure maintains the same texture as that of the deformed microstructure. This means that the basal texture is typically maintained in Mg alloys following recrystallisation. The recrystallisation of a basal texture is attributed to the nucleation mechanisms activated during annealing.[107] The following subsections will discuss the four main nucleation sites and their influence on the recrystallised texture of Mg alloys.

2.3.1 Grain Boundary Nucleation

Grain boundaries are common sites for nucleation in Mg alloys. During deformation dislocations can easily pile up at grain boundaries, resulting in an increase in stored energy. This is relived through bulging of the boundary into the adjacent grain. These sites act as potential nucleation sites during SRX, owing to the build-up of internal stored energy. In typical Mg alloys produced via cold forming techniques where dislocations readily pile up at grain boundaries, these sites act as the predominate nucleation sites during subsequent annealing.[115] Generally, grains nucleated along prior grain boundaries have similar orientations to the deformed microstructure. Consequently, in Mg alloys where the deformed microstructure typically exhibits a strong basal texture, so too does the recrystallised microstructure post annealing.[115-117]

2.3.2 Twin Boundary Nucleation

Nucleation from deformation twins during annealing can result in a shift in texture from the original microstructure following recrystallisation. As described, there are several deformation twinning mechanisms activated within Mg alloys with $\{10\bar{1}2\}$ tensile twinning, $\{10\bar{1}1\}$ compression twinning and $\{10\bar{1}1\}$-$\{10\bar{1}2\}$ double twinning being the most common. These twinning mechanisms result in the reorientation of the grains by 86°, 56° and 38° respectively.[118] Typically, grains nucleated from within twins tend to grow with similar orientations to the twinned region meaning nucleation of grains from within compression and double twins have non-basal orientation.[119, 120]

Nucleation from tensile twins is not frequently observed as the reorientation of the grains by 86° means the grains are poorly aligned for the activation of basal slip. Consequently, during further deformation this results in a low build-up of internal stored energy at tensile twins meaning nucleation is initiated first from regions of higher internal stored energy, such as compression and double twins.[118, 120] The reorientation seen with compression and double twins more favourably aligns grains for basal slip, resulting in a build-up of high internal energy at these bands. The high internal stored energy at these bands makes compression and double twins' ideal sites for nucleation. The contribution of grains nucleated from compression and double twins to the overall texture post recrystallisation is limited as often the number of these twins formed during deformation are relatively limited in common Mg alloys. Further, recrystallised grains tend to not grow beyond the twin boundary meaning their influence on the

final microstructure is limited.[119-122] However, grains nucleated from intersections between double twins with grain boundaries and twin boundaries have been reported to grow into the surrounding matrix and consequently have a higher influence on the final recrystallised texture. Grains nucleated from these regions grow with non-basal orientations and have been associated with recrystallisation of non-basal textures.[118]

Nucleation within tensile twins has been observed when the twin band thickness is much wider than the surrounding matrix. Xin et al.[123] loaded a Mg-3Al-Zn alloy (in an orientation to promote the activation of tensile twinning) to varying extents to produce deformed microstructures with a high density of tensile twins with varying thicknesses. The samples deformed to a lesser extent developed thin twins where the adjacent matrix was much larger than the twin boundary. In the highly deformed sample, the twins were thicker than the surrounding matrix. Following annealing the authors noted that a clear thickness effect was apparent. During annealing the narrow twins were consumed by the surrounding matrix whereas when the twin thickness was larger than the surrounding matrix the grain nucleated from within the twin consumed the surrounding matrix. Consequently, in the deformed samples with large, thick, twin boundaries nucleation from within the tensile twins dominated. Consequently, the recrystallised texture had an 86° rotation from the deformed texture, as the recrystallised grains nucleated with the same orientation as the tensile twins. In contrast in the samples with thin twins, the deformation texture was maintained following recrystallisation. A similar shift in texture has been observed by Kim et al.[115] following recrystallisation of an Mg alloy where recrystallised grains from tensile twins dominated the final microstructure.

2.3.3 Shear Band Nucleation

Shear bands are ideal nucleation sites in Mg alloys as they are bands of high internal energy, where nucleation will preferentially activate. Within shear bands there is generally a spread in internal orientation, meaning that grains nucleated from these bands exhibit a wide range of orientations. Consequently shear band nucleation can contribute to weakening of the strong basal texture developed during forming.[124-126] However, in common Mg alloys typically few, large shear bands are developed meaning any contribution of shear band nucleation to the overall recrystallised microstructure is generally limited. Nevertheless, it has been shown that in Mg alloys, grains nucleated from shear bands typically exhibit a range of orientation spreads and can contribute to weakening of the strong basal texture of Mg alloys.[117] Should the number of

shear bands present throughout the deformed microstructure be increased, the contribution of grains nucleated from within these bands to the overall, recrystallised, texture will also increase.

2.3.4 Particle Stimulated Nucleation

Particles distributed throughout the microstructure can both act to suppress and promote recrystallisation. Small particles can act to pin boundaries, restricting their mobility and retard recrystallisation, whilst larger particles (>1μm) can act as potential nucleation sites.[127] Larger secondary phase particles act as barriers to dislocations during forming which results in strengthening. This results in a build-up of internal stored energy at these particles, making them ideal sites for nucleation of new grains during thermal processing.[127] The deformation zone around the particle generally has high misorientation and consequently grains nucleated from PSN have random orientations. However, PSN is in competition with all other nucleation mechanisms during thermal processing. Typically grains nucleated from PSN are small and tend to lose out to other nucleation mechanisms which have a growth advantage and dominate the final microstructure. Therefore, grains nucleated through PSN have little contribution to the overall texture developed in Mg alloys.[117, 127-130]

2.4 Rare Earth Alloys

The rare earth elements (REE) describe 17 chemical elements that have similar chemical properties, they are made up of the Lanthanides, Sc and Y. REE that are commonly alloyed with Mg are La, Ce, Nd, Eu, Gd, Dy, Er and Y. REE were originally alloyed with MgAl alloys to improve strength and creep resistance.[131] Since, REE have been widely applied to Mg alloys to improve strength through both precipitation and solution strengthening, such as Y and Gd which exhibit increased strengthening capabilities over other alloys in solid solution.[132, 133] REE have also been shown to improve ductility of Mg alloys through increasing the activation of non-basal slip and weakening of the strong basal texture developed during forming of Mg alloys.[134-136]

2.4.1 Rare Earth Texture

As described in Section 2.2.4 Mg alloys generally develop a basal texture during standard forming processes. This texture limits the formability of the alloys during further deformation in the forming direction and creates the yield anisotropy seen in Mg alloys. Ball and Prangnell[137] were one of the first to observe weakening of this texture following extrusion of the MgRE alloy WE53. They observed that the basal plane had no alignment with the extrusion direction, which

resulted in reduced yield asymmetry of this alloy compared to a non-RE alloy.[137] Since, alloying Mg alloys with REE has been extensively researched for the purpose of weakening the strong basal texture and formation of the characteristic "rare earth texture".[126, 138-141] There are competing hypothesis on the underlying mechanisms responsible for the formation of the RE texture.[129, 142] These competing hypotheses generally centre on different recrystallisation mechanisms that will be discussed further in the following section. Although the underlying mechanisms are not well understood the effect on the mechanical properties of the RE texture is better understood as well as the effect the alloy composition and thermal processing conditions have on its development.

The RE texture is primarily beneficial in improving the ductility and reducing the anisotropy of Mg alloys. Wu et al.[143] investigated the effect of the rare earth texture in a range of MgY binary alloys. The authors prepared extruded pure Mg, Mg2Y and Mg4Y samples with the same grain size for tensile testing. The pure Mg sample exhibited a standard strong basal texture with the c-axis of the grains perpendicular to the extrusion direction, whereas the Mg2Y and Mg4Y alloys developed a more random texture post annealing. As a result, the tensile elongation to failure of the pure Mg increased from 15% to 21 and 30% for the Mg2Y and Mg4Y alloys respectively. With the grain size remaining constant between the alloys the authors attributed the increased ductility to the weakened basal texture. Though with the texture developed in the Mg2Y and Mg4Y alloys being similar, texture alone cannot explain the increase in ductility between these two samples. Stanford et al.[144] showed a similar effect in the investigation of a range of four rolled MgGd alloys with varying Gd content.[144] They demonstrated that the Gd containing alloys developed weaker textures post annealing and hence increased ductility as seen in Figure 2.8. Stanford et al.[144] showed that the texture intensity of the MgGd alloys decreased rapidly up to ~1 wt% of Gd and remained relatively unchanged above this, yet there was a clear increase in ductility. This suggests that the improvements in ductility seen in RE alloys is not solely attributed to weakening of the basal texture.[144]

In order for the RE texture to be developed in MgRE alloys some minimum RE content is required, termed the critical concentration. Hantzsche et al.[145] found that the RE texture in Ce, Nd and Y binary alloys only developed once some minimum concentration of alloying additions was reached, as shown in Figure 2.9. When the RE content is below the critical concentration a

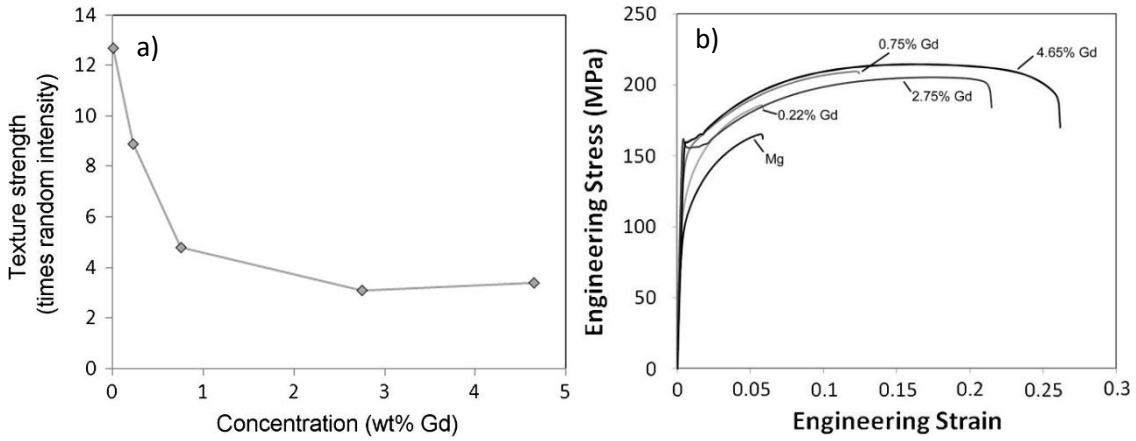

Figure 2.8: a) Effect of alloy content on the recrystallisation texture strength of Mg–Gd binary alloys b) Typical stress–strain curves for the alloys examined, all with a fully recrystallised microstructures and a 10 µm grain size[144]

basal texture is recrystallised but once the critical level is reached a RE texture is recrystallised in each alloy. No further weakening of the texture was seen as the RE content was increased beyond the critical concentration.

2.4.2 Static Recrystallisation

The formation of the rare earth texture is generally developed post recrystallisation as opposed to being related to alterations in the deformation texture. The RE texture can be developed in MgRE alloys (with sufficient RE content) during thermomechanical processing and post forming following an annealing process. This work focusses on the application of a cold drawn Mg alloy wire so therefore the focus here will be on the SRX of MgRE alloys. There are many competing

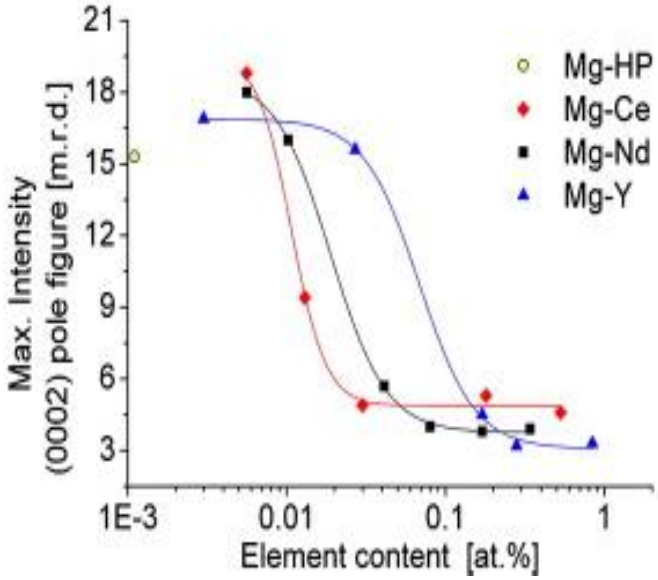

Figure 2.9: Maximum (0 0 0 2)-pole figure intensity after annealing[145]

mechanisms suggested for the recrystallisation of the RE texture such as, increased non-basal slip, preferential nucleation sites, orientated grain growth and solute drag.[126, 140, 146]

A number of studies have demonstrated that a high density of shear bands are developed during forming of MgRE alloys and the recrystallised microstructure is dominated by randomly orientated grains nucleated from these bands.[121, 124, 126, 139, 147, 148] Compression and double twins are often both present in MgRE alloys microstructure along with a high density of shear bands, meaning it is often difficult to decern if nucleation from either are primarily responsible for the formation of the RE texture. However, a study by Guan et al.[140] addressed this by investigating the recrystallisation of a WE43 alloy deformed to contain few shear bands but a high density of double twins. Their work showed that the preferred nucleation site in the samples were from double twins (in particular at double twin-double twin and double twin-grain boundary intersections). As these sites were the main nucleation sites and dominated the microstructure they were responsible for the RE texture developed post annealing in the samples investigated.[140] Despite both double twins and shear bands being shown to be, in part, responsible for the RE texture their presence alone is not sufficient to develop the RE texture as in non-RE alloys with a high density of shear bands, the RE texture is not developed during SRX.[149]

It has been proposed that the segregation of RE atoms to the grain boundaries results in oriented growth that promotes the formation of the RE texture through a solute drag effect that retards some recrystallisation mechanisms.[146, 150, 151] The segregation of these RE atoms restricts recrystallisation along grain boundaries (that generally nucleate and grow grains with the same orientation as the deformed microstructure) and promote nucleation at sites that nucleate and grow grains with a more random orientation, such as from shear bands and double twins.[129, 151] Robson et al.[152] showed that the segregation of solute atoms to the grain boundaries can be estimated by the size-misfit between the solute atoms relative to the Mg matrix.[152] All REE have larger atomic radii compared to Mg, meaning they cause misfit strains to form in the matrix of the smaller Mg atoms. These misfit strains are relaxed through the diffusion of the larger REE to the grain boundaries.[151, 152] The segregation of REE can lead to high local concentrations of REE along the grain boundaries compared to the Mg matrix. In a Mg0.15Y (at%) alloy there was found to be a concentration of 2.4at% Y in a grain boundary.[150] Segregation of REE to the grain boundaries results in a solute drag effect that restricts boundary mobility, resulting in the growth rate of grains nucleated along the boundaries decreasing.[117, 152, 153] This allows grains nucleated from shear bands (with off-basal orientations) to have a growth advantage over those nucleated

from the grain boundaries (with basal orientations), resulting in shear band nucleation dominating and developing the RE texture.[117, 154] Solute drag is temperature dependant and its drag effect is increased with increasing temperature up until approximately 500°C and decreases above 500°C. This is attributed to the balance between increased solute diffusivity and boundary mobility at higher temperatures. As temperature is increased the diffusivity of the REE increases meaning the concentration of REE at the boundaries increases, thus increasing the drag effect. However, as the temperature continues to increase so does boundary mobility and when sufficiently high the boundary can break free of the solute atmosphere formed, which has been shown to correspond with the recrystallisation of the typical basal texture during high temperature annealing.[154] However, during the SRX of a WE43 alloy with a high density of shear bands and double twins at 545°C (where solute drag and Zenner pinning would be suppressed) a non-basal texture was still recrystallised, indicating that the density of shear bands and double twins must also play a role in the formation of the RE texture.[126]

Further, Basu et al.[124] demonstrated in a MgGd binary alloy the RE texture was not developed during annealing at lower temperatures (<350°C) but following annealing at 350°C and above a RE texture was developed. In a follow up study Basu et al.[117] it was shown that in a quaternary alloy (Mg–1Zn–0.6Zr–1Gd) the transition temperature for RE texture formation was lowered compared to the binary MgGd alloy, to 300°C. This was attributed to increased shear band formation and segregation of both RE and Zn atoms to grain boundaries resulting in increased solute drag. The greater effect of solute drag combined with increased shear banding allows the dominant recrystallisation mechanism to transfer to shear band nucleation at lower temperatures compared to the binary MgGd alloy.[117] As mentioned the RE texture is generally associated with MgRE alloys however the RE texture has been shown to be developed in Ca containing alloys.[121, 147, 155, 156] As with REE Ca atoms are larger than the Mg atoms and as such segregate to the boundaries, which can restrict grain boundary mobility through solute drag and activate texture weakening. However, in MgCa alloys, generally only weakening of the basal texture is observed rather than development of more random RE textures. Though this weakening effect can be amplified in MgCaZn ternary alloys. The segregation of both Ca and Zn to the grain boundaries decreases the boundary mobility more than Ca alone, resulting in increased solute drag and as such increased texture weakening.[147, 156]

2.5 Current Mg Alloys for bioresorbable devices

Numerous Mg alloys have been investigated for application in BVS technology, however of the range of alloys three, in particular, have gained much attention. Firstly, WE43, the alloy used in the Magmaris device is the most relevant Mg alloy in terms of BVS technology as it is the only alloy to be applied in a device applied widely in the clinical setting. MeKo (Sarstedt, Germany) have developed a MgRE alloy (Resoloy) specifically for application in BVS technology.[89] Finally a RE free alloy, ZX10, will be described. This alloy was developed specifically for bioresorbable medical devices and has been investigated for a range of applications. Its potential for use in BVS technology is clear with Biotronik currently holding a patent "Magnesium-zinc-calcium alloy and method for producing implants containing the same" (US-11499214-B2) for its use in a range of devices including in BVS technology.[157]

For each of the three alloys described, a range of mechanical properties can be found within the literature. However, concerning the topic of this work, data has been collated from articles investigating small diameter wires for application in bioresorbable medical devices.[158, 159] This data is summarised in Table 2-2 and will serve to provide a comparison for the alloys investigated as part of this work.

2.5.1 WE43

WE43 is a creep resistant MgRE alloy originally developed for the aerospace industry for use in components exposed to high temperatures. WE43 alloys contain 4wt% Y and 3wt% of a mixture of REE consisting mainly of Nd, often Zr is added as a grain refiner. WE43 is an age hardenable alloy, meaning its mechanical properties can be controlled through altering the aging process to control the size, distribution and structure of precipitates formed. The precipitation reactions in

Table 2-2: Mechanical properties of the small diameter WE43, Resoloy and ZX10 alloys

ALLOY	DIAMETER OF TEST SAMPLE (mm)	GAUGE LENGTH (mm)	UTS (MPa)	YS (MPa)	ELONGATION TO FAILURE (%)
WE43[158]	0.5	127	≈300	≈260	≈17
RESOLOY[158]	0.5	127	≈350	≈280	≈18
ZX10[159]	0.28	50	222	160	18.4

*It should be noted that the data on WE43 and Resoloy has been read from tensile plots from the relevant reference meaning some reading error in the values reported in the above table are to be expected

Mg-Y-Nd alloys have been widely studied and tend to follow a 4-stage precipitation process as follows.[160, 161]

Mg (SSSS)→β″ (DO_{19})→β′ (bco)→β1 (fcc)→β(fcc)

The above sequence is considered an acceptable approximation of the precipitation process but there are still conflicting reports on the composition of the phases present.[162] Regardless of the composition it is better understood how these precipitates develop throughout the aging process and how they affect the properties of the alloy.

The properties of WE43 are controlled through altering the aging process to produce the desired precipitate morphology and distribution to achieve the optimum mechanical properties for its application. Generally, when in solid solution WE43 exhibits maximum ductility and minimum strength. As the aging time is increased and a greater volume fraction of inter metallic particles (IMP) form, the strength increases whilst ductility decreases. In creep resistant applications where ductility is not required often the material will be aged for up to 48h at 280°C. When ductility is of more concern, such as in BVS design, the alloy may undergo a solution treatment, or be aged for only a short time to marginally increase the strength whilst minimising loss of ductility.[161, 163]

The type and volume fraction of precipitates formed can also directly affect the behaviour of WE43 in corrosive environments. A study by Argade et al.[163] investigated solution annealed, under, peak and over aged WE43 alloys corrosion resistance, through static immersion testing. The authors also conducted slow strain rate testing in NaCl solution to investigate the alloy's susceptibility to stress corrosion cracking (SCC). During static immersion testing all conditions of WE43 corroded through pitting. The solution annealed sample showed the highest corrosion resistance, which the authors attributed to the presence of Y and Nd in solid solution reducing the micro-galvanic effect seen in the aged samples between the Mg matrix and IMP. During the slow strain rate testing the various samples were tested at a strain rate of $10^{-6}s^{-1}$ in NaCl solution. The over aged sample exhibited the lowest susceptibility to SCC followed by the solution annealed sample. The aged samples all failed predominantly through intergranular cracking caused by anodic dissolution of the Mg matrix adjacent to cathodic IMP. As the particles precipitate along the grain boundaries in WE43, the matrix adjacent to these undergoes anodic dissolution, which can cause crack initiation and then propagation along the adjacent grain boundary. The over aged sample however shows the lowest susceptibility to SCC, which is attributed to the increased aging time allowing for the microchemistry between the grain

boundaries and Mg matrix to reach equilibrium. This is shown when analysing the fractured surfaces, as the authors note reduced intergranular cracking of the over aged sample, caused by more stable grain boundary chemistry.[163]

2.5.2 Resoloy

Resoloy (Mg-10Dy-1Nd-1Zn-0.2Zr) is an alloy designed specifically for use in bioresorbable medical implants. Resoloy's main alloying addition is Dy and was developed considering the impressive mechanical properties and corrosion resistance of Mg-10Dy.[164] Dy has a high solubility in magnesium (23.5wt% at 561°C) meaning it can improve the properties of magnesium through both solid solution and precipitation strengthening. Zr is alloyed to refine the grain structure and remove impurities during casting to improve corrosion resistance. In contrast to Dy, Nd has a low solubility in magnesium and is used to strengthen Resoloy through formation of precipitates along the grain boundaries. These precipitates also aid in stabilising the grain boundaries preventing excessive grain growth during annealing. Zn is alloyed to form long period stacking order structures with the Dy to primarily improve corrosion resistance.[158, 165] The strengthening effect of the Nd precipitates and long period stacking order phase on Resoloy are what sets it apart from the two other alloys discussed in this section.

As Resoloy was developed specifically for use in resorbable medical devices it was considered how it would corrode under static and dynamic loading in corrosive environments. Maier et al.[158] investigated the corrosion resistance of Resoloy and WE43 500µm wires during static immersion testing in Ringers solution at 37°C. Both alloys corroded through the formation of wide, shallow, and overlapping corrosion pits. Formation of these pits resulted in uniform corrosion of both alloys and neither developed pits that would act as stress concentration sites if they were subject to loading. Though both alloys corroded homogeneously the WE43 experienced more rapid corrosion attack. The Resoloy wire outperformed the WE43 wire during fatigue testing in air due to its higher YS (see Table 2-2). Despite the performance of Resoloy during the previous two tests, the WE43 alloy outperformed the Resoloy wire during corrosion fatigue testing. The WE43 alloy corroded in a similar manner to how it did during static immersion testing however the Resoloy wire was more susceptible to pitting and cracking. The authors reasoned that the poor performance of Resoloy during corrosion fatigue testing could be attributed to an inhomogeneous microstructure caused by restricted recovery of the drawn microstructure during annealing. During drawing of metal wires, the grains become elongated in the DD, which is undesirable for further deformation. Subsequent heat treatment procedures are required to

restore the microstructure. Both alloys in this study were recrystallised post wire drawing with the WE43 wire displaying a homogeneous globular microstructure, however the Resoloy wires microstructure partially maintained the drawing texture. The authors attribute this to the higher volume fraction of second phases present in Resoloy elongating in the DD and restricting the full recrystallisation of the microstructure.[158] In another study by Maier et al.[165] elongated IMP were also seen in extruded Resoloy tubes with a diameter of 35mm and wall thickness of 5mm. Only after solution heat treatment for 72h at 500°C were the elongated second phases removed from the microstructure, which increased the grain size significantly. These studies reveal a limitation in Resoloy caused by the elongation of the secondary phase particles during drawing and extrusion only being removed after solution treatment for a long time, which results in significant grain growth which is not desirable for mechanical properties.

2.5.3 ZX10

There is a growing desire to develop RE free magnesium alloys due to uncertainty over the long-term effects of RE elements.[166, 167] Mg-Zn-Ca alloys (ZX alloys) are proposed as a suitable RE free alloy due impressive mechanical properties brought about by the alloying additions of Zn and Ca which are essential elements in the body.[168] The solid solution strengthening capabilities of Zn in Mg is a well published effect.[133] Depending on the Zn/Ca atomic ratio different compositions of IMP are formed that restrict grain growth during thermal mechanical processing.[169] Grain refinement results from the restricted grain growth which improves both the strength and ductility of these alloys through the Hall-Petch effect and activation of non-basal slip.[170]

Originally ZX50 (Mg-5Zn-0.25Ca) was investigated as it showed impressive mechanical properties. As mentioned, the alloys in the ZX series achieve impressive ductility through suppressing grain growth through the formation of IMPs. ZX50 forms a noble $Mg_6Zn_3Ca_2$ phase, which acts as a cathodic site to the magnesium matrix, leading to severe localised corrosion and pitting.[168] Bakhsheshi-Rad et al.[169] showed that the IMPs formed in MgZnCa alloys is affected by the Zn/Ca atomic ratio and that for a ratio below 1.23, Mg_2Ca IMPs are formed. $MgCa_2$ is less noble than the Mg matrix meaning it acts as an anodic site and prevents the rapid dissolution of the bulk magnesium matrix, improving static corrosion resistance.[171] The ZX10 (Mg-1Zn-0.3Ca) alloy was developed as its Zn/Ca ratio falls below 1.23 so forms the anodic IMP $MgCa_2$ to benefit from improved corrosion resistance compared to the ZX50 alloy.[168]

The less noble $MgCa_2$ IMP is beneficial in improving the corrosion resistance in ZX10, though does not remove fully the consequences of galvanic corrosion, which can cause issues during fatigue testing. Electrochemical differences between the $MgCa_2$ IMP and Mg matrix result in preferential corrosion of the $MgCa_2$ phase. The preferential corrosion of the $MgCa_2$ phase still improves the static and dynamic corrosion resistance compared to ZX50 alloy however during cyclic loading dissolution of the $MgCa_2$ IMP can accelerate crack growth by creating an easy path for crack propagation.[168] A study by Jafari et al.[172] investigated the stress corrosion cracking and corrosion fatigue resistance of two ZX10 alloys heat treated at 325 and 400°C. Both alloys exhibited a bimodal microstructure, with regions of unrecrystallised and recrystallised grains, with a basal texture. The alloy treated at 325°C is expected to have contained a higher percentage of $MgCa_2$ IMPs in agreement with the work of Hofstetter et al.[173] The results showed the alloy treated at 325°C had improved mechanical properties compared to the alloy treated at 400°C owing to its more refined grain structure and greater volume fraction of IMPs but was more susceptible to corrosion fatigue. Both alloys contained $MgCa_2$ IMPs that would undergo anodic dissolution and provide an easy path for crack propagation but as the alloy treated at 325°C had a higher volume fraction of IMPs it was shown to be more susceptible to corrosion fatigue. Despite this ZX10 remains an attractive biomaterial that can undergo uniform corrosion in *vivo* but it is susceptible to corrosion fatigue, caused by anodic dissolution of its IMPs.

2.6 Summary

The potential to improve patients' quality of life with the successful development of BVS devices is clear. However, the relatively limited range of materials suitable for application in BVS technology makes developing BVS technology a challenging endeavour, meaning new alloys must be developed that exhibit suitable degradation and mechanical properties. Of the available materials, Mg alloys offer the most attractive solution owing to their appropriate degradation rates. One of the major limitations of Mg alloys is their lack of ductility which limits their application in the design of new balloon expandable BVS devices that are required to undergo high levels of plastic deformation during deployment. The reduced ductility of Mg alloys is known to be caused by both the limited number of available slip systems active at room temperature and the strong basal texture typically developed during recrystallisation following deformation. Careful tailoring of the processing routes applied during device manufacture can be carried out to improve the mechanical performance of Mg based devices.

The Magmaris device (manufactured from WE43) is the only Mg based BVS device that has been made available commercially. Limited data is available on microstructure and mechanical performance of the device. However, it is known that poor performance of the device in *vivo* has resulted in Biotronik applying a new alloy (Mg-6.25Al) in their most recent device iteration (Dreams 3G) that is currently in first-in-man clinical trials. The continued development of the Magmaris/Dreams device demonstrates that the promise of the successful development of a BVS device remains. However, new Mg alloys and device processing routes must be investigated to overcome the limitations associated with the poor ductility of Mg alloys.

The purpose of this thesis is to investigate two new Mg-Li-Y alloy wires for application in a novel wire form BVS device. To the author's knowledge no other Mg based wire form BVS device is being developed currently. This, coupled with the bulk of research regarding bioresorbable applications of Mg alloys not focusing on the use of fine wires, means that the available literature concerning the investigation of small diameter Mg alloy wires is limited. Consequently, this thesis is novel in its approach in characterising two new Mg alloy wires for application in an innovative wire form BVS device. Thus, the findings from this thesis will contribute to influencing the direction of travel for the development of new geometry Mg based BVS devices through assessing the feasibility of, not only, the two new alloys under investigation but also the suitability of the new geometry. Consequently, new processing routes are investigated and developed for application during the manufacture of the novel wire form device to optimise its mechanical performance. One of the key limitations of Mg based BVS devices is their limited expansion range which is influenced by the limited ductility of available alloys, which is controlled by several microstructural characteristics. Very limited in-depth analysis of Mg based BVS devices microstructure is reported in the available literature. This thesis is novel in its approach of investigating the microstructural development and mechanical properties of the Mg alloy wires used to manufacture the device. Characterisation of the microstructural development through the complete manufacturing processes (from cold drawn wire to final device) allows for a deeper understanding of the alloy wire's response to processing to be gained. Consequently, recommendations of future work and alloy development can be made.

Chapter 3: Materials and Experimental Methodology Development

3.1 Introduction

This chapter focuses on the development and validation of the various manufacturing and testing protocols used in the manufacture and analysis of the new Mg based BVS device under investigation. Bespoke manufacturing and testing protocols were required to be developed to analyse the Mg alloy wires under investigation, owing to their small diameter and reactive nature to environmental conditions. Initially, a vacuum oven was used to conduct an annealing study on the alloy wires provided. The known limitations of this setup, described in detail in Chapter 4, led to the development of a bespoke vacuum tube furnace. This chapter discusses the validation of both thermal processing routes and the design and manufacture of the vacuum tube furnace. The microstructural analysis and mechanical testing of the alloy wires and devices generally followed standard test protocols (described in Chapters 4 and 5). However, a new microhardness test protocol was required to be developed to determine appropriate loads for investigation of the microhardness of the fine alloy wires.

The design and manufacture of the BVS under investigation is also described in this chapter. The geometric design and configuration of the proprietary device was not investigated as part of this work, however during testing of the final BVS device, described in Chapter 5, it was found that a surface treatment step was required to be developed to improve device performance in expansion. The development of this procedure is described in detail in Section 3.6.

3.2 Materials

Two Mg-Li-Y alloy wires with compositions by weight of Mg-4Li-0.5Y (0.5Y) and Mg-4Li-2Y (2Y) were provided by the manufacturer cold drawn to a diameter of 125µm, in their cold drawn state and following an annealing process post the final drawing step. The 0.5Y and 2Y alloy wires underwent different drawing processes, with the final drawing step imparting 80% and 65% cold work respectively. As both alloys were supplied by an outside company, no further detail on the casting, drawing and annealing processes were provided and therefore cannot be included here.

3.3 Annealing Protocols

Two different annealing setups were investigated in this work to develop optimised thermal processing routes for both cold drawn alloy wires and the final device. The annealing optimisation studies on the cold drawn wires aimed to maximise the elongation to failure of each alloy wire as one of the key limitations in the application of Mg alloys in BVS technology is their limited ductility. Generally increased ductility is accompanied by a reduction in strength post annealing. However, as the strength of the wire influences the radial force of the final device, which is also influenced by wire size and device design it is complex to define some minimum YS/UTS that the wire must exhibit. Therefore, no minimum YS/UTS was defined during development of the annealing protocols. Instead, investigation of the radial force of the final device was used to assess the appropriateness of the alloy wires under investigation. Consequently, the annealing optimisation studies on the final device aimed to, first, maximise its expansion range before assessing if the radial force of the devices met a pre-defined minimum requirement. Chapter 5 discusses how the minimum expansion range and radial force targets were defined prior to testing. A vacuum oven and a vacuum tube furnace were used to optimise the properties of the cold drawn alloy wires and the final device. Both furnaces operated in a protective atmosphere (vacuum) in order to limit oxidation of the reactive Mg alloy wires during exposure to high temperatures. It is known that atmospheric annealing of Mg alloys can result in significant oxidation which is detrimental to the mechanical performance of the alloys, these effects will be amplified in small samples such as the 125µm wire analysed in this work.[174, 175] First, the vacuum oven was used to optimise the properties of the cold drawn alloy wires and final device, but limitations in the heating/cooling rates of this setup led to the design and manufacture of a bespoke vacuum tube furnace setup.

3.3.1 Vacuum Oven Test Protocol

The vacuum oven (Vacuum Drying Oven - Nannyang Xinda Electrico-Mechanical co. Ltd) was available from project start and was initially used to conduct an annealing study on both alloy wires. The setup of the vacuum oven was limited in that samples had to be placed inside the furnace at room temperature, a vacuum could then be pulled on the chamber before the furnace was slowly brought to the desired soak temperature. Following annealing at the desired soak temperature for the set soak time the furnace was switched off and allowed to cool naturally to room temperature, before the vacuum could be released, and the samples removed for further

testing and analysis. The annealing study investigated soak temperatures of 300, 320 and 340°C for durations between 10 and 40mins.

Due to the prolonged heating and cooling cycles, the wires were exposed to temperatures above their recrystallisation temperature for longer periods of time than the stated soak time for each treatment. The heating and cooling cycles were characterised at the three annealing temperatures investigated during this study to understand the complete heating cycle the samples were exposed to during the various annealing tests. To assess this, the vacuum oven was set to heat to each of the soak temperatures investigated (300, 320 and 340°C) held for ten minutes and then set to cool. Temperature measurements were taken at 10-minute intervals up to 180mins with two further measurements taken at 210 and 300mins. The results from this investigation are shown in Figure 3.1. Plotted also in Figure 3.1 is a line denoting the recrystallisation temperature to demonstrate the total length of time the samples will be exposed to temperatures above the recrystallisation temperature during each annealing protocol. As is known, the true recrystallisation temperature of an alloy is dependent on alloy composition and prior cold work, as such a conservative estimate of 250°C was selected for the recrystallisation temperature.[176] The area of each annealing protocols heating/cooling cycle plot above the recrystallisation temperature was calculated to determine the total time the wires would be exposed to temperatures above 250°C. Not considering the 10-minute soak time that was defined, the slow heating and cooling cycles resulted in the oven being above 250°C for an

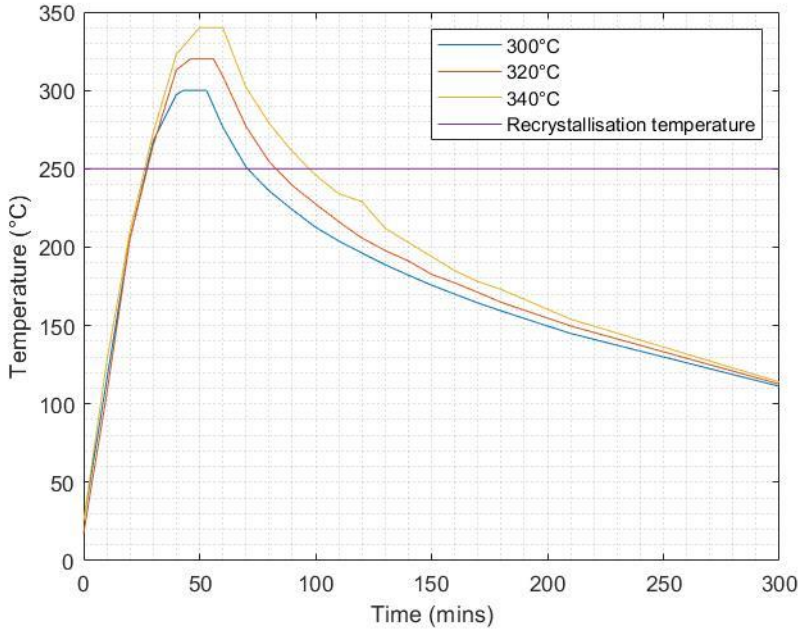

Figure 3.1: Heating and cooling cycles of the vacuum oven when set to the various soak temperatures investigated

additional 34, 45 and 61mins for the 300, 320 and 340°C cycles respectively. Therefore, describing the cycles by their soak time is not fully representative of the total time above the recrystallisation temperature, which should be considered when analysing differences between the various annealing protocols.

3.3.2 Vacuum Tube Furnace

During testing, which will be discussed in detail in Chapters 4 and 5, it was found that the slow heating and cooling cycles of the vacuum oven limited the properties of the alloy wires, resulting in a new furnace setup being designed. A Carbolite Gero vacuum tube furnace was adapted to allow for rapid heating and cooling cycles to be employed during annealing under vacuum conditions. The design approach behind the new setup was that through using a tube furnace with a tube manufactured from a material with low thermally conductivity (quartz glass) a "heating" zone could be created adjacent to a "cooling zone", a schematic of the design is shown in Figure 3.2. The tube furnace has a 300mm long heating element, highlighted in red in Figure 3.2a, creating a 300mm heating zone within the region of the quartz glass tube housed within

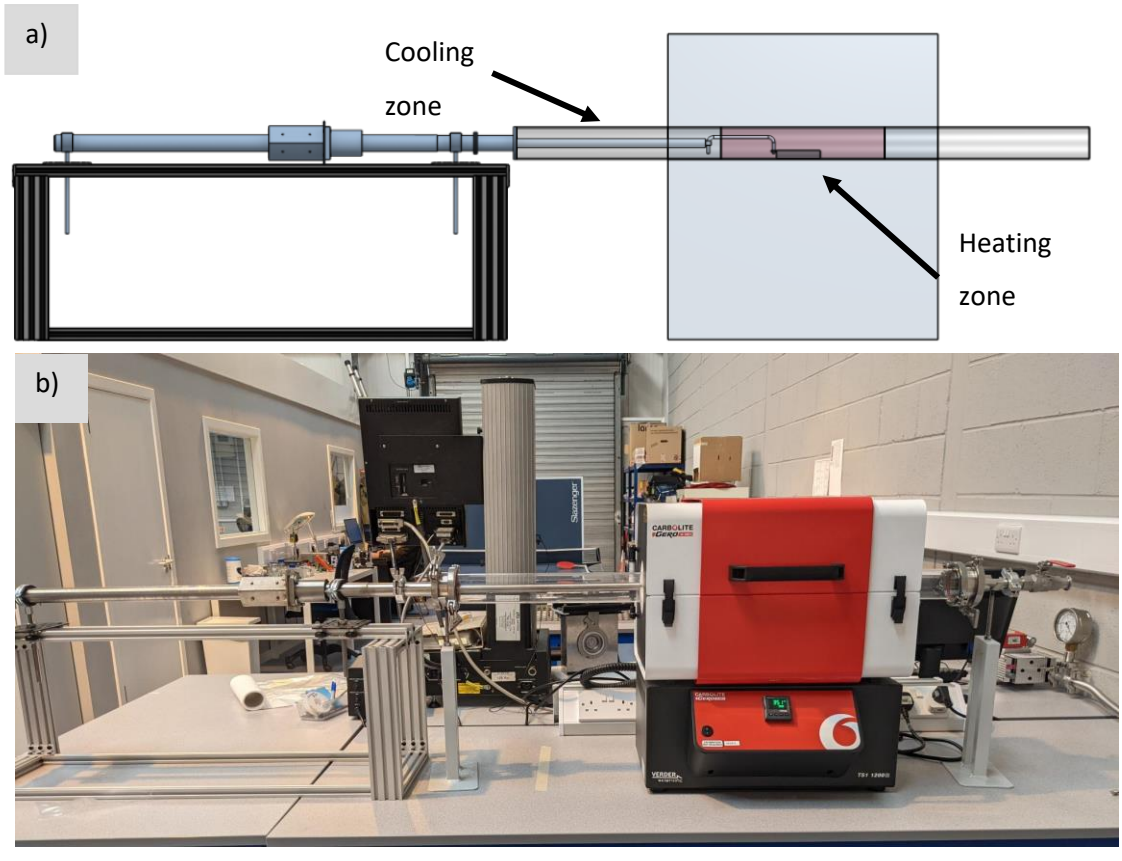

Figure 3.2: a) Schematic of vacuum tube furnace showing the heating zone in red b) manufactured and installed vacuum tube furnace

this zone. The section of the tube held out with the furnace was designed to remain at room temperature to create the cooling zone, through the restriction of heat transfer via conduction (owing to the low thermal conductivity of the quartz glass) and convection (owing to the furnace operating under vacuum conditions) from the heating zone.

As the furnace is operating under vacuum conditions, a bespoke system was required to transfer the wire/devices from the cooling zone, into the heating zone and then back again without breaking the vacuum. A magnetic "transfer arm" was designed to transfer the samples between zones. The final installed transfer arm is shown in Figure 3.2b and a schematic is shown in Figure 3.3. A sealed tube was manufactured with a vacuum flange on one end for attaching to the vacuum tube furnace. Housed within the tube was a linear bearing and metal rod to transfer the samples between the two zones. Magnets were fixed to the rear of the metal rod housed within the sealed tube and also to a "handle" consisting of a linear bearing slid over the sealed tube. The magnetic attraction between the two magnet arrays allowed the rod housed within the tube to be moved, by manually sliding the handle over the outer diameter of the sealed tube. To prevent heat transfer through the steel transfer arm, a quartz glass rod and sample holder were attached to its end, so that during the heating cycle only the components made of quartz glass were sat within the heating zone, along with the wire/final devices.

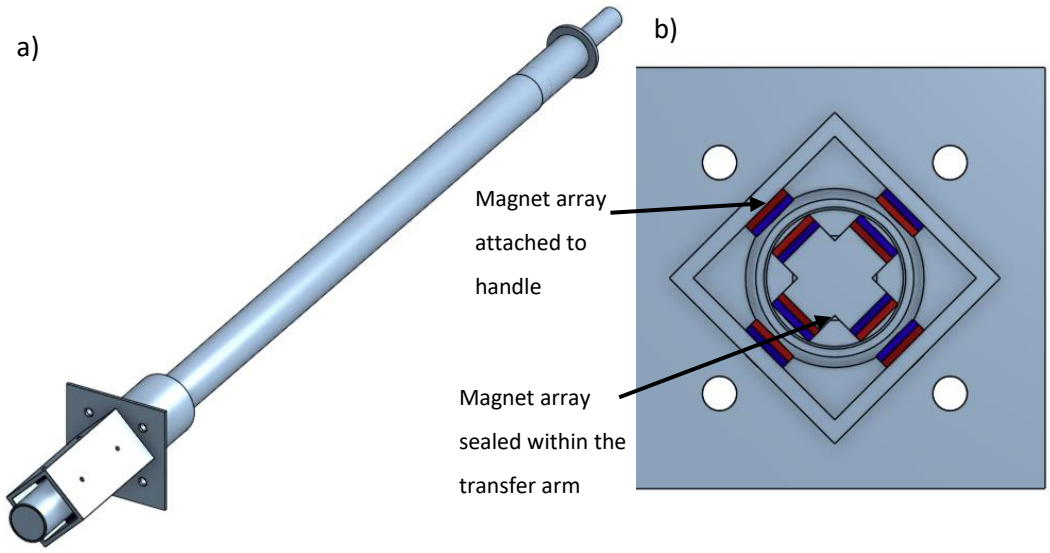

Figure 3.3: a) Full schematic of magnetic transfer arm b) rear view of transfer arm showing magnet array

3.3.2.1 Validation

As the vacuum tube furnace was modified to provide appropriate heating and cooling cycles under vacuum conditions a series of validation tests were conducted. Firstly, as no pressure gauge was incorporated into the supplied furnace a pressure gauge (RS Pro 9684684 Analogue Vacuum Gauge) was attached to the vacuum tube furnace to validate that a suitable vacuum could be achieved and maintained over time. The pressure gauge measured from a maximum gauge pressure of 0bar to a minimum of -1bar, with an accuracy rating of +/-1.6% (at 20°C). Validation testing proved that when the full system was installed as shown in Figure 3.2b, the vacuum gauge read -1bar, which was maintained over a 4 hour period (longer than any thermal processing tests conducted in this work).

Next, the temperature within the heating and cooling zones of the furnace were validated. Temperature measurements were taken at five locations along the tube furnace as shown in Figure 3.4 using a thermocouple. The thermocouple was fed into the furnace and positioned at one of the measurement locations. To prevent air leakage at the interface where the thermocouple was fed into the furnace it was wrapped in PTFE tape and throughout testing the vacuum level was monitored with the attached vacuum gauge. Despite the PTFE tape, it was found that over the duration of each test the pressure within the system increased to

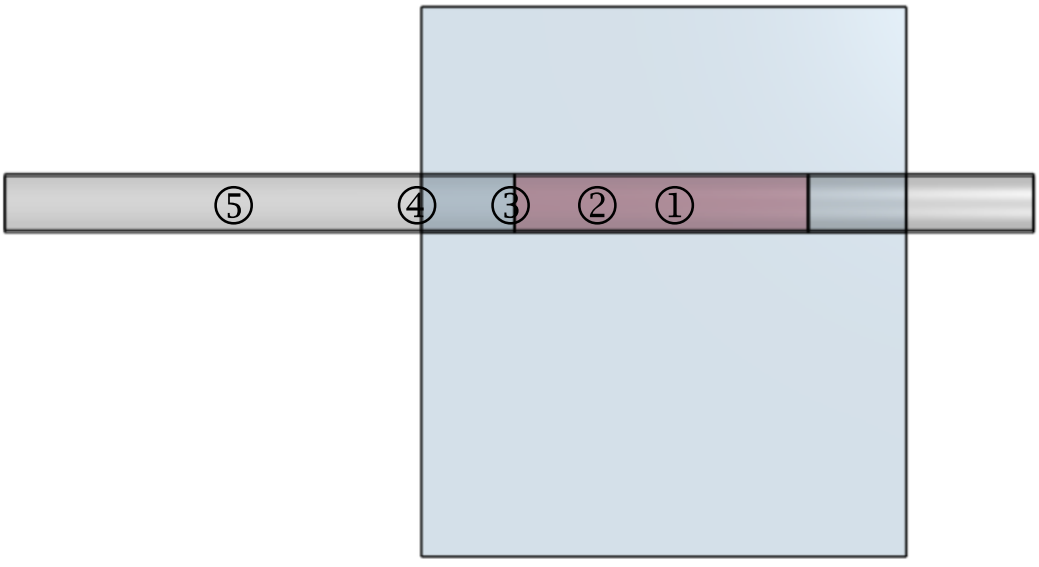

Measurement point	1	2	3	4	5
Distance from centre of heating zone (mm)	0	75	150	250	415

Figure 3.4: Temperature measurement locations for validation testing

approximately -0.6bar. The temperature of the furnace was validated at 300, 350 and 400°C. For each test at the positions outlined in Figure 3.4, the furnace was set to 300°C and allowed to come to temperature and settle for 10mins before the first temperature measurement was made, subsequently 2 additional temperature measurements were taken at 5min intervals. The furnace was then set to 350°C and allowed to settle for 10mins before three temperature measurements were taken at 5min intervals. This process was repeated at 400°C before the furnace was allowed to cool and the thermocouple could be repositioned at the next location. The previous steps were repeated for each point indicated in Figure 3.4 and the results are plotted in Figure 3.5. As can be seen from the results, the temperature at the centre of the heating zone for each temperatures investigated was the same as the set furnace temperature. At point 2, 75mm from the centre of the heating zone, the temperature was slightly lower than each of the soak temperatures investigated. The largest difference between the measured and pre-set temperature was at the highest temperature investigated (400°C) where the measured temperature was 391°C. Moving to point 3, at the interface between the heating zone and the start of the cooling zone, the temperature decreased significantly for each of the temperatures investigated (approximately 60°C at each soak temperature). At point 4 (250mm away from the centre of the heating zone), the temperature was under 75°C for each of the three tests. Finally, the temperature in the centre of the cooling zone, point 5, was found to remain at room temperature for each of the tests conducted.

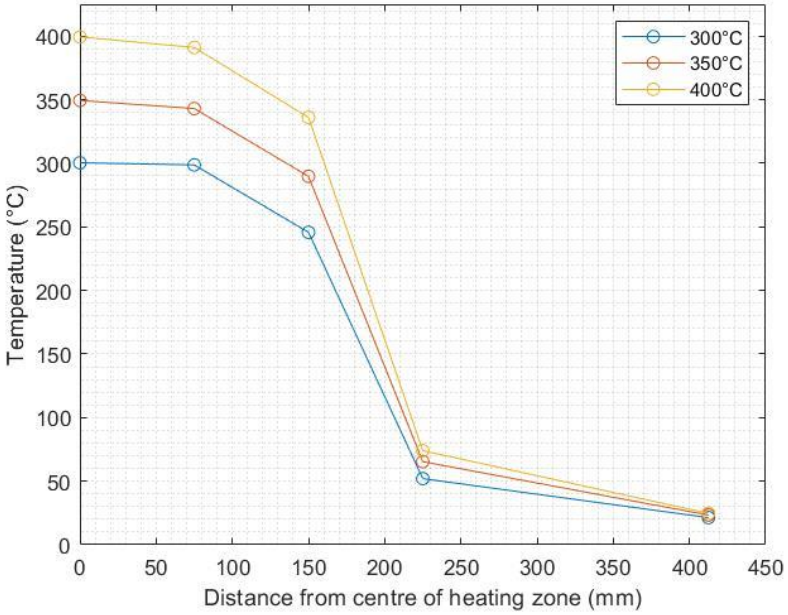

Figure 3.5: Temperature validation results for the vacuum tube furnace

One limitation, in this test protocol, was the need to feed a thermocouple through the furnace meaning there was some slight leakage of air into the system throughout testing. The air leakage into the system will result in some convective heat transfer through the system that may be responsible for the decrease in temperature between points 1 and 2. The decrease in temperature at point 2 from the pre-set temperature was not anticipated but considering the limitations of the setup, it was determined that the discrepancy was acceptable. These tests did confirm that the cooling zone remained at room temperature throughout testing, proving that the system would allow for rapid heating and cooling cycles to be carried out.

3.4 Hardness Testing

Microhardness testing was conducted on the alloy wires to investigate the hardness distribution through their cross section and its evolution during annealing. Owing to the small diameter of the alloy wires under investigation, selection of an appropriate load for microhardness testing was integral in ensuring accurate and repeatable results could be obtained. Hardness testing involves indenting a material with an indenter (of specific geometry) with a constant load. The dimensions of the indent are measured and combined with knowledge of the load to determine the hardness of the material within the region of the indent. As the hardness obtained through this method calculates the hardness over the area of the indent, the size of the indent should be considered when determining the hardness distribution in small samples. Smaller indents are preferred when investigating the hardness at specific locations, however small indents are challenging to accurately measure and the measurement error will increase with decreasing indent size. Consequently, a load validation test was conducted to identify the most appropriate load to accurately determine the hardness distribution whilst maintaining sufficient repeatability.

Load values from 1g to 10g were tested on the cold drawn 0.5Y alloy wire to determine the most suitable load to be used for the bulk of hardness testing conducted in this work. To prepare the wires for hardness testing the samples were mounted in epoxy resin and ground using 1200grit SiC paper followed by 2400grit SiC paper with a final 2-minute polish using colloidal silica. For each load, seven measurements were taken at the centre of the cross section of the wire, the highest and lowest values were removed and the mean and standard deviation for each load is shown in Figure 3.6. The variation in results for the samples tested with a 1g load were largest which is attributed to the small indent size (diagonal length of ≈4.5μm) making measuring challenging. In contrast the variation in results for the higher loads were relatively similar with

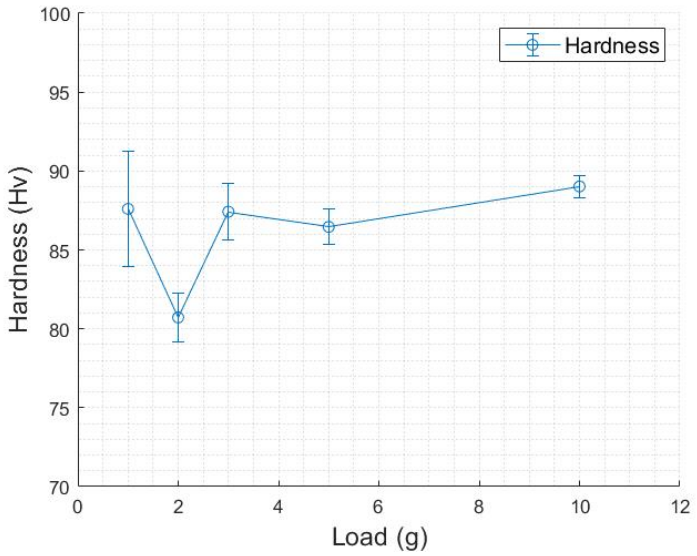

Figure 3.6: Hardness testing load determination

the samples tested with a 10g load having the lowest variation and largest diagonal size, ≈14.5µm. As the aim of the hardness tests were to determine the hardness at key points through the cross section of the wire, consideration had to be made of the size of the indent as well as the consistency in measurement. As such it was determined that a load of 3g be used for testing as it provided suitable consistency in measurement and the ident size was also appropriate, ≈8µm.

3.5 BVS Design and Manufacture

The final BVS devices were manufactured from both the 0.5Y and 2Y alloy wires with a final annealing procedure conducted by the wire suppliers following the final drawing step. This final annealing protocol was required to improve the formability of the alloy wires before forming into the final device. During forming of the devices, the wire undergoes plastic deformation meaning the cold drawn alloy wires are not used, to avoid risk of cracking caused by the reduced ductility of the cold drawn wire compared to the annealed wire. The devices are manufactured through, first forming the wire into a “sine” like waveform as shown in Figure 3.7. The waveform is then coiled around a mandrel with a diameter of 1.83mm. At this point an annealing step is required to restore the mechanical properties of the wire to allow for safe device expansion. Using both the vacuum oven and tube furnace this annealing protocol was optimised for each alloy to allow for maximum device expansion. Following thermal processing, some devices were tested at this stage. However, as will be described in the following section, it was determined that a supplementary electropolishing process was required to improve device performance. As

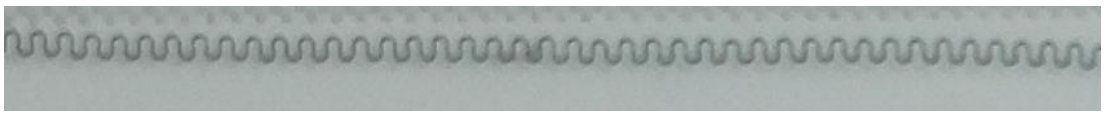

Figure 3.7: Wire formed into sine like waveform

such for the bulk of testing devices underwent an electropolishing process that was developed as described in Section 3.6. Figure 3.8 shows a device following electropolishing.

For the final verification testing of the devices, a polymer coating and a series of polymer connectors were incorporated into the final device. The polymer connectors provide longitudinal stiffness to the device and prevent any unravelling during expansion. Detail of the design and manufacture of these connectors are omitted from this thesis as they are proprietary intellectual property and are not investigated herein. However, this brief comment has been included as, in some representative images in this thesis, the connectors and coatings are visible.

3.6 Electropolishing

Owing to the reactive nature of Mg and its alloys, when exposed to air, an oxide layer forms on their surface. Consequently, during fabrication of the wires, storage, and manufacture of the final device an oxide layer is developed on the wires surface that is required to be removed. As described in Chapter 5, initial device testing was conducted on devices manufactured without a final electropolishing step. Testing of these devices revealed that there was potential need for an electropolishing procedure to be developed during the manufacture of the devices. This section describes the development of this process whilst the effects on final device performance are described in detail in Chapter 5.

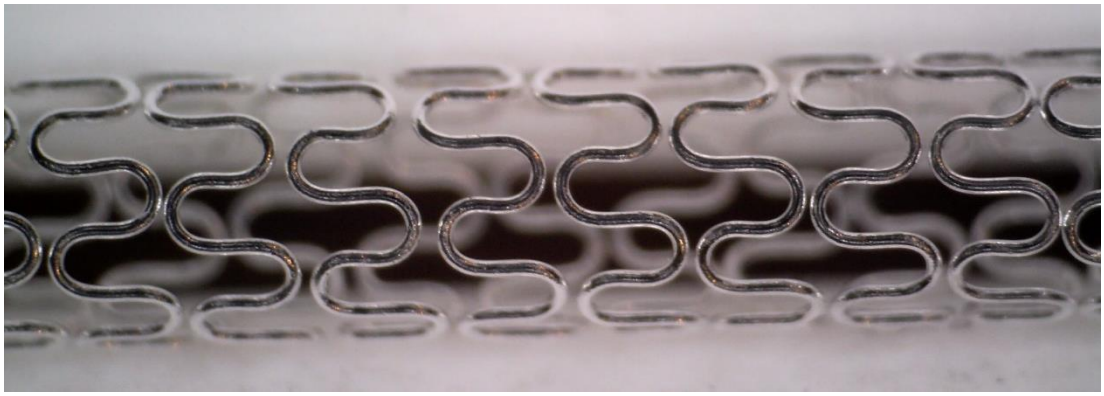

Figure 3.8: Device post electropolishing

Electropolishing is a process used to smoothen rough metallic surfaces by the removal of surface material through anodic dissolution. It is typically conducted through connecting the metallic sample to the positive terminal of a power supply and submersing it in a viscous electrolyte (commonly maintained at a set temperature), whilst the negative terminal is attached to a cathode, also submerged in the electrolyte. Current then passes from the anode, through the electrolyte to the cathode. At the anodic surface the metal is dissolved into the electrolyte, with a reduction reaction occurring at the cathode, generally producing hydrogen.[177] A simple schematic of an electropolishing setup is shown in Figure 3.9.[178] Commonly the current (which can be controlled through altering the voltage) and time of the electropolishing process are modified to produce a repeatable procedure that results in a smooth surface finish with consistent material removal.[179] Electropolishing is a common technique used in the manufacture of medical devices as it can remove material from devices with complex geometries without introducing any surface deformation.[180] As such an electropolishing procedure was developed to remove the surface oxide layer present on the wires surface.

There are several variables to be considered when developing an electropolishing procedure, including electrolyte composition, cathode material, temperature, agitation, voltage and electropolishing time. This work aimed to develop a simple electropolishing setup and as such only the electropolishing time and voltage were investigated. Consequently the remaining variables were selected through referring to the ASTM E1558 – 09 Standard Guide for

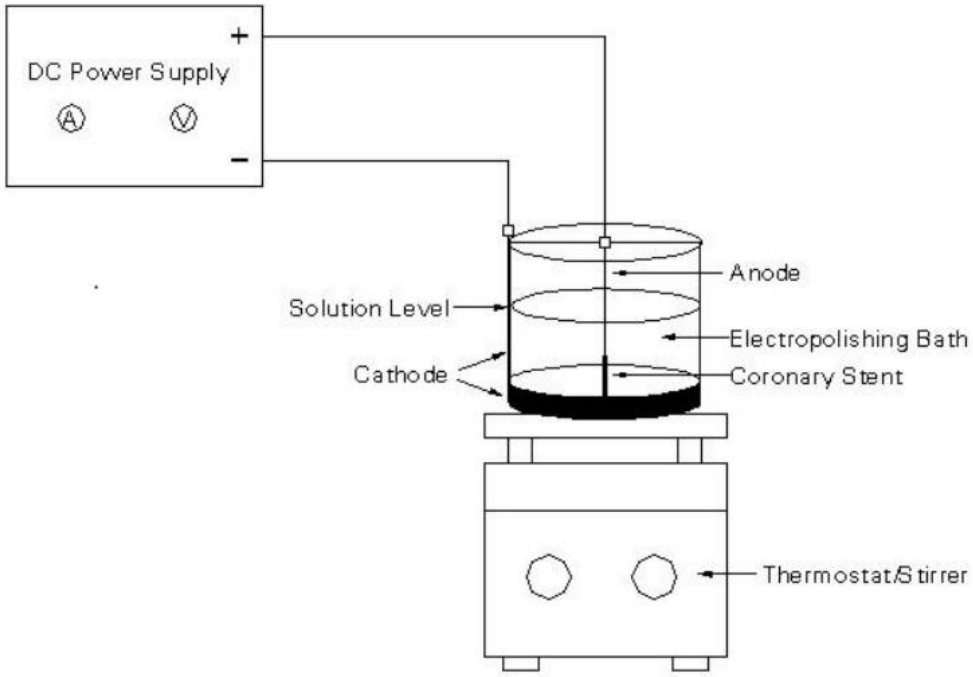

Figure 3.9: Schematic of electropolishing setup[178]

Electrolytic Polishing of Metallographic Specimens.[181] From this standard it was determined that an electrolyte of 5 parts ethanol to 3 parts phosphoric acid, heated to between 25-30°C should be used with an aluminium cathode. The solution was also agitated using a magnetic stirrer spinning at approximately 500rpm. An investigation into the most suitable voltage was first conducted before determining the optimal time for the electropolishing procedure.

The current density of an electropolishing process generally determines the rate of material removal and can be affected by many different parameters, including agitation and temperature. Plotting how the current density varies as voltage is steadily increased from 0V typically gives a graph that follows a standard trend, as shown in Figure 3.10, which allows for the optimal voltage for an electropolishing process to be selected.[182] This graph can be broken down into three distinct regions, with each resulting in slightly different polishing behaviour. At low voltages etching of the material (uncontrolled attack of the surface at the highest energy positions) occurs, whilst at high voltages, gas evolution (where the there is a high evolution of oxygen gas bubbles) results in the activation of pitting along the samples surface. Within the current limiting plateau region, the most suitable polishing conditions are found which results in the final sample developing a smooth surface finish.[177] In general the most optimal polishing conditions are found at voltages close to the end of the current limiting plateau region, point D in Figure 3.10.

To determine the optimal voltage for use during electropolishing of the alloys under investigation, a "voltage sweep" test was run to create a current density vs voltage plot. This was conducted through placing a 20mm length of wire in the electropolishing solution, with 0V

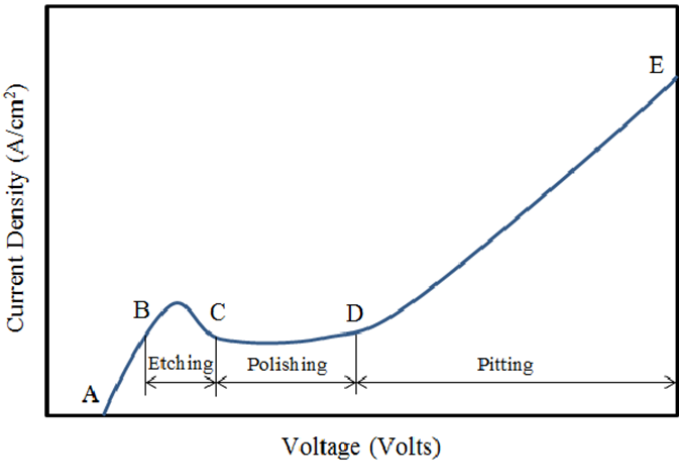

Figure 3.10: Example current density vs voltage plot[182]

through the system, recording the current and slowly increasing the voltage to 3.5V whilst, taking readings of the current at 0.25V intervals. Figure 3.11 shows the results from this investigation. A plateaued region exists between ≈0-2.75V before sharply increasing from 2.75-3.5V. limitations in the setup meant that the current density curve will not identify the etching zone however it does reveal the beginning of the gas evolution region ≈2.5-2.75V. As it is known that the optimal electropolishing conditions are found when using voltages close to the end of the current limiting plateau, it could be estimated that the optimal voltage to be used for this setup should be ≈2.5-2.75V. In order to confirm these assumptions based on the current density curve, three wire samples were electropolished at voltages ranging from 0-3.5V at 0.5V intervals for 120s. The samples were then cleaned in water and dried using a hot air gun, before being analysed using a scanning electron microscope (SEM). The results are shown in Figure 3.12. At 0.5V and 1V the surface of the wire appears rough. When polished using voltages of 1.5-2.5V the wire surface appears relatively smooth with no clear pits on the surface of the wire. At the higher voltages of 3 and 3.5V a rougher surface is apparent, caused by small pits developing across the wires surface. The observations made from the SEM analysis agree with the assumptions made from the current density plot, that optimal polishing conditions will occur at voltages close to 2.5-2.75V. As such, it was determined that the optimal voltage for use in this work was 2.5V

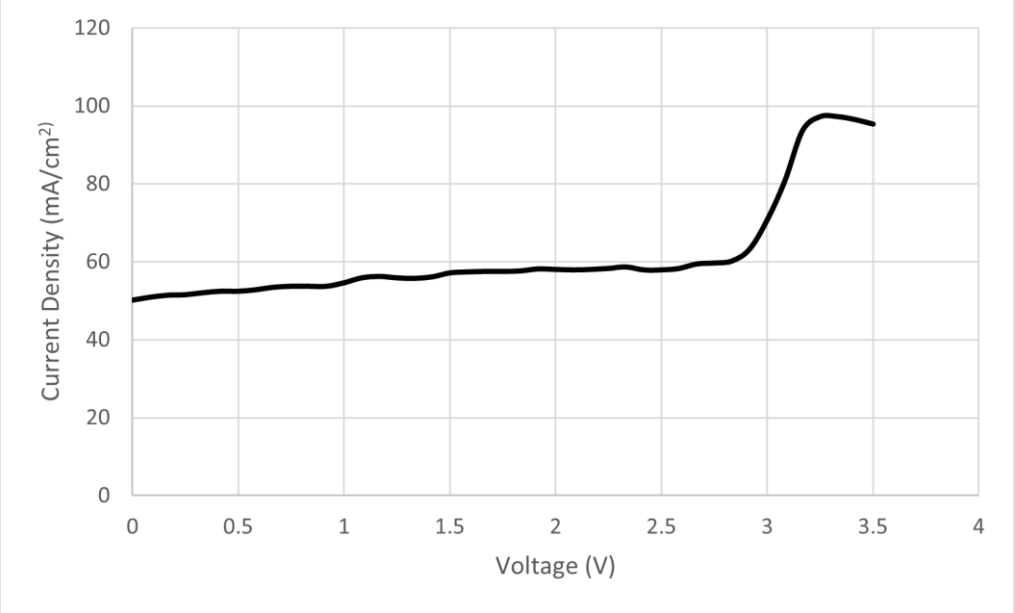

Figure 3.11: Voltage sweep test results

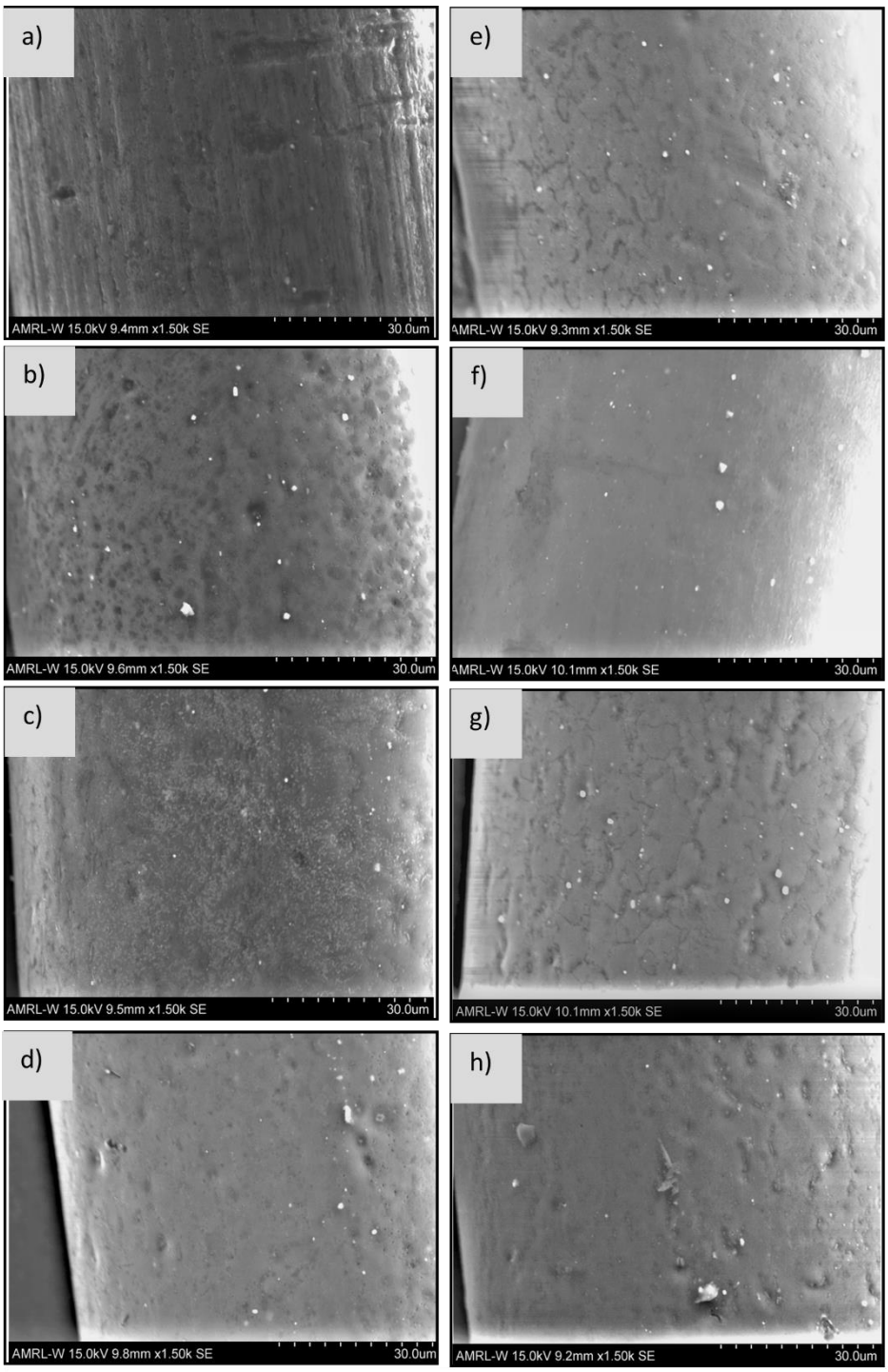

Figure 3.12: Surface images of the wire a) as supplied and following electropolishing for 30s at b) 0.5V c) 1V d) 1.5V e) 2V f) 2.5V g) 3V h) 3.5V

The final stage of this process development was to determine the required polishing time. The primary aim of this polishing step was to remove the surface oxide layer whilst minimising the loss of the bulk Mg matrix. To determine this, nine wire samples were electropolished using a voltage of 2.5V for varying times between 15 and 90s. The diameter of the wire was measured

using a micrometre following each polishing procedure, the results are shown in Figure 3.13. After 15s the diameter loss is 2.5µm and follows a general linear trend as polishing time increases with a total diameter loss of 20.1µm after polishing for 90s. All samples appeared bright to the naked eye after polishing meaning the oxide layer was likely removed after 15s. However, as polishing for 15s removed 2.5µm from the diameter of the wire, any defects of greater the 1.25µm on the wires surface would remain post polishing. Though no such defects were observed it was determined that a removal of ≈5µm from the wire's diameter was preferred, to ensure a smooth final surface. Consequently, a polishing time of 30s was set for this process. The final electropolishing parameters were set and are summarised in Table 3-1.

3.7 Summary

Prior to characterising the two alloy wires being investigated in this work, the test equipment/protocols had to be verified to ensure repeatability of the testing. Firstly, the vacuum oven used as part of this work was investigated to understand the complete thermal cycle the wires would experience during the annealing treatments conducted. It was shown that during annealing in the vacuum oven, the samples will be exposed to temperatures above their recrystallisation temperature for significantly longer than the stated soak time. This should be considered when analysing the results. Based upon the response of the alloy wires to the

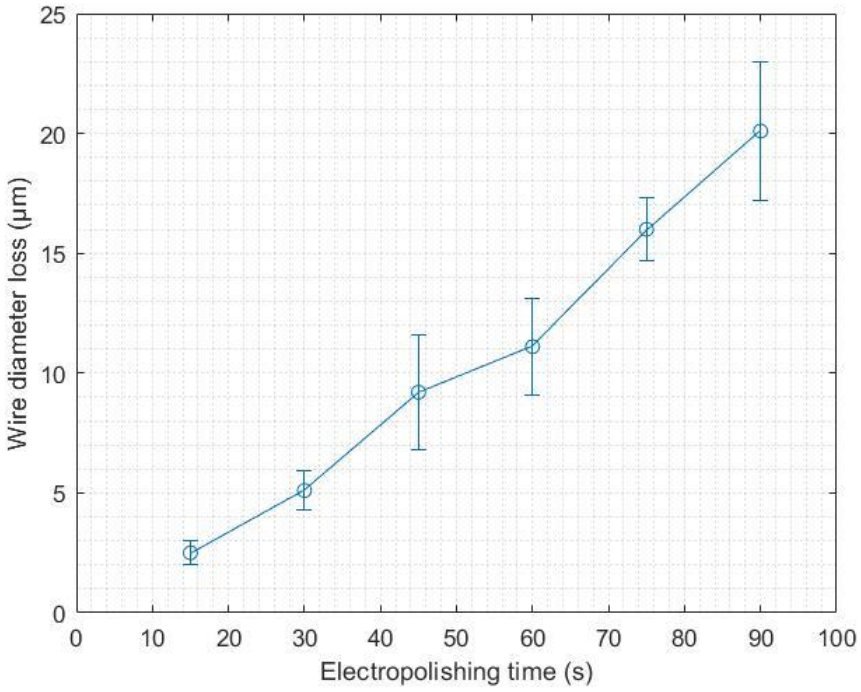

Figure 3.13: Diameter loss vs electropolishing time

Table 3-1: Electropolishing parameters

ELECTROPOLISHING VARIABLE	DESCRIPTION
ELECTROLYTE	150ml ethanol and 90ml phosphoric acid
CATHODES	2x aluminum
TEMPERATURE	≈25°C
VOLTAGE	2.5V
TIME	30s
CLEANING PROTOCOL	Dipped in water and dried in hot air

thermal processing conditions made available with the vacuum oven, a vacuum tube furnace was modified to improve the range of thermal processes available during this work. The modified tube furnace allowed for rapid heating and cooling cycles to be conducted during the annealing processes investigated. The validation testing described in this chapter demonstrated that the bespoke setup allowed for a heating zone (held at temperatures >250°C) to be adjacent to a room temperature cooling zone, both under the same vacuum conditions. Microhardness testing is commonly carried out on small samples. However, it is important to ensure the repeatability of results before conducting a large study. It was demonstrated that using a 3g load to measure the hardness of the alloy wires was appropriate in ensuring repeatable results and allowing for different regions of the wire to be investigated. Finally, an electropolishing procedure was developed that resulted in the removal of ≈5µm of material from the diameter of the alloy wires. This procedure was shown to be appropriate in removing the oxide layer present on the wires surface and the effects of this are described in further detail in Chapter 5. It should be noted that this electropolishing procedure was developed solely for the purpose of removing the oxide layer and any surface defects. Further optimisation of this process could be conducted through investigation of several of the controlling parameters of the electropolishing process, however for the purpose of improving the mechanical response of the alloy wires under investigation the process developed was deemed appropriate.

Chapter 4: Annealing Optimisation of Alloy Wires

4.1 Introduction

This chapter focuses on maximising the ductility of both the supplied cold drawn alloy wires through developing optimised annealing processes and investigating the underlying microstructural behaviour behind the mechanical response of each alloy. One of the major limitations in the application of Mg alloys in bioresorbable medical devices is their lack of ductility. The poor ductility of Mg alloys both limits their formability during device manufacture and performance in devices that are required to undergo high levels of plastic deformation during their deployment, such as in balloon expandable BVS. The HCP crystal structure of Mg is responsible for its poor ductility as it limits the number of easily activated slip systems available during room temperature deformation. Further the dominance of basal slip during drawing results in the wires developing a fibrous microstructure with a strong basal texture, whereby the grains tend to align with their c-axis perpendicular to the DD, causing the wires to exhibit high strength, low ductility, and anisotropic properties.[183-185] The poor ductility of Mg can be improved through altering alloying and processing routes applied during both the fabrication of the Mg alloy wires and manufacture of the final device.[186] A post drawing heat treatment process is essential, to improve the mechanical properties for further processing during manufacture of the final device. Alloying is required to improve the formability of pure Mg to first survive the cold drawing process and then provide the ductility necessary for application in medical devices that undergo high levels of plastic deformation, such as wire form BVS.[185, 187-189]

Li and Y are both shown to improve the mechanical properties of Mg and are considered safe in *vivo* within the alloying limits investigated in this study.[190, 191] Li improves the ductility of Mg alloys through increased activation of non-basal slip, caused by reducing the c/a axis ratio of the HCP unit cell, when alloyed below 5.5wt%. Above this limit, a Li rich beta phase forms that further improves ductility but reduces both strength and corrosion resistance.[103, 104] Y was selected to increase the strength of the alloy through solid solution strengthening, to avoid any galvanic corrosion or limited ductility that is associated with precipitation hardened alloys.

Further, through alloying with Y, it is considered that some weakening of the strong basal texture can be achieved.

The main body of published research into Mg based BVS design has been conducted on laser cut hypo tube designs. This means that the reported literature on the bulk of these alloys has been conducted on extruded rods and/or tubing making direct comparison between the alloy wires investigated in this work challenging. However, within the literature, tensile testing of WE43, Resoloy and ZX10 wires (with diameters <1mm) has been reported to exhibit tensile elongation to failure of 17, 18 and 18.4% respectively.[158, 159] From this, a baseline target for elongation to failure could be set for the alloy wires under investigation in this work. Here, the target was for the alloy wires to achieve tensile elongations to failure of approximately 20% following thermal processing. This study therefore seeks to develop a heat treatment process for both Mg-Li-Y alloy wires to maximise their ductility, targeting approximately 20%. The effect these treatments have on the microstructure and mechanical properties of the two alloy wires is also investigated, and conclusions are drawn on their suitability for application in medical devices that undergo severe plastic deformation.

4.2 Methodology

4.2.1 Annealing Protocols

In this Chapter the mechanical properties of both alloy wires will be optimised following annealing in both the vacuum oven and vacuum tube furnace. Chapter 3 detailed the design and manufacture of the vacuum tube furnace and the validation of both.

For the vacuum oven furnace processing, both alloy wires underwent annealing at 300, 320 and 340°C for soak times between 10 and 40mins. For each procedure, the samples were placed in the vacuum oven (at room temperature), a vacuum was pulled, and the furnace turned on and set to heat to the desired soak temperature. Once the furnace had reached the set soak temperature, it was left to anneal for the desired soak time before the furnace was turned off and allowed to cool naturally. The vacuum was only released, and the wire removed, once the furnace was at room temperature. As described in Chapter 3, during the heating and cooling cycles the wire is, of course, exposed to temperatures above its recrystallisation temperature for longer than the stated soak time. It was shown that during the procedures conducted at 300, 320 and 340°C the wires were exposed to temperatures >250°C for an additional 34, 45 and 61mins respectively in addition to the procedures soak time.

For the vacuum tube furnace, both alloy wires underwent annealing between 250 and 450°C for soak times between 10 and 120mins. As described in Chapter 3 the vacuum tube furnace consisted of two zones, a “heating”, and a “cooling” zone. Firstly, the sample wire was placed in the tube furnace, within the cooling zone and a vacuum was pulled on the entire system. The furnace was then set to the desired soak temperature and allowed to settle at the soak temperature for 10mins before the sample wire was transferred into the centre of the heating zone and held for the desired soak time. Once the wire had been annealed for the set time, it was withdrawn from the heating zone, into the cooling zone and the lid of the furnace was opened, allowing the furnace to cool naturally. The vacuum was only released, and samples removed once the tube furnace was reading below 45°C within the heating zone.

4.2.2 Microstructure

Investigation of the wires’ microstructure was performed on cross sections in the normal direction, using optical microscopy (Olympus GX51), SEM analysis, energy dispersive spectroscopy (EDS) and electron backscatter diffraction (EBSD). Samples analysed using optical microscopy were mounted in epoxy resin and mechanically ground and polished using 1200 and 2400 grit SiC paper followed by polishing with colloidal silica and etched with a solution of 75ml of ethylene glycol, 10ml distilled water and 1ml of nitric acid. Samples for SEM and EDS analysis were mounted and prepared with the same method as above without the etching process. Images were taken using the backscatter electron (BSE) detector. To enhance conductivity a thin layer (≈10nm) of gold was deposited on the surface prior to analysis. Samples for EBSD analysis were mounted in conducting Bakelite and prepared with the same methods as above, without the etching process, followed by ion milling with a Gatan precision etching and coating system. EBSD analysis was carried out on a 50x50µm area in the centre of the cross section of the wires using a step size of 0.1µm, with a JEOL 7900F field emission gun SEM.

X-ray diffraction (XRD) (Bruker D8 Advance) was carried out for phase identification. The XRD analysis used Cu Kα radiation (λ = 1.5406Å) with an acceleration voltage of 45kV, current of 40mA, step size of 0.0025°, step time of 0.1s, and a 2θ range of 10 to 90°.

4.2.3 Mechanical Testing

Vickers microhardness testing was carried out on the alloy wires in their cold drawn and annealed states. Samples for analysis were mounted axially in epoxy resin and mechanically polished following the same procedures as described for optical microscopy, without the final

etching step, in order to obtain a flat surface for indentation. As described in Chapter 3 the optimal indentation load was found to be 3g and as such all measurements were taken using a 3g load. Microhardness measurements (Hv 0.003) were taken at 3 locations through the wire's cross sections (Figure 4.1) in order to determine the hardness distribution throughout the wire's cross section. The centre point (point 2) was used to determine the hardness at the centre of the wires cross section, whilst the data from points 1 and 3 were collated and used to determine the hardness of the wire midway between the centre and OD, from here referred to as the mid-radial position. The centre point (point 2) of each sample was measured first, then the samples were reground and polished before indents 1 and 3 were measured. A total of 12 samples were analysed per wire condition and, to improve accuracy, the maximum and minimum values were removed from each data set.

An Instron 4400 equipped with a 100N load cell and capstan style grips, to limit damaging the wire at the grip interface, was used to conduct tensile testing of each alloy wire. A gauge length of 110mm and a crosshead speed of 6.6mm/min (corresponding to an initial strain rate of $0.001s^{-1}$) were used for each test. The elongation to failure was output from the Instron as the total crosshead displacement. Combined with the initial gauge length (110mm) the strain at failure for each tested was determined. For each wire condition a total of 5 samples were tested and the mean and standard deviation were calculated to plot the results.

Minimum bend diameter (MBD) testing was conducted to assess the performance of the wires under more complex loading than simple uni-axial tensile testing. MBD testing was performed by wrapping each alloy wire around progressively smaller pins of diameter <0.3mm in accordance with the ISO 7802:2013 standard.[192] Three wrapping tests were conducted for each

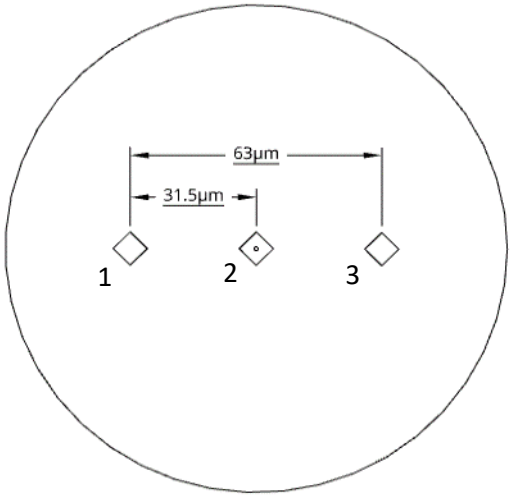

Figure 4.1: Hardness indent locations

wire condition, for each pin diameter tested. Successful tests were defined by whether the wire could be successfully wrapped 5 times around the pin with each wrapped diameter in contact with the previous without failure (as defined within the standard). The wire was held taught during the wrapping tests using a 0.01Kg mass (as specified by the ISO 7802:2013 standard this mass was <5% of the tensile strength).[192]

4.3 Results

Before any annealing processes were conducted, both cold drawn alloy wires were characterised. Following characterisation of each of the cold drawn wires' microstructure and mechanical properties, two separate annealing studies were complete on both alloy wires using the vacuum oven and vacuum tube furnace. The results are presented here and discussed in Section 4.4.

4.3.1 Characterisation of the Cold Drawn Alloy wires

4.3.1.1 Microstructure

As described the 0.5Y and 2Y alloy wires were provided cold drawn to a diameter of 125µm with the final drawing step imparting 80 and 65% CW respectively. Figure 4.2 shows the microstructure of both cold drawn alloy wires in their normal direction following etching. As can be seen both alloys exhibit a typical deformed structure with no equiaxed grains visible. SEM analysis (Figure 4.3) of the cross-sections of both cold drawn wires identified a number of bright cubic particles were present in both alloy wires, with an increased number and size present in the 2Y alloy wire. These particles are later confirmed as Y-rich secondary phases. EBSD analysis of both alloy wires in their normal directions, with a step size of 0.1µm, output no useable data,

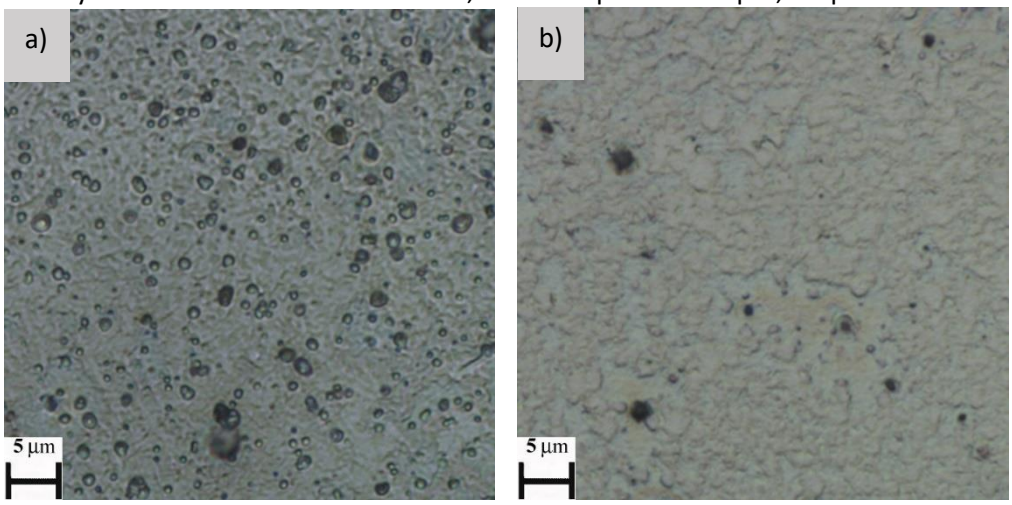

Figure 4.2: Microstructure of cold drawn alloy wires a) 0.5Y b) 2Y

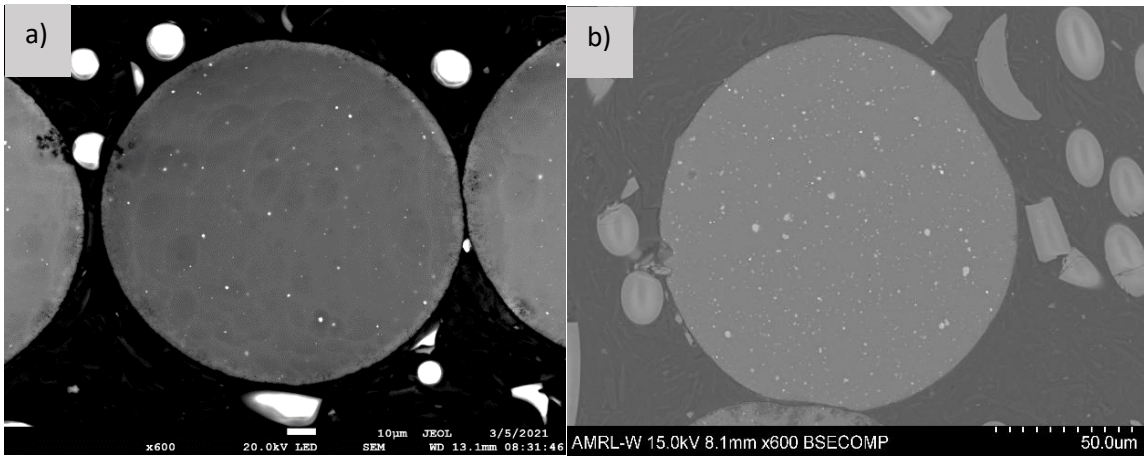

Figure 4.3: SEM images of the cold drawn alloy wires a) 0.5Y b)2Y

owing to the high levels of deformation. It is assumed both alloy wires exhibit a typical as-drawn, fibrous microstructure associated with drawn wires, whereby the grains are elongated in the DD and have a strong transverse basal texture, with the c-axis of the grains aligning perpendicular to the DD.[185, 188]

4.3.1.2 Mechanical Testing

Microhardness testing of the cold drawn alloy wires was conducted, and the results are shown in Figure 4.4. The hardness at the centre of the 0.5Y and 2Y alloy wires was found to be 87.1±2.7

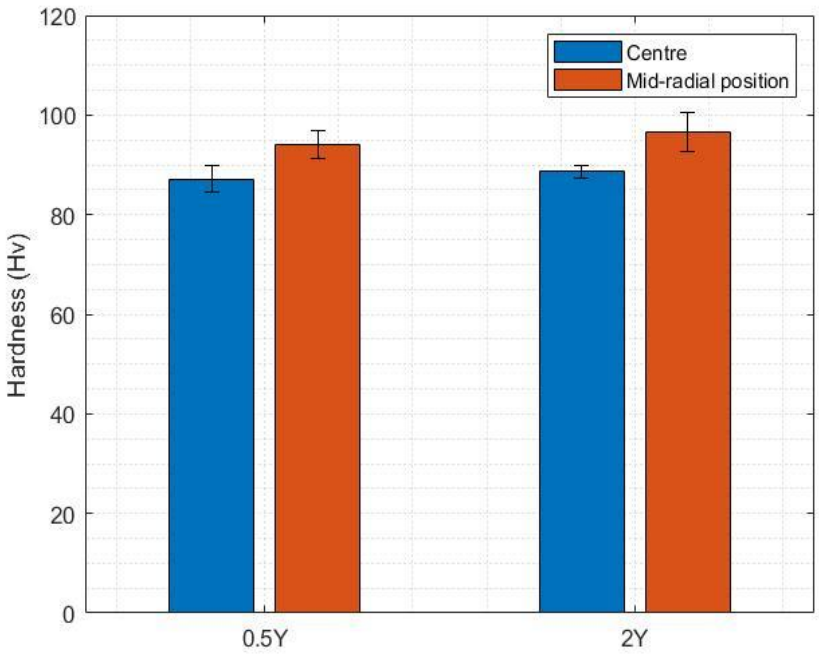

Figure 4.4: Hardness distribution at the centre and mid-radial position of the 0.5Y and 2Y cold drawn wires

and 88.6±1.4Hv respectively. Both the 0.5Y and 2Y alloy wires have increased hardness at their mid-radial positions (94.08±2.3 and 96.6±1.4Hv respectively) compared to their centres. Representative stress-strain curves of both cold drawn alloy wires are shown in Figure 4.5. The cold drawn 0.5Y wire exhibits relatively high strength (YS = 271.2±7.0MPa and UTS = 322.0±0.4MPa) and elongation (11.8±1.0%) for cold drawn Mg wires. The 2Y wire has slightly higher YS (302.9±8.2MPa) but similar UTS (327.6±3.6MPa) and reduced elongation (8.4±2.5%) compared to the 0.5Y wire. Finally, MBD diameter tests were conducted on both alloys, where it was found that the 0.5Y alloy could survive wrapping around a pin diameter 0f 0.135mm (Figure 4.6a). Owing to complications in wrapping such fine wire around such small diameters, the smallest bend diameter tested was 0.135mm, meaning the true MBD of the 0.5Y alloy could not be determined from these tests. During wrapping around a diameter of 0.135mm the 2Y alloy failed during one of the three tests (Figure 4.6b). Repeat testing found that the cold drawn 2Y alloy wire could consistently survive wrapping around a pin with a diameter of 0.16mm (Figure 4.6c), meaning it's MBD can be stated as 0.16mm. Converting the bend diameters into idealised bending strains on the wires surface, it can be determined that the cold drawn 0.5Y wire can survive idealised bending strains of at least 48%, whilst the 2Y alloy wire could survive a maximum idealised bending strain of 44%.

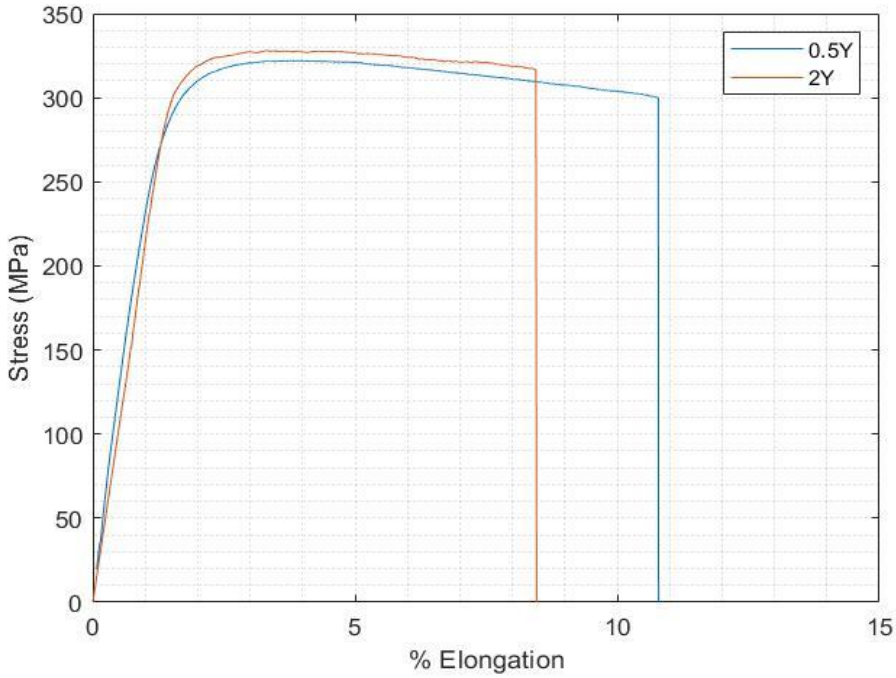

Figure 4.5: Representative stress strain curves of 0.5Y and 2Y cold drawn wires

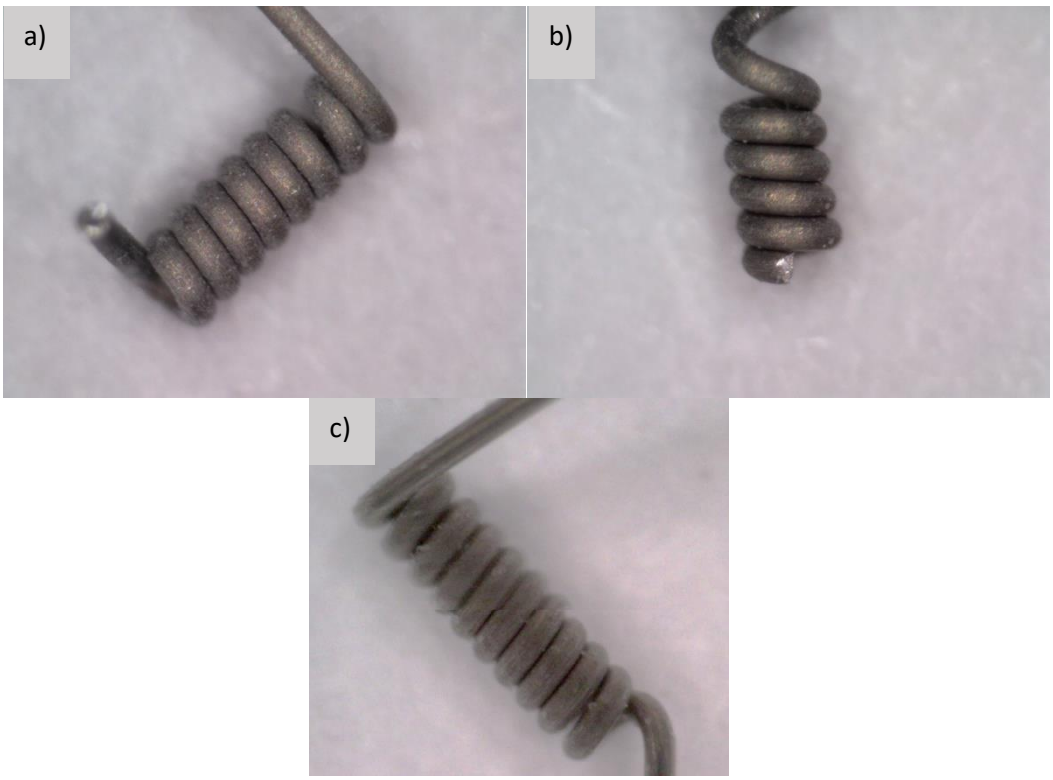

Figure 4.6: MBD tests of cold drawn wire a) 0.5Y 0.135mm b) 2Y 0.135mm and c) 2Y 0.16mm

4.3.2 Vacuum oven Annealing Study

4.3.2.1 Microstructure

Both cold drawn alloy wires were annealed in the vacuum oven at 300, 320 and 340°C for soak times between 10 and 40mins, the microstructure of each alloy annealed at the various soak temperatures for 10mins is shown in Figure 4.7. In each image shown in Figure 4.7 small dark cubic regions are observed distributed throughout the wire cross sections. These cubic regions are assumed (and confirmed in the proceeding sections) to be Y-rich secondary phase particles. Though quantification of the number and size of these particles has not been conducted it can be determined that the size and number of these particles is increased in the 2Y alloy wire compared to the 0.5Y alloy wire (as in the cold drawn alloy wires).

Figure 4.7a shows that in the 0.5Y alloy wire after annealing for 10mins at 300°C equiaxed grains are developed around the OD of the wire cross section with a region of more refined grains in the wire core. In order to analyse the centre of the cross sections in more detail Figure 4.8 shows a 50x50µm region in the centre of the cross section of the same samples from Figure 4.7 at 1000x mag. Figure 4.8a shows the refined grains at the centre of the 0.5Y alloy wire when treated at 300°C for 10mins. At the higher soak temperatures of 320 and 340°C a more uniform grain

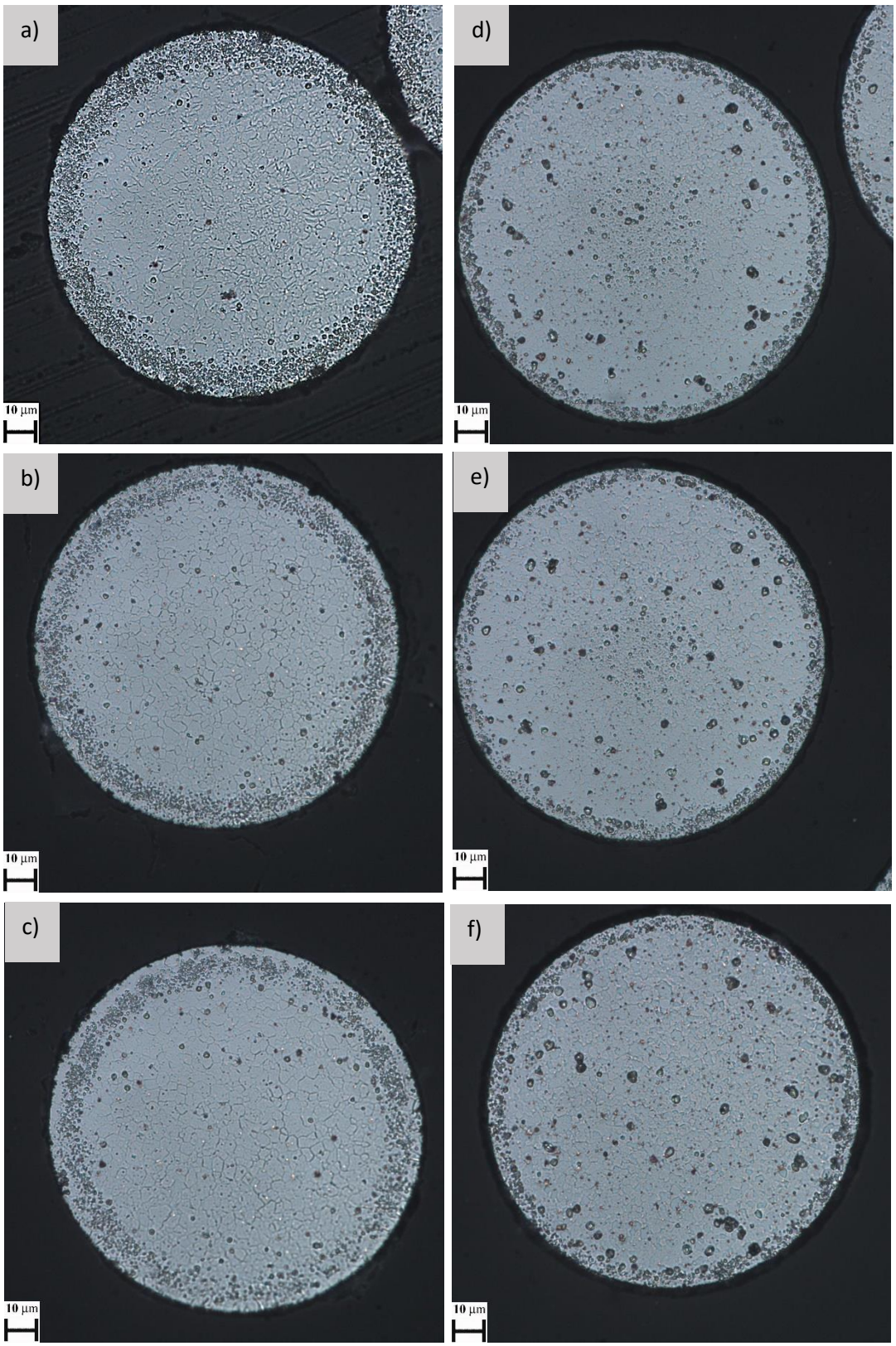

Figure 4.7: Microstructures of 0.5Y and 2Y alloy wires following annealing at various soak temperatures for 10mins a) 0.5Y 300°C b) 0.5Y 320°C c) 0.5Y 340°C d) 2Y 300°C e) 2Y 320°C f)2Y 340°C

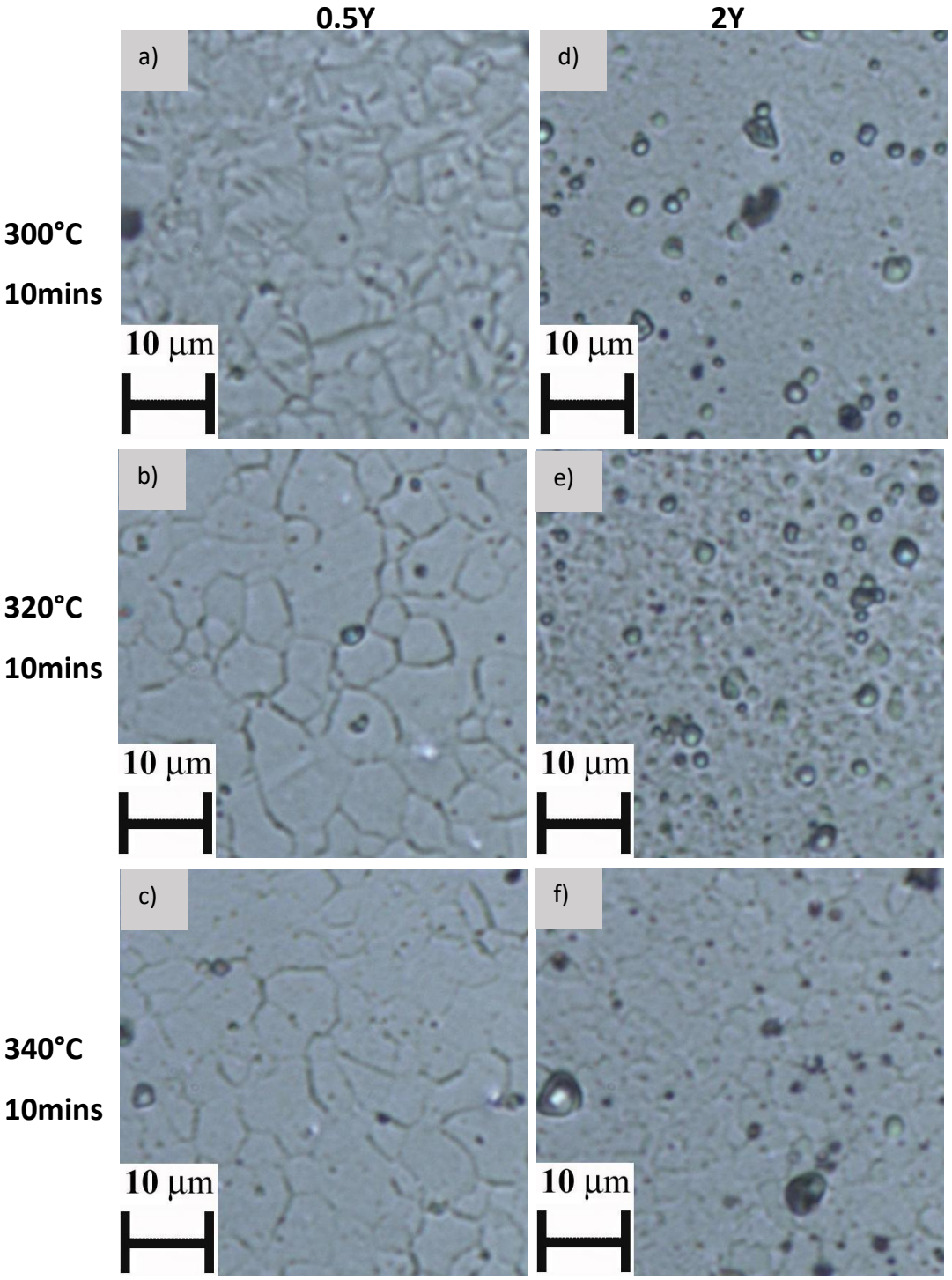

Figure 4.8: Microstructure of both alloy wires annealed at various soak temperatures for 10mins, 50x50µm section in the centre of the cross section a) 0.5Y 300°C b) 0.5Y 320°C c) 0.5Y 340°C d) 2Y 300°C e) 2Y 320°C f) 2Y 340°C

size distribution is developed throughout the wire (Figure 4.8b and c). In the 2Y alloy wire when heat treated at 300 and 320°C for 10mins, equiaxed grains are seen to develop around the OD of the wire (Figure 4.7d and e) but the wire core remains unrecrystallised (Figure 4.8d and e). Recrystallised grains are developed throughout the full wire cross section after annealing at

340°C for 10mins, in the 2Y alloy wire (Figure 4.8f). The grain size of all the samples are on the order of 1-3µm, meaning resolving all of the boundaries through etching and optical microscopy is challenging and as such no grain size measurements were taken from these images, more accurate grain size measurements were taken using EBSD analysis (Section 4.3.2.3).

To better visualise the secondary phase, particle evolution over the range of annealing treatments carried out, SEM analysis was conducted (Figure 4.9) through imaging a cross section of each sample, where the Y-rich particles would appear brighter compared to the bulk Mg

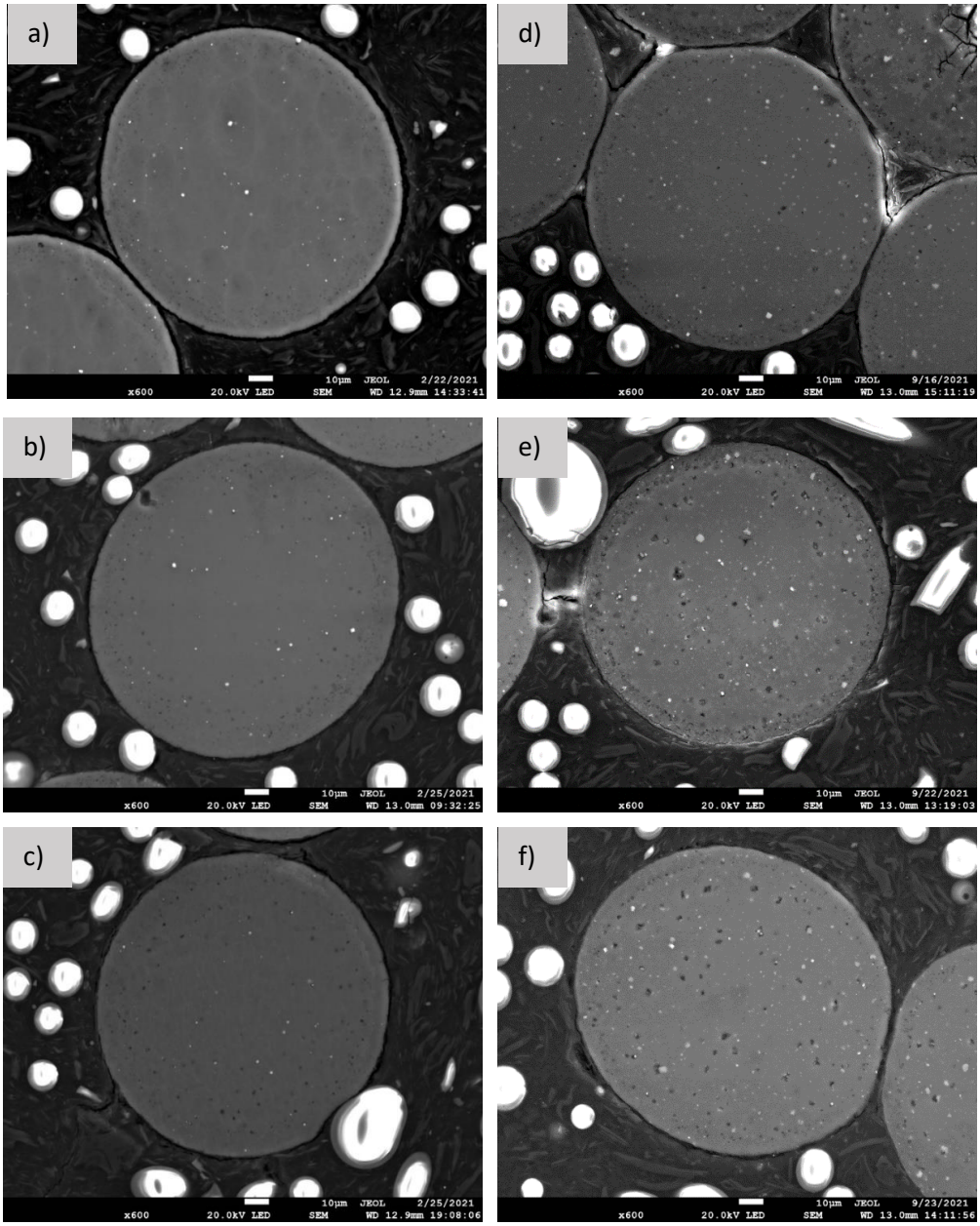

Figure 4.9: SEM analysis of both alloy wires annealed at various soak temperatures for 10mins a) 0.5Y 300°C b) 0.5Y 320°C c) 0.5Y 340°C d) 2Y 300°C e) 2Y 320°C f) 2Y 340°C

matrix. Again, it is clearly shown that an increased number and size of particles are present in the 2Y alloy wire compared to the 0.5Y alloy. As soak temperature is increased in the 0.5Y alloy wire samples, the number and size of particles remains relatively consistent. Whereas, in the 2Y alloy wire samples, as soak temperature is increased to 320 and 340°C, an increased number and size of particles is seen to develop. Several of these larger particles in the 2Y alloy wire following annealing at 320 and 340°C are shown to have been dislodged during sample preparation, leaving behind dark, cubic, voids in the samples in Figure 4.9.

4.3.2.2 Mechanical Properties

Hardness testing was conducted at the centre and mid-radial positions of the samples investigated with optical microscopy in Figure 4.8. Figure 4.10 shows the hardness distributions of the samples analysed at their centre and mid-radial positions. In the 0.5Y alloy wire (Figure 4.10a) the hardness of each sample is relatively similar at the centre and mid-radial positions (≈60Hv following annealing at 300°C and ≈54Hv following annealing at 320 and 340°C), however in the 2Y samples investigated there is a clear difference in hardness between the two positions. In the 2Y alloy wire, heat treated at 300°C for 10mins, the hardness at the centre is 103.5±3.1Hv whilst at the mid-radial position it is 84.0±9.6Hv. When annealed at 340°C for 10mins the hardness at the both the centre and mid-radial position are reduced to 64.9±6.4Hv and 55.3±3.6Hv respectively.

The results from the tensile testing of both alloy wires are displayed in Figure 4.11, with the properties of the respective cold drawn alloy wires shown at time point 0 on the x-axis. No clear trend in the elongation to failure of the 0.5Y alloy wire over the range of heat treatment procedures carried out can be observed. In total four separate procedures were found that resulted in an elongation to failure of greater than 20%: 300°C/30mins (20.1+/-0.7%),

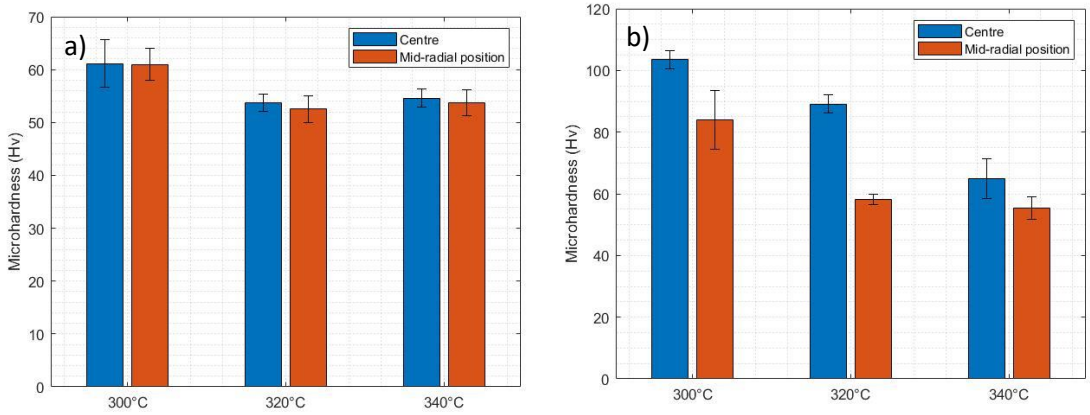

Figure 4.10: Hardness at the centre and mid-radial positions of the a) 0.5Y and b)2Y alloy wires after annealing for 10mins at various temperatures in the vacuum oven

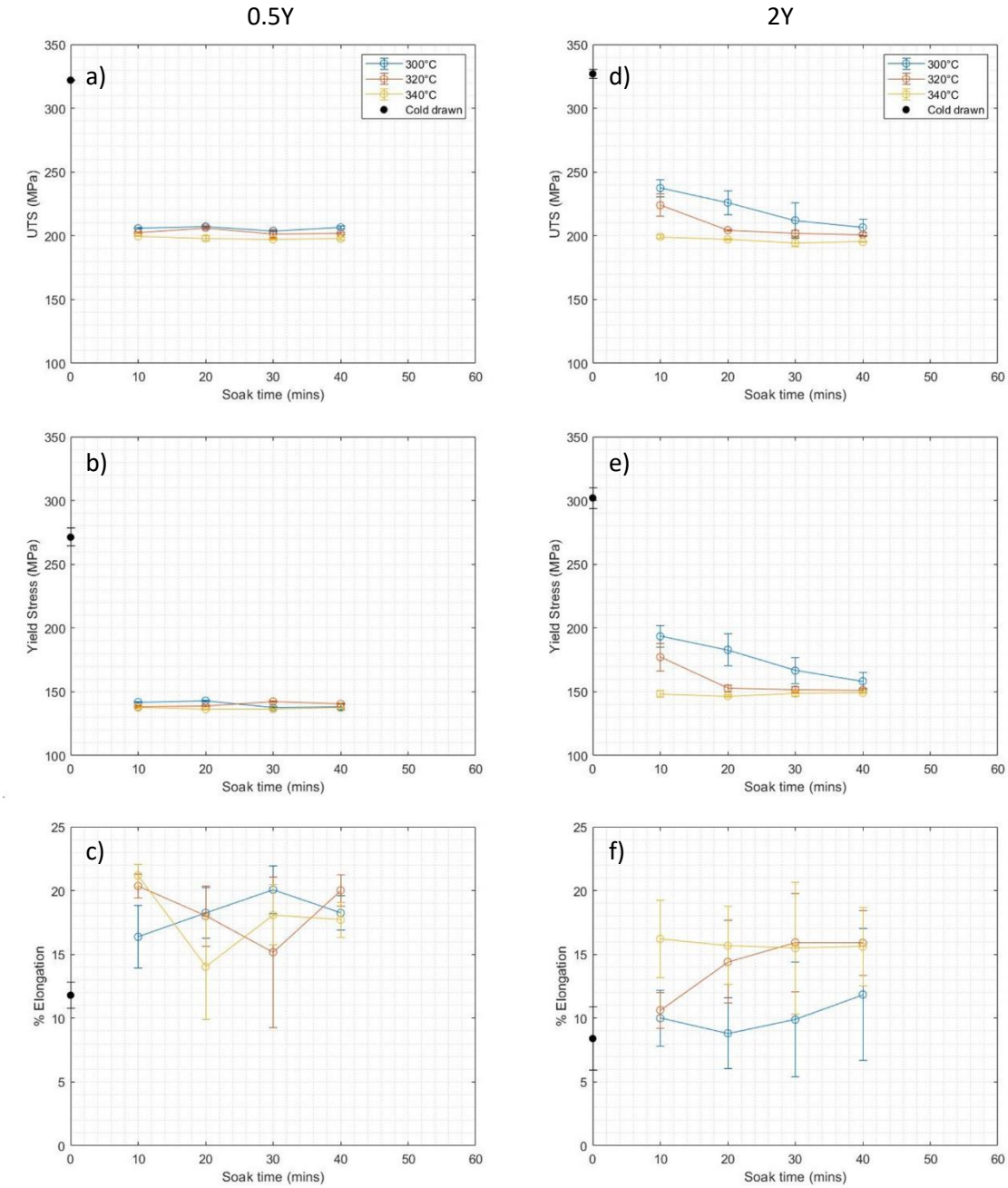

Figure 4.11: Tensile test results from annealing study a) 0.5Y elongation to failure b) 0.5Y UTS c) 0.5Y YS d) 2Y elongation to failure e) 2Y UTS f) 2Y YS

320°C/10mins (20.4+/-0.9%), 320°C/40mins (20.0+/-1.2%) and 340°C/10mins (21.2+/-0.9%). As can be seen from Figure 4.11b and c there was very little variation in UTS and YS for all of the procedures investigated, and the standard deviations were low for each test on the 0.5Y alloy wire. An "optimum" procedure was required to be defined for further testing and analysis (MBD and EBSD analysis). Therefore, annealing at 340°C for 10mins was defined as the optimum procedure. Under these conditions the wire had an elongation to failure, UTS and YS of 21.2+/-

0.9%, 199.6+/-0.3MPa and 137.7+/-0.6MPa respectively. Compared to the results from the 0.5Y alloy wire the mechanical properties of the 2Y alloy wire follow a more typical trend whereby the strength of the alloy wire decreases with increased soak time and temperature. Figure 4.11d shows that the elongation to failure of the 2Y wire trended upwards when treated at 300°C, increasing the soak temperature to 320°C shows a similar trend as the elongation to failure trends upwards to approximately 15% when treated for 30mins before plateauing at approximately 15% as soak time was increased to 40mins. At the higher soak temperature of 340°C the elongation to failure remained relatively consistent across the soak temperatures investigated: 16.2+/-3.0%, 15.7+/-2.1%, 15.5+/-5.2% and 15.6+/-3.1% at 10, 20, 30 and 40mins respectively. Compared to the 0.5Y alloy wire there was a much larger variation in results for the 2Y alloy at all soak times and temperatures for both the strength of the wire as well as elongation to failure. Treating the 2Y wire at 340°C for 10mins was defined as the optimum treatment for further testing. Under these conditions the wire had an elongation to failure of 16.2+/-3.0%, UTS and YS of 199.6+/-0.3MPa and 137.7+/-0.6MPa respectively.

MBD diameter testing was next complete on each of the alloy wires following annealing for optimal ductility, Figure 4.12. The wrapping tests found that the 2Y wire when annealed for maximum ductility had a MBD of 0.22mm. The 0.5Y alloy wire on the other hand could survive wrapping around the smallest diameter tested (0.135mm) and as such its true MBD could not be determined from these tests. Therefore, it was found that the 0.5Y alloy wire could survive idealised bending strains of at least 48.1% whereas the 2Y alloy wire could survive maximum idealised bending strains of 36.2%.

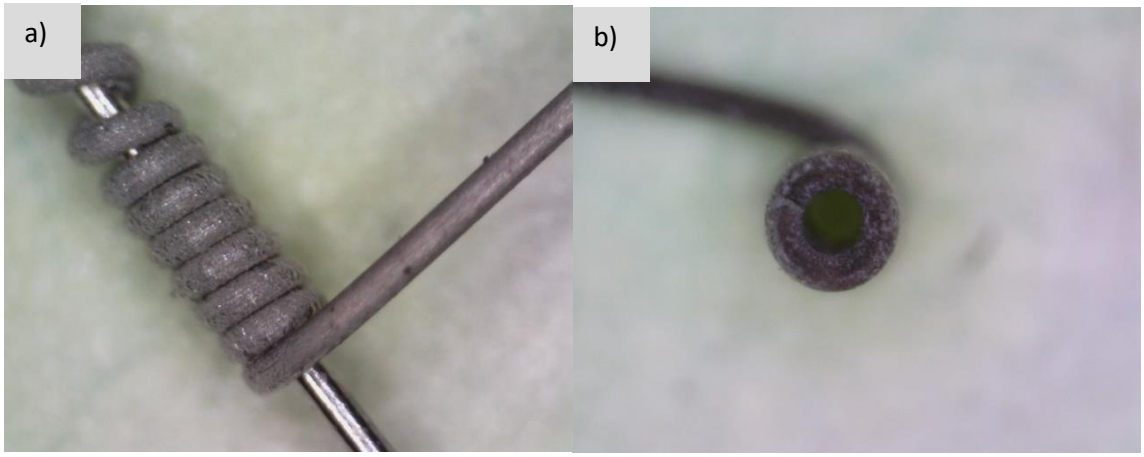

Figure 4.12: MBD tests a) 0.5Y alloy wire annealed at 340°C for 10mins wrapped around 0.135mm pin b) fracture of a 2Y alloy wire annealed at 340°C for 10mins wrapped around 0.2mm pin

4.3.2.3 EBSD Analysis

EBSD analysis was carried out on select samples to investigate the texture of each alloy and obtain accurate grain size measurements. The inverse pole figure (IPF) maps of the select 0.5Y samples are shown in Figure 4.13. Increasing the soak temperature had little effect on the grain size of the 0.5Y alloy wires, with the sample annealed at 300°C for 10mins having a mean grain size of 1.56+/-0.98µm and only increasing to 1.91+/-1.20 and 2.15+/-1.43µm at 320°C and 340°C respectively. The pole figures of each of the 0.5Y alloy wire samples analysed are displayed in Figure 4.14 and show that all of the samples exhibit a strong transverse basal texture with the soak temperature having no effect on the texture intensity.

The IPF maps of the 2Y alloys annealed at 300, 320 and 340°C for 10mins are shown in Figure 4.15. There is a large unindexed region in the centre of the samples treated at 300 and 320°C which corresponds to the unrecrystallised core observed in the optical micrographs. In the sample treated at 300°C the unindexed/unrecrystallised region is measured to be ≈75µm in diameter which is reduced to ≈60µm in the sample treated at 320°C. Following annealing at 340°C a fully recrystallised microstructure is developed, with a mean grain size of 1.31+/-0.82µm. Owing to the large unindexed regions in the 2Y alloy wire when treated at 300 and 320°C, only the pole figures for the sample treated at 340°C are shown in Figure 4.16. Similarly, to the 0.5Y allow wire a transverse basal texture is developed in the 2Y alloy wire, however it has a weaker intensity compared to the 0.5Y alloy wire samples.

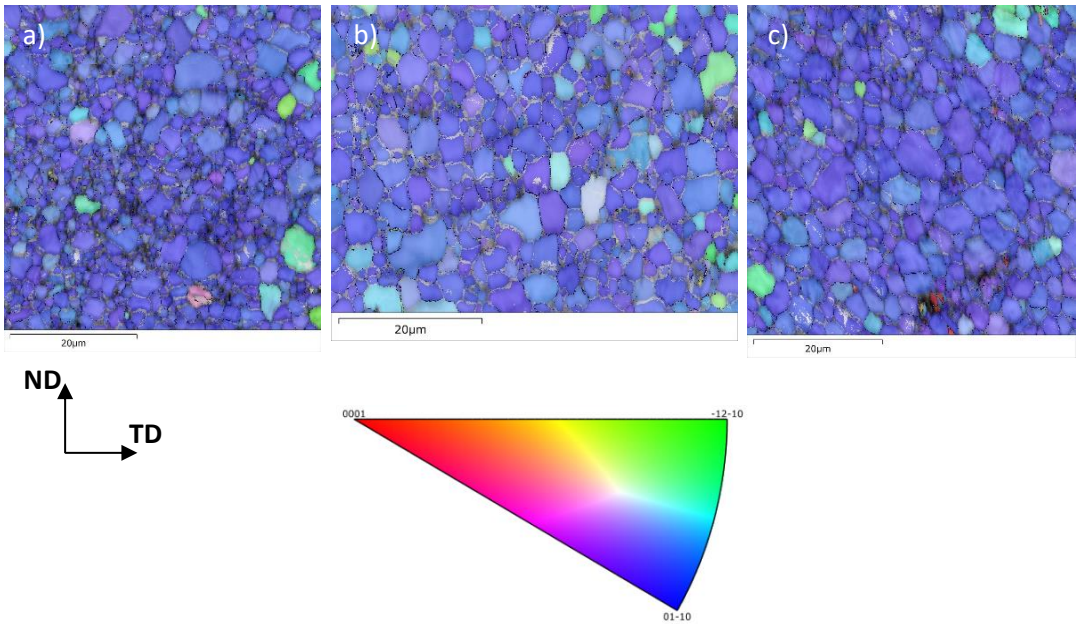

Figure 4.13: IPF maps for the 0.5Y alloy wire annealed at a) 300°C for 10mins b) 320°C for 10mins c) 340°C for 10mins

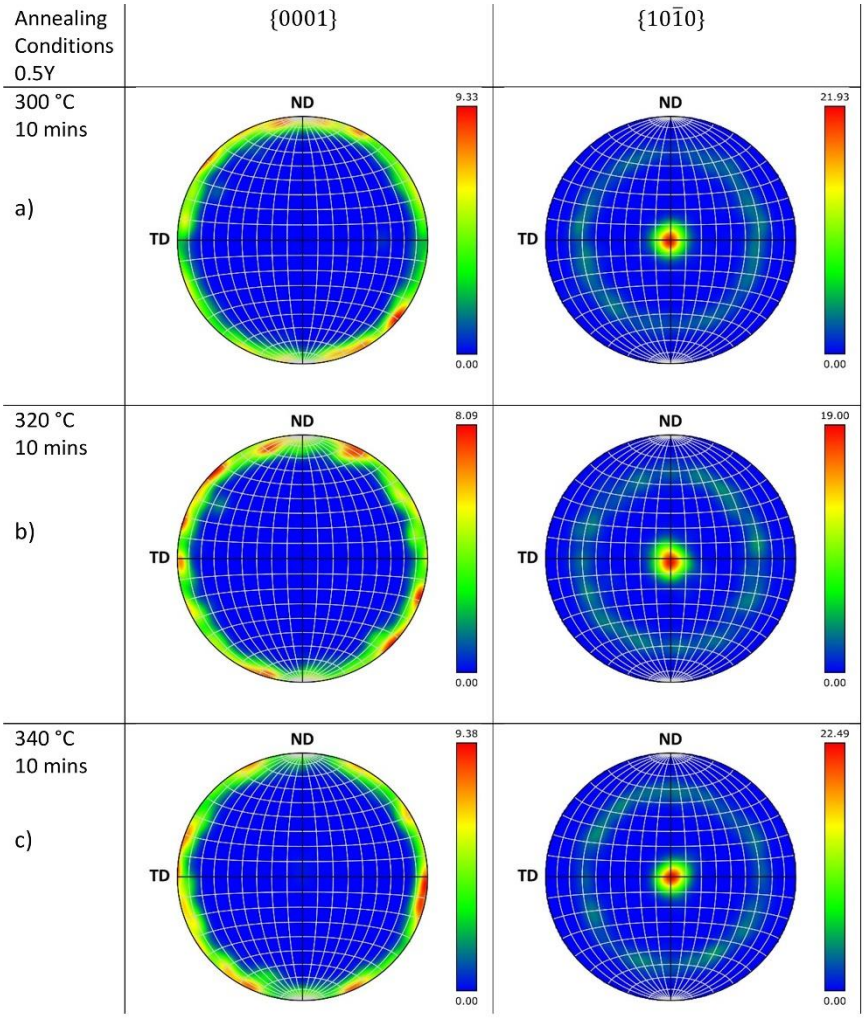

Figure 4.15: Pole figures for the 0.5Y alloy wires annealed in the vacuum oven

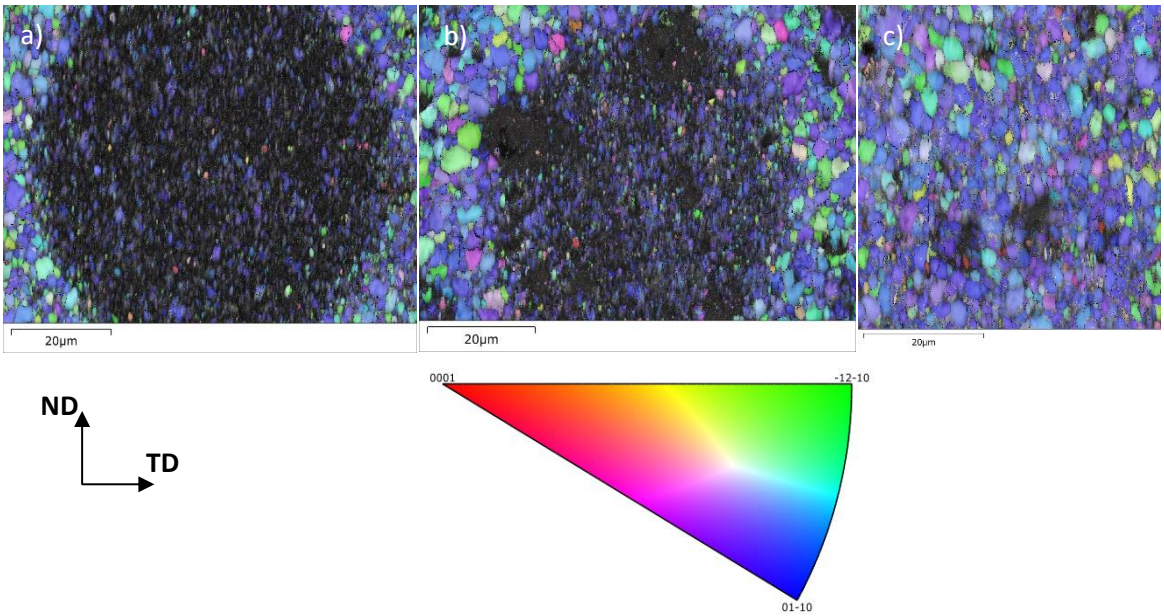

Figure 4.14: IPF maps for the 2Y alloy wire annealed for 10mins at a) 300°C b) 320°C c) 340°C

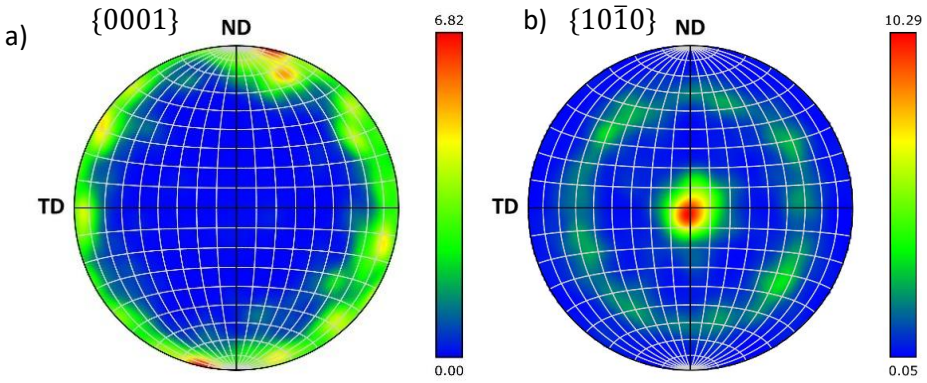

Figure 4.16: Pole figures for 2Y alloy wire annealed at 340°C for 10mins a) basal pole figure b) prismatic pole figure

4.3.3 Vacuum Tube Furnace

4.3.3.1 Microstructure

Samples were annealed at temperatures from 250 to 450°C for soak times between 10 and 120mins and the microstructural evolution of a range of samples were analysed. It was found that recrystallised grains began to from near the OD of the 0.5Y alloy wire following annealing at 250°C for 10mins, with no recrystallised grains observed in the wires core, Figure 4.17a-c. A higher soak temperature of 300°C was required for recrystallised grains to be observed developing near the OD of the 2Y alloy wire following annealing for 10mins, Figure 4.17d-f.

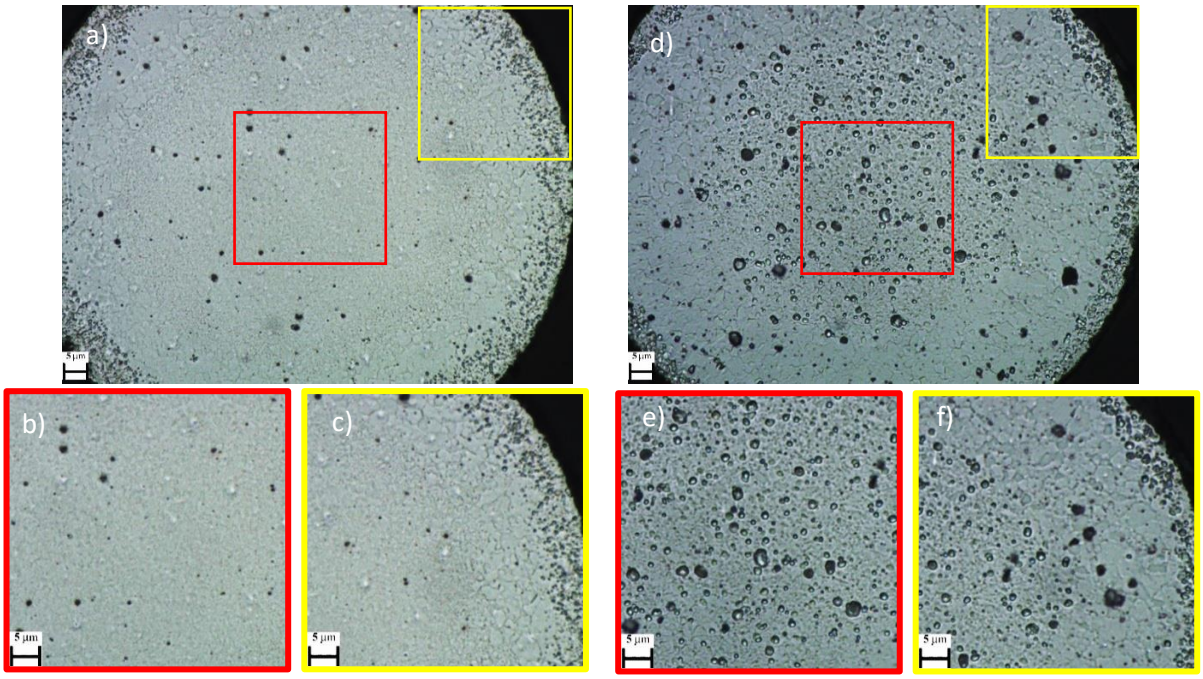

Figure 4.17: Microstructure of 0.5Y wire annealed at 250°C for 10 mins a) full cross section b) centre c) OD and 2Y wire annealed at 300°C for 10 mins d) full cross section e) centre f) OD

Again, no recrystallised grains were observed in the wire core and as such it is assumed recrystallisation is not complete in these regions whereas, near the OD of both alloy wires, recrystallisation is assumed complete.

Following on from these observations the microstructural evolution of the 0.5Y and 2Y alloy wires was investigated at 250 and 300°C, respectively, for increasing soak times. Figure 4.18 analyses a 50x50µm region at the centre of the wires cross-section at x1000 magnification in order to assess the progression of recrystallisation in each alloy wire. Figure 4.18 a1 shows that after 20mins at 250°C the wire core remains unrecrystallised in the 0.5Y alloy wire. As soak time is increased to 30mins recrystallised grains are observed throughout the full 50x50µm region, though a more refined grain size is observed at the centre of the image/wire. At the increased soak time of 60mins a more uniform grain size distribution is observed throughout the wires with little change as soak time is increased further to 120mins. In the 2Y alloy wire a fully recrystallised microstructure is developed throughout the wire after 20mins at 300°C (Figure 4.18 b1) with a uniform grain size distribution, with little change in the grain size as soak time is increase to 120mins. As the grain size of both alloys is on the scale of 1-2µm, it is challenging to resolve all grain boundaries using optical microscopy. Therefore, no attempt was made to determine grain size from the optical micrographs and instead more accurate grain size measurements are obtained for select samples using EBSD analysis in Section 4.3.3.3. In both alloy wires small dark cubic particles are observed through each of the optical micrographs and marked with black arrows, these are identified with SEM and XRD analysis and are discussed further in this section.

The microstructure of both alloy wires annealed at higher temperatures for various soak times was investigated and the results are shown for the 0.5Y and 2Y alloy wires in Figure 4.19 and Figure 4.20 respectively. When the soak temperature is increased to 350°C in the 0.5Y alloy wire grain coarsening is observed. Abnormal grain growth is observed in the 0.5Y alloy wire when treated at 400°C for 30 and 120mins and at each soak time investigated at 450°C. Comparatively in the 2Y alloy, little grain coarsening is observed at the higher soak temperatures. In both alloy wires however, the number and size of secondary phase particles precipitated out of solution is increased with increasing soak temperature.

SEM/EDS analysis was carried out on the 0.5Y and 2Y alloy wires following annealing for 30 mins at 250°C and 20 mins at 300°C respectively, to investigate the distribution of secondary phase particles in the wires upon complete recrystallisation (Figure 4.21). Areas with a higher

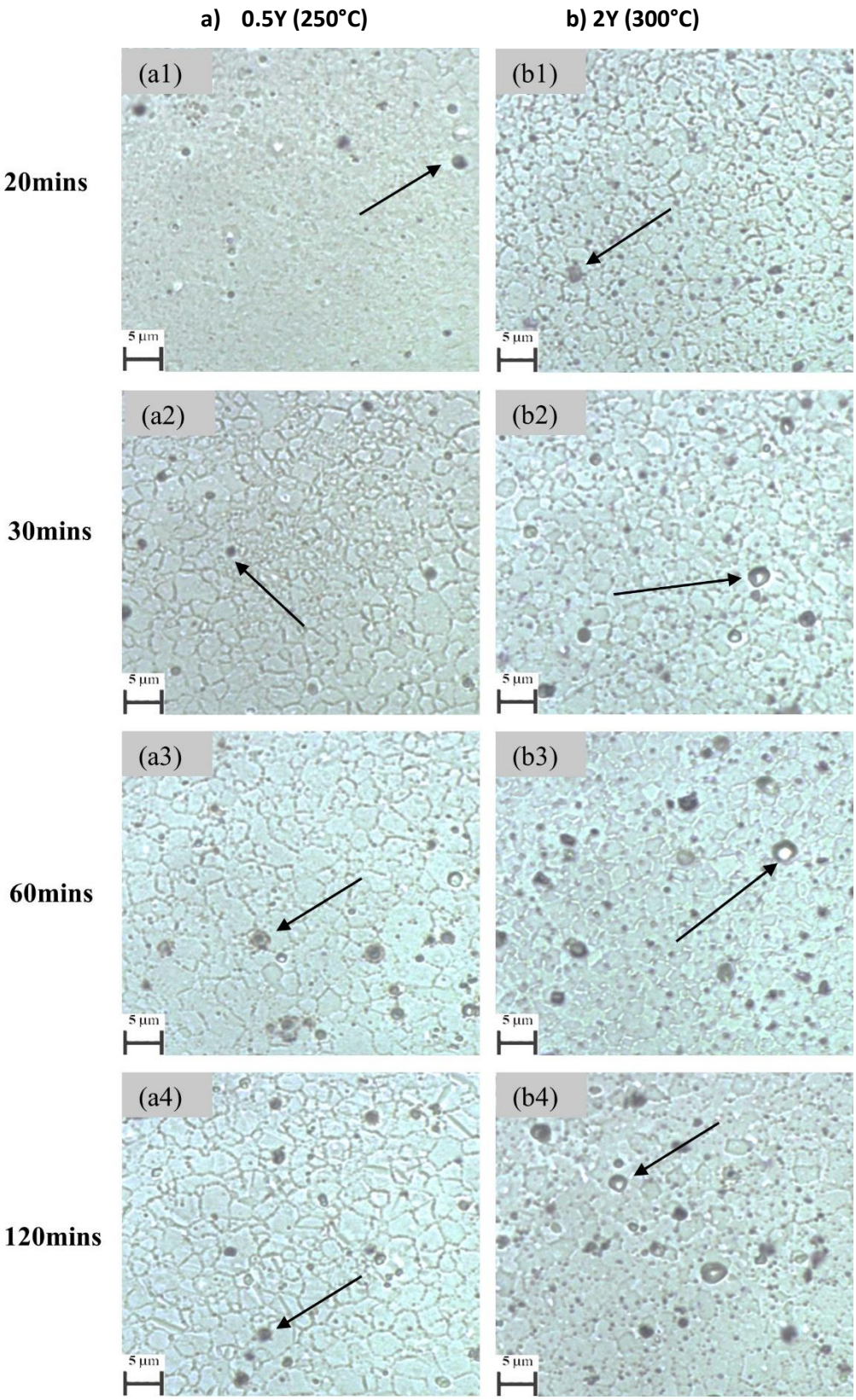

Figure 4.18: Annealed microstructures of both alloys over a range of soak temperatures, arrows highlight secondary phase particles a) 0.5Y b) 2Y

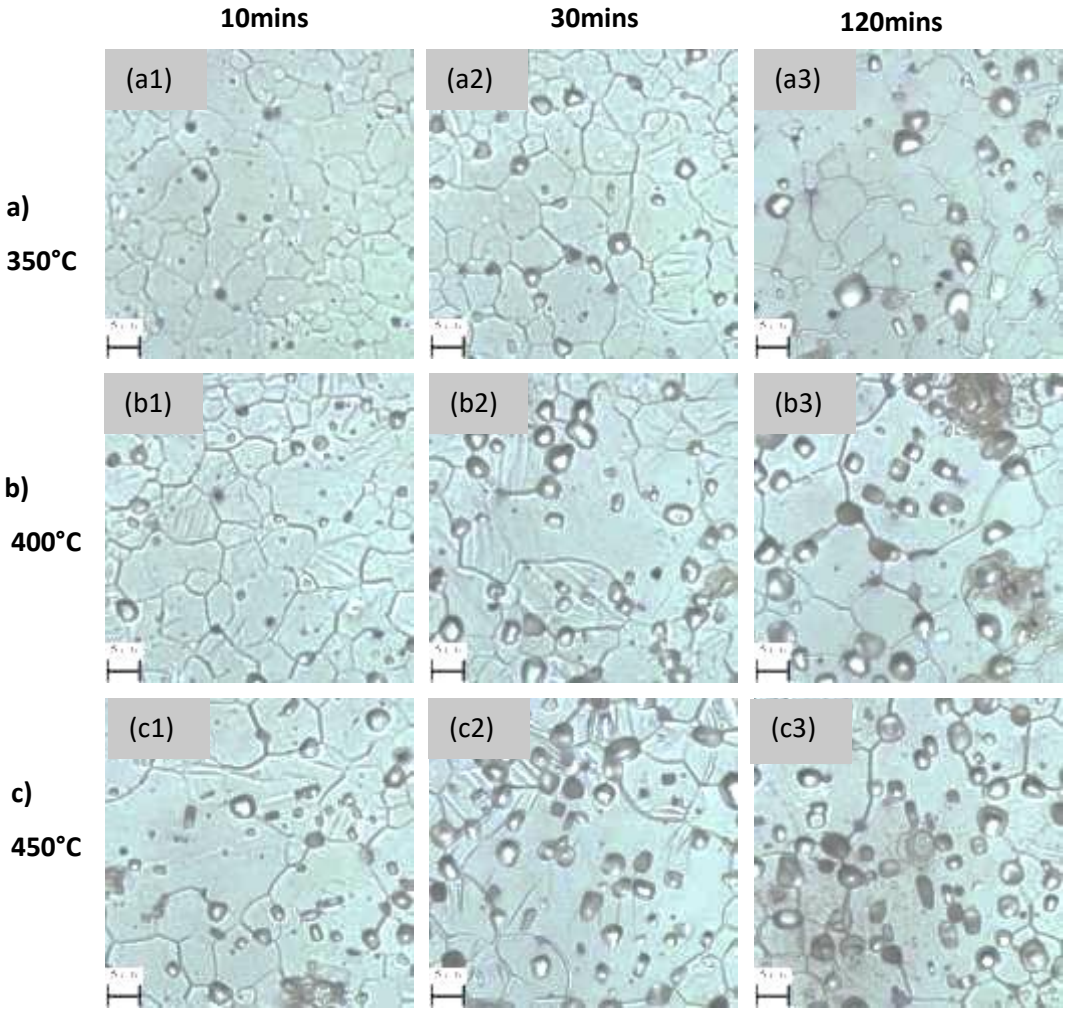

Figure 4.19: 0.5Y wire microstructures annealed at different temperatures for 10, 30 and 120mins a) 350°C b) 400°C c) 450°C

concentration of Y will appear bright compared to the Mg matrix using the BSE detector. The small cubic particles observed in optical microscopy are also apparent in Figure 4.21a and b and appear brighter compared to the Mg matrix, indicating they contain increased concentrations of Y compared to the bulk Mg matrix. Figure 4.21a and b, each include an inset higher magnification SEM image which show such particles. EDS analysis of these particles estimated the Y content to be 36.4 and 31.7at% for the 0.5Y and 2Y alloys respectively. To identify the true composition of these particles XRD analysis was conducted on the 0.5Y alloy wire following annealing at 450C for 30mins (Figure 4.22). As can be seen the XRD analysis identified these particles as $Mg_{24}Y_{5.}$ It is assumed that the structure of these particles is consistent in both alloy wires following the range of thermal processes investigated in this work. It should also me noted that the XRD analysis did not identify any Li-rich phase, indicating that Li is maintained in solid solution.

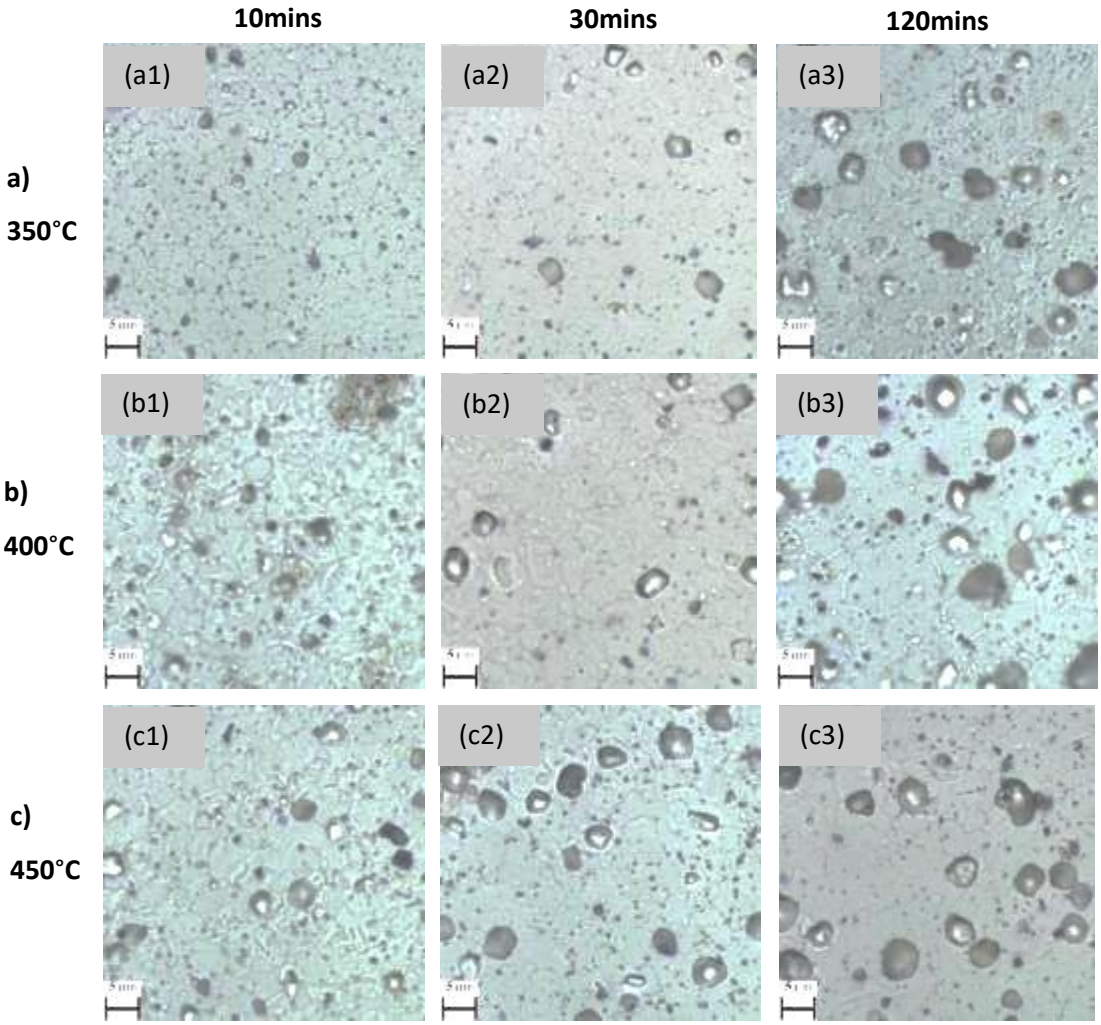

Figure 4.20: 2Y wire microstructures annealed at different temperatures for 10, 30 and 120mins a) 350°C b) 400°C c) 450°C

4.3.3.2 Mechanical Properties

First the microhardness of the 0.5Y and 2Y alloy wires were measured on samples treated at 250 and 300°C respectively for a range of soak times, Figure 4.23. The hardness of the cold drawn wire is represented as time point 0 on the x-axis. As recrystallisation progresses in both alloys the hardness at both the centre and mid-radial position follow a similar trend: rapidly decreasing as soak time is increased from 0 to 30mins and subsequently stabilising in the range 50-54 Hv as soak time is increased to 120mins. In both alloys, the hardness at the mid-radial position of the wire decreases at a faster rate compared to the centre.

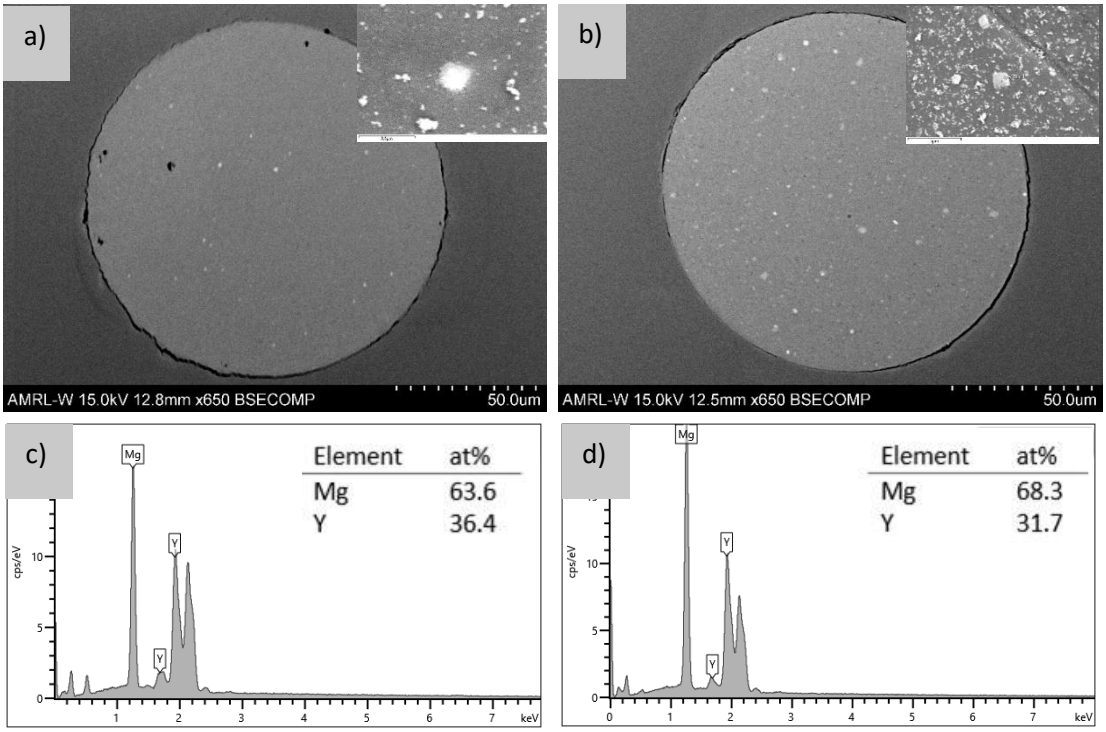

Figure 4.21: BSE images of wire cross sections with zoomed in SEM image of representative secondary phase particle analysed with EDS a) 0.5Y wire annealed at 250 °C for 30 mins b) 2Y wire annealed at 300 °C for 20 mins. EDS spectra of representative secondary phase particle from c) 0.5Y wire annealed at 250 °C for 30 mins d) 2Y wire annealed at 300 °C for 20 mins

The results from the tensile tests from the annealing study are plotted in Figure 4.24, with the properties of the respective cold drawn alloy wires shown at time point 0 on the x-axis. For the 0.5Y alloy wire after annealing at 250°C for 10mins, the UTS and YS remain close to that of the

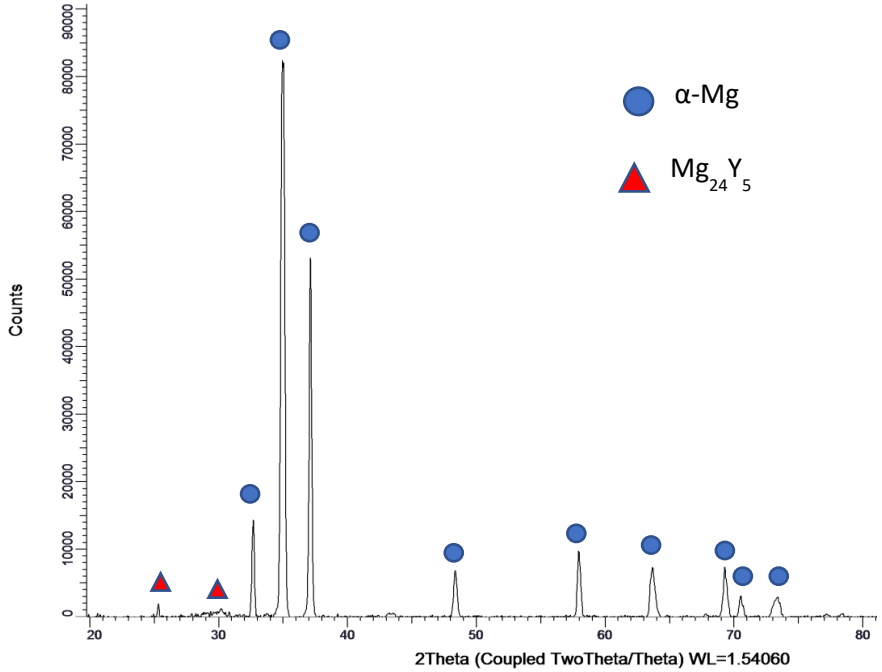

Figure 4.22: XRD spectrum of 0.5Y wire annealed at 450°C 30mins

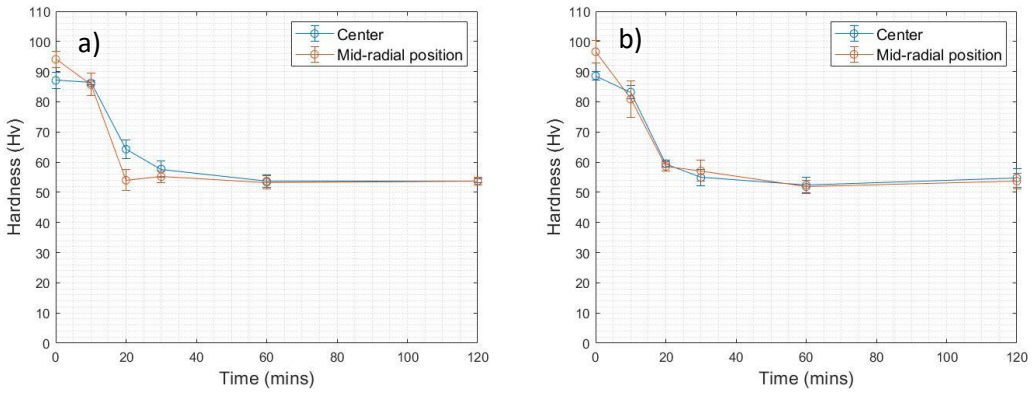

Figure 4.23: Microhardness values at the centre and mid-radial position of each alloy wire a) 0.5Y wire annealed at 250°C b) 2Y wire annealed at 300°C. Error bars show standard deviation

cold drawn wire whilst the elongation is relatively low. As soak time is increased at 250°C to 20mins the UTS and YS drop significantly whilst the elongation begins to increase, after annealing for 30mins at 250°C the elongation to failure is maximised at 20.3±0.4%, whilst the YS and UTS fall to 133±2.6MPa and 196±0.8MPa respectively. As soak time is further increased at 250°C these properties remain relatively consistent. At the higher soak temperatures, the results follow a different trend where the elongation to failure is highest after 10mins of annealing before decreasing as soak time is increased. The UTS and YS of the 0.5Y alloy wire when treated at 250-350°C remained relatively consistent over the soak times analysed (approximately 130MPa and 195MPa respectively). When treated at 400 and 450°C strengthening of the wire was observed as soak time increased. It should be noted that the 0.5Y sample treated at 450°C for 120mins fractured before yield and as such the YS value has been omitted from Figure 4.24b.

As in the 0.5Y alloy wire the UTS and YS of the 2Y wire remained similar to that of the cold drawn wire following annealing at 250°C for 10mins. As soak time increased at 250°C the UTS and YS were both seen to decrease rapidly, reaching approximately 149 and 200MPa respectively after annealing for 120mins. Similarly, after annealing for 10mins and 300°C the 2Y wire maintained relatively high strength. The strength of the wire decreased rapidly following annealing for 20mins at 300°C where the UTS and YS were 150±2.0MPa and 207±0.4MPa respectively, whilst the elongation to failure of the wire was maximised at 19.7±1.1%. As soak time increased at 300°C the strength of the wire remained relatively consistent whilst the elongation to failure decreased. As with the 0.5Y alloy wire following annealing at the higher soak temperatures of 400 and 450°C, strengthening was observed as soak time increased. It should be noted that the strengthening effect was not as clear in the UTS data as the samples fractured soon after yield meaning work hardening was limited in the range of samples analysed.

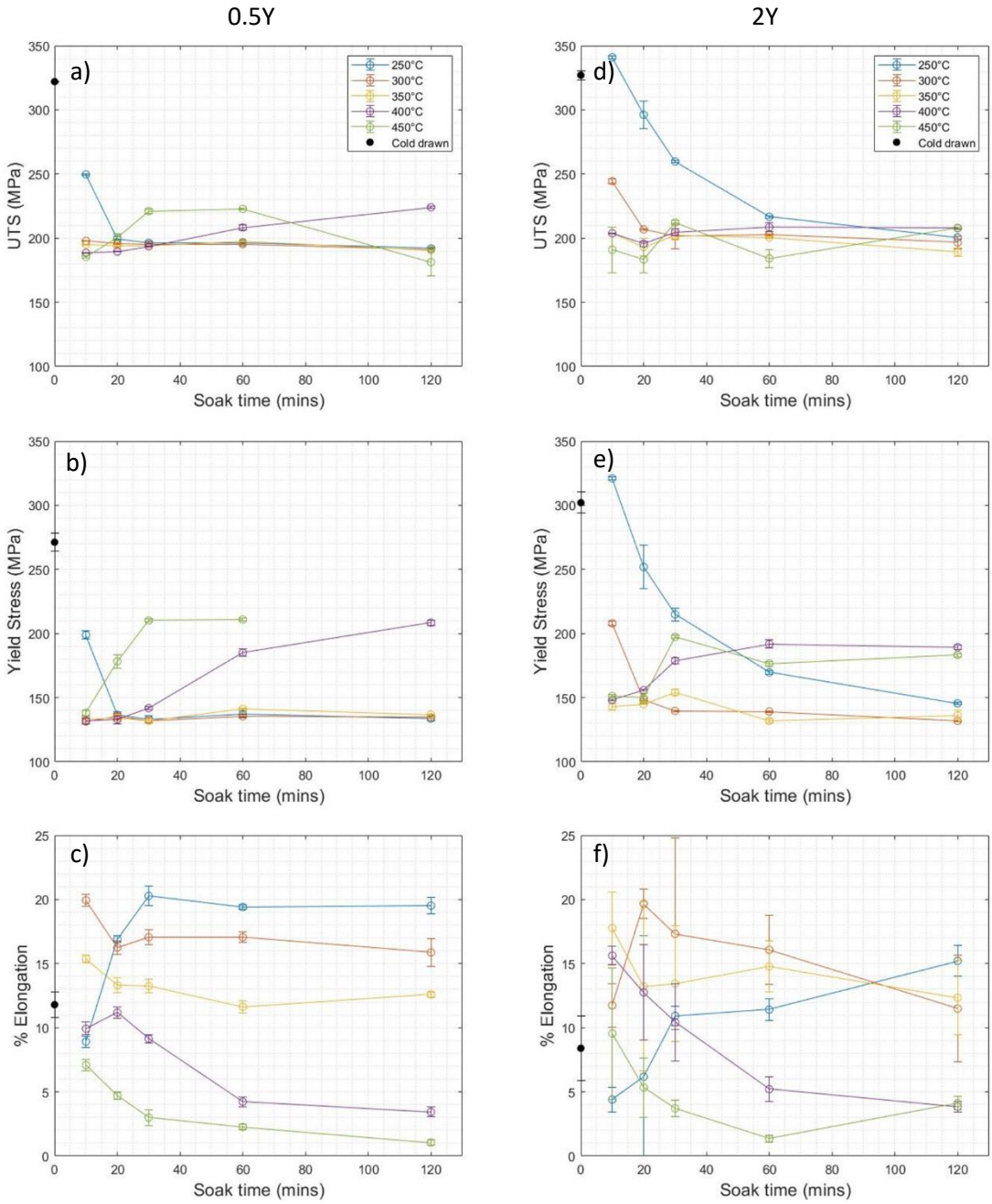

Figure 4.24: Mechanical properties of both alloys post annealing a) 0.5Y UTS b) 0.5Y YS c) 0.5Y % Elongation to failure d)2Y UTS e) 2Y YS f) 2Y % Elongation to failure. Error bars show standard deviation

As with the oven annealing study an annealing process had to be defined as optimum and applied to the wires for MBD test investigation and to base the EBSD analysis around. As such it was defined that annealing the 0.5Y alloy wire at 250°C for 30mins as optimum and for the 2Y alloy wire the process selected was 300°C for 20mins. Wrapping tests found that both the 0.5Y and 2Y alloy wires when optimally annealed could survive wrapping around 0.135mm pins, corresponding to a maximum idealised bending strain of 48%, Figure 4.25

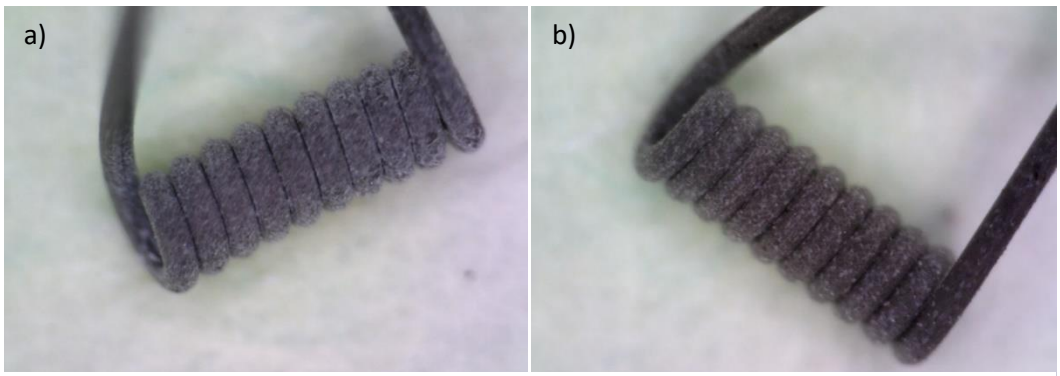

Figure 4.26: MBD testing of a) 0.5Y alloy wire annealed at 250°C for 30mins b) 2Y alloy wire annealed at 300°C 20mins, wrapped around 0.135mm pins

4.3.3.3 EBSD Analysis

EBSD analysis was carried out on selected samples of the 0.5Y and 2Y alloy wires following different annealing processes in order to gather accurate grain size measurements as well as analyse the recrystallised texture. The IPF maps of the select samples are displayed in Figure 4.26. The IPF maps in Figure 4.26a and d show the microstructure of the 0.5Y and 2Y alloy wires

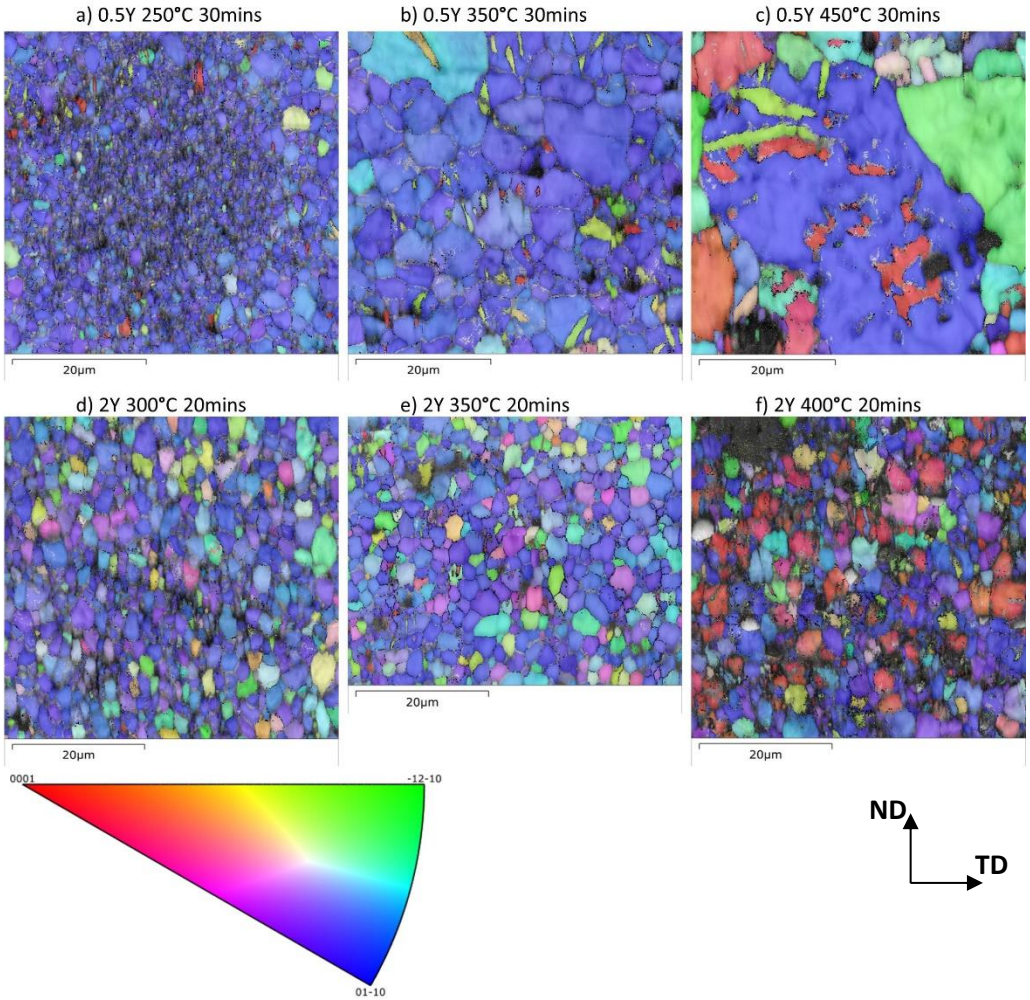

Figure 4.25: Inverse pole figure maps of both alloys post annealing a) 0.5Y 250°C 30mins b) 0.5Y 350°C 30mins c) 0.5Y 450°C 30mins d) 2Y 300°C 20mins e) 2Y 350°C 20mins f) 2Y 450°C 20mins

when annealed for maximum ductility. The uneven grain size distribution in the 0.5Y alloy wire treated at 250°C for 30 mins is shown more clearly here compared to the optical micrographs. Figure 4.27 highlights the central region (Figure 4.27a) and edge of the map (Figure 4.27b) where the mean grain size has been calculated as 1.18 and 2.12µm respectively. The full map has a mean grain size of 1.87µm. As grain growth progresses in the 0.5Y samples annealed at higher temperatures, coarsening of some grains takes place. In the sample treated at 350°C the mean grain size increases to 6.4µm and in the sample treated at 450°C one grain with a diameter of ≈30µm dominates the IPF map. A more uniform grain size distribution is developed in the 2Y alloy wire post annealing at all temperatures analysed, with the samples treated at 300, 350 and 400°C grain sizes being 2.48, 2.57 and 2.68µm respectively.

The corresponding pole figures of the samples shown in Figure 4.26 are displayed in Figure 4.28 and Figure 4.29 for the 0.5Y and 2Y alloy wires respectively. It can be observed that when annealed for optimal mechanical properties (250°C for 30mins) the 0.5Y alloy wire exhibits a strong transverse basal texture, whereby the basal planes are aligned parallel with the DD. This basal texture is maintained in the 0.5Y alloy wire treated at 350°C for 30mins. The pole figure of the 0.5Y alloy wire annealed at 450°C for 30mins exhibits an intense basal texture as the pole figure is dominated by the large grain observed in the IPF map (Figure 4.26c). Figure 4.29a shows that the 2Y alloy wire also exhibits a transverse basal texture following annealing for optimal mechanical properties (300°C for 30mins) however the intensity is weaker compared to that of the 0.5Y alloy wire. A similar texture to that developed at 300°C is developed at 350°C for the 2Y

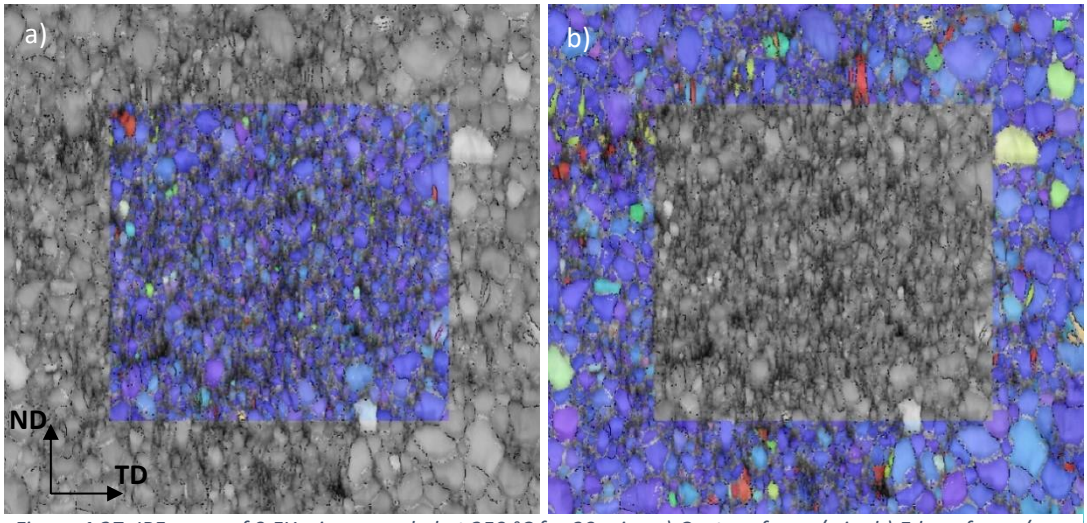

Figure 4.27: IPF maps of 0.5Y wire annealed at 250 °C for 30 mins a) Centre of map/wire b) Edge of map/area closer to the OD

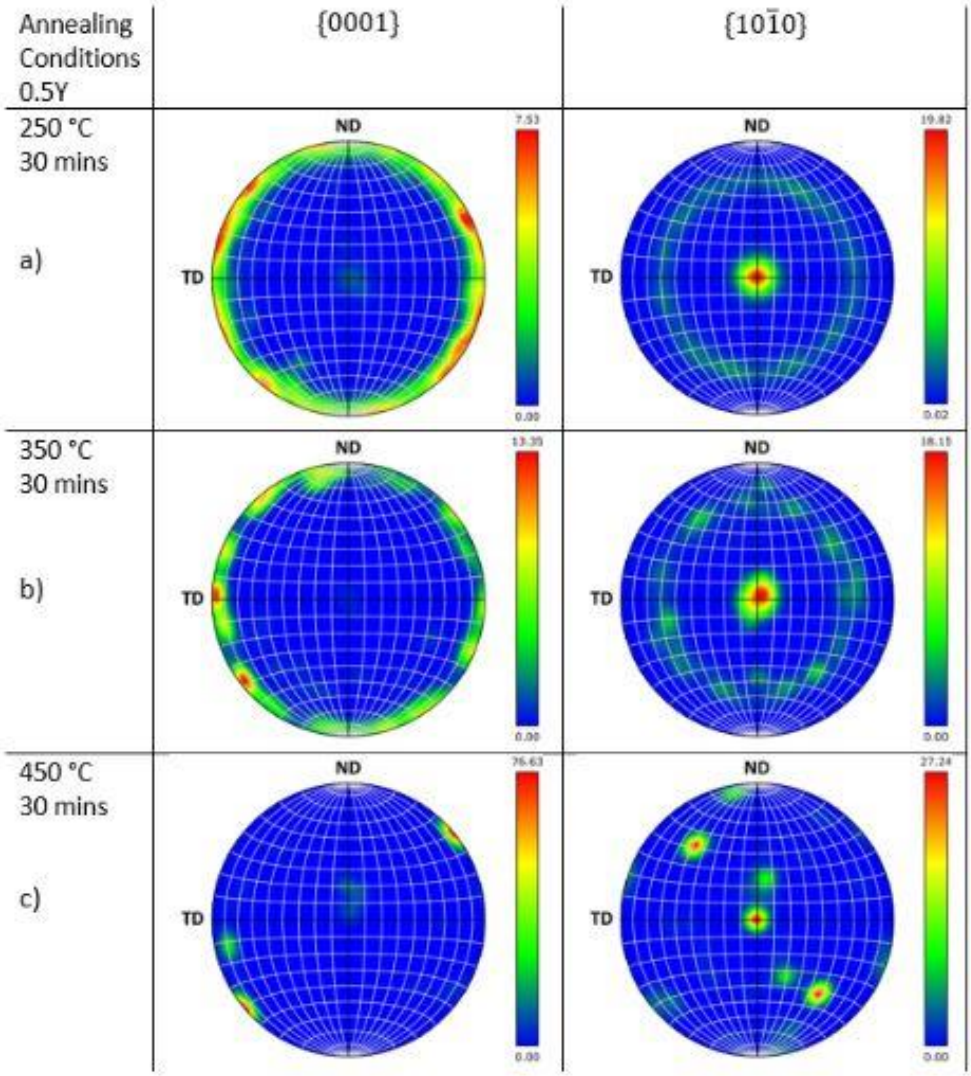

Figure 4.28: Pole figures of 0.5Y alloy wires post annealing

alloy wire. Following annealing for 20mins at 400°C however there is a distinct shift in texture where the basal plane of some grains has tilted by ≈90° to align perpendicular to the DD.

4.4 Discussion

4.4.1 Grain growth

The microstructural investigations revealed that in both alloy wires recrystallisation is initiated first close to the OD of the wire and progresses towards the wire core. This is seen most clearly in the IPF maps of the 2Y wire following annealing in the vacuum oven at 300, 320 and 340°C (Figure 4.14). Recrystallised grains are developed around the edge of the IPF map (corresponding to the regions of wire closest to the wires OD) of the 2Y alloy wire treated at 300°C for 10mins with the central region of the map (corresponding to the wire core) remaining

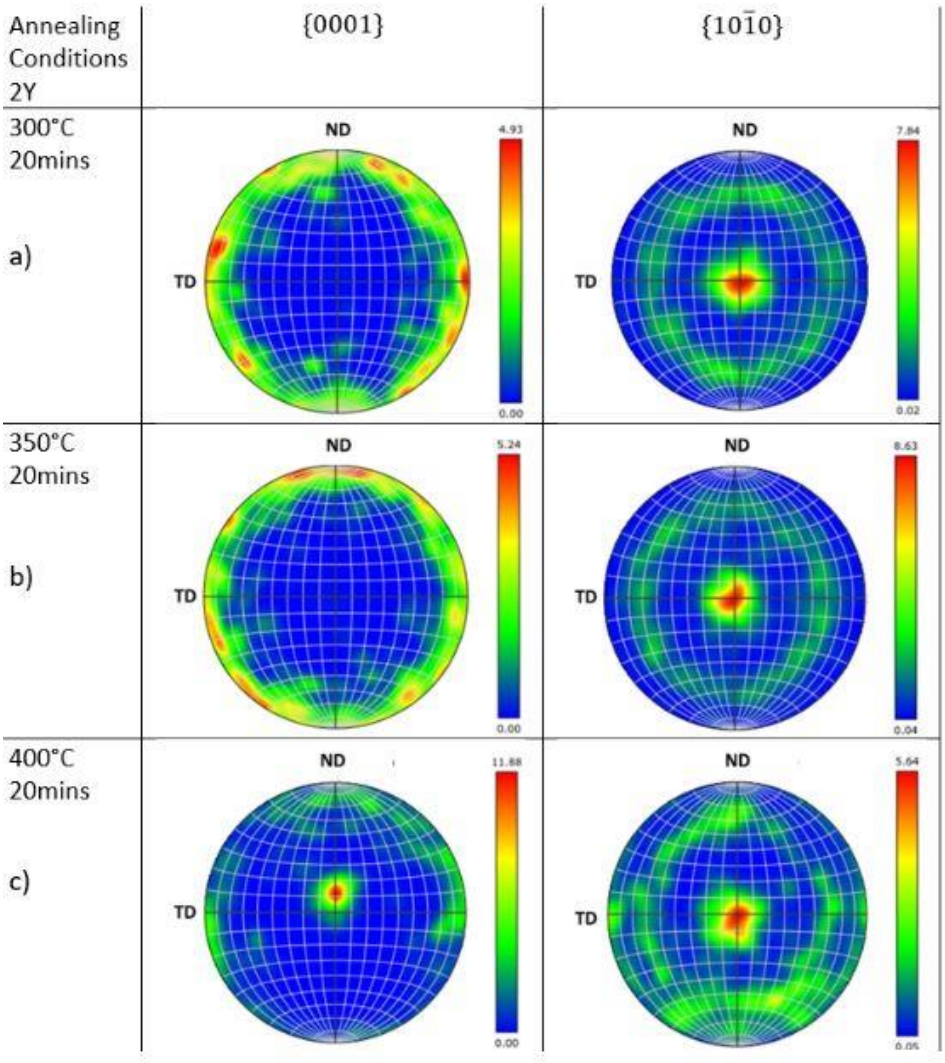

Figure 4.29: Pole figures for 2Y alloys wires post annealing

unindexed and assumed unrecrystallised. This unrecrystallised region is circular suggesting that recrystallisation initiated from regions close to the OD and progressed inwards towards the wire core radially. The unindexed region following annealing at 300°C for 10mins has a diameter of ≈75µm, this is reduced to ≈60µm following annealing at 320°C for 10mins. A fully recrystallised microstructure is developed in the wire following annealing at 340°C for 10mins. This progression of recrystallisation is also observed in both the 0.5Y and 2Y alloy wires when heat treated in the vacuum tube furnace at 250°C and 300°C respectively (Figure 4.18). This recrystallisation behaviour can be explained through considering the deformation profile induced during the cold drawing process. During cold drawing process, the outer diameter of the wire will undergo increased deformation compared to the wire core, resulting in increased internal stress within the regions of wire closest to the wires OD.[176, 193] Consequently, as internal stress acts as the driving force for nucleation and recrystallisation, new grains will be nucleated

first from the regions of highest internal stress closer to the OD of the wire, progressing inwards to the wire core as soak time is increased.

Measuring the internal stress distribution through the cold drawn wire is a costly and challenging process. However, as internal stress of a material increases so too does the hardness. As such Vickers microhardness testing was conducted to represent variations in internal stress between the wire core and the mid-radial position. It was found that in both cold drawn alloy wires there was increased hardness at the mid-radial position compared to the wire core (Figure 4.4). The relative differences between the hardness at the mid-radial position and wire core for the 0.5Y and 2Y alloy wires was 7.4 and 8.3% respectively. This hardness distribution suggests that, as expected, the OD of the wire has undergone increased deformation compared to the wire core during drawing, explaining why recrystallisation is seen to activate first from these regions. Following on from this, Figure 4.10 and Figure 4.23 plots how the hardness at these two locations varied as recrystallisation progressed in both alloy wires during annealing in the vacuum oven and vacuum tube furnace respectively. In the 0.5Y alloy wire treated in the vacuum oven the hardness was relatively consistent at the mid-radial position and the wire core (Figure 4.10a), owing to the sample being fully recrystallised at the lowest temperature investigated. However, in the 2Y alloy wire, annealed in the vacuum oven, it was clear that the hardness at the centre of the wire was increased compared to the mid-radial position following annealing at 300 and 320°C for 10mins Figure 4.10b, as the wire core remained unrecrystallised (Figure 4.14). Following annealing in the vacuum tube furnace a similar hardness evolution was seen in both alloy wires (Figure 4.23). Upon complete recrystallisation in both alloy wires it was shown that the hardness at the centre and mid-radial positions plateaued at approximately the same level. This result, combined with the optical micrographs showing recrystallised grains developed first around the OD of the wire confirms that recrystallisation was initiated first from the regions of highest internal stress, near the OD of the wire, and progressed inwards to the wire core with increased soak time.

Differences in grain growth, following complete recrystallisation, was observed between both alloys. In the 0.5Y alloy samples heat treated in the vacuum oven little grain growth was observed between the samples treated at 300°C and 340°C. With recrystallisation only being complete in the 2Y samples following annealing at 340°C for 10mins little investigation of grain growth could be conducted from this annealing study. However, clear differences in grain growth behaviour were identified from the tube furnace annealing study. Firstly, in the 0.5Y alloy

wire it was shown that, when annealed for maximum elongation to failure (250°C for 30mins), an inhomogeneous grain size distribution was developed; with refined grains in the wire core and larger grains towards the OD of the wire. As annealing progressed a more homogeneous microstructure was developed, however no increase in ductility was observed. At the higher soak temperatures of 300 and 350°C grain coarsening was observed in the 0.5Y alloy wire, with the sample treated at 350°C for 30mins having a grain size of 6.4µm. Abnormal growth was observed when annealed at 400 and 450°C with the IPF map in Figure 4.26c being dominated by a grain with a diameter of approximately 30µm. No abnormal grain growth was activated in the 2Y alloy wire during any of the annealing procedures investigated in this work with the grain size only increasing from 2.48µm, when treated at 300°C for 20mins, to 2.68µm at 400°C for 20mins. The cold drawn 2Y alloy wire contained an increased number of precipitates (Figure 4.3) that may act to restrict boundary mobility during prolonged annealing, through particle pinning. A large number of precipitates are also developed in the 0.5Y alloy (Figure 4.19) that might be expected to restrict boundary mobility. However, it is shown that these particles develop following complete recrystallisation, once grain coarsening is already underway. Therefore, these particles are shown to not promote recrystallisation of a more homogeneous microstructure. Additionally, Y and other RE elements are known to segregate to grain boundaries, restricting their mobility during thermal processing which can promote texture weakening and recrystallisation of a more homogenous microstructure.[150, 194] It is shown that increasing the Y content to 2wt% develops a more homogeneous microstructure and prevents grain coarsening during annealing at higher temperatures, either through particle pinning, solute drag or some combination of both.

4.4.2 Secondary Phase Particle Evolution

Analysis of the secondary phase particle distribution was conducted using optical microscopy, SEM/EDS analysis and XRD analysis. Using optical microscopy these particles appeared as small dark cubic regions as they often were dislodged from the surface during sample preparation. These particles were identified as being Y-rich using EDS analysis (Figure 4.22) and confirmed to be $Mg_{24}Y_5$ particles with XRD analysis (Figure 4.21). As the particles were Y-rich they appeared brighter than the Mg matrix in SEM imaging. EDS and XRD analysis were only conducted on select samples and as such it is assumed that the particles developed in all samples were $Mg_{24}Y_5$. Nevertheless, the exact composition of the particles is not of great concern but rather their evolution during the range of annealing procedures carried out and how their presence may

affect microstructural evolution and the mechanical properties of the alloy wires. Some consideration of the composition should be made when considering biocompatibility and corrosion resistance of these alloys, which is out with the scope of this work. However, concerning corrosion in *vivo* it is known that there are three main secondary phase particles developed in MgY alloys ($Mg_{24}Y$, Mg_2Y and MgY), each of which are more noble than the Mg matrix and as such can result in micro-galvanic corrosion activating in the alloy, accelerating the degradation rate.[195, 196] Consequently, not considering the effect on mechanical properties, the uncontrolled precipitation of the Y-rich secondary phases should be avoided when developing MgY alloys for application in biomedical devices.

SEM analysis identified that secondary phase particles were present in both cold drawn alloy wires with the 2Y alloy wire having an increased number compared to the 0.5Y alloy wire. Owing to the increased Y content of the 2Y alloy wire it was anticipated that an increased number of particles would be present in this alloy compared to the 0.5Y. However, it was not the aim of either alloy to contain a high number of precipitates, as this can lead to galvanic corrosion of Mg alloys in *vivo*, and also secondary phase particles can act as stress concentration sites that can lead to failure.[196, 197] As such considering the final application of these alloy wires it is preferable for the Y to remain in solution during processing. As the fabrication of the alloy wires was not conducted as part of this work no control was had over the prior processing and as such, improvements could not be made to increase the volume fraction of Y in solution. As described in Section 4.4.1, the presence of these particles may contribute to restricting abnormal grain growth in the 2Y alloy wire at high temperatures. The increased precipitation was likely responsible for the increased YS of the cold drawn 2Y alloy wire compared to the 0.5Y wire (302±8.2 and 271±7.0MPa respectively), though had little effect on the UTS of both alloy wires (327±3.6 and 322±0.4MPa for the 2Y and 0.5Y alloys respectively).

Analysis of the secondary phase particle evolution in both alloy wires during annealing in the vacuum oven can be carried out by considering the SEM analysis of the cross sections of select samples (Figure 4.9). Little change is observed in the number and size of particles precipitated out of solution in the 0.5Y alloy wire over the temperatures investigated. The number of particles present in the 2Y alloy wires following annealing in the vacuum oven remains relatively similar over the range of soak temperatures investigated. However, as soak temperature is increased to 320 and 340°C coarsening of some particles is observed in the 2Y alloy wire (Figure 4.9e and f). As is known precipitation is generally promoted during prolonged exposure to moderate

temperatures. In the case of Mg alloys age hardening in generally conducted at temperatures between 200 and 300°C.[198] As described in Chapter 3 when annealed at 300, 320 and 340°C the samples were exposed to temperatures >250°C for 34, 45 and 61mins respectively, in addition to the procedures soak time. Consequently, the coarsening of secondary phase particles during these annealing cycles is not surprising and is one potential benefit of the rapid heating and cooling cycles made possible with the vacuum tube furnace. No such coarsening of particles was observed in the 0.5Y alloy wires. However, with fewer particles present in the cold drawn alloy wires prior to annealing and few cross sections investigated, it may be the case that coarsening of some particles was present but not identified from the analysis conducted here.

When treated in the vacuum tube furnace where rapid heating and cooling cycles were applied and the samples were treated at higher temperatures compared to the vacuum oven, a slightly different evolution of the secondary phase particles were observed. Upon complete recrystallisation of both alloy wires, they contained a similar number and size of particles compared to their respective cold drawn states. As soak time was increased at 250°C for the 0.5Y alloy wire and at 300°C for the 2Y alloy wire little change was observed in the number and size of secondary phases present post annealing, Figure 4.18. However, post annealing at temperatures >350°C, increased precipitation was observed in both alloy wires (Figure 4.19 and Figure 4.20). As mentioned previously, generally low temperatures (200-300°C) are used to develop precipitates in Mg alloys and fewer particles are developed at elevated temperatures (e.g., >400°C).[198] However, Guan et al.[199] reported a similar phenomenon to that observed in this work, in WE43, whereby concurrent precipitation and recrystallisation was observed during high temperature annealing (490°C), suggesting it was caused by a combination of high residual strain and high solute concentration along prior grain and twin boundaries.[199] Both wires investigated here have been severely cold drawn and as such will have high residual strain prior to annealing. Secondly, it is assumed the bulk of Y content is maintained in solution prior to annealing. Therefore, the alloys analysed here have similar characteristics to those investigated by Guan et al.[199] Consequently, the increased precipitation in both alloys following high temperature annealing in the tube furnace may be explained by the high levels of residual strain and segregation of Y along prior grain and twin boundaries in the cold drawn wires.

4.4.3 Texture Evolution

EBSD analysis was conducted on both alloy wires to assess the texture evolution following a range of select annealing procedures using both the vacuum oven and tube furnace. As

mentioned, scans were run on the cold drawn wires but returned no useable data owing to the high levels of deformation making indexing challenging and assessment of the initial cold drawn wires' microstructures not possible. As such it is assumed that both cold drawn wires exhibit a typical deformed microstructure, with a fibrous grain structure with a strong basal texture.[185, 188] In all of the 0.5Y and 2Y samples (excluding the 2Y alloy wire annealed at 400°C for 20mins in the vacuum tube furnace) a transverse basal texture, was developed during annealing, similar to that observed in other Mg alloy wires.[183-185] However it was observed that a weaker texture was developed in the 2Y alloy wires compared to the 0.5Y alloy.

Firstly, it can be seen that there is very little variation in the texture developed in each of the 0.5Y samples from both annealing studies. An intense (≈7.5-9.5mrd intensity in the basal pole figure) transverse basal texture is developed in each of the samples treated in the vacuum oven and when annealed for maximum ductility (250°C for 30mins) in the vacuum tube furnace. When annealed at the higher temperatures in the vacuum tube furnace (350 and 450°C) grain coarsening results in an insufficient number of grains being indexed to accurately measure the texture intensity of the 0.5Y alloy. This is particularly clear in the sample annealed at 450°C for 30mins where a grain of ≈30µm dominates the IPF map (Figure 4.26c) causing the pole figure to be dominated by the orientation of this abnormal grain. It is expected that should a larger area be analysed, and an increased number of grains indexed, then the texture intensity would decrease.

A weakened transverse basal texture is developed in the 2Y alloy wire when annealed at 340°C for 10mins in the vacuum oven, compared to the 0.5Y alloy wires with a texture intensity of 6.82 and 10.29mrd in the (0001) and (10-10) pole figures respectively. When annealed for maximum ductility in the vacuum tube furnace (300°C for 20mins) a slightly weaker texture is developed in the 2Y alloy wire compared to when treated in the vacuum oven, with the (0001) and (10-10) pole figures having an intensity of 4.93 and 7.84mrd respectively. Weakening of the texture in the 2Y alloy wire compared to the 0.5Y demonstrates that increasing the Y content in the alloy to 2wt% is sufficient to activate texture weakening during annealing. This finding is in agreement with Hantzsche et al.[145] who concluded that an Y content of greater than 0.17at% is required to activate texture weakening in MgY alloys.[145] The 0.5Y and 2Y alloys investigated here contain 0.12 and 0.50at% Y respectively, agreeing with the work of Hantzsche et al.[145] that there is insufficient Y content in the 0.5Y alloy to activate texture weakening. Despite a weaker texture being developed in the 2Y alloy wire compared to the 0.5Y alloy they exhibited similar

mechanical properties. This demonstrates that the weaker basal texture developed in the 2Y wire did not result in improved the tensile elongation to failure. However, the weaker texture developed in the 2Y alloy wire may improve its ductility under complex loading and if smaller bend diameters could have been tested the 2Y alloy may outperform the 0.5Y alloy wire.

A large range of annealing temperatures (250-450°C) were investigated in the vacuum tube furnace annealing study as it has been reported that the RE texture only develops during static recrystallisation at elevated temperatures (these temperatures vary depending on alloy composition).[117] In no sample was the typical RE texture developed, however in the 2Y alloy wire annealed in the vacuum tube furnace at 400°C for 20mins a shift in texture was observed. As can be seen in Figure 4.26e and Figure 4.29c, a split in texture is developed whereby several grains retain the transverse basal texture (with their c-axis perpendicular to the DD) whilst the remaining grains have rotated approximately 90° from the transverse basal texture (aligning with their c-axis parallel to the DD). From the analysis conducted here it is unclear on the origin of this texture however, it was observed that the cold drawn 2Y alloy wire contained a high number of secondary phase particles that, upon annealing at 400°C for 20mins, increased in number and size. From the work carried out here it is unclear, if precipitation of these particles occurred pre, post or concurrently with recrystallisation in the 2Y alloy wire. However, it is known that particles can act to, both, promote and restrict recrystallisation.[200] Depending on the sequence of precipitation and recrystallisation this texture may be better understood as the precipitates could be affecting the recrystallisation mechanisms activated or grain growth post nucleation. However, it is clear that the texture developed in this sample is not beneficial for optimising the ductility of the sample along the DD, as the c-axis of the rotated grains will be loaded in tension, meaning the activation of prismatic slip will be severely restricted in these grains. This was confirmed during tensile testing where samples heat treated at 400°C for 20mins exhibited poor ductility, though this was likely a combination of both the texture and high number of secondary phase particles.

4.4.4 Mechanical Properties

As mentioned previously, based on the literature concerning other Mg alloys considered for use in BVS technology an approximate elongation to failure target of 20% was set as a target value to reach through annealing optimisation. Of course, as is known, simple uni-axial tensile testing will not fully characterise the loading the alloy wires will experience in the final device. As such, MBD testing was also conducted to investigate the performance of each alloy during bending.

The microstructural analysis revealed that there was little variation in the microstructure developed in the 0.5Y alloy wire annealed in the vacuum oven over the conditions investigated. Consequently, over the full range of conditions investigated, there was little variation in the YS and UTS of the alloy wires, 135-145MPa and 200-210MPa respectively. As previously mentioned, owing to the prolonged heating and cooling cycles implemented during each heat treatment process there is less variation between each process than would be assumed from comparing the relative soak temperatures and times stated for each. When heated at 300, 320 and 340°C the samples will be exposed to temperatures above 250°C for an additional, 34, 45 and 61mins respectively. Thus, for the samples treated at 340°C where there appears to be 4 times increase in the soak time investigated (10-40mins) it is only 1.42 times increase in soak time above 250°C. This lack in variation between cycles explains the similar microstructures developed between the various cycles, and consequently the similar strength of the wire over the range of conditions investigated. However, there was greater variation in the elongation to failure, with a minimum of 14.0±4.1% and a maximum of 21.2±0.9%, found after annealing at 340°C for 20 and 10mins respectively. The samples that exhibited lowest elongation to failure (e.g., 340°C for 20mins) tended to exhibit the largest standard deviation in results. Over the range of conditions tested, at least one sample from the set of five had an elongation to failure of >18% whilst many of the test sets had outliers that fractured early causing a decrease in mean elongation to failure. The early failures observed during testing of various conditions may be attributed to secondary phase particles. It was observed that the number and size of secondary phase particles remained relatively consistent to that observed in the cold drawn state over the range of conditions analysed here, however relatively few samples were analysed. It is known that long exposure to relatively high temperatures promotes precipitation (as observed in the 2Y alloy wire). As such it might be expected that some coarsening of the precipitates present in the cold drawn alloy wires occurs during annealing in the vacuum oven that was not observed in the microstructural analysis owing, in part, to both the relatively few particles present prior to annealing and relatively few cross sections of wire analysed. Should coarsening of these particles occur within the 110mm gauge length of the alloy wires it may lead to stress concentration around these particles, leading to early failure during tensile testing. Consequently, the variation in elongations to failure observed in these samples, despite exhibiting a relatively similar microstructure, may be attributed to uncontrolled precipitation/coarsening of secondary phases particles.

A much clearer trend is present in the mechanical properties of the 2Y alloy wire, which can be understood through the accompanying microstructural investigation. Following annealing at 300°C for 10mins the wire core remains unrecrystallised and as a result the strength of the wire remains high and the elongation to failure is low. As soak time is increased at 300°C, both the YS and UTS continuously decrease. Again, following annealing at 320°C for 10mins the wire core remains unrecrystallised and YS and UTS decrease as soak time is increased. The microstructural evolution revealed that following annealing at 340°C for 10mins the wire was fully recrystallised and consequently the elongation to failure was maximised at 16.2+/-3.0%. Increasing the soak time following complete recrystallisation at 340°C had little effect on the mechanical properties of the 2Y alloy wire.

During the wrapping tests it was found that the 0.5Y cold drawn alloy wire could survive wrapping around a pin of diameter 0.135mm whilst the cold drawn 2Y alloy wire failed during wrapping around a pin of 0.16mm. The tensile ductility of the 2Y cold drawn wire was lower than that of the 0.5Y and as such may explain the reduced ductility in bending. However, the optimally annealed 2Y alloy wire had a MBD of 0.22mm yet a higher elongation to failure than both the 0.5Y and 2Y cold drawn wires. This shows that increased tensile ductility does not always indicate good performance in bending. This is similar to the work of Nienaber et al.[201] who demonstrated that a 1mm diameter AZ80 wire had increased elongation to failure compared to a 1mm AZ31 alloy wire, but a decreased MBD. The authors attributed this to increased precipitation in the AZ80 alloy wire causing stress peaks to develop around these particles that can initiate premature failure. Consequently, the reduced bending performance of the annealed 2Y alloy wire compared to its cold drawn state may be attributed to the increase in coarse secondary phase particles present in the microstructure acting as stress concentration sites, resulting in premature failure during wrapping.

During annealing in the vacuum tube furnace, much clearer trends in the mechanical properties could be identified in both alloy wires. First, in the 0.5Y alloy wire after annealing for 10mins at 250°C the wire is not fully recrystallised and as a result exhibits high strength and low ductility, similar to the 0.5Y cold drawn alloy wire. The microstructural investigation revealed that a fully recrystallised microstructure was developed following annealing at 250°C for 30mins which resulted in maximised elongation to failure of 20.3±0.4%, whilst the YS and UTS fall to 133±2.6MPa and 196±0.8 MPa respectively. These properties remain relatively consistent as the soak time is increased further at 250°C, showing that no increase in ductility was achieved as a

more homogeneous grain size distribution developed. At the higher soak temperatures, ductility is maximised after annealing for 10 or 20mins and follows a downward trend with increasing soak time. When treated at 400 and 450°C there is a general upward trend in YS as soak time progresses. In all of the 400°C and 450°C samples, ductility is severely reduced, and they fail soon after yield, meaning the upward trend is not as visible in the UTS values as little strain hardening takes place. The increased strength at higher soak temperatures is attributed to increased precipitation of $Mg_{24}Y_5$ particles, whilst the reduced ductility is attributed to both the increased precipitation and grain coarsening. When annealed for maximum elongation to failure (250°C 30mins) the 0.5Y alloy wire survived wrapping around pins of 0.135mm.

The 2Y wire displays a similar trend to the 0.5Y wire, though as shown in the microstructural analysis, increased temperature and/or soak time is required to fully recrystallise the microstructure. When treated at 250°C the wire exhibits relatively high strength and low ductility until prolonged annealing for 120mins where the YS and UTS fall to 146±0.7 and 201±1.2MPa respectively whilst the elongation to failure is 15.2±5.6%. A fully recrystallised microstructure is developed when treated at 300°C for 20mins resulting in a maximised elongation to failure of 19.7±1.1%. As the soak time is increased at 300°C increased precipitation was observed and consequently the elongation to failure decreases. As in the 0.5Y wire, strengthening and loss of ductility is seen during annealing at high temperatures (400 and 450°C) with long soak times. As the grain size remains relatively constant as soak time and temperature are increased this loss of ductility is attributed solely to the increased precipitation of $Mg_{24}Y_5$ particles in the 2Y alloy wire. The optimised annealing procedure developed (300°C for 20mins) for the 2Y alloy wire allows it to survive wrapping around 0.135mm pins, demonstrating that the ductility in bending of the cold drawn wire can be improved through thermal processing should both the size and number of secondary phase particles be maintained similar to that of the cold drawn wire.

4.5 Conclusions

The microstructure and mechanical properties of two Mg-Li-Y alloy wires were investigated in their as-drawn state and two annealing optimisation investigations were carried out to maximise their ductility. It was shown that recrystallisation initiated near the OD of both alloy wires and progressed to the centre of the wire as soak time/temperature increased. This was attributed to increased internal stress being developed close to the OD of the wire during the cold drawing process and recrystallisation being activated first from the regions of high internal stress. In both

cold drawn alloy wires secondary phase particles were present with an increased number and size present in the 2Y alloy wire. During annealing in the vacuum oven no change in the number and size of these particles was observed in the 0.5Y alloy wire during the annealing treatments investigated. However, coarsening of these particles was observed in the 2Y alloy after annealing at 320 and 340°C in the vacuum oven. During annealing in the vacuum tube furnace an increased number and size of these particles was observed in both alloy wires when annealed at 350-450°C, resulting in decreased ductility and increased strength. The increased number of these particles in the cold drawn 2Y alloy wire is expected to have contributed to the restriction of grain growth during high temperature annealing of the 2Y alloy wires. In contrast, grain coarsening was observed in the 0.5Y alloy wires when annealed at 350-450°C in the vacuum tube furnace. A weaker basal texture was developed in the 2Y alloy wires following annealing in the vacuum oven and tube furnace, showing that there was insufficient Y content in the 0.5Y alloy wire to activate texture weakening. However, with both alloys exhibiting similar mechanical properties following annealing for maximum ductility, the weaker texture developed in the 2Y alloy wire was shown to not result in increased elongation to failure during tensile testing. The weaker texture may contribute to reduced anisotropy compared to the 0.5Y alloy wire, resulting in improved formability under more complex loading.

Both alloy wires were shown to achieve elongations to failure of ≈20% after appropriate thermal processing. After annealing in the vacuum oven for 10mins at 340°C the elongation to failure of the 0.5Y alloy wire was maximised at 21.2+/-0.9%. In contrast no procedure developed for the 2Y alloy in the vacuum oven allowed for an elongation to failure of ≈20%. The elongation to failure of the 2Y alloy wire was maximised at 16.2+/-3.0%, when annealed at 340°C for 10mins in the vacuum oven. The lower elongation to failure (and increased variation), of the 2Y alloy wire, annealed in the vacuum oven, was attributed to the increased number and size of secondary phase particles present in the wire. Consequently, during MBD testing of each alloy wire following optimal annealing in the vacuum oven, only the 0.5Y alloy wire could survive wrapping around 0.135mm pins. The 2Y alloy wire failed during these tests and was identified to have a MBD of 0.22mm. This was in contrast to the cold drawn 2Y alloy wire that had reduced tensile elongation to failure (8.4±2.5%) but had an increased MBD (0.16mm). As such it was demonstrated that improved tensile elongation to failure does not always correspond to increased ductility in bending. Following annealing in the vacuum tube furnace for maximum ductility the 0.5Y (250°C for 30mins) and 2Y (300°C for 20mins) alloy wires were shown to achieve elongations to failure of 20.3±0.4 and 19.7±1.1% respectively, whilst both could survive

wrapping around 0.135mm pins. These processes were found to maximise the elongation to failure of the alloy wires during the tensile testing conducted and were defined as “optimum” processes for the purpose of the microstructural investigations. However, further analysis would be required to identify the true optimal thermal processing route for each alloy wire. However, a plateau in elongation to failure occurred during thermal processing at 250°C for soak times beyond 30mins in the vacuum tube furnace for the 0.5Y alloy wire. Further a peak in tensile elongation to failure was observed in the 2Y alloy wire annealed in the vacuum tube furnace following annealing at 300°C for 20mins. Consequently, from the range of thermal processing routes investigated in this work it can be considered that any possible increase in the elongation to failure values defined as optimum would be minimal in both alloy wires.

It was shown that annealing in the vacuum oven and tube furnace allowed for the 0.5Y alloy wire to achieve the target elongation to failure of ≈20%. Whilst only annealing in the vacuum tube furnace allowed for the 2Y alloy wire to achieve the target elongation to failure of ≈20%. As such when developing thermal processing routes for the final BVS device, in Chapter 5, both the vacuum oven and tube furnace were investigated for the 0.5Y alloy wire and only the vacuum tube furnace was investigated for the 2Y alloy wire.

Chapter 5: BVS Optimisation

5.1 Introduction

In this chapter, the two alloys under investigation are applied in the manufacture of a new wire form BVS device and the processing parameters applied during fabrication are optimised to maximise the expansion range of the device. The limited success of BVS devices is widely reported to be caused by the poor mechanical properties of available materials.[202, 203] The early research into BVS devices largely focussed on the development of polymer-based devices however today, more focus is being given to bioresorbable metals, such as Mg, Zn and Fe owing to their improved mechanical properties compared to polymers.[53] The first, and only, metallic BVS device to gain CE approval in Europe (in 2016) is the Magmaris device developed by Biotronik.[204] A more detailed review of the device was previously included in Chapter 2, where it was described how the Magmaris device exhibited promising early results however concern begun to grow over the presence of a long-lasting degradation product several years post implantation.[89] More recent findings have shown, potentially, more concerning issues, such as early vessel collapse. Some have attributed early vessel collapse to the poor mechanical performance of the Magmaris device, leading to mallaposition, under expansion and rapid loss of radial force.[205-207] Biotronik have sought to address the issues of the Magmaris device in their newest device, the Dreams 3G, which has increased radial force and reduced strut thickness. A 5-year clinical trial (BIOMAG-I) of the Dreams 3G device enrolled the last of a total of 116 patients in 2022.[208] This shows that the interest in BVS devices remains, as the benefits are clear, however, so too are the challenges associated with developing these devices.

The BVS investigated in this work is targeting to initially treat BTK arteries, which have an approximate diameter of 3mm in adults.[32] Currently there are no FDA approved stents for use in BTK arteries, though as described in Chapter 1, spot repair through the FDA approved Tack Endovascular system has provided some promising results in the treatment of dissections within BTK arteries compared to the full metal jacket coverage provided by stents.[25, 39] Though there remains the belief that, through temporary scaffolding of lesions in BTK arteries, improved patient outcomes can be achieved. Despite no stents being FDA approved for use in BTK arteries, off-label application of stents designed for coronary and superficial femoral arteries is regularly applied in the treatment of BTK arteries.[13] Consequently, the design criteria for the present device are set through consideration of DES performance with reference to the available

information on Magmaris. The device under investigation has a nominal diameter of 3mm, however, to appropriately treat the full patient range, expansion beyond the device's nominal diameter will be required. DES with a nominal diameter of 3mm, are generally capable of over expansion to 5mm.[209] However, achieving an over expansion of 2mm above the nominal diameter in Mg based device's may be challenging, and lead to premature fracture, as demonstrated by the Barkholt et al.[210] during benchtop testing of the Magmaris device. The authors demonstrated that no strut fractures were observed during the unconstrained expansion of a Magmaris BVS, with a nominal diameter of 3mm, in a SBF bath at 37°C using noncompliant 4mm balloons. Fractures were observed during expansion with a 4.5mm noncompliant balloon, though it should be noted that fractures only occurred when expanded beyond an ID of 4.4mm.[210] Thus a target over-expansion range of 1mm was targeted for the new device being investigated in this work. The target radial strength to achieve was based of comparable 3mm coronary devices that exhibit a radial force of 1N/mm.[211]

Based on the design requirements identified for BVS devices for the treatment of BTK arteries, the mechanical performance of devices manufactured from both alloy wires is optimised in this chapter. An annealing optimisation study is conducted, first, using the vacuum oven, on devices manufactured from 0.5Y alloy wire. Following this, an annealing study is conducted on devices manufactured from both alloy wires using the vacuum tube furnace. The mechanical performance of the device is assessed through expansion and radial force testing, whilst the underlying microstructural features influencing these properties are also investigated.

5.2 Methodology

5.2.1 Scaffold Manufacture

The design and manufacture of the devices was described in Chapter 3, where it was explained that the devices were required to undergo an annealing process following forming of the sine like waveform into a tubular scaffold. The primary purpose of the annealing process was to restore the mechanical properties of the alloy wires, allowing for maximum expansion range of the device during deployment. The heat treatment protocol had the secondary benefit of heat setting the device in place on the mandrel, preventing any unravelling of the waveform. The scaffolds were manufactured from both the 0.5Y and 2Y alloy wires supplied following annealing by the wire suppliers. No information on these protocols was provided. As such, prior to device

manufacture and testing, both supplied alloy wires were investigated using the same methods described in Chapter 4, so these protocols are not repeated here.

An annealing optimisation study was performed, firstly on devices manufactured from the 0.5Y alloy wire using the vacuum oven. The devices manufactured from the 0.5Y alloy wire were placed in the vacuum oven at room temperature, a vacuum was then pulled on the system and set to heat to the desired soak temperature. Once at the set soak temperature, the devices were held for the desired soak time, before the furnace was turned off and allowed to cool naturally to room temperature before the vacuum was released and the samples removed.

The vacuum tube furnace was also used to develop an optimum annealing protocol for devices manufactured from both the 0.5Y and 2Y alloy wires. Again, these devices were annealed following the same protocol as described in Chapter 4 for the cold drawn alloy wires. The samples were placed in a quartz glass boat linked to the magnetic transfer arm and held within the cooling zone. A vacuum was then pulled on the system and allowed to heat to the set soak temperature. Once the furnace had reached temperature, the furnace was held for 10mins before the samples were transferred into the centre of the heating zone. The samples were then held in the heating zone for the desired soak time before being transferred back into the cooling zone. The vacuum was only removed once the furnace temperature was below 45°C.

5.2.2 Scaffold Expansion Testing

Based on preceding work, it was known that achieving consistent expansion of the devices to 4mm from the as manufactured diameter of 1.83mm was not possible prior to the work described in this thesis. Consequently, for the initial annealing study, it was determined that a procedure that allowed for consistent expansion to 4mm from the as manufactured diameter should first be developed prior to incorporating the crimping process. As such, in the initial study all testing was conducted through expanding the devices from their as manufactured diameter of 1.83mm to 4mm.

A two-stage expansion process was used to assess the performance of the devices. The device was placed over a noncompliant 3mm balloon catheter (with a folded diameter of 1.5mm) and placed in a water bath at 37°C in order to mimic body temperature. The balloon/device system was held in the water bath for 1 minute before inflating the balloon to its rated pressure (12atm), which expands the balloon to 3mm. The balloon is held at 12atm for at least 5s before being deflated and the device removed. Preliminary testing measured the diameter of the stent

balloon system whilst the balloon was still expanded to ensure the device was expanded to 3mm ID at 12atm. On removal of the expanded device from the balloon any strut fractures were immediately visible and recorded. The devices were then investigated using optical microscopy at x50 and x200 mag for signs of cracks and to image and record any complete strut fractures. Devices that survived expansion to 3mm were placed over a second balloon tipped catheter and expanded to 4mm ID using the same process as described above in the water bath. Again, on removal of the devices from the balloon they were investigated for signs of cracking using optical microscopy.

For the remainder of the expansion testing a crimping process was conducted prior to expansion, as required prior to deployment in *vivo*. Firstly, the devices were crimped onto the noncompliant 3mm balloon tipped catheter using a Machine Solutions crimp head. The balloon tipped catheters had a folded diameter of 1.5mm, meaning the devices were crimped from an as manufactured ID of 1.83mm to 1.5mm. The devices were placed over the balloon and placed in the crimp head, which is linked to an Instron that is used to control the loading applied to the device, see Figure 5.1. The Instron only measures the load applied to the crimp head lever and not the true circumferential force applied to the device in the centre of the crimp head. It has been approximated that the circumferential load on the device is approximately four times that of the load measured by the Instron. The device undergoes two crimping stages. First a “pre-crimp” is carried out where the device is crimped until a load of 10N is read on the Instron. At this stage, should the devices not lie entirely on the balloon (out with the radial markers shown in Figure 5.2) the device can be carefully repositioned to lie within the markers. A final crimp is conducted to fully secure the device on the balloon, where a load of 50N is applied to the crimp head by the Instron. It can be approximated that a circumferential load of approximately 40N is applied during the pre-crimp stage, whilst a 200N load is applied during the final crimp to the device. This is a crude crimping process and one that will be modified in future, however the primary focus here is the reduction in internal diameter of the device, so as to understand the cyclic loading of the device during crimping and expansion. Once crimped onto the balloons the devices were analysed at 50x magnification for signs of defects or fractures prior to expansion testing. Expansion testing was conducted following the same procedure described above.

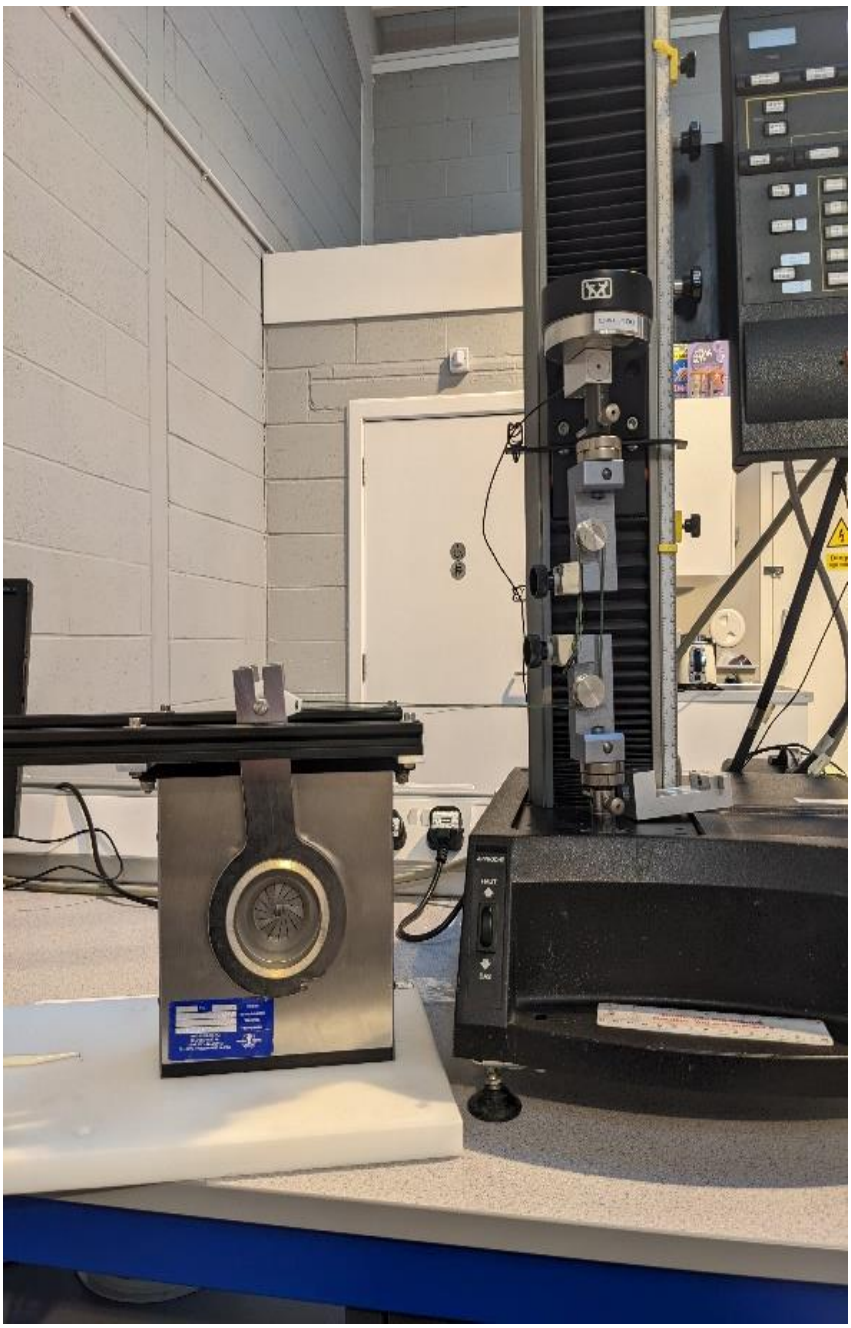

Figure 5.1: Crimp head linked to Instron

5.2.3 Radial Force Testing

Radial force testing was conducted on devices following annealing for optimal expansion as defined in the following sections. The radial force tests, using a test protocol and specification developed by the present author, were conducted by an outside lab using a segmented head radial force tester. The test started at a diameter approximately 0.5mm larger than measured scaffold diameter and had an end diameter of 1.5mm. The segmented head had a speed of

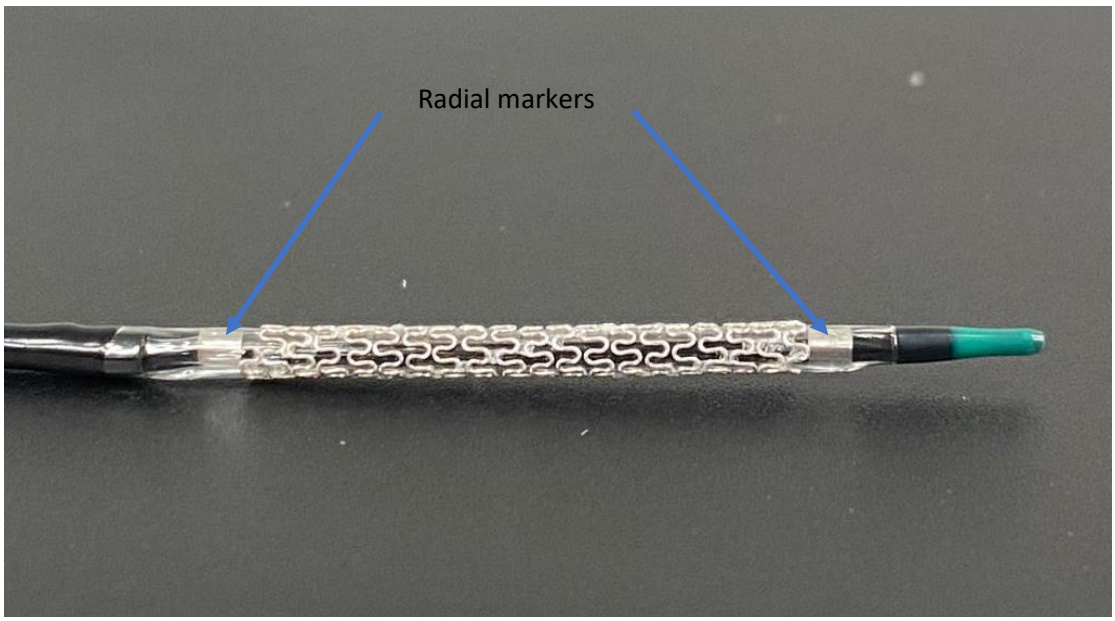

Figure 5.2: Crimped device

0.1mm/s with a short idle time at 1.5mm. Devices were tested at expanded IDs of 3 and 3.5mm. The raw data was provided by the outside company and analysed, where possible, in accordance with the ASTM F3067 – 14 Standard Guide for Radial Loading of Balloon-Expandable and Self-Expanding Vascular Stents.[212]

A standard plot output from a typical radial force test using a segmented head radial force tester is displayed and described in the ASTM F3067 – 14 Standard.[212] Figure 5.3 shows this plot from the ASTM Standard that displays the loading as one complete cycle, whilst it has been modified to show 4 separate regions that describe the loading curve: A) initial loading B) plasticity increasing C) unloading D) return.[212] Within the initial loading region, there is a clear non-linear portion of the curve and this region is considered to not be representative of the stent response as much of the device has yet to fully contact the loading surfaces. Upon full engagement with the stent, the initial loading region is approximately linear, and the device undergoes elastic or elastic-plastic deformation. A linear line (loading line) can be fitted to this region and its intercept with the x-axis can define the zero-compression diameter of the device. As plasticity builds up within the device the loading curve begins to flatten, and the force increases at a slower rate as plasticity increases (B). Once the predefined maximum compression is reached the device is unloaded and in the unloading region (C) the load decreases linearly with approximately the same gradient as the initial loading region. Once the device loses contact with the segmented head, the loading is zero and the full loading cycle is complete as the segmented head returns to its initial diameter (D). To determine the radial force in accordance with the

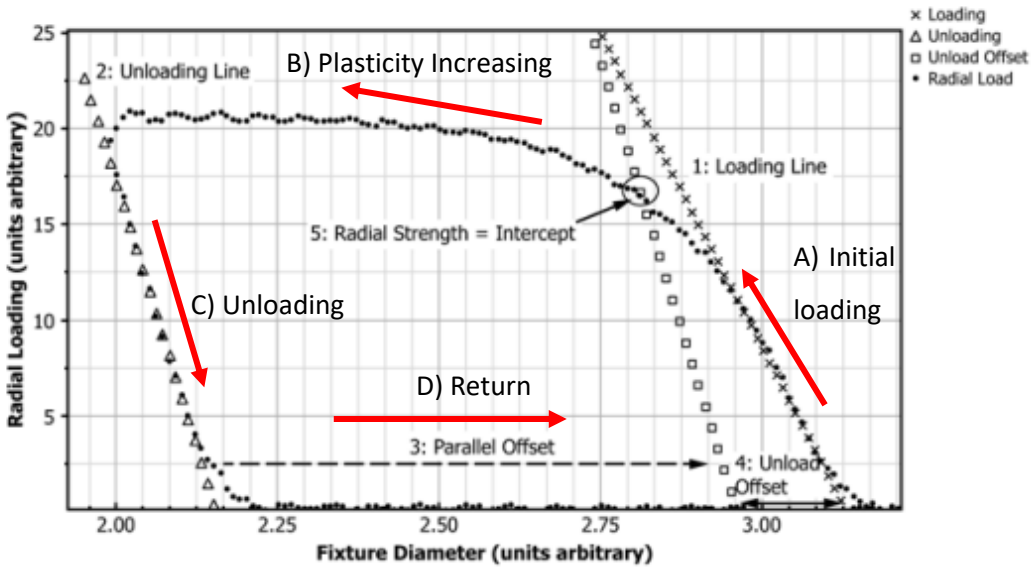

Figure 5.3: Representative radial loading plot for a balloon expandable stent using a segmented head apparatus[212]

ASTM standard, an unloading line is created in a similar manner to the loading line, whereby a linear line is fitted to the steepest section of the unloading curve and extended to meet the x-axis. This unloading line can be used to determine the radial force by offsetting it by some specific value from the zero-compression diameter of the device. The extent of this offset should be selected with consideration of clinical relevance.[212]

The data gathered from the analysis conducted in this work is only provided with regions A and B meaning an offset line cannot be created from the unloading line and used to determine the radial force. However, as the unloading and initial loading regions are approximately parallel an offset line was created from the line of best fit from the initial loading line. This line was then offset by 0.1mm from the zero-compression diameter and the point at which it intersected the loading curve defined the radial force. An example data set from the analysis conducted in this work is plotted in Figure 5.4 with both the linear loading line and offset line plotted.

5.2.4 Microstructural Analysis

Microstructural analysis of the devices was conducted using a range of microscopy techniques, including, optical microscopy, SEM and EBSD analysis. Surface analysis of the devices was conducted using a dino-lite microscope where no sample preparation was required. Using an Olympus GX51 optical microscope the microstructure of the devices was analysed. Devices prepared for analysis using the Olympus GX51 microscope were mounted longitudinally in epoxy resin and prepared through grinding with 1200grit SiC paper followed by 2400grit SiC paper with

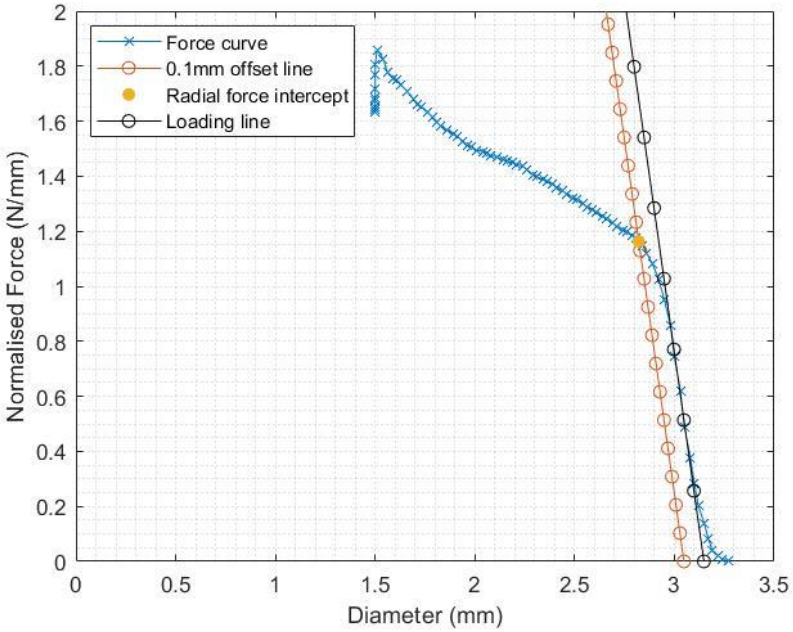

Figure 5.4: Representative radial force results from testing

a final 2min polish using OPS solution. Samples were analysed in this condition to investigate and identify signs of cracking. A final etching step was applied to investigate the microstructure of the devices using a solution of 75ml of ethylene glycol, 10ml distilled water and 1ml of nitric acid. SEM analysis was conducted on samples mounted in epoxy resin and prepared in the same manner as for optical microscopy (described in Chapter 4), both with and without the final etching step.

EBSD analysis required the samples to be mounted in conducting Bakelite. Analysis of the BVS devices was conducted in their as manufactured state, post crimping, and post expansion to 3mm. Owing to the high pressures exerted during mounting in Bakelite, it was not possible to mount a complete device in Bakelite without crushing and deforming the device. As such a single helix from final device was cut (Figure 5.5a) and placed in the Bakelite mounting press so that the pressure was applied axially, as shown in Figure 5.5b where the red arrows denote the pressure applied during mounting. When loaded circumferentially, it led to crushing of the helix. The sample was then ground and polished (following the same procedure as described for optical microscopy, without the final etching step) to reveal approximately half of one wave (Figure 5.5c). A final polish was conducted through ion milling with a Gatan precision etching and coating system. The EBSD scan was then run on an area approximately 50x100µm at the

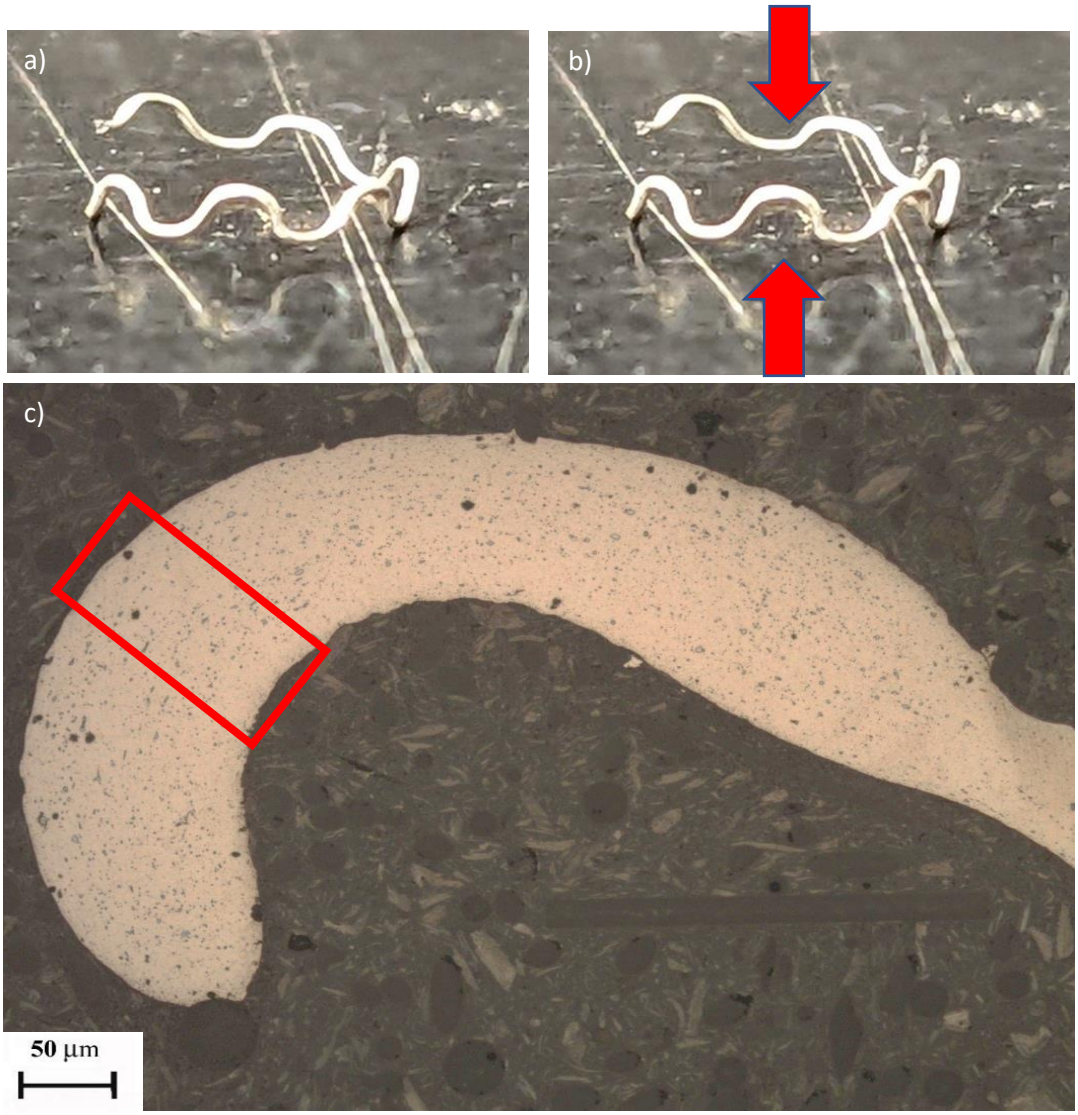

Figure 5.5: Images showing how devices were mounted in conducting Bakelite a) representative helix used for analysis b) diagram showing loading direction of the devices c) final image of polished waveform prepared for EBSD analysis

apex of the wave so as to gather data on the most severely deformed region of the device at both the OD and ID of the wave. A representative region is highlighted in red in Figure 5.5c.

5.3 Results

5.3.1 Characterisation of Wire

The BVS devices under consideration were manufactured from both alloy wires with a final annealing step post drawing conducted by the wire suppliers. Prior to analysis of the devices, the microstructure and mechanical properties of the two wires were investigated.

Firstly, analysis of the two alloys microstructure using optical microscopy (Figure 5.6) revealed both alloys had a refined grain size (measured accurately using EBSD analysis) throughout the bulk of the cross section, however around the OD of both alloys wires a “skin” of coarse grains was observed. This skin of coarse grains is measured at 5 locations for both alloys. The layer extends approximately 14/15µm into the wire core from the surface in both alloy wires. SEM analysis was also conducted on each alloy wire, where the presence of Y-rich secondary phase particles could be observed as they appear brighter in both images compared to the Mg matrix. Figure 5.7 shows the SEM analysis of both alloy wires where there are a number of secondary phase particles present in each, however there are an increased number and size in the 2Y alloy wire compared to the 0.5Y. Finally, the microstructure of both alloy wires was analysed with

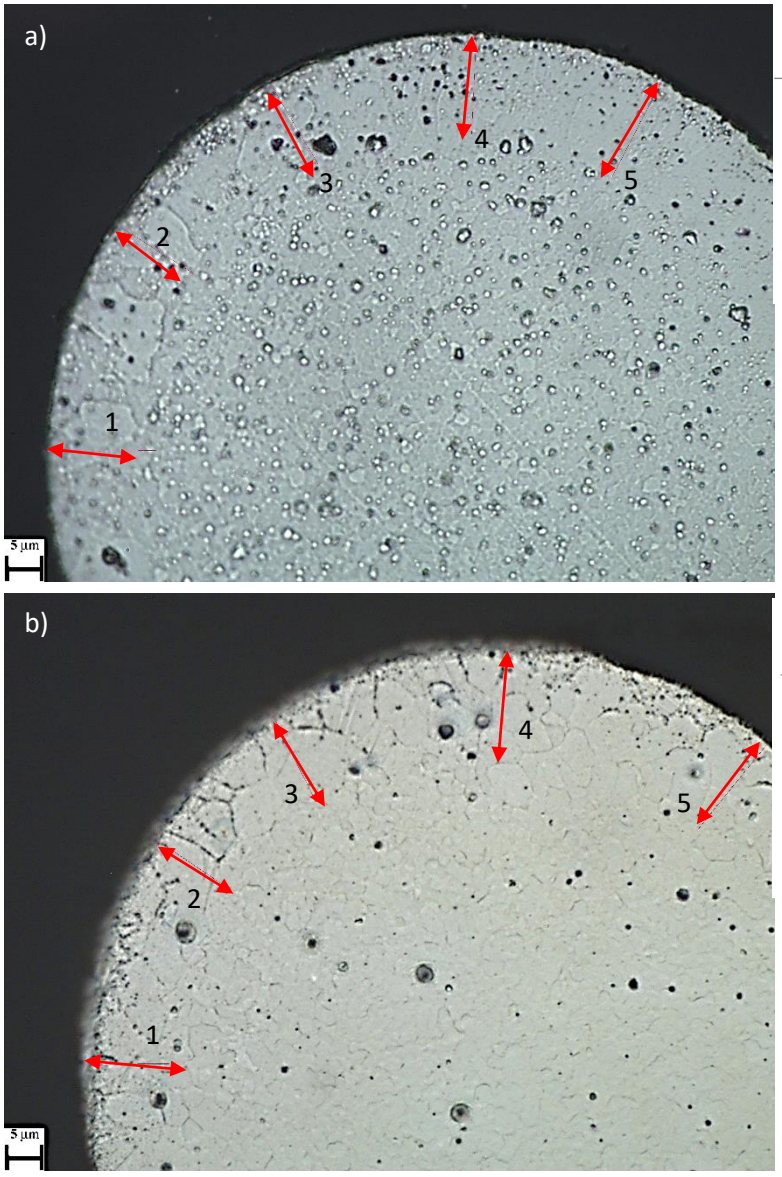

Measurement Point	Length (µm)
1	15.9
2	12.9
3	13.6
4	14.9
5	15.8
mean	14.6

Measurement Point	Length (µm)
1	13.8
2	12.2
3	14.4
4	16.0
5	16.1
mean	14.5

Figure 5.6: Microstructure of both supplied annealed wires a) 0.5Y b) 2Y

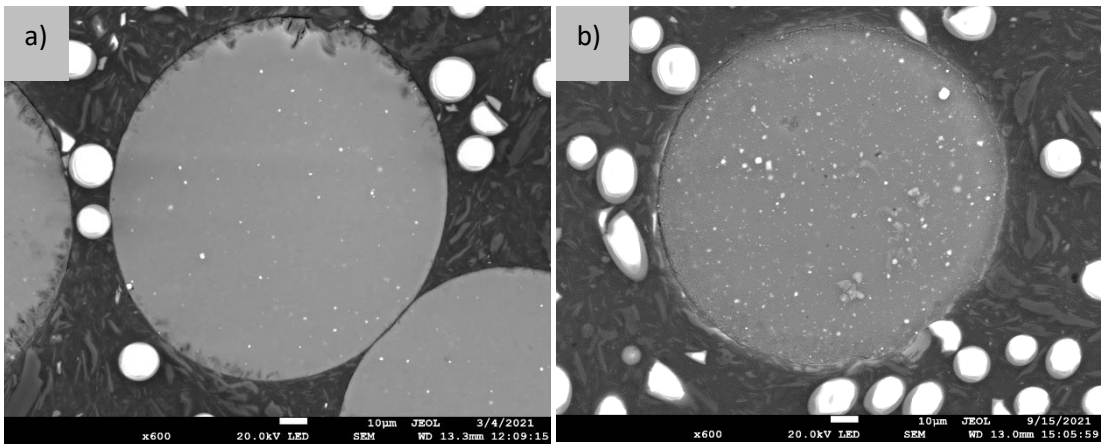

Figure 5.7: SEM images of each alloy wire a) 0.5Y and b) 2Y

EBSD analysis. The IPF maps of both alloys are shown in Figure 5.8. Note that a 50x50µm area was analysed for the 0.5Y alloy whilst sample drift in the 2Y alloy led to only a 36x48µm area being analysed. Both alloys developed a basal texture with the 2Y alloy having a weaker texture

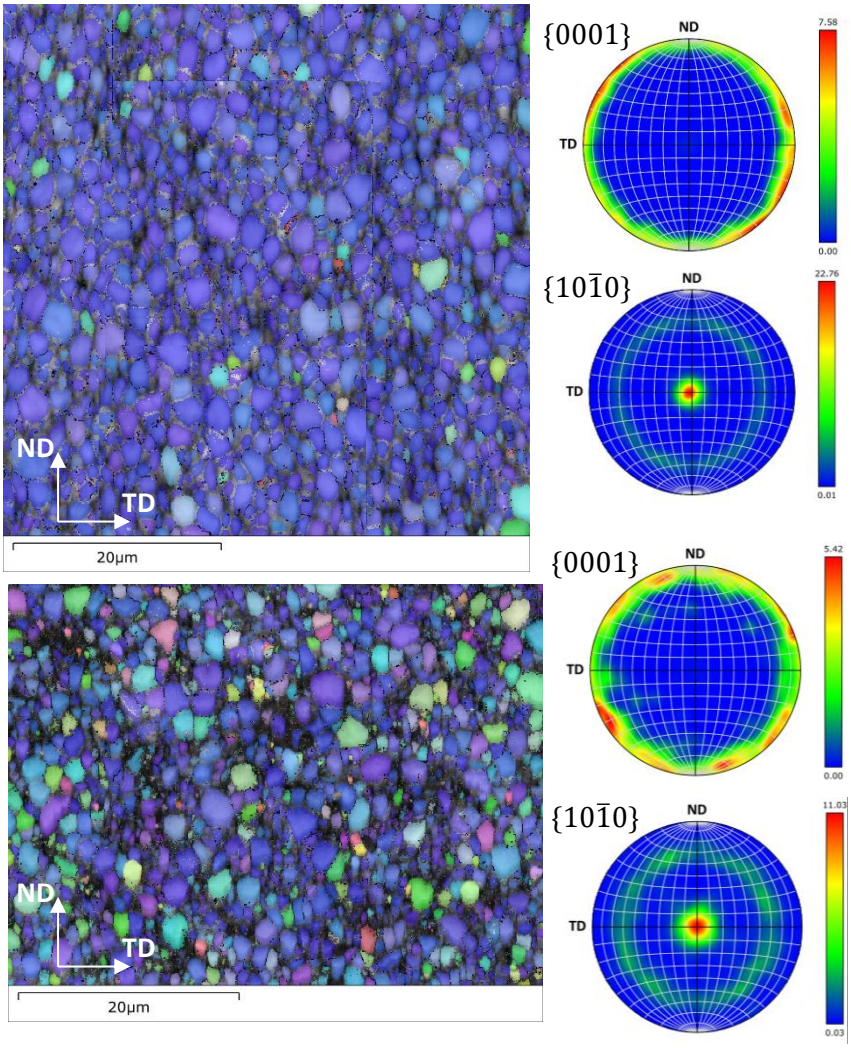

Figure 5.8: IPF maps of a) 0.5Y and b) 2Y wire

compared to the 0.5Y alloy wire. From the EBSD analysis the grain size of the 0.5Y and 2Y alloys were found to be 2µm and 1.6µm respectively.

Tensile and MBD tests were also conducted on both alloy wires. Figure 5.9 shows representative stress/strain curves for the two alloy wires. It was found that the 0.5Y alloy had an elongation to failure, UTS and YS of 19.8±0.8%, 222.9±0.7MPa and 156.0±0.5MPa respectively. The annealed 2Y alloy wire exhibited lower elongation to failure (13.8±1.6%) but higher strength, UTS and YS of 241.0±0.8MPa and 196.9±0.7MPa respectively. MBD testing found that both alloy wires could survive wrapping around the smallest diameter tested (0.135mm), the results are shown in Figure 5.10.

5.3.2 Annealing Optimisation Study

Annealing optimisation of devices manufactured from both alloy wires was carried out using both the vacuum oven and tube furnace. As described in Chapter 4, annealing the cold drawn 2Y alloy wire in the vacuum oven resulted in increased precipitation of Y-rich secondary phase particles. Consequently, the wire had relatively poor elongation to failure and MBD. Therefore, an annealing process was only optimised for devices manufactured from 0.5Y alloy wire using the vacuum oven. In Chapter 4 it was shown that this increased precipitation could be prevented in the 2Y alloy wire through annealing in the vacuum tube furnace. Therefore, an annealing process was optimised for both alloy wires using the vacuum tube furnace.

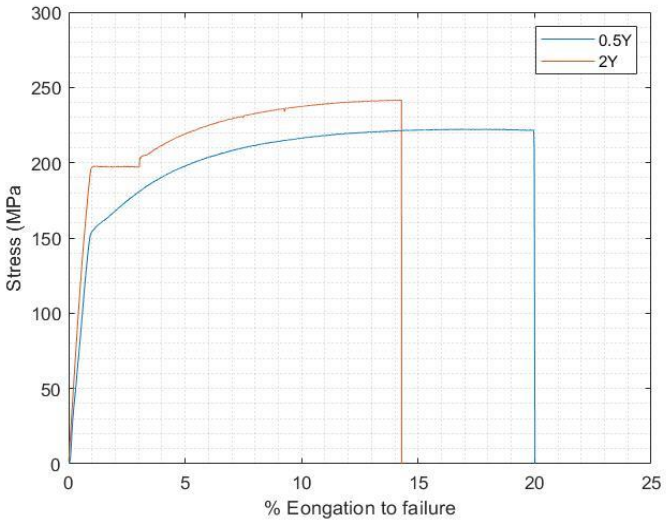

Figure 5.9: Representative stress strain curves of supplied 0.5Y and 2Y annealed wires

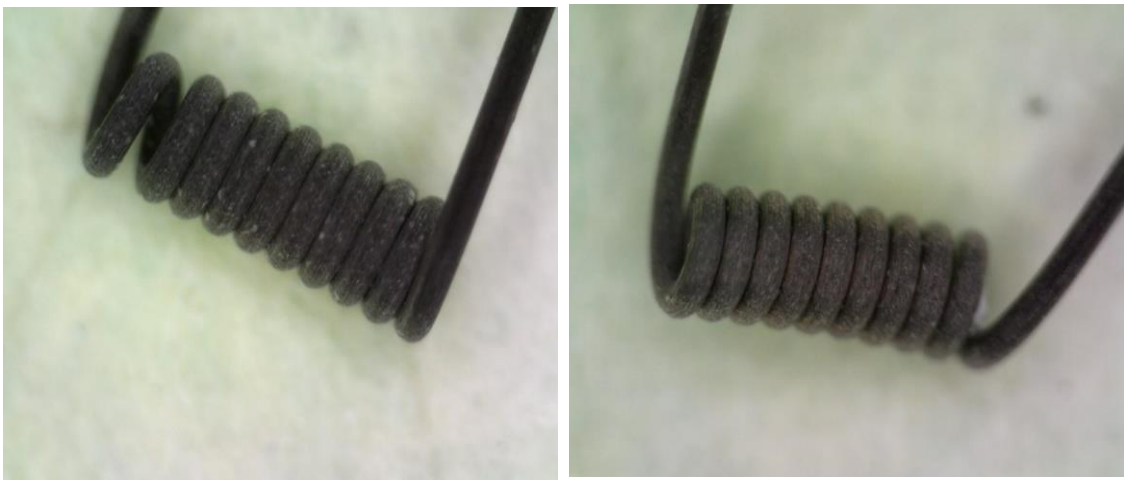

Figure 5.10: MBD testing a) 0.5Y supplied annealed wire b) 2Y supplied annealed wire

5.3.2.1 Vacuum Oven Process

Based on the annealing study conducted on the cold drawn wire, where annealing at 340°C for 10mins was found to be optimum, this process was selected as the starting point for this study. As described in Section 5.2.2 these initial expansion tests were conducted on devices without the crimping stage, meaning they were expanded from an ID of 1.83mm, first, to an ID of 3mm then to 4mm. Each of the three devices treated under these conditions exhibited no strut fractures when expanded to 3mm but all failed during expansion to 4mm. The soak temperature was then reduced to 320°C and three additional tests conducted. Each of these devices also survived expansion to 3mm but failed during secondary expansion to 4mm. It was found that treating the devices at 300°C for 30mins resulted in all three devices surviving expansion to 4mm. Analysis of the surface of the devices post expansion to 4mm with optical microscopy identified no visible cracks forming on the surface of the wire. An additional two samples were tested under these conditions to confirm treating the devices at 300°C for 30mins allowed for expansion to 4mm. The results from these tests are summarised in Table 5-1. It was then determined that samples treated at 300°C for 30mins should be tested through the full

Table 5-1 Results from expansion testing of 0.5Y devices expanded in the vacuum furnace (without crimping process)

Annealing conditions	*Number of devices tested/number that survived to 4mm*	*Cracking observed on devices that survived to 4mm*
340˚C for 10mins	3/0	n/a
320˚C for 10mins	3/0	n/a
300°C for 30mins	5/5	No

deployment cycle; crimping to an ID of 1.5mm followed by expansion to 3 then 4mm. Each of the five devices tested survived expansion to 3mm, but all failed during the secondary expansion to 4mm, Figure 5.11 shows a device fracture following expansion to 4mm.

Characterisation of the surface of the wire post heat treatment was conducted on the devices using SEM analysis to investigate if any surface defects could be causing failure during expansion to 4mm. Figure 5.12 shows an SEM image of the peak of a single wave where an oxide layer is clearly present on the surface of the wire. Cracking of this oxide layer is visible across the OD of the waveform (Figure 5.12c). Considering the failures observed during device expansion and the presence of these cracks, the electropolishing procedure described in Chapter 3 was developed to remove the surface oxide layer post annealing.

Following the development of the electropolishing procedure five additional samples were manufactured, annealed at 300°C for 30mins, electropolished and tested. It was found that two of the five scaffolds experienced complete fracture of one strut whilst 3 survived expansion to 4mm. However, each of these devices showed signs of cracks initiating from the ID of the waves, Figure 5.13a shows an example of a complete fracture whilst Figure 5.13b shows a crack developing along the ID of a single wave.

5.3.2.2 Microstructural Analysis

Figure 5.14 shows the microstructure of a single wave of a device manufactured from 0.5Y alloy wire following annealing for 30mins at 300°C in the vacuum oven. Large coarse grains are developed around the wave peak with a more refined grain structure, similar to that of the wire

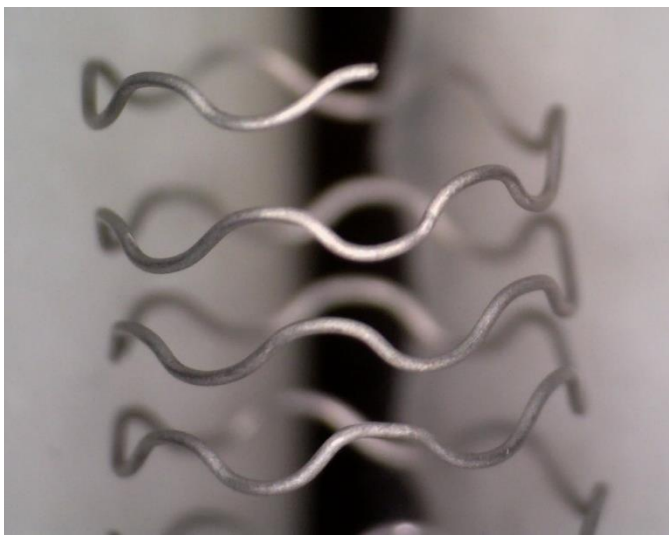

Figure 5.11: 0.5Y device heat treated at 300°C for 30min in the vacuum furnace expanded to 4mm with no electropolishing

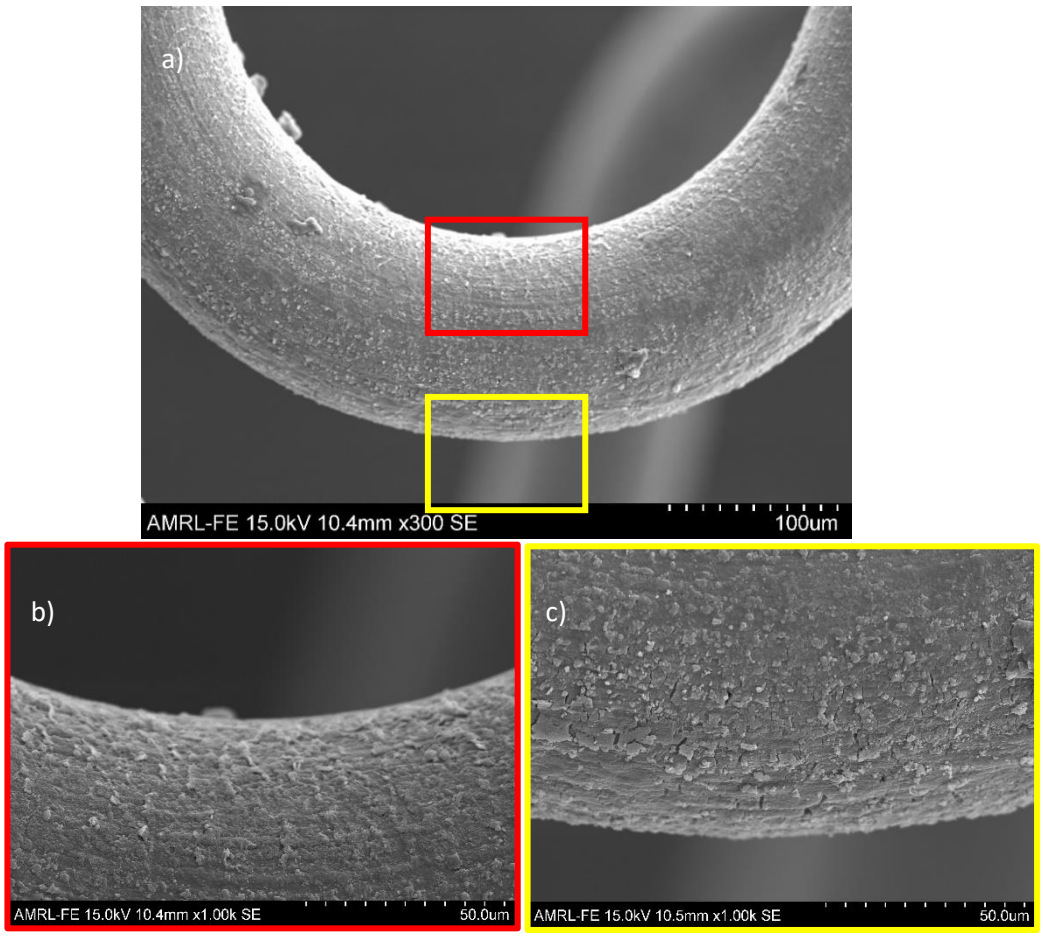

Figure 5.12: Cracking of oxide layer of devices post manufacture a) full peak of waveform b) ID of wave c) OD of wave

used to manufacture the device, along the wave strut. These features are shown in more detail in Figure 5.15 which shows the microstructure developed in a device along the strut (Figure 5.15a) and along the peak of the wave (Figure 5.15b) at a higher magnification. Figure 5.15a displays the microstructure developed through the strut as it begins to curve into the wave peak towards the left-hand side of the image. A refined grain structure is developed throughout the strut. As the wire begins to curve at the base of the wave peak (left hand side of Figure 5.15a)

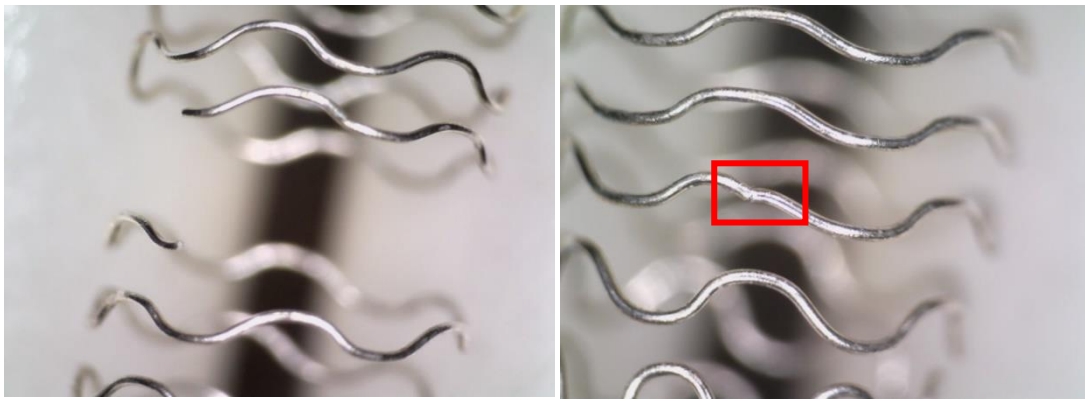

Figure 5.13: Devices electropolished and expanded to 4mm a) fractured device b) cracking along the ID of a wave in a device that survived expansion to 4mm

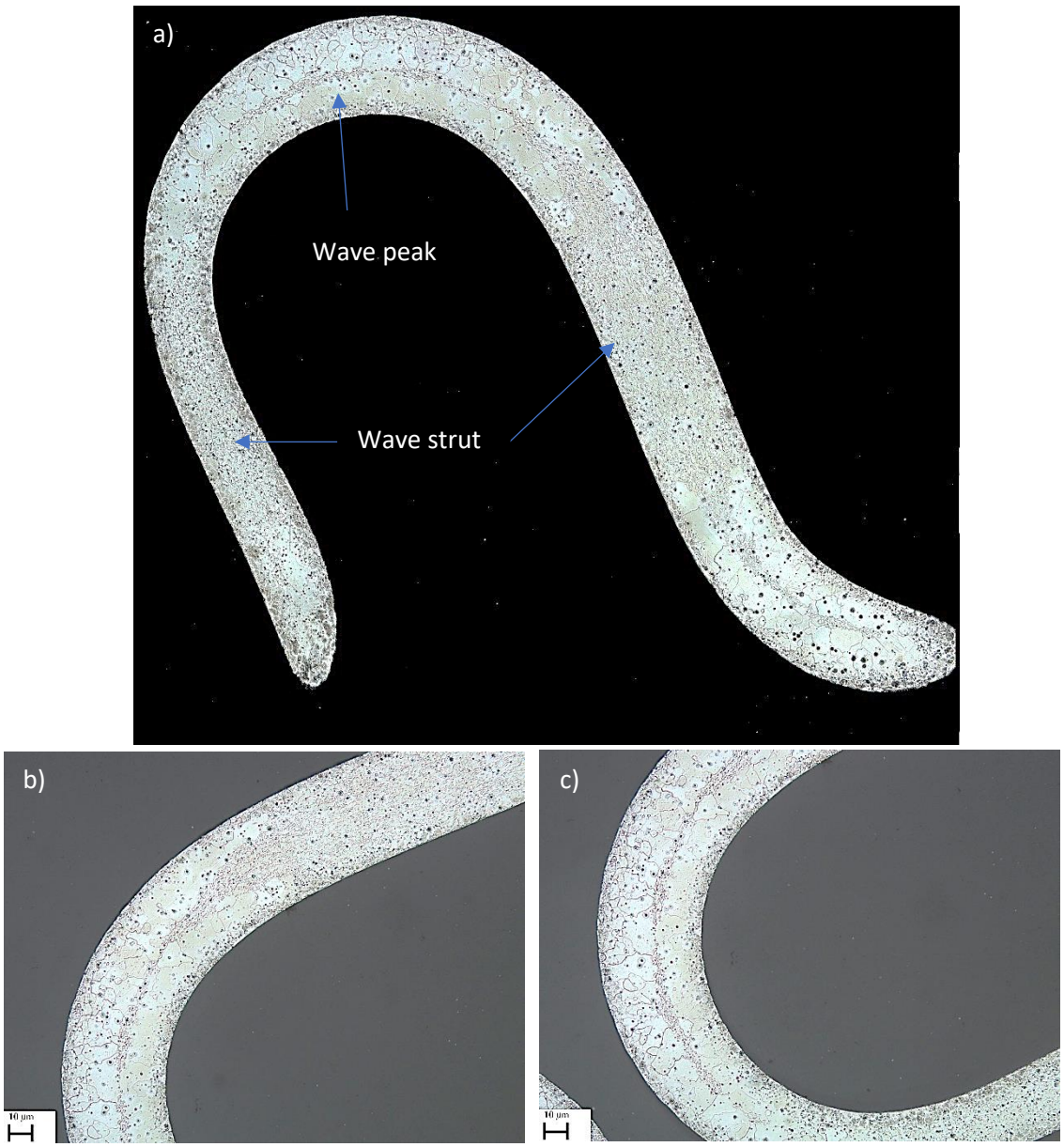

Figure 5.14: Microstructure of a single wave of a 0.5Y device annealed in the vacuum furnace for 30mins at 300°C a) complete wave b) wave strut c) wave peak

grain coarsening is observed to develop from the surface of the wire and progresses towards the wire core as the curvature of the wave increases. Figure 5.15b shows the microstructure developed at the peak of a single wave of the device. Coarse grains are developed around the wires surface at the OD and ID of the wave and are separated by a small region of refined grains running through the approximate centreline of the wave.

5.3.2.3 Tube Furnace Annealing Study

For each of the following tests each device was manufactured, heat treated and electropolished prior to expansion. The annealing study conducted using the vacuum oven demonstrated that

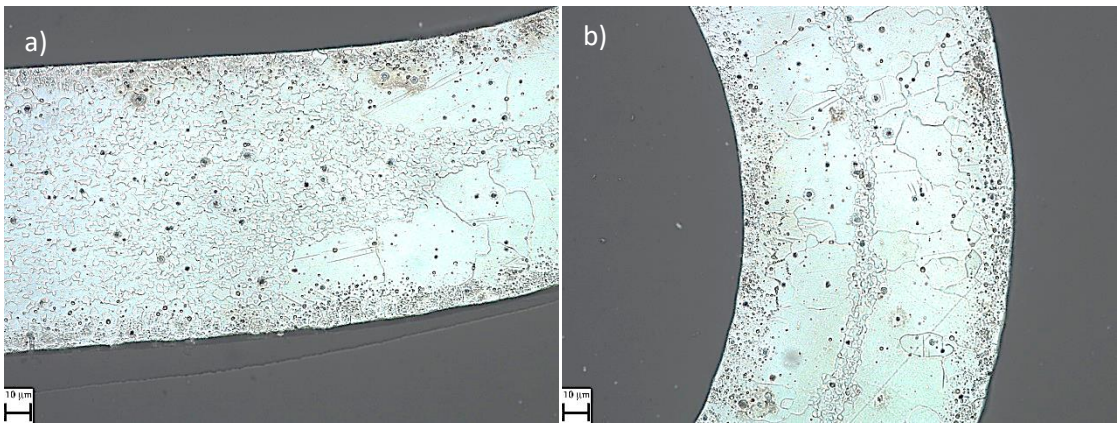

Figure 5.15: Microstructure of 0.5Y device annealed at 300°C for 30mins a) strut b) peak of a wave

devices manufactured from the 0.5Y alloy wire could inconsistently expand to 4mm from a crimped ID of 1.5mm. Therefore, all tests expansion tests described in this section underwent a crimping process prior to expansion to 3mm.

Firstly, an annealing protocol was optimised for devices manufactured from 0.5Y alloy wire. The initial process applied in this study was selected based on the annealing optimisation study finding that annealing the 0.5Y alloy wire at 250°C for 30mins maximised ductility. It was found that annealing the device under these conditions resulted in two of three devices surviving expansion to 4mm. From here the soak time was continually reduced at 250°C to investigate the performance of the device, these results are summarised in Table 5-2. When annealed at 250°C for 20mins, 1 of 3 devices failed on expansion to 4mm with cracking observed on the devices that did not experience a full struct fracture. Figure 5.16 shows an example of complete fracture and crack initiation in two separate devices treated at 250°C for 20mins. All signs of cracking were observed initiating from the ID of the waves. When treated at 250°C for 10mins all devices survived expansion to 4mm with no cracking observed initiating from the ID of waves when analysed with optical microscopy and SEM analysis, Figure 5.17. To improve confidence in the procedure an additional 9 devices were annealed at 250°C for 10mins and tested. Each of these

Table 5-2: Expansion results from the tube furnace annealing study on devices manufactured from 0.5Y alloy wire

Annealing conditions	Number of devices tested/number that survived to 4mm	Cracking observed on devices that survived to 4mm
250°C for 30mins	3/2	n/a
250°C for 20mins	3/1	n/a
250°C for 10mins	12/12	no

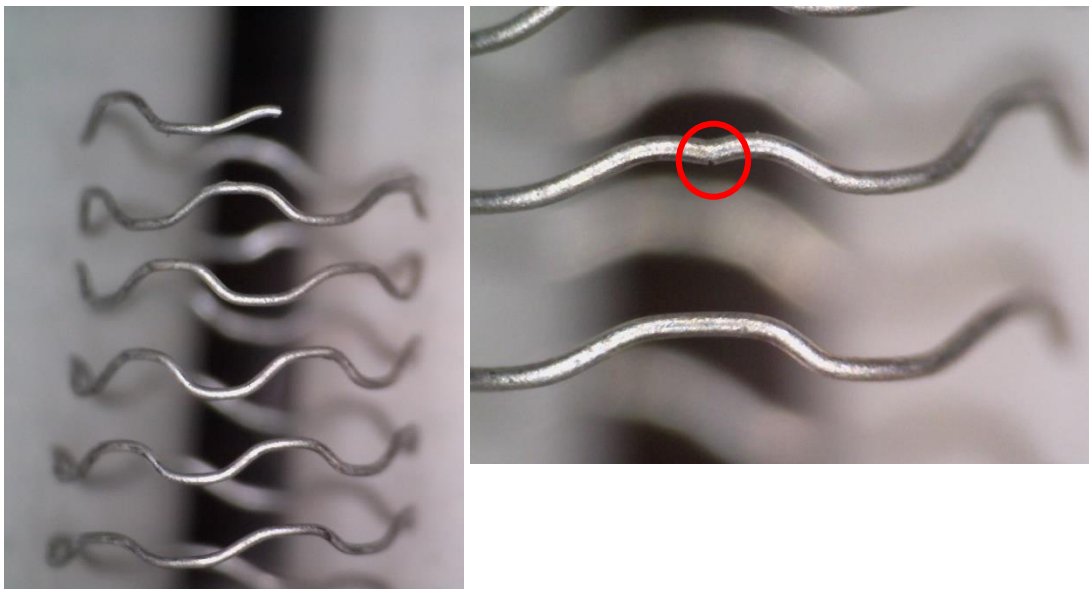

Figure 5.17: 0.5Y scaffolds expanded to 4mm after being annealed at 250°C for 20mins a) complete strut failure b) crack initiation.

devices survived expansion to 4mm and exhibited no signs of cracks initiating from the ID of the waves when analysed with optical microscopy.

The results from the annealing optimisation study of devices manufactured from the 2Y alloy wire are summarised in Table 5-3. As can be seen no treatment protocol was developed for the 2Y alloy wire that allowed for consistent expansion of the devices to 4mm. When treated under the same conditions that maximised the ductility of the cold drawn wire (300°C for 10mins) all

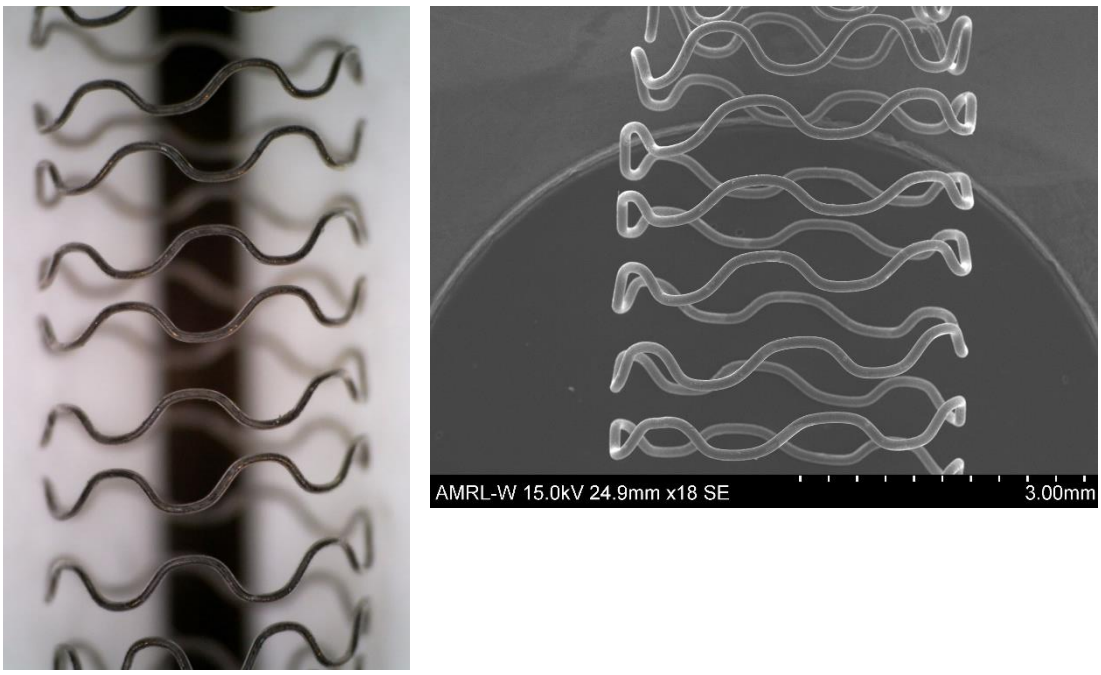

Figure 5.16: 0.5Y scaffolds expanded to 4mm after being annealed at 250°C for 10mins a) optical image of successful device expansion b) SEM image of successful device expansion.

Table 5-3: Results from annealing optimisation on 2Y devices

Annealing conditions	Number of devices tested/number that survived to 4mm	Cracking observed on devices that survived to 4mm
300°C for 40mins	3/0	n/a
300°C for 20mins	3/0	n/a
300°C for 10mins	3/0	n/a
300°C for 7.5mins	3/0	n/a
300°C for 5mins	3/0	n/a
250°C for 15mins	3/0	n/a
250°C for 12.5mins	3/1	No
250°C for 10mins	6/4	No

the devices fractured during expansion to 4mm. Reducing the soak temperature to 250°C and holding for 10mins resulted in the most consistent expansion results. Following annealing under these conditions, 4 from 6 devices survived expansion to 4mm. No visible signs of crack initiation were seen in the devices that survived expansion to 4mm.

5.3.2.4 Electropolishing Investigation

As the annealing studies conducted in the vacuum tube furnace were carried out on devices that had all been electropolished post annealing, a study into the effects of the electropolishing procedure was conducted on devices manufactured from 0.5Y alloy wire annealed in the vacuum tube furnace. Unpolished devices (annealed under optimal conditions – 250°C for 10mins) as well as those polished for 10s, and 20s underwent expansion testing. The surface quality of devices that had undergone electropolishing for 10-30s are shown in Figure 5.18. As can be seen after electropolishing for 10s (Figure 5.18b) the oxide layer appears to be fully removed, though there is clear “dimpling”, marked by red arrows, along the OD of the waves. As the electropolishing time is increased to 20 and 30s this dimpling effect remains around the OD of the waves, but their apparent depth is decreased compared to the sample polished for 10s. The removal of the oxide layer has revealed the presence of Y-rich particles, which appear as bright particles in Figure 5.18b-d.

Following on from the surface investigation, three devices were manufactured and expanded to 4mm in the 3 conditions described; non-polished, polished for 10s and polished for 20s. The expansion testing found that all the devices tested survived expansion to 4mm. However, SEM investigation of the device surface revealed cracking and partial strut failures in each of the devices. Figure 5.19 shows cracking along the outer and inner diameters of an expanded wave

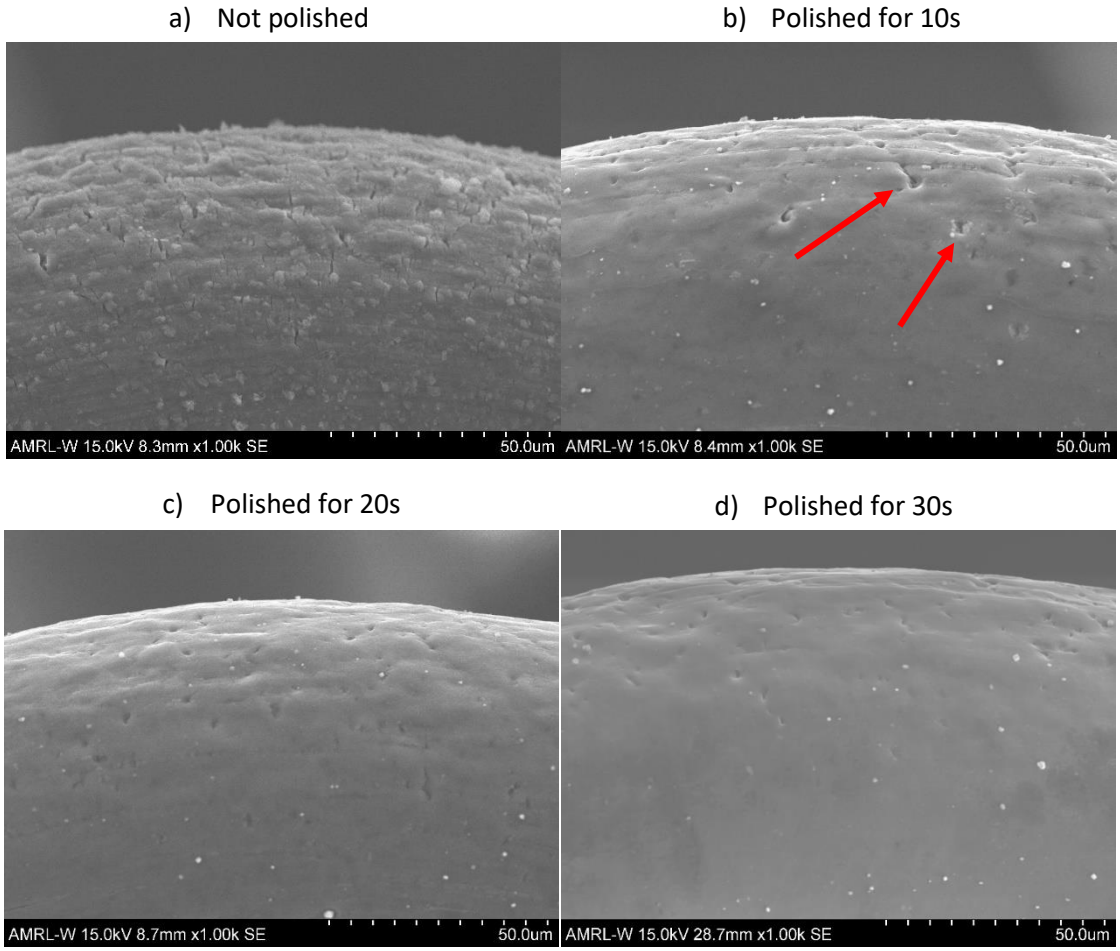

Figure 5.18: 0.5Y devices post electropolishing for various times

in a non-electropolished device expanded to 4mm. As well as the cracks present in the as manufactured state (Figure 5.18a) still being present post expansion (Figure 5.19c) cracking was also observed along the inner diameter of the wave (Figure 5.19d). Despite the cracking observed along the waves of each device only 1-2 partial fractures were observed across the range of devices analysed. One of these fractures is shown in Figure 5.20 in a device polished for 20s and expanded to 4mm. All partial strut fractures were observed to initiate from the ID of waves at their apex.

5.3.2.5 Microstructural Analysis

Microstructural analysis of devices manufactured from both alloys following annealing in the vacuum tube furnace for optimal expansion (250°C for 10mins), revealed that a more homogeneous microstructure was developed throughout the scaffolds compared to the 0.5Y devices heat treated in the vacuum oven. Figure 5.21 and Figure 5.22 show the microstructure of the peak of a wave in a 0.5Y and 2Y alloy scaffold, respectively, when heat treated under these

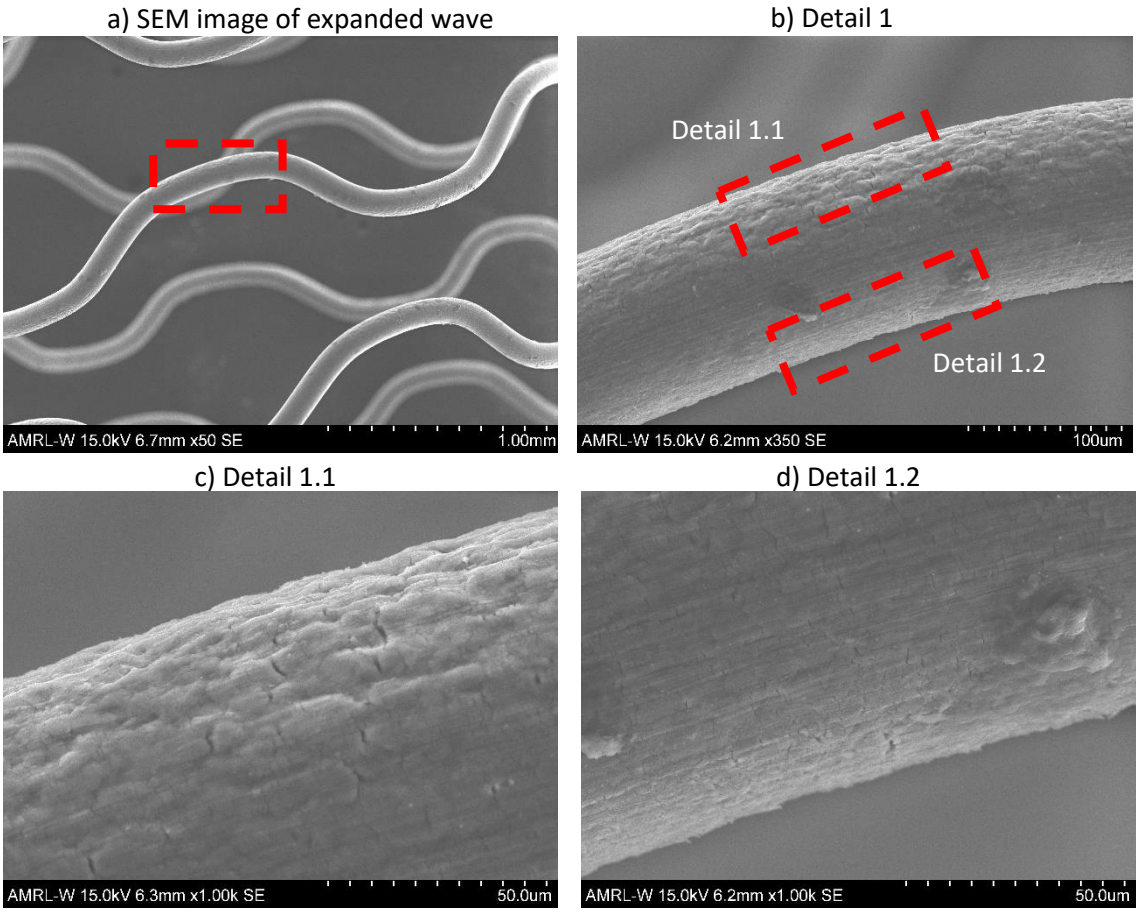

Figure 5.19: Cracking on waveform of unpolished device

conditions. As can be seen in both devices the wire maintains a refined grain size throughout the peak of the wave. However, a "skin" of larger grains is observed around the OD of the wire in devices manufactured from both alloys, this is observed more clearly with EBSD analysis. A number of dark cubic regions are observed throughout both devices in Figure 5.21 and Figure 5.22, with an increased number observed in the 2Y device. From optical microscopy of the annealed wires in Chapter 4 these were identified as Y rich secondary phases, however from

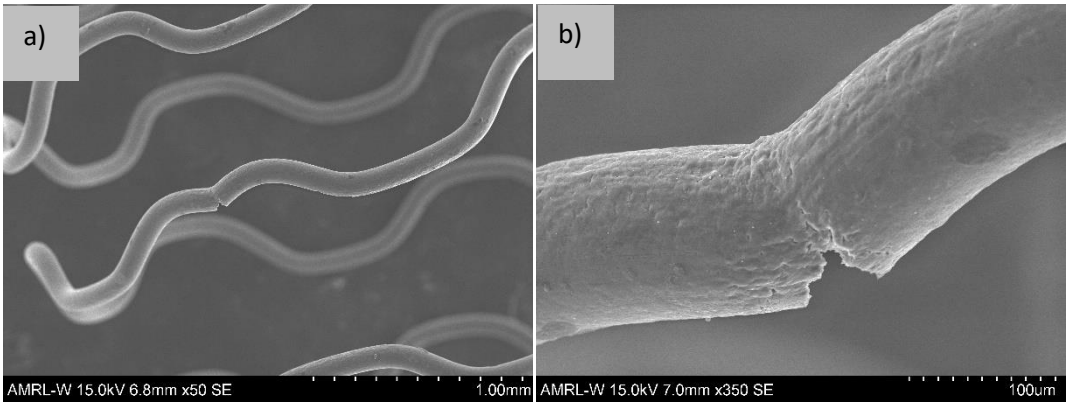

Figure 5.20: Partial cracking of device polished for 20s

Figure 5.21: 0.5Y device annealed at 250°C for 10mins

Figure 5.21 and Figure 5.22 it cannot be certain whether these dark regions are particles or etching pits. Consequently, SEM analysis of devices manufactured from both alloys was carried out, where the Y-rich secondary phases will appear brighter compared to the bulk Mg matrix. Figure 5.23 and Figure 5.24 show SEM images of the 0.5Y and 2Y devices respectively. As can be seen the 0.5Y device contains relatively few particles distributed throughout the wire, whereas there are a significant number in the 2Y device. Further a large, coarse particle is seen in Figure

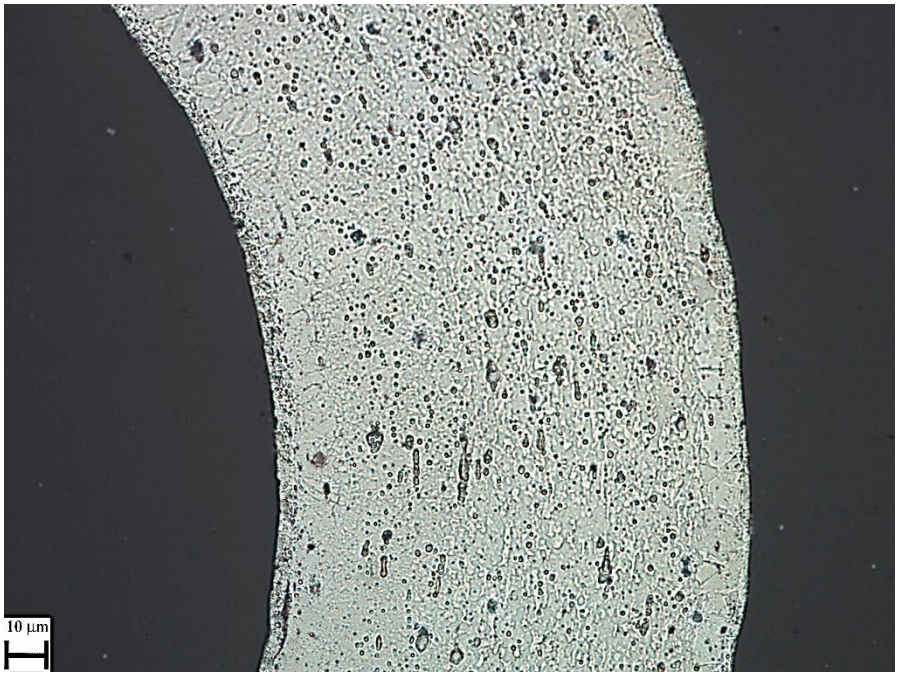

Figure 5.22: Microstructure of 2Y alloy device

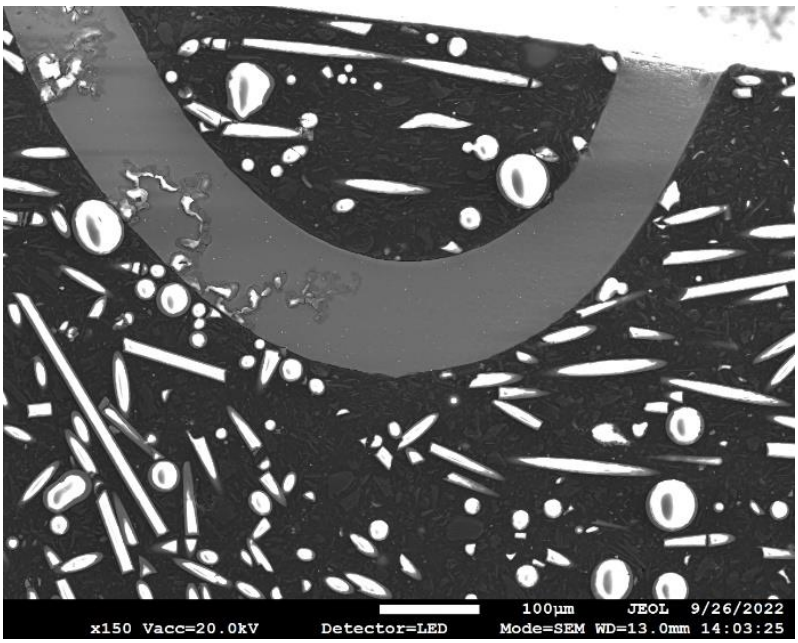

Figure 5.24: SEM analysis of 0.5Y device

5.24. This particle has been enhanced and is shown in Figure 5.25, where it can be seen that a void has been created either side of the particle.

The results from the EBSD analysis of a 0.5Y scaffold, taken at the peak of a wave, where the top and bottom of the image correspond to the OD and ID of the wave respectively, is shown in Figure 5.26. An arrow is added to the bottom of the IPF map to denote the DD of the wire. It should be noted that the EBSD map has dimensions of 81x85µm, meaning the map does not

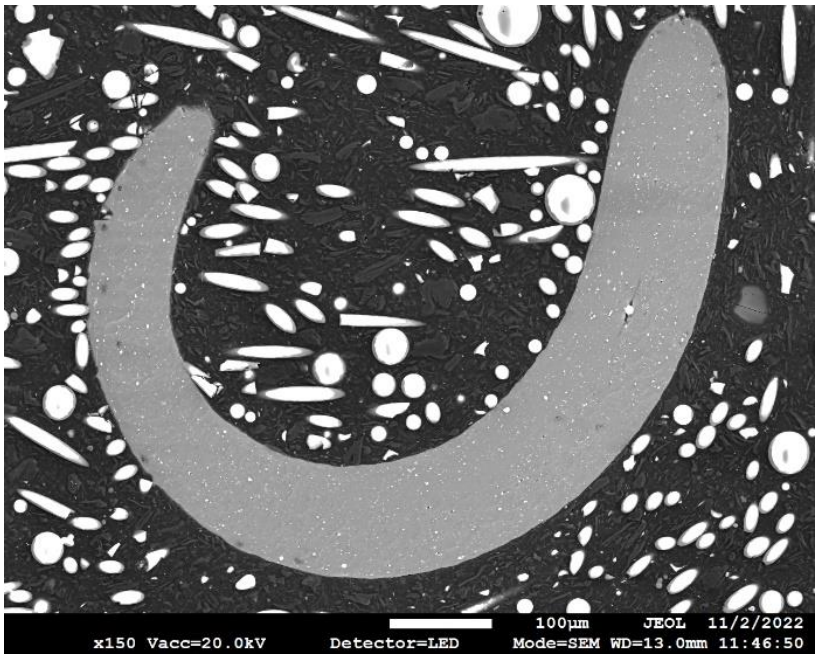

Figure 5.23: SEM image of 2Y device

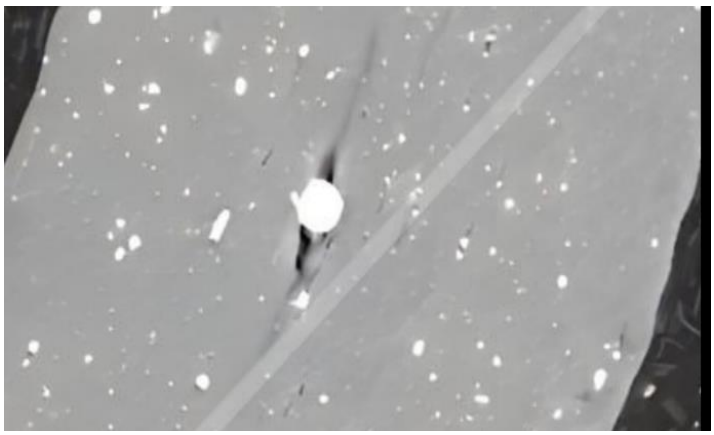

Figure 5.25: Coarse particle in 2Y device

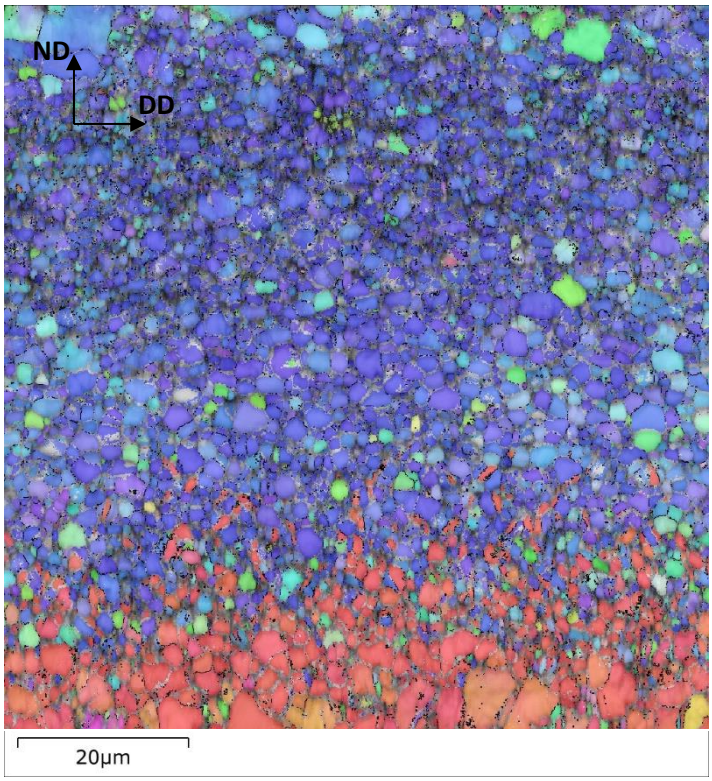

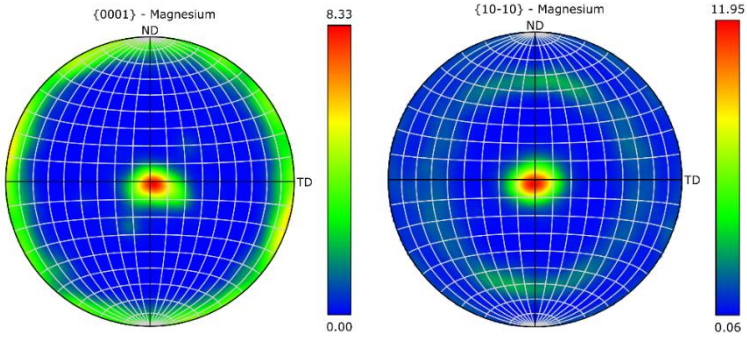

Figure 5.26: IPF map and pole figures of the as annealed 0.5Y alloy device

capture a full region from the OD to ID and consequently the skin on the surface of the wire is

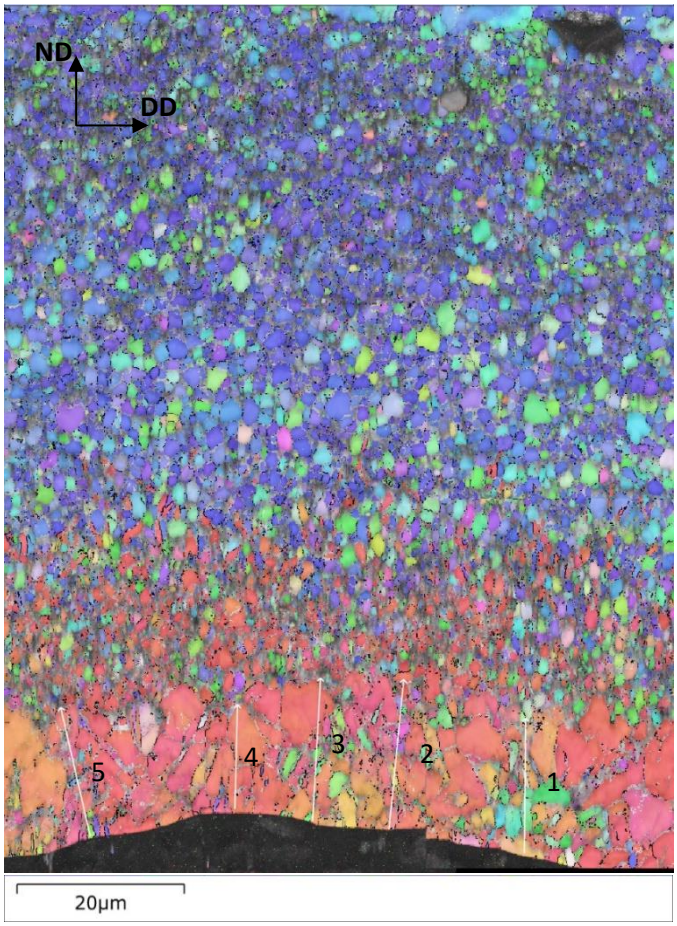

Measurement point	*Distance (µm)*
1	16.2
2	18.0
3	17.1
4	12.5
5	15.8
Mean (±SD)	15.9 ±1.9

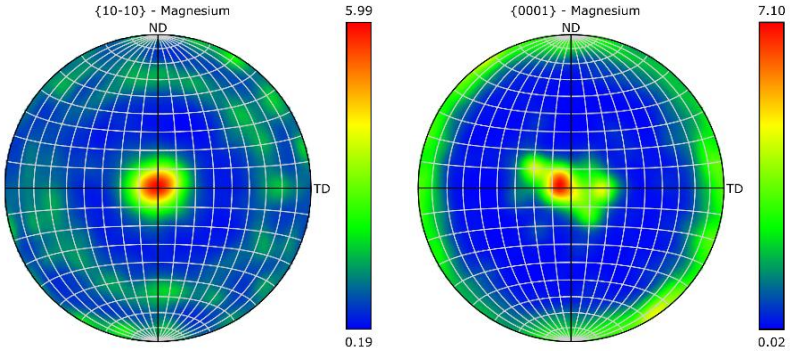

Figure 5.27: IPF map and pole figures of the as manufactured 2Y device

not shown. The skin of large grains around the wires surface is captured in the EBSD analysis of the deformed sample. Figure 5.26 shows a transverse basal texture is developed around the OD of the wire and progresses through the centre of the map, which corresponds to the centre of the waveform. Along the ID of the wave, a shift in texture is observed where the grains are rotated by approximately 90°, compared to the OD, meaning the basal plane now lies perpendicular to the DD of the wire. This shift in texture is also shown in the (0001) pole figure in Figure 5.26, where the texture along the ID is shown by the peak in intensity at its centre,

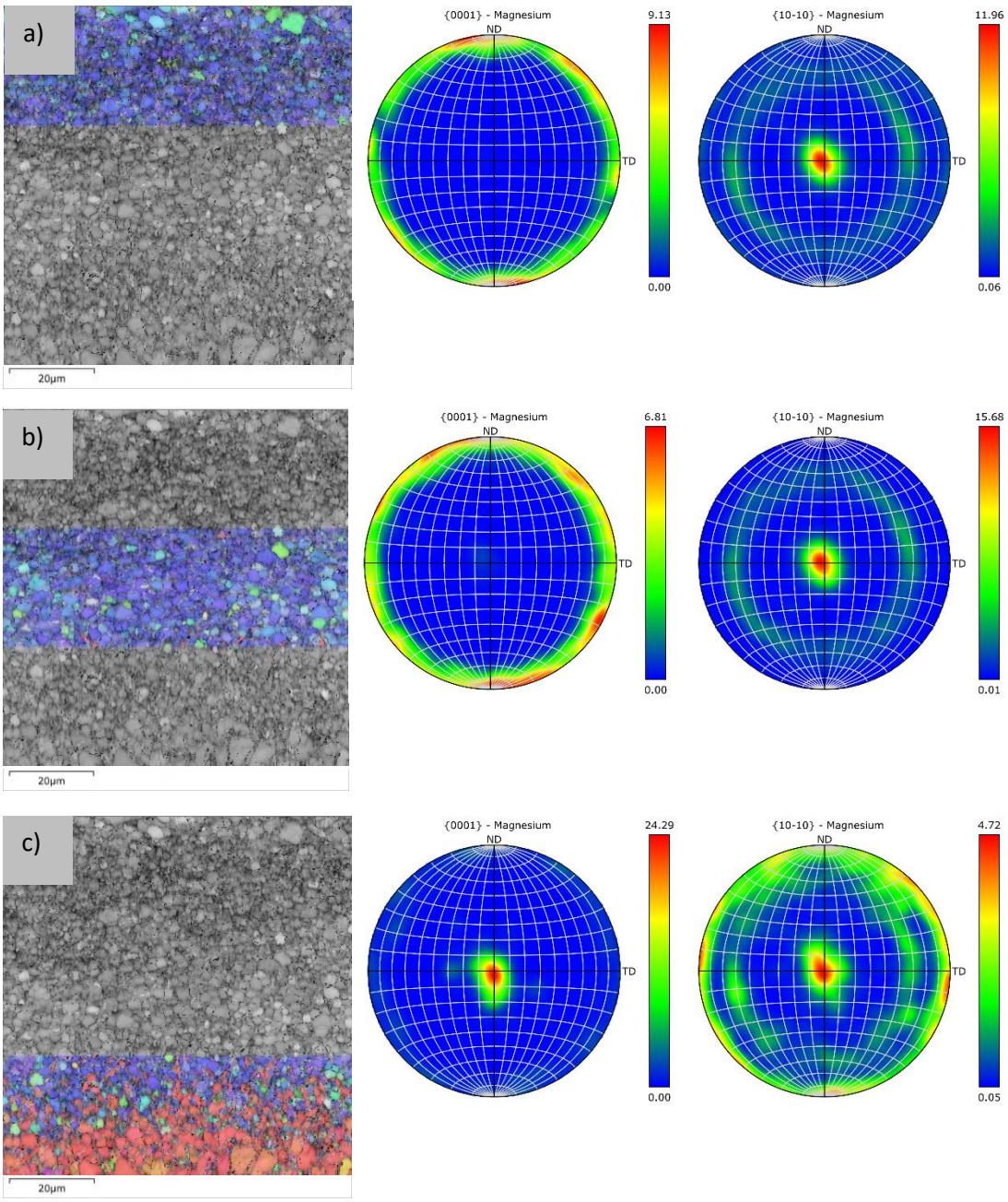

Figure 5.28: IPF maps and pole figures of subsets of 0.5Y device annealed in the vacuum tube furnace a) OD b) centre c) ID

whilst the spread around the edge is associated with the transverse basal texture developed through the remainder of the waveform.

A similar texture is developed in the 2Y device, with a transverse basal texture developed around the OD of the wave with the grains along the ID of the wire rotated approximately 90° about the normal direction. Figure 5.27 shows the IPF and accompanying pole figures for the 2Y device, where the top and bottom of the image correspond to the OD and ID of the wave respectively. The full ID of the wave is captured in Figure 5.27, meaning the skin of coarse grains present

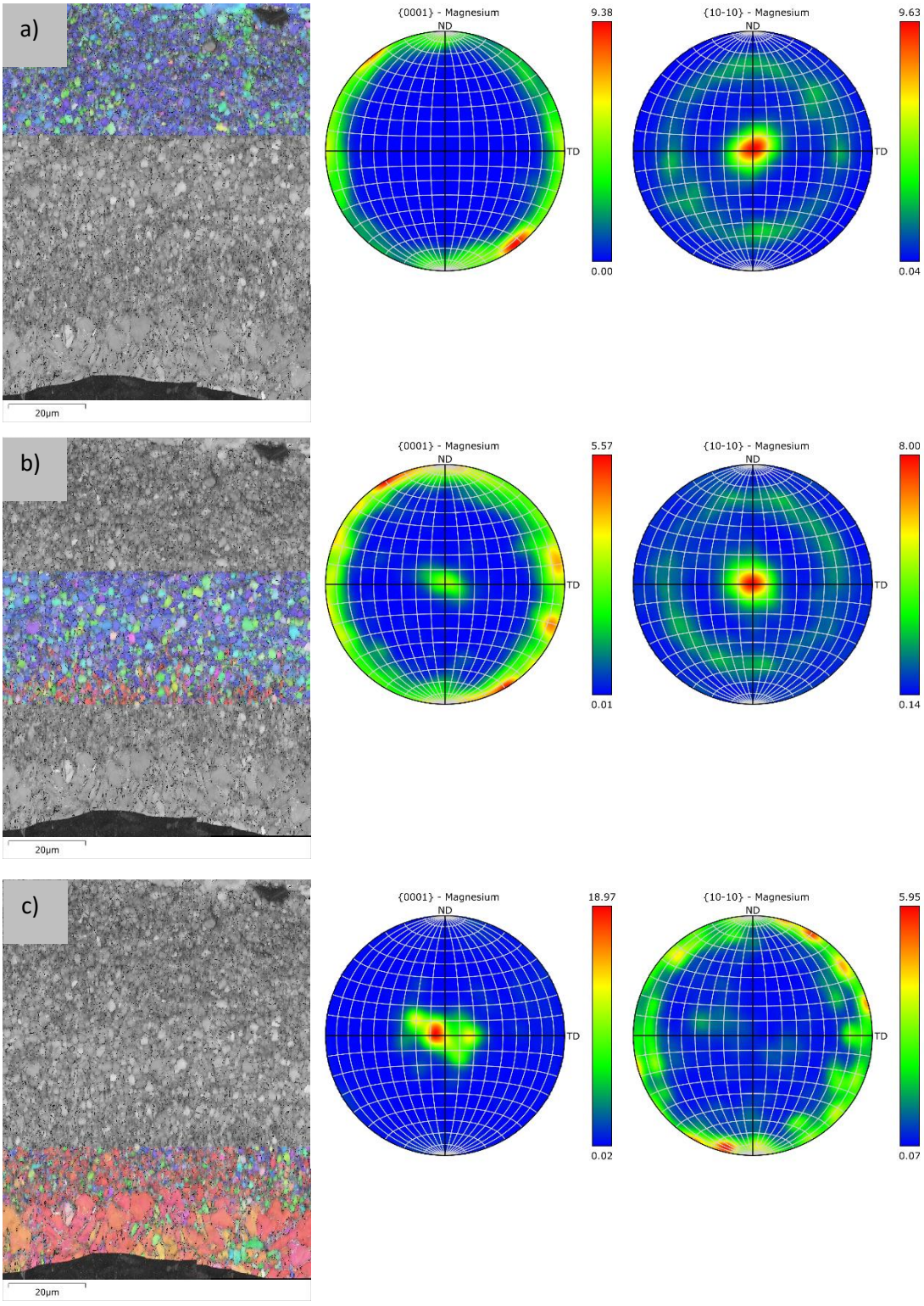

Figure 5.29: IPF maps and pole figures of subsets of 2Y device annealed in the vacuum tube furnace a) OD b) centre c) ID

around the surface of the wire can be observed and is measured through taking five measurements. The mean thickness of this layer was found to be 15.9±1.9µm.

Table 5-4: Grain size measurement of both as manufactured devices annealed in the vacuum tube furnace

Device	*Position*	*Mean grain size (±SD)*
0.5Y	Full map	1.10±0.71
	OD	1.02±0.73
	Centre	1.14±0.68
	ID	1.09±0.73
2Y	Full map	0.92±0.63
	OD	0.87±0.51
	Centre	0.94±0.51
	ID	0.94±0.89

Further, from Figure 5.26 and Figure 5.27 it can be seen that the grain size is reduced either side of the central region of the wave, in both devices. Therefore, each map is split into three subsets of the same size along the ID, centre and OD of the respective IPF maps and shown in Figure 5.28 and Figure 5.29 for the 0.5Y and 2Y devices respectively. Also shown in these figures are the accompanying (0001) and $(10\bar{1}0)$ pole figures for each region highlighted, to show the split in texture along the ID of the waves more clearly. The mean grain sizes are presented for the separate regions of each device in Table 5-4. In the 0.5Y device the mean grain size is reduced along the ID and OD compared to the centre region measured. Similarly, in the 2Y device the grain size is smaller around the OD of the device compared to the central region. In the 2Y device the mean grain size was calculated to be the same in the central region and along the ID, however this is caused by the IPF map capturing the complete ID, meaning the more refined region is captured along with the coarse skin of grains developed around the wires surface. This results in the mean grain size being similar to the centre of the wire but there is increased variation (shown by the higher standard deviation).

5.3.2.6 Fracture Analysis

In Sections 5.3.2.1 and 5.3.2.2, it was shown that in devices that failed, fracture was observed to initiate from the ID of the waves and progress through the wire towards the waves OD. It was aimed to investigate the source of these cracks through optical microscopy and SEM analysis of cross-sections of the scaffolds, prepared through mounting in epoxy resin, grinding, polishing

and etching to reveal any signs of cracking along the ID. However, as no cracks were observed in devices manufactured from the 0.5Y alloy wire (when annealed for optimal expansion capabilities – 10mins at 250°C) and few cracks were observed in the 2Y devices annealed under the same conditions, it was determined to increase the level of deformation applied to devices manufactured from both alloys, to increase the likelihood of cracking. Consequently, a device of each alloy was manufactured and annealed for 10mins at 250°C and crimped down to an ID of 1mm, Figure 5.30 shows a device crimped down to 1mm. Compared to the crimped ID of 1.5mm used for the bulk of testing this, decreased, crimped diameter will result in the devices undergoing increased deformation, before expansion to 4mm. The 0.5Y device crimped down to 1mm and expanded experienced 2-3 complete strut fractures, whilst the 2Y device experienced more than five complete strut fractures. Figure 5.31 shows one such fracture in the 0.5Y device. Both devices were then mounted in epoxy resin and their cross sections analysed for signs of cracking.

Figure 5.32 shows optical microscopy of cracks present along the ID of the waveforms in both 0.5Y and 2Y devices. SEM/EDS analysis was conducted to further investigate the source of these cracks in the 2Y device. Figure 5.33 shows two cracks identified using SEM analysis. The high magnification used, accompanied with charging caused by mounting in non-conducting epoxy,

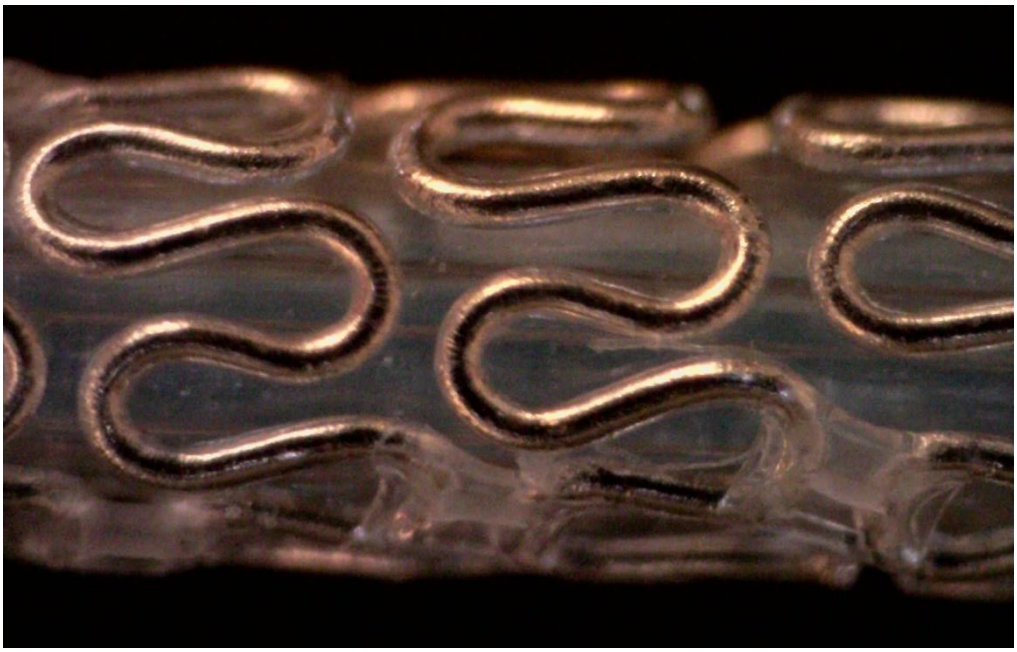

Figure 5.30: Crimped 0.5Y device on a balloon with 1mm folded diameter

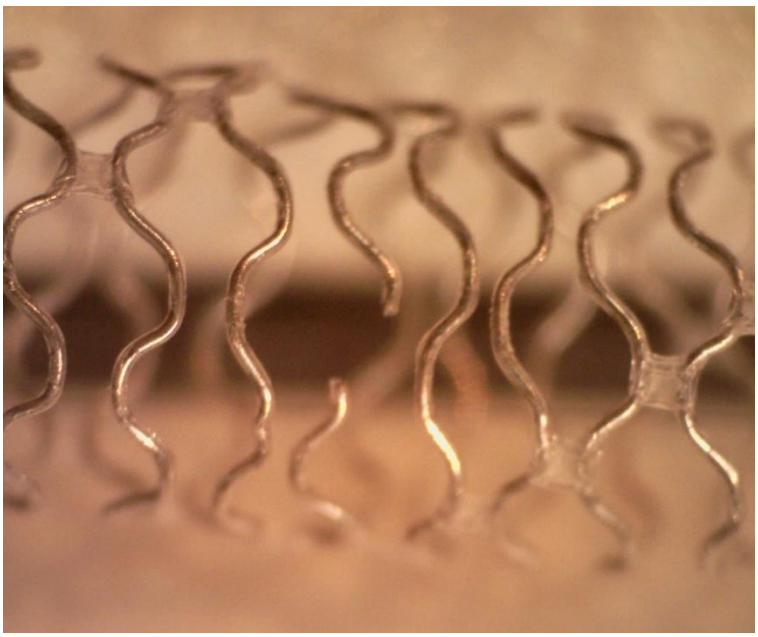

Figure 5.31: Fracture in 0.5Y devices expanded to 4mm from a crimped ID of 1mm

limited the clarity of the images taken, however adjacent to both cracks, two particles were observed. Using EDS analysis these particles were shown to be Y-rich.

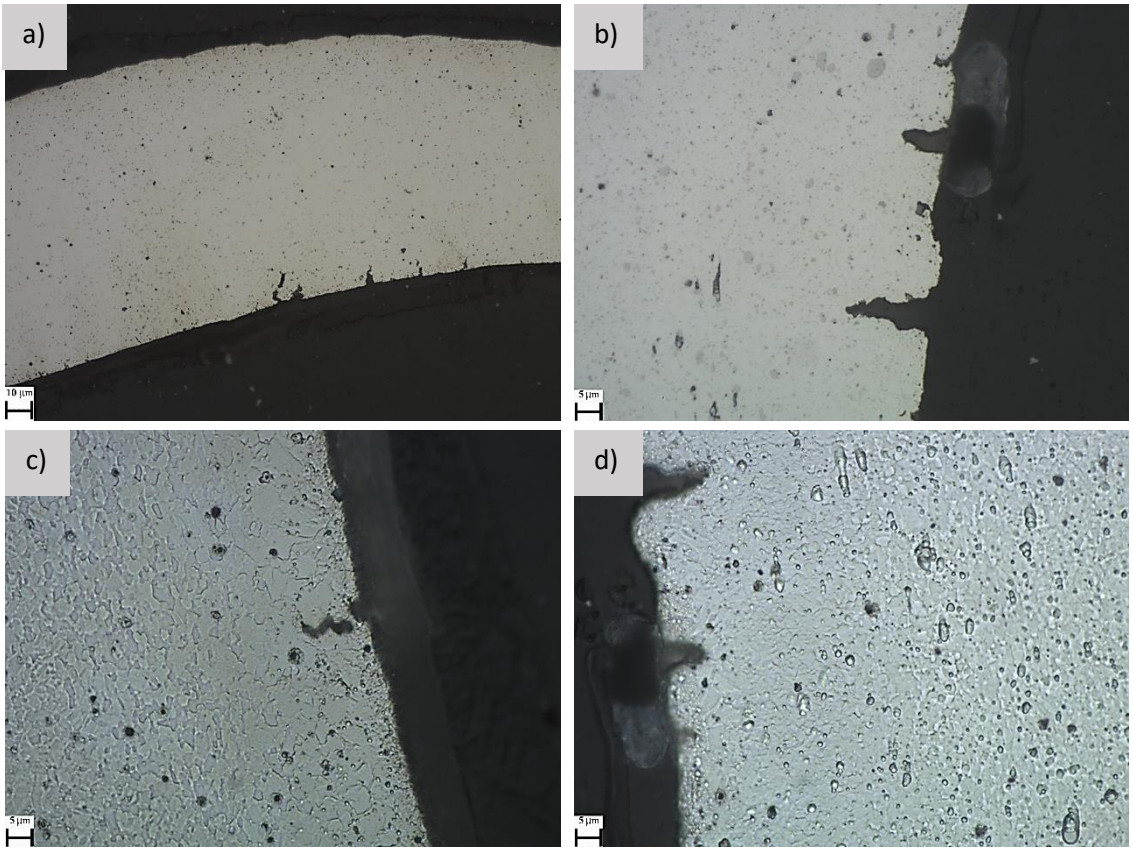

Figure 5.32: Cracking along ID of a+c) 0.5Y and b+d) 2Y devices

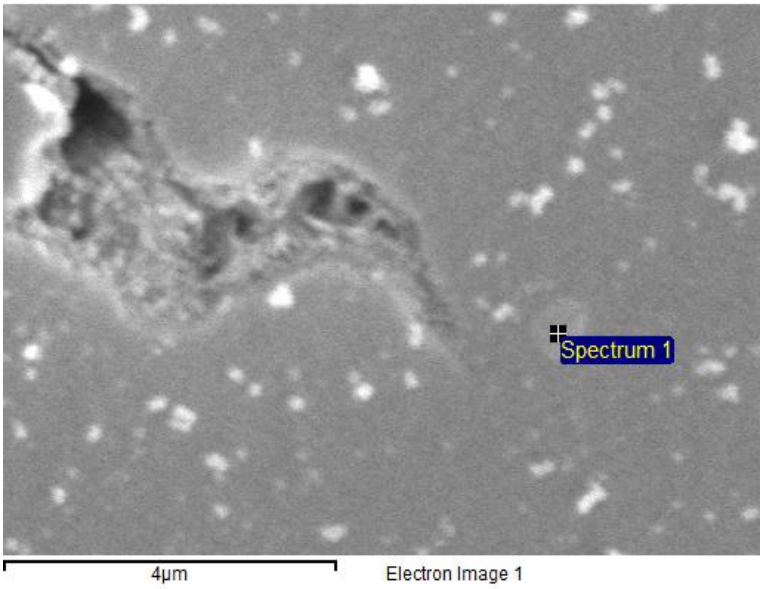

Element	*Composition (wt%)*
Mg	77.8
Y	22.2

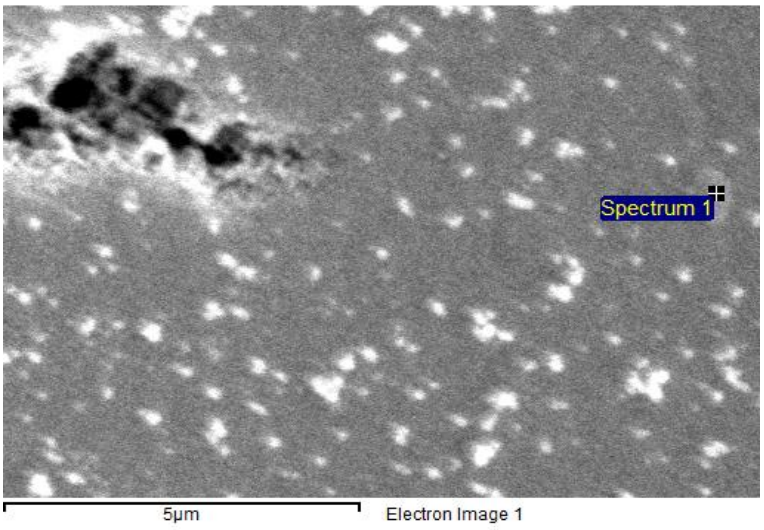

Element	*Composition (wt%)*
Mg	67.2
Y	32.8

Figure 5.33: Cracks initiating from secondary phase particles

5.3.2.7 Expansion

EBSD analysis was also conducted on the 0.5Y and 2Y devices, annealed in the vacuum tube furnace at 250°C for 10mins, post crimping and expansion to 3mm to investigate the microstructural evolution during the expansion process. The results for the 0.5Y and 2Y devices in their crimped and expanded states are shown in Figure 5.34 and Figure 5.35 respectively. As before the top and bottom of each image correspond to the OD and ID of the waves respectively. Similarly, to the EBSD analysis of the as supplied conditions the analysis was carried out at the apex of a wave with the aim, to scan both the OD and ID of the waves, but with drift in the scans

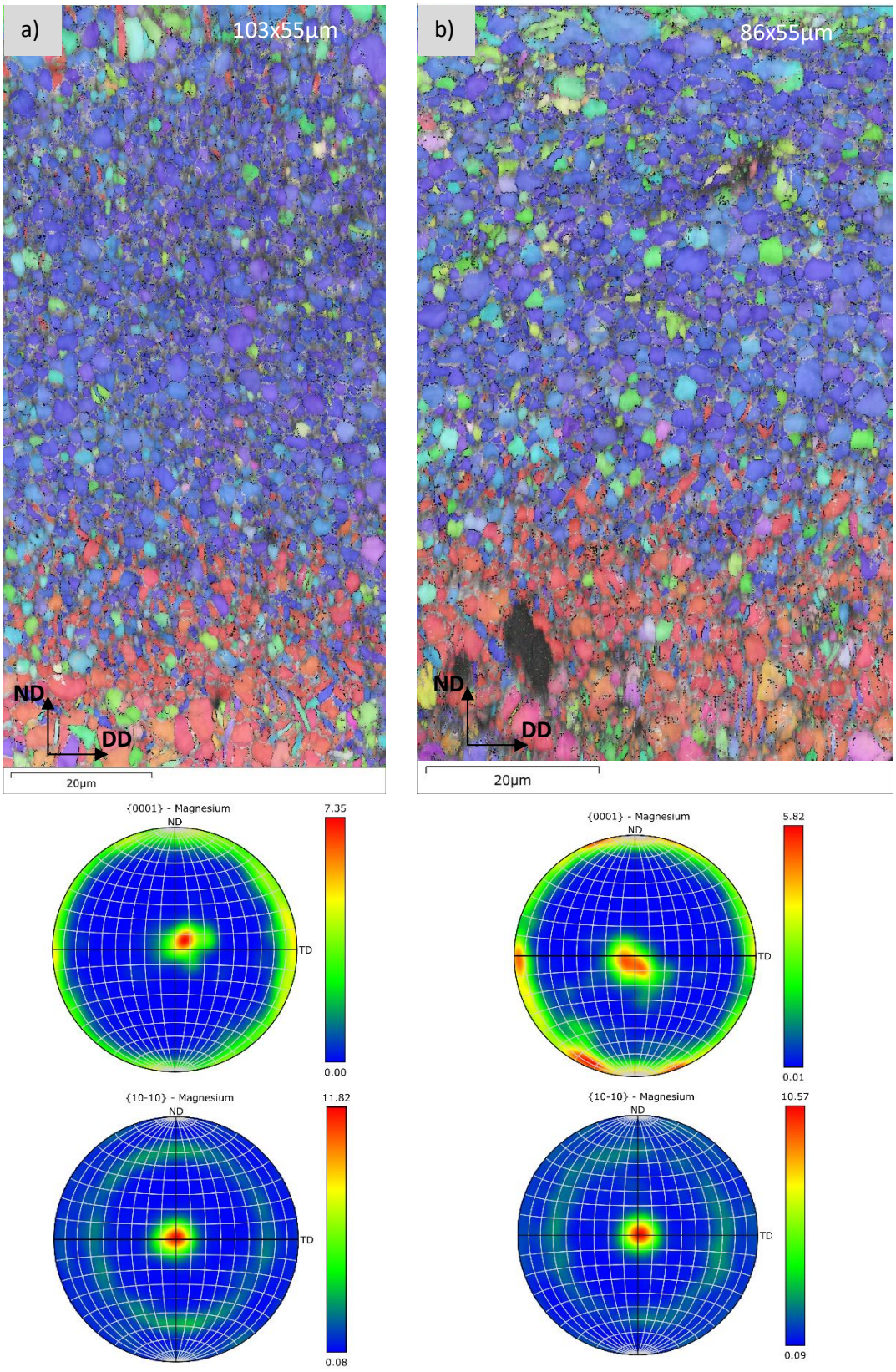

Figure 5.34: IPF map and pole figures for 0.5Y devices following a) crimping to 1.5mm and b) expansion to 3mm

the

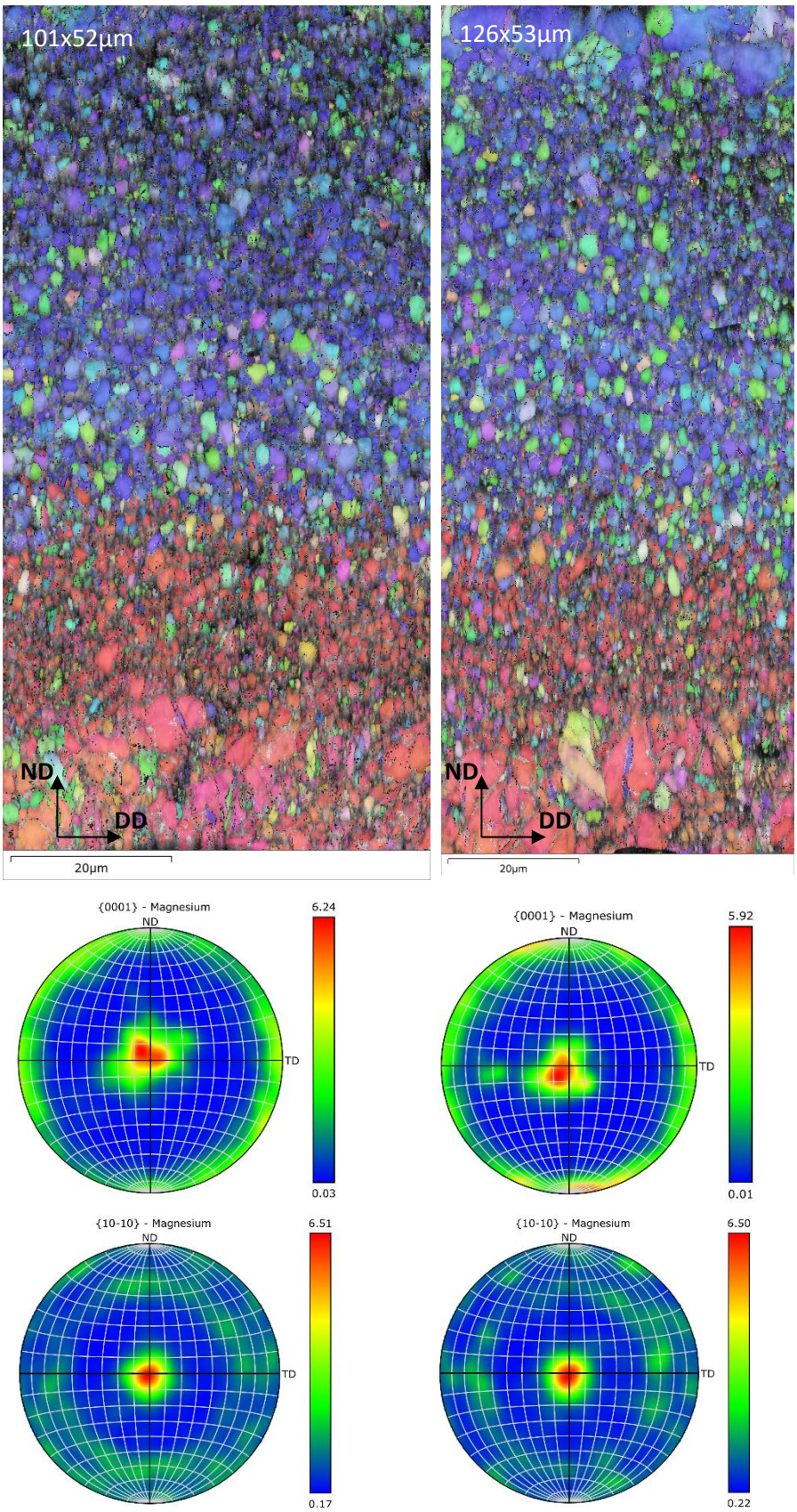

Figure 5.35: IPF map and pole figures for 2Y devices following a) crimping to 1.5mm and b) expansion to 3mm

size of the maps varied, and the full ID and OD is not captured in each image. As such at the top of each IPF map the dimensions are given.

The texture developed along the ID in the as manufactured state is maintained along the ID following crimping, in both alloys, but the area of the ID with modified texture appears thicker compared to the as-manufactured state. This is observed most clearly in the IPF for the 2Y device in Figure 5.35. In the as-manufactured state, the region of wire with the altered texture can be measured to be approximately 30µm thick from Figure 5.27. Whereas, following crimping the thickness of this section can be measured to be approximately 43µm thick, from Figure 5.35a. The scans of the 0.5Y devices did not capture the full ID of the waveforms so the thickness of this layer could not be determined but it is assumed that similar to the 2Y alloy wire, the thickness of this layer will increase during crimping and be maintained on expansion.

5.3.3 Radial Force Analysis

Radial force testing was conducted on devices manufactured and annealed for optimal expansion in the vacuum oven and tube furnace at diameters of 3 and 3.5mm, the results are summarised in Table 5-5 below. Only one device per alloy/annealing condition was tested and as such no standard deviations are calculated. When expanded to 3mm the 0.5Y and 2Y devices, annealed in the vacuum tube furnace, have similar radial force (1.15 and 1.22N/mm respectively). When treated in the vacuum tube furnace and expanded to 3.5mm however, the

Table 5-5: Radial force results of devices expanded to 3 and 3.5mm

Wire composition	*Annealing conditions*	*Expanded diameter (mm)*	*Radial Force (N/mm)*	*Radial Stiffness (N/mm^2)*
0.5Y	Oven (300°C 30mins)	3	0.58	2.05
0.5Y	Oven (300°C 30mins)	3.5	0.75	2.92
0.5Y	Tube (250°C 10mins)	3	1.15	4.62
0.5Y	Tube (250°C 10mins)	3.5	1.32	4.99
2Y	Tube (250°C 10mins)	3	1.22	3.31
2Y	Tube (250°C 10mins)	3.5	1.65	5.38

2Y device has increased radial force (1.65N/mm) compared to the 0.5Y device (1.32N/mm). When annealed in the vacuum oven and expanded to 3 and 3.5mm the 0.5Y devices have decreased radial force of 0.58 and 0.75N/mm respectively, compared to the 0.5Y devices annealed in the vacuum tube furnace.

5.4 Discussion

5.4.1 Annealed Wire Characterisation

Optical microscopy of the cross section of each alloy wire (Figure 5.6) found that both alloys developed a refined grain structure in the wire core with a “skin” of coarse grains around their OD, this skin was approximately 15µm thick in both alloy wires. EBSD analysis of a 50x50µm region in the centre of the wire cross sections found the grain size of the annealed 0.5Y and 2Y alloy wires to be 2.0µm and 1.6µm respectively. The accelerated growth phenomena of grains close to the OD is similar to that observed in the annealing optimisation study in Chapter 4 though there are some key differences.

Firstly, in the annealing optimisation study carried out on the cold drawn 0.5Y and 2Y alloy wires from Chapter 4, recrystallisation was observed to initiate first in regions closest to the surface and progresses inwards as soak time/temperature was increased. An uneven grain size distribution was only observed in the 0.5Y alloy treated in the vacuum tube furnace upon complete recrystallisation from the work conducted in this study. Though as the soak time was increased at the same temperature (250°C), a homogeneous grain size distribution was developed throughout the entire cross section. The cold drawn 2Y alloy wires, when annealed for maximum ductility in the vacuum tube furnace, developed a homogeneous grain size distribution. Thus, the supplied annealed wires were shown to develop a slightly different microstructure compared to the treatments developed as part of this work. It is known, and shown in Chapter 4, that the cold drawn wires have an uneven hardness distribution through the wires cross section, with increased hardness at the mid-radial position compared to the wires core. It is assumed this corresponds to an uneven internal strain distribution developed during the drawing process. Consequently, during thermal processing this skin of larger grains may be attributed to the grains nucleated within the regions of highest internal strain gaining a growth advantage compared to those nucleated from the regions of lower internal strain, closer to the wire core. Without knowledge of the annealing parameters applied to both alloy wires, it is not possible to conclude on the nature of the mechanisms behind the formation of this layer.

However, it is important to identify its presence as following the processing of the final device the skin of large grains around the wires surface remains and consequently will influence the performance of the device.

Similar to the cold drawn alloy wires, both annealed wires contained a number of Y-rich secondary phase particles distributed throughout their microstructure, with an increased number and size of these particles observed in the 2Y alloy wire. Compared to the cold drawn wires, there does appear to be an increased number of particles present in the supplied annealed 2Y wire. This would suggest that the annealing protocol applied results in the precipitation of additional Y-rich particles. As mentioned before this should be avoided for the intended application of these devices, as uncontrolled precipitation can decrease ductility, increase corrosion rate, and provide little improvement in strength.

Considering the EBSD results, similar textures were developed in both alloy wires compared to that of the same alloy wires when treated for optimal ductility in the vacuum oven and vacuum tube furnace. A transverse basal texture is developed in both, with the 2Y alloy wire having a slightly weaker texture in comparison to the 0.5Y alloy. The intensities of the as supplied annealed wires are similar to that developed upon optimal annealing of their respective cold drawn wires in the vacuum tube furnace. The supplied annealed 2Y alloy wire does exhibit a slightly higher intensity in the $\{10\bar{1}0\}$ pole figure compared to the 2Y alloy wire following optimal annealing in the vacuum tube furnace (10.99 vs 7.64). This could be, in part, to the as supplied annealed 2Y alloy wire not appearing to be fully recrystallised. The IPF map of the 2Y alloy wire has reduced indexing compared to that of the other optimally annealed samples (from both the as supplied 0.5Y alloy wires and those prepared within this work). Reduced indexing rate can be caused by incomplete recrystallisation as unrecrystallised regions are challenging to index.

Tensile testing of the two annealed alloy wires revealed the 0.5Y wire had similar mechanical properties compared to the optimally annealed cold drawn 0.5Y wire in the annealing studies from Chapter 4, whilst the 2Y alloy wire had increased strength and reduced ductility. The relative, low ductility and high strength could be attributed to the increased number of secondary phase particles present in the 2Y alloy wire. However, the analysis of the two cold drawn wires in Chapter 4 showed, that despite the increased number of secondary phase particles in the cold drawn 2Y alloy wire, compared to the 0.5Y alloy wire, both exhibited similar YS and UTS. Further, the annealing optimisation in Chapter 4 showed that following annealing

for maximum ductility, both alloy wires exhibited similar strength. Therefore, it was considered that there may be another effect causing the increased strength and reduced ductility in the 2Y alloy wire, compared to the optimally annealed 2Y wire from Chapter 4. The EBSD analysis suggested that the annealed 2Y alloy wires are not fully recrystallised, owing to the reduced indexing rate, which would result in increased strength and reduced ductility of the wire, compared to a fully recrystallised microstructure. To assess this, using the vacuum tube furnace, a series of annealing protocols were conducted on the supplied annealed 2Y alloy wire, the results are summarised in Table 5-6, with the results for the supplied annealed 2Y wire included for ease of comparison. It was found that additional thermal processing of the 2Y alloy wire increases its ductility and reduces its strength. As such the increased strength and reduced ductility of the supplied 2Y alloy wire, compared to the 0.5Y alloy wire, is attributed to incomplete recrystallisation, as opposed to any strengthening effect provided by the increased number of secondary phase particles. Thus, the unindexed regions of wire from the EBSD analysis can be attributed to the incomplete recrystallisation of the sample.

5.4.2 Annealing Optimisation Study – Optimising for Expansion Range

5.4.2.1 Vacuum Oven

The first annealing study was conducted on devices manufactured from 0.5Y alloy wire annealed in the vacuum oven. Firstly, the annealing procedure developed in Chapter 4 to optimise the ductility of the cold drawn 0.5Y alloy wire (340°C for 20mins) was applied to the final device. It was shown that each of the three devices could survive expansion from an ID of 1.83mm to 3mm but failed during secondary expansion to 4mm. Considering the different levels of CW likely imparted between the cold drawing process and the forming of the device it was thought that application of the annealing protocol optimised for the cold drawn wire may result in "over annealing" of the final device, leading to loss of ductility. The cold drawn alloy wire is supplied

Table 5-6: Results from annealing study on the supplied 2Y annealed wire

Annealing Conditions	UTS (MPa)	YS (MPa)	% Elongation to failure
As supplied annealed wire	241.0±0.8	197.0±0.7	13.8±1.6
10mins 300° C	224.6±0.4	180.7±0.6	16.4±0.9
17.5mins 300°C	205.1±0.3	148.0±1.1	20.9±1.0
20mins 300°C	204.4±0.3	144.3±1.4	19.86±1.2

with 80% CW applied in the final drawing step whereas during forming of the waveform only the wire along the wave peaks and troughs will have been deformed, whilst the struts undergo no deformation. Further, considering the waveform is deformed through bending, there will be a gradient of deformation throughout the curvature of the waveform. A maximum compressive strain is applied to the ID of the waveform progressing to a maximum tensile strain (equal in magnitude to the compressive strain on the ID) around the OD of the waveform. This loading regime is visualised in Figure 5.36, with red and blue arrows denoting tensile and compressive loading respectively, with the maximum idealised bending strain along the ID and OD of the waveform being 26.9%. If this is considered to be the magnitude of CW applied to the wire during manufacture of the waveform, it can be assumed that the final device would require a different annealing protocol compared to the cold drawn wire to optimise its microstructure and consequently its mechanical performance. Coiling of the waveform into the cylindrical scaffold will impart some additional CW throughout the entire waveform, though it is considered to be relatively low considering the large bend radius compared to the radius of the wire.

It was considered that either the soak time or temperature should be reduced from the process optimised for the cold drawn wire. Owing to the setup of the vacuum oven where the slow heating and cooling cycles limited the variation achievable through altering the soak time, the soak temperature was decreased to optimise the annealing procedure. When the soak temperature was lowered to 300°C (with a soak time of 30mins) it was shown that the devices could survive expansion from an ID of 1.83mm to 4mm without failure. When the crimping stage was introduced, the devices manufactured from the 0.5Y alloy wire and heat treated at 300°C for 30mins all failed during expansion to 4mm. This led to the development of the

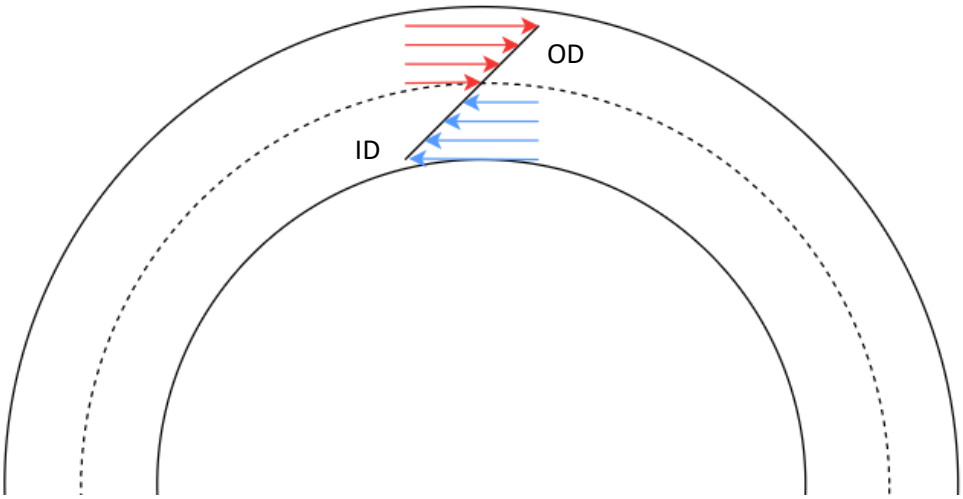

Figure 5.36: Loading experienced by the wire during forming of the waveform

electropolishing procedure. The introduction of the electropolishing procedure, resulted in devices that were treated at 300°C for 30mins being capable of expansion to 4mm from a crimped ID of 1.5mm. The effect of the electropolishing procedure is discussed in greater depth in Section 5.4.4.1, with reference to the underlying microstructural features.

5.4.2.2 Vacuum Tube furnace

The vacuum tube furnace was used to develop an optimum heat treatment process for devices manufactured from both alloy wires. As with the vacuum oven, the initial process investigated for devices manufactured from both alloys was the same as that optimised for their respective cold drawn alloy wires. When treated under these conditions' devices manufactured from both alloy wires consistently failed during expansion to 4mm from a crimped ID of 1.5mm with an electropolishing procedure conducted post annealing. Similar to the vacuum oven study the assumption was that these annealing processes were over annealing the devices and consequently the soak time was reduced for each. In the 0.5Y alloy wire it was shown that reducing the soak time to 10mins (at 250°C) resulted in consistent expansion of the device to 4mm from a crimped ID of 1.5mm. For the 2Y alloy wire, the soak time at 300°C was progressively reduced to 5mins. All 2Y devices treated at 300°C failed during expansion to 4mm. Consequently, the soak temperature was reduced to 250°C and several soak times investigated. No conditions were found that allowed for consistent expansion to 4mm, however when treated at 250°C for 10mins, 4 out of 6 devices were found to survive expansion to 4mm. Considering the application of these devices', failure of 1 in 3 devices during expansion to 4mm is deemed unacceptable. However, the mechanisms of failure are discussed in the following sections, which reveal that there may be potential benefits of applying the 2Y alloy wire in the final device if the complete processing route (from ingot to BVS) can be optimised.

5.4.3 Microstructure

5.4.3.1 Vacuum Oven Annealing Study

When treated in the vacuum oven, the 0.5Y devices developed an uneven grain size distribution through the device. A refined grain structure was developed through the struts, with a band of refined grains running through the neutral axis of the curved waveform separating two regions of large grains around the waveforms OD and ID. The recrystallisation of this microstructure can be explained through considering the deformation imparted on the individual waves during manufacture of the device. Figure 5.36 showed a representation of the loading imparted on the wire during forming of the waveform, with the OD of the wave loaded in tension whilst the ID is

in compression. The region of wire closest to the OD and ID of the wave undergoes the highest level of deformation with the neutral axis of the wave undergoing the least deformation. As such, the internal strains developed throughout the wire will be highest at the OD and ID. As internal strain is the driving force for nucleation, grains will nucleate first from these regions, allowing them to gain a growth advantage and dominate the final microstructure. Theoretically, the neutral axis will be strain free (or close to it), as will the straight struts as they have undergone no deformation. During heat treatment, for new grains to be nucleated there must be some minimum level of internal strain. As a refined grain structure, with a similar grain size to the annealed wire used to manufacture the device, remains through the device's straight struts and neutral axis it is assumed there was insufficient internal strain to activate recrystallisation through these regions of the device.

5.4.3.2 Tube Furnace

Compared to the 0.5Y devices annealed in the vacuum oven, where the prolonged heating and cooling cycles resulted in large coarse grains developing around the waveform's ID and OD, the rapid heating and cooling cycles applied using the vacuum tube furnace resulted in a more homogeneous microstructure developing through the entire waveform. In both devices, the mean grain size calculated from EBSD analysis at the apex of the wave was calculated to be approximately 1μm. However, this does not fully describe the grain size distribution observed in devices manufactured from both alloy wires. Firstly a "skin" of larger grains is present around the surface of the wire in both devices. This skin was observed during optical microscopy of both devices but only captured in full in the IPF of the 2Y device, Figure 5.27, and was calculated to be approximately 16μm hick. The skin of coarse grains is approximately the same thickness as the skin of coarse grains present in both alloy wires used to manufacture the devices (measured to be approximately 15μm). Discrepancy in these measurements is expected as there will be some angular offset during the mounting and polishing procedures. In general, the grain size post recrystallisation of a deformed material is dependent on the level of deformation and prior grain size.[213] Consequently, this skin of coarse grains is a remnant from the microstructure of the wires used to manufacture the devices, rather than being a consequence of the annealing procedures applied. Considering the fact that the grain size post recrystallisation is also dependant on the level of deformation applied, the refined bands of grains either side of the central region of the wires can therefore be explained. Figure 5.36 shows a representation of the loading on the wire during forming, where the strains applied would be highest at the surface of the wire and reduce towards the neutral axis of the bend. Therefore, during thermal

processing recrystallisation will theoretically not activate within the undeformed neutral axis, as shown from the refined band of grains developed in the 0.5Y devices annealed in the vacuum furnace, whilst more refined grains will be recrystallised from the more deformed regions further from the neutral axis. Within the skin of coarse grains about the surface of the wire, where the theoretical strains will be highest, the recrystallised grain size is predominantly controlled by the prior grain size.

As well as measuring the grain size, EBSD analysis of the devices was used to investigate the texture of devices manufactured from both alloys. Firstly, considering Figure 5.26 and Figure 5.27, it can be observed that both the 0.5Y and 2Y alloy devices develop a similar texture. Around the OD of the waves, a transverse basal texture, similar to that of the annealed wires used to manufacture the devices, is maintained. The subsets of each device (shown in Figure 5.28 and Figure 5.29), where the OD has been separated from the central region show that despite a transverse basal texture being developed in both regions, there is a difference in the intensity of this basal texture in the (0001) pole figures. In the 0.5Y devices, the basal pole figure for the OD and central regions have a maximum intensity of 9.13 and 6.81mrd respectively. Similarly, in the 2Y device the maximum intensity of the (0001) pole figure is reduced in the centre (5.37mrd) compared to the OD (9.38mrd). The texture intensity developed through the central region of each alloy is similar to that of the corresponding annealed wires used to manufacture each device. Upon forming and subsequent annealing, the texture intensity increases along the OD of each device, compared to the wire used to manufacture the devices. In contrast a distinct texture shift is observed along the ID, whereby the grains have rotated approximately 90° so that the c-axis of the grains lies parallel to the DD of the wire used to manufacture the devices.

The alteration in texture at the ID of the waves compared to the original wire and OD of the device upon recrystallisation can be explained through consideration of the deformation mechanisms, likely, activated during forming of the waveforms. Referring to Figure 5.36, it can be seen that during forming, the ID of the waves will undergo compressive loading whereas the OD will be loaded in tension. As such, considering the transverse basal texture of the annealed wires used to manufacture the devices, during forming, the grains along the ID of the wave will be loaded with their c-axis in tension whereas the grains at the OD will be loaded with their c-axis in compression. As such, tensile twinning, the second most readily activated deformation mode in Mg alloys, will be promoted along the ID of the waves. As is known, tensile twinning results in reorientation of the c-axis of the grains by approximately 86°.[109, 214] The matrix within

the tensile twins remains unfavourably aligned for basal slip following this reorientation which typically limits the accumulation of dislocations. Consequently, it has been reported that recrystallisation from tensile twins in Mg alloy is limited and instead recrystallisation is preferred to nucleate from compression and double twins, where their reorientation results in more favourable activation of basal slip, resulting in a build-up of internal stored energy.[118] However, recrystallisation has been observed activating from tensile twins in heavily twinned Mg alloys, resulting in the deformation texture being maintained post recrystallisation.[115, 123] Xin et al.[123] demonstrated that following annealing of AZ31 rods, with a typical extruded texture, compressed to various levels, the deformation texture was maintained when the twin thickness was much larger than that of the surrounding matrix. The authors showed that annealing of samples compressed to only 2% strain resulted in the formation of "thin" twins that were consumed by the matrix during recrystallisation, however in the samples strained to 5%, thicker twins were developed and the deformed texture was maintained in the final recrystallised texture.[123] Consequently the texture observed along the ID of the waveforms analysed in this work is assumed to be a consequence of the deformation during forming being dominated by tensile twinning. Subsequently following annealing the recrystallised texture is expected to be dominated by grains nucleated along the tensile twin boundaries, with an 86° rotation from the original texture, resulting in the texture observed in devices manufactured from both alloys.

5.4.4 Deformation and Fracture Analysis

It was shown that during expansion of the devices, struct fractures always initiated from the ID of the device, before progressing through the entire waveform. This suggests that the mechanism of failure is consistent in the devices manufactured from both alloy wires and, if identified, possible conclusions could be drawn on how to reduce its affect so as to improve device performance. The various mechanisms that may contribute to this failure are discussed in this section.

5.4.4.1 Surface effects

During the annealing study on 0.5Y devices annealed in the vacuum oven it was shown that electropolishing of the devices resulted in improved expansion capabilities of the device. Without electropolishing post annealing in the vacuum furnace at 300°C for 30mins, all devices tested failed during expansion to 4mm from a crimped diameter of 1.5mm. Figure 5.12 shows that during manufacture of the devices cracks are formed in the oxide layer around the OD of

the device. Figure 5.18d shows that following electropolishing for 30s these cracks are fully removed and as a result devices manufactured from 0.5Y alloy wire, annealed at 300°C for 30mins, could inconsistently (3 of 5) survive expansion to 4mm, though in devices with no strut fractures cracks were still observed along the ID of the waves.

In contrast, 0.5Y devices annealed in the vacuum tube furnace were shown to be able to survive expansion to 4mm without complete strut fracture when not electropolished. However, it was shown that in these devices and those polished for only 20s (as opposed to the 30s applied for the bulk of expansion testing) cracking was observed along the ID of some waves in devices expanded to 4mm. This shows that the oxide layer present on the wire prior to manufacture of the device can lead to cracks forming during scaffold expansion. In the coarse-grained devices, annealed in the vacuum oven, it was shown that these cracks propagate through the complete strut, leading to complete device failure in all the devices tested. However, in the refined grained devices annealed in the vacuum tube furnace these cracks did not lead to any complete strut failures. The effect of grain size on device failure will be discussed further in Section 5.4.4.2.

In the 2Y devices (when annealed for optimal performance – 250°C for 10mins) and those 0.5Y devices when improperly annealed, complete strut fracture was still observed. As such device failure cannot be solely attributed to crack initiation within the oxide layer. However, it is shown that if the complete oxide layer is not removed it can increase the likelihood of cracks developing along the ID of the waves, which will likely compromise the structural integrity of the device and accelerate failure due to fatigue. Therefore, electropolishing is a key step in the design of these devices. However, failure is still observed in the 2Y devices that cannot be attributed to improper polishing conditions alone.

5.4.4.2 Grain size

From the work conducted across the two annealing studies, there was a clear difference observed in the grain size of devices annealed in the vacuum oven and tube furnace, consequently leading to variation in device performance. In the 0.5Y devices treated in the vacuum oven, the struts of the waveform and neutral access of the wave had a refined grain size whilst coarse grains developed either side of this refined band. In the 0.5Y and 2Y devices treated in the vacuum tube furnace, a refined grain structure was maintained through the entire waveform with a skin of coarser grains around the wires surface.

From investigation of the expansion capabilities of each device, conclusions can be drawn on the influence of grain size on device performance. Firstly, no complete strut fractures were

observed in the 0.5Y device heat treated in the vacuum tube furnace, including when manufactured and tested without an electropolishing procedure conducted post annealing. Figure 5.20 did show however that cracking was apparent along the ID of the waves in the 0.5Y devices treated in the vacuum tube furnace without an electropolishing procedure conducted. These cracks are assumed to be caused by the oxide layer as they are not present in the devices electropolished for 30s. With cracks forming within the oxide layer of unpolished 0.5Y devices treated in the vacuum oven and vacuum tube furnace but failure only occurring in the coarse grained 0.5Y device treated in the vacuum oven, the influence coarse grains have on crack propagation should be considered.

Owing to the Hall-Petch effect, where the mechanical properties of a metal are increased with refined grain size, it can be assumed the coarse grained, vacuum oven annealed 0.5Y devices will have reduced ductility compared to the devices annealed in the tube furnace.[215] However, when electropolished, these devices can inconsistently survive expansion to 4mm. Which suggests the alloy is sufficiently ductile to survive expansion. Owing to the coarse grains the device will naturally have fewer and larger grain boundaries. Grain boundaries can act as both an easy path for crack initiation and propagation, and as barriers to crack propagation from the interior of grains.[216] As such in the coarse-grained device, there are fewer boundaries to suppress crack propagation from the interior of grains and should cracks develop along the large grain boundaries (that in some cases are close to half the diameter of the wire) they will have an easy path to propagate along. In the refined grained device, the increased number of grain boundaries will act to impede crack growth. As such rapid crack propagation along the large grain boundaries in the 0.5Y device treated in the vacuum oven may be responsible for their failure when not electropolished. However, when electropolished it was shown that inconsistent expansion to 4mm from the crimped state can be achieved in the 0.5Y devices treated in the vacuum oven, meaning device fracture cannot be attributed solely to surface effects and coarse grains.

Further, a study by Tian et al.[217] revealed how an uneven grain size distribution in a Mg alloy led to the concentration of deformation within the small grains, resulting in intergranular fracture occurring at the boundaries between the large and small grains. The authors noted that cracking at the interface between small and coarse grains was increased when there was a large misorientation between the two grains, as slip within the small grains will not be easily transmitted into the neighbouring coarse grains.[217] Consequently, in the coarse skin developed

around the surface of the 0.5Y and 2Y devices treated it is shown that both of these conditions are met, where large coarse grains are developed adjacent to more refined grains with approximately a 90° misorientation. Figure 5.37 shows a kernel average misorientation (KAM) map (where a higher KAM corresponds to a higher dislocation density) of the 2Y device following expansion to 3mm. It can be seen that there is a higher dislocation density within the regions of refined grains about both the OD and ID of the device compared to the coarser grains. Considering that the coarser grains are further from the centreline of the waveform, it would be expected that they would undergo increased deformation compared to the regions of refined grains closer to the centreline of the waveform. Therefore this agrees with Tian et al.[217] that the dislocation density is increased within the smaller grains, leading to uneven strain distribution at the interface between the small and refined grains. Therefore, despite failure not being observed in the 0.5Y device annealed in the tube furnace the presence of this uneven microstructure may contribute to early failure in the 2Y device and may limit the performance of the 0.5Y device should more extreme loading cycles (i.e. reduced crimped diameter) be applied.

5.4.4.3 Texture

EBSD analysis was only conducted on the devices heat treated in the vacuum tube furnace, where a transverse basal texture was developed along the OD of the waves whilst along the ID the basal plane was rotated ≈90° relative to the OD texture. The formation of different textures along the OD and ID of the devices was discussed in detail in Section 5.4.3.2 however the consequences these textures will have on the deformation of the device was only briefly described.

Owing to the differences in texture along the ID and OD of the waveforms they will experience different loading relative to their c-axis during the crimping and expansion processes, this is represented in Figure 5.38. During crimping of the devices, the ID of the wave is loaded in compression whilst the OD is in tension, Figure 5.38a. Owing to the different textures developed along the ID and OD this loading regime results in the c-axis of grains along both the ID and OD being loaded in compression. Thus, tensile twinning will be restricted and consequently Mg alloys typically loaded in this manner have reduced ductility.[218] The tensile testing conducted as

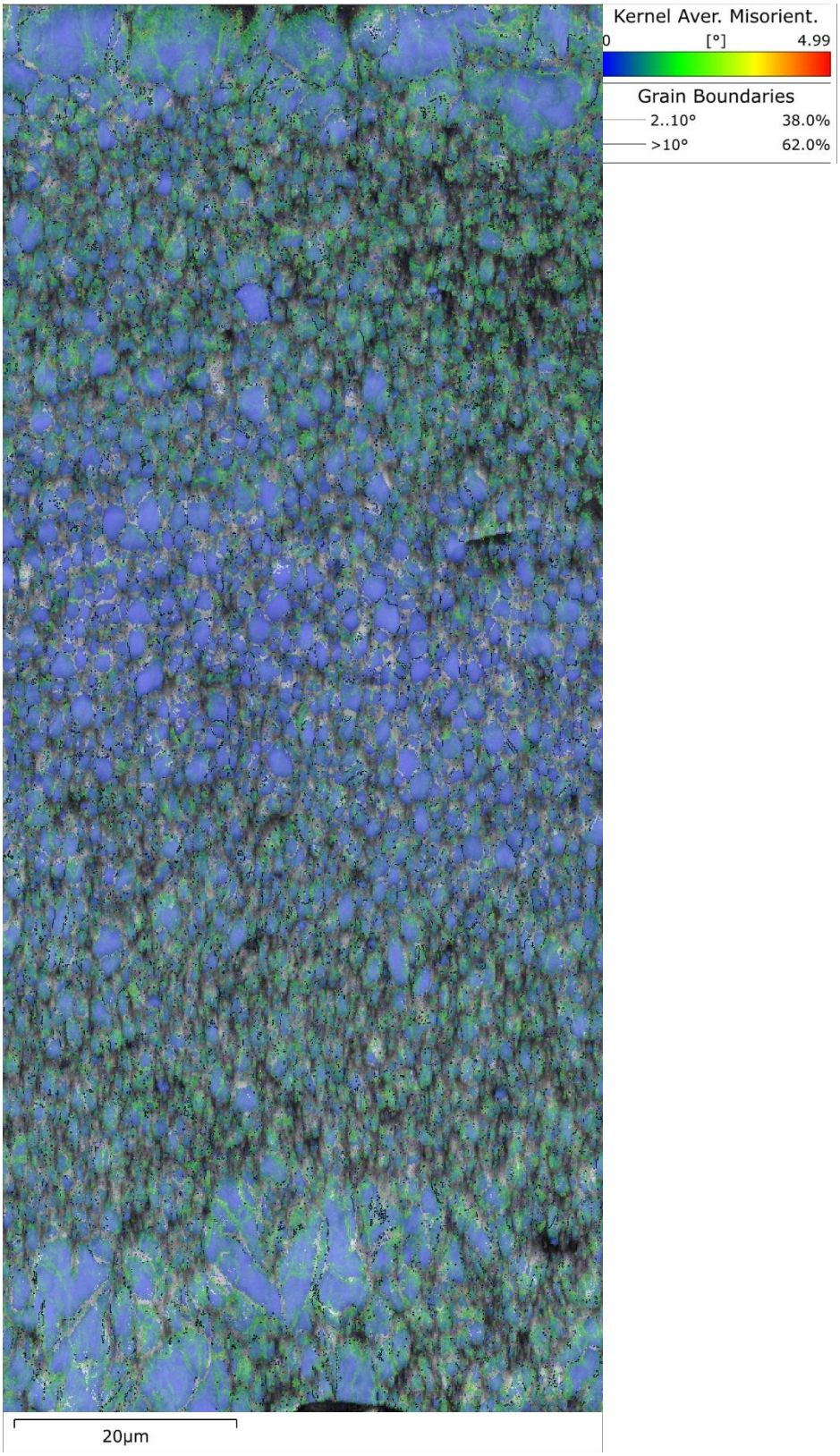

Figure 5.37: KAM map of the 2Y device following expansion to 3mm

part of this work loaded the grains in a similar manner to that expected about the OD of the wire and as such it can be assumed that the results obtained from tensile testing will appropriately

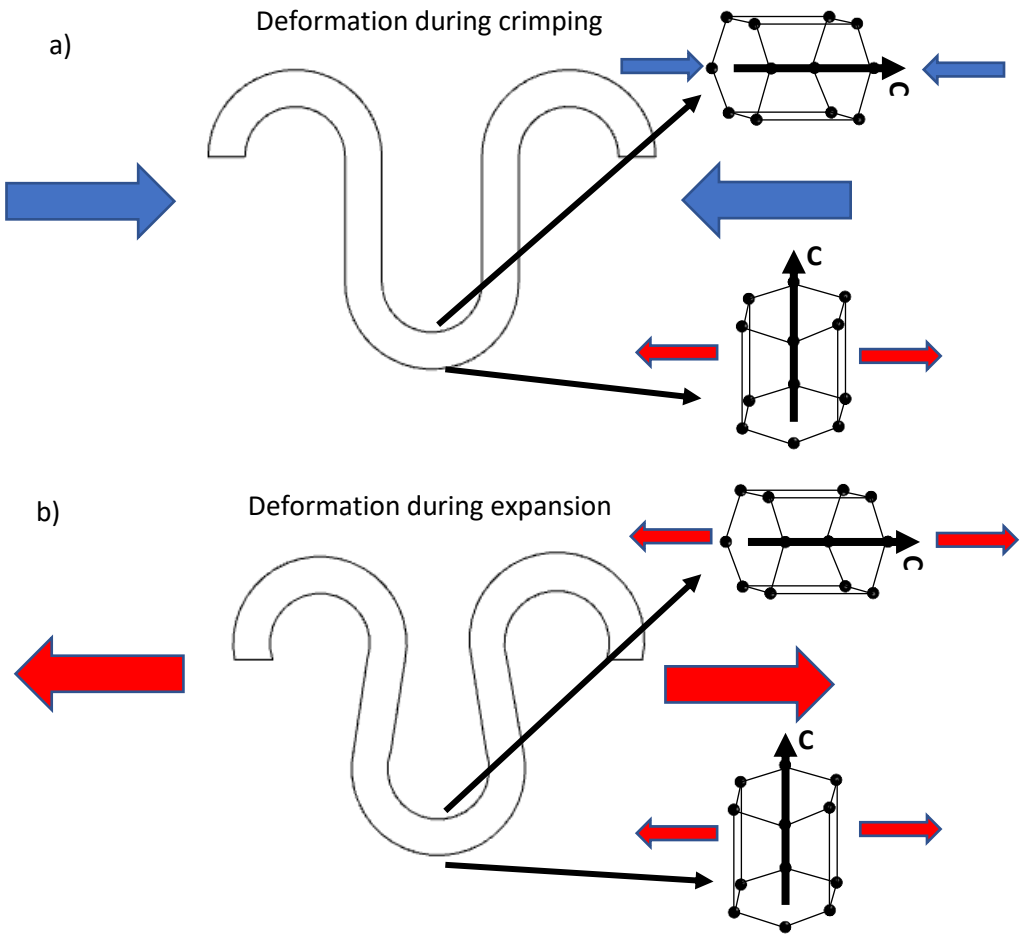

Figure 5.38: Loading of the c-axis during a) crimping b) expansion

represent the behaviour of the wire along its OD. Owing to the anisotropic properties of Mg, the tensile tests will not appropriately represent the behaviour along the ID. Compression testing of the alloy wire perpendicular to its DD would be required to accurately represent the loading occurring along the ID of the wire, however for such fine wire, this testing is not possible. The loading regime experienced by the grains along the OD and ID will both limit the activation of basal slip and tensile twinning. However, the grains along the OD of the wire are favourably aligned for prismatic slip, whereas along the ID prismatic slip will be restricted. Figure 5.39 shows that the Schmid factor for basal slip is similar through the entire cross-section of the waveform. However, along the OD of the wave the grains are loaded more favourably for the activation of prismatic slip. Consequently, with fewer easily activated deformation mechanisms along the ID, cracking will be more likely during crimping, compared to the OD.

During expansion the loading along the ID of the devices will be different to that experienced during crimping. The loading experienced by the crimped devices during expansion is represented in Figure 5.38b. As can be seen, the ID and OD are both loaded in tension, meaning

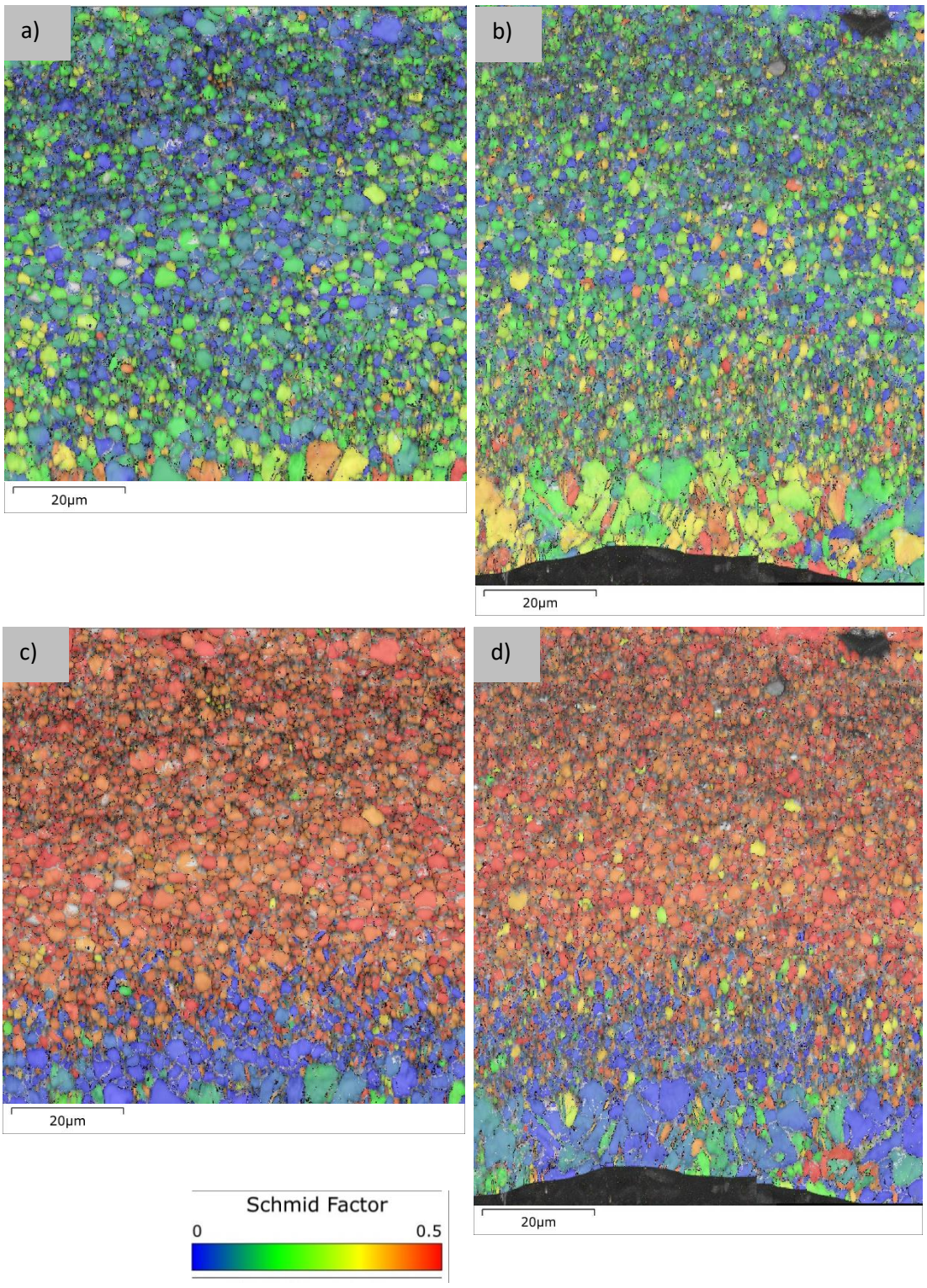

Figure 5.39: Schmidt factor colouring during loading along the x-axis for the as manufactured devices of both alloys for a) basal slip in the 0.5Y device b) basal slip in the 2Y device c) prismatic slip in the 0.5Y device d) factor prismatic slip in the 2Y device

that the loading along the OD is the same as what is experienced during crimping. Along the ID, the loading is reversed compared to that during crimping, meaning the grains are loaded in

tension, parallel to their c-axis. Compared to the compressive loading experienced during crimping this loading will promote the activation of tensile twinning. However, similarly to the crimping stage, the activation of basal and prismatic slip along the ID is limited, as shown by their relatively low Schmid factors in Figure 5.40. Consequently, it would be expected that with restricted prismatic slip along the ID of waves, that ductility would be reduced and as such could be a contributing factor in why failure is observed initiating along the ID of waves. Although, as the 0.5Y devices, when annealed for optimal expansion capabilities, do not fracture, this texture split cannot be fully responsible for the fractures seen in the 2Y device. However, the texture developed along the ID is undesirable for ductility and even although it does not cause failures in the 0.5Y device, it will affect the performance of the device and may play a role in the fractures observed when crimped down to an ID of 1mm. The texture developed along the ID of the waveform in the 0.5Y device will limit the ability to undergo more extreme loading cases and consequently considerations should be made on how alloy design and processing of the device could be altered to prevent this shift in texture along the ID of devices.

5.4.4.4 Secondary Phase Particles

It was shown that both alloy wires used to manufacture the devices contained secondary phase particles with an increased number present in the 2Y alloy wire. These particles remained in the final device, with Figure 5.24 showing that the 2Y devices contained a large number of these particles distributed throughout the matrix. Secondary phase particles are, generally, associated with strengthening and reduced ductility, as they act as obstacles for dislocation motion.[219] Dislocations can pile up at secondary phase particles, meaning they can effectively act as stress concentration sites, which can lead to crack initiation.[220]

Investigation of the microstructure of the 2Y devices found evidence of cracks initiating close to secondary phase particles. Considering that the 2Y device developed a relatively similar microstructure to the 0.5Y devices in terms of grain size and texture but did contain an increased number of secondary phase particles it may suggest that these particles play a key role in the failure of the 2Y devices. However, it was shown that 2 in 3, 2Y devices treated in the vacuum tube furnace could survive expansion to 4mm. This demonstrates that despite the high number of particles developed in the devices, failure does not always occur during expansion and consequently it cannot be said that the high density of these particles in the 2Y devices, alone, explains the failures observed.

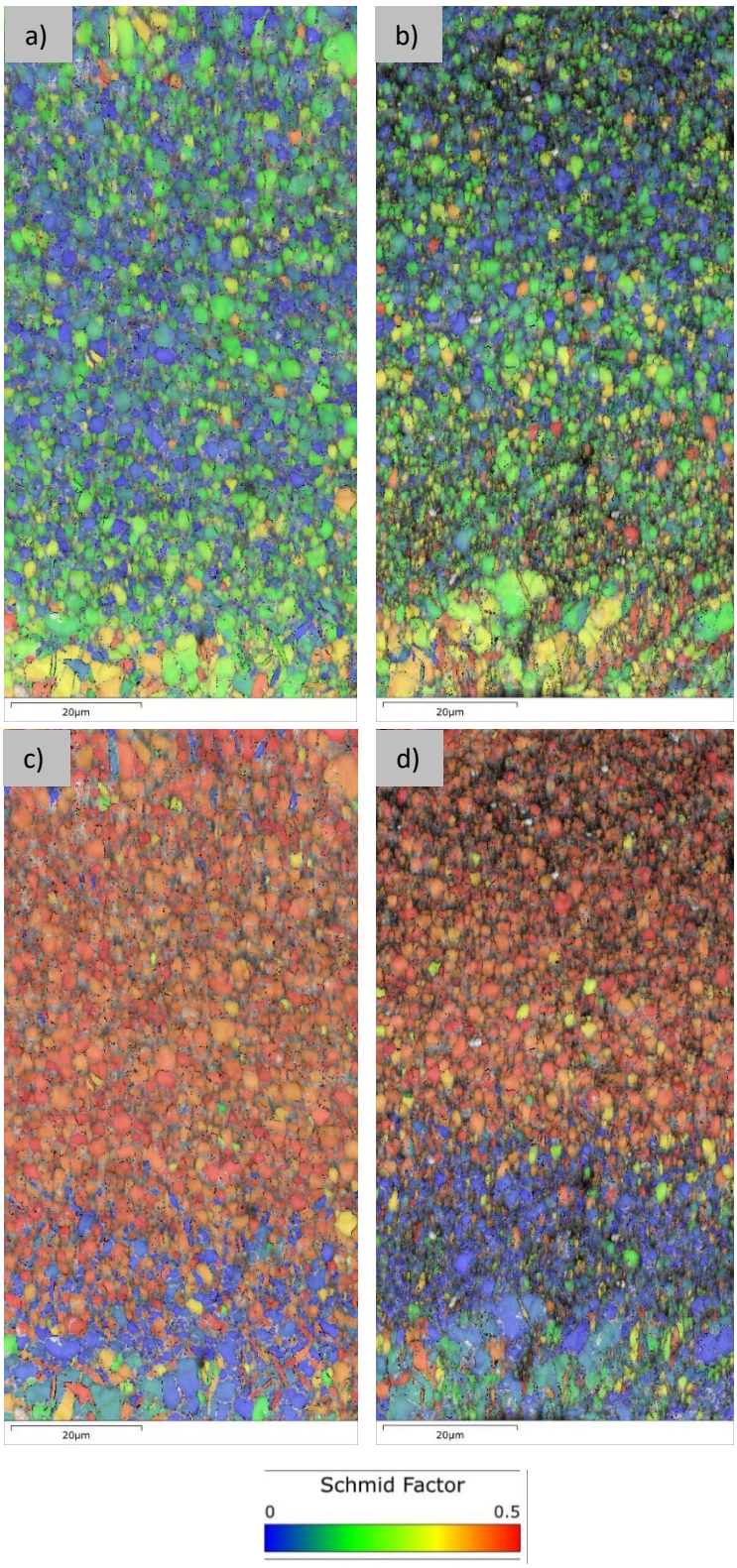

Figure 5.40: Schmidt factor colouring during loading along the x-axis for the crimped devices of both alloys for a) basal slip in the 0.5Y device b) basal slip in the 2Y device c) prismatic slip in the 0.5Y device d) prismatic slip in the 2Y device

5.4.5 Radial Force

Radial force testing found that only the devices annealed in the vacuum tube furnace could achieve a radial force greater than 1N/mm. The 0.5Y alloy devices annealed in the vacuum oven had radial force values of 0.58 and 0.75N/mm when expanded to 3 and 3.5mm respectively. In contrast the 0.5Y alloy devices treated in the vacuum tube furnace that had a radial force of 1.15 and 1.32N/mm at diameters of 3 and 3.5mm respectively. The relatively, low radial force of the devices treated in the vacuum oven was attributed to the large grains present around the peak of the waveform. Consequently, the higher strength of the devices treated in the vacuum tube furnace is attributed to the more refined grain structure developed. At a diameter of 3mm, the 2Y alloy devices treated in the vacuum tube furnace exhibited similar strength to the 0.5Y at 3mm. However, it was shown that when expanded to 3.5mm, the 2Y device exhibited higher radial force than the 0.5Y device expanded to the same diameter. It is unexpected that the 2Y device would exhibit higher force than the 0.5Y device at only one diameter.

5.5 Conclusion

At the outset of this chapter two criterion for device performance were set, to indicate they were suitable for the treatment of BTK arteries. Firstly, the devices had to be capable of surviving expansion to an ID of 4mm from a crimped ID of 1.5mm. Exhibiting a similar performance to the Magmaris device which exhibited consistent expansion to 4mm for their device with 3mm nominal diameter during benchtop testing.[210] Also, at their nominal diameter (3mm) they were required to have a radial force of at least 1N/mm. It was found that only devices manufactured from 0.5Y alloy wire and heat treated in the vacuum tube furnace were capable of achieving both of these criteria. Devices manufactured from the 2Y alloy wire could achieve inconsistent expansion to 4mm, with 2 in 3 devices surviving expansion to 4mm. However, the 2Y devices did meet the radial force criteria set whilst the 0.5Y devices treated in the vacuum oven did not meet either criterion.

One of the key findings of this chapter was the shift in texture developed along the ID of the devices. It was shown that the transverse basal texture present in the wire was maintained around the OD of the waveforms of devices manufactured from both alloy wires. However, around the ID a rotation of ≈90° of the grains occurred, with the basal plane aligning perpendicular to the DD of the wire. This was attributed to the deformation during forming of the waveforms being dominated by tensile twinning, and the recrystallised grains developed

during annealing, maintaining the texture of the deformed microstructure. The texture developed along the ID will restrict the activation of prismatic slip during crimping and expansion of the device, consequently increasing the likelihood of fracture along the ID of the waveforms. In all devices that showed signs of cracking during expansion, the cracks were observed along the ID of waves. However, this split in texture was present in the 0.5Y devices annealed for optimal expansion capabilities in the vacuum tube furnace, that were shown to be capable of consistent expansion to 4mm. Consequently, failure in the 0.5Y devices treated in the vacuum oven and the 2Y devices cannot solely be attributed to this shift in texture.

The microstructural investigation of the 0.5Y and 2Y devices annealed in the vacuum tube furnace revealed they both developed similar microstructures, in terms of grain size and texture. However, the 2Y device contained an increased number of secondary phase particles. Cracks were observed close to these secondary phase particles in the 2Y device, indicating their contribution to the failure of these devices. Although, as the failure of the 2Y devices was inconsistent and 2 in 3 devices survived expansion to 4mm, it cannot be stated that the high density of particles, alone, is responsible for failure, as it would be expected that all of the 2Y devices would fail. However, SEM analysis of the 2Y devices, did reveal the presence of a large coarse particle present in the microstructure of an unexpanded device. Voids were observed either side of the coarse particle, that would act as favourable sites for crack initiation. With an increased number of particles present in the 2Y device, it can be expected that there is increased likelihood of large, coarse particles being present in the microstructure. If these particles are present close to the regions of the device that experience the highest strains during deployment such as along the ID of the waveform, it follows that failure will be initiated from these regions.

It is therefore proposed that the failure seen in these devices is attributed to some combination of the altered texture, secondary phase particles and coarse grains. These factors may all play a role in the fracture of these devices. The texture developed along the ID of the devices will limit the activation of basal and prismatic slip during expansion. Cracks will initiate close to coarse secondary phase particles owing to their high density, and lack of available deformation mechanisms to overcome these barriers. Finally, the coarse grains present on the wire's surface result in large grain boundaries that allow for easy propagation of cracks initiated close to secondary phase particles. Therefore, if one of these contributing microstructural features could be improved it may result in the 2Y devices being capable of expansion to 4mm. Potential steps to address these microstructural features will be described in more detail in Chapter 6.

Chapter 6: Conclusions and Recommendations

This work presented herein investigated two new Mg-Li-Y alloy wires and their application in the manufacture of a novel wire form BVS scaffold. The two alloy wires were provided cold drawn to a diameter of 125µm and a series of annealing treatments were conducted to maximise their ductility. The alloy wires were characterised through investigation of their microstructure and mechanical properties. Following this, both alloy wires were applied in the manufacture of a new wire form BVS device and their performance characterised and microstructure investigated. From these studies, an optimised annealing protocol was developed for both alloy wires using the bespoke vacuum tube furnace, designed, and manufactured as part of this research programme. Characterisation of the microstructure and mechanical properties of the two new alloy wires identified them as suitable new materials for application in BVS technology owing to their relatively high ductility and strength. Application of both alloys in the novel wire form BVS and optimisation of the processing applied during manufacture demonstrated that the 0.5Y device exhibits comparable performance, during benchtop testing, to the current best in class Mg based BVS devices available on the market.

This chapter summarises the key conclusions found during this work. Based on these conclusions, a series of recommendations is provided to further understand the underlying mechanisms behind both alloy wires behaviour and further advance the development the BVS device investigated as part of this work.

6.1 Conclusions

- During annealing of the two cold drawn alloy wires, recrystallisation initiates first from regions close to the OD of the wires and progresses towards the wire core as recrystallisation progresses. This is attributed to the regions of wire closest to the surface undergoing increased deformation during the cold drawing process resulting in increased internal strain (and hardness) of these regions compared to the wire core. As internal strain acts as the driving force for recrystallisation, it follows that recrystallisation will initiate first close to the OD of the wire and progress towards its core.

- Both alloys develop a basal texture following annealing, however a weaker basal texture is developed in the 2Y alloy wire compared to the 0.5Y alloy. This shows that there is sufficient Y content in the 2Y alloy wire to activate texture weakening however the RE texture, associated with many MgRE alloys, is not observed to develop in either alloy.
- The increased Y content restricts abnormal grain growth at higher temperatures. During annealing at high temperatures (>400°C) abnormal grain growth is observed in the 0.5Y alloy wire, whilst the 2Y alloy wire maintains a more homogeneous grain size distribution. The underlying mechanism behind this behaviour was not identified but may be attributed to both the increased number of Y-rich secondary phase particles and Y in solution restricting boundary mobility during thermal processing.
- Despite the weaker texture and increased number of secondary phase particles developed in the 2Y alloy wire, both alloys exhibit relatively similar mechanical properties following annealing for optimal ductility. When annealed for maximum ductility in the vacuum tube furnace (250°C for 30mins) the 0.5Y alloy wire has an elongation to failure, YS and UTS of 20.3±0.4%, 133±2.6MPa, and 196 ±0.8MPa respectively. Whilst the 2Y alloy wire has an elongation to failure, YS and UTS of 19.7±1.1%, 150±2.0MPa, and 207±0.4MPa respectively following annealing for 30mins at 300°C. Both alloy wires can survive idealised bending strains of 48%. This shows that the weaker texture developed in the 2Y alloy wire does not translate to improved ductility. The 2Y wire exhibits slightly increased strength compared to the 0.5Y alloy wire. However, the increase is relatively small meaning that the increased number of secondary phase particles in the 2Y alloy wire does not result in a significant strengthening effect. Both alloys exhibit comparable mechanical properties to similar alloys being developed for BVS technology and as such are identified as suitable materials for application in bioresorbable medical devices.
- A split in texture is developed through the waveform of devices manufactured from both alloy wires, post annealing in the vacuum tube furnace. Along the OD of the waveform the transverse basal texture of the as supplied wire is maintained. Along the ID of the waveform the basal plane is rotated by approximately 90°, aligning itself to be perpendicular to the DD of the wire. This texture split is attributed to the deformation along the ID of the waves, likely, being dominated by tensile twinning, which results in the reorientation of the basal plane by 86°. The recrystallised texture is subsequently

dominated by grains nucleated from within these twins, along the ID of the wire, which grow with the same orientation as the deformed microstructure.

- Fracture of devices is observed to initiate from the ID of the waveforms at their apex. Only devices manufactured from the 0.5Y alloy wire and heat treated at 250°C for 10mins in the vacuum tube furnace, consistently survive expansion from a crimped ID of 1.5mm to an ID of 4mm. Inconsistent expansion of the 2Y devices (following annealing at 250°C for 10mins) is achieved, however, 1 in 3 devices fail during expansion. Both the 0.5Y and 2Y devices develop relatively similar microstructures in terms of grain size and texture, however the 2Y device contains an increased number of secondary phase particles. Cracking is observed close to these particles in the 2Y devices. Although, as inconsistent expansion to 4mm of the 2Y devices can be achieved, device failure cannot be attributed to the high density of secondary phase particles alone.
- The texture developed along the ID of waves along with the high density of secondary phase particles and layer of coarse grains around the wires surface are all expected to contribute to the failure of devices. The texture developed will limit the activation of prismatic slip during the crimp and expansion process. Coarse secondary phase particles will act as stress concentration sites. Once cracking occurs close to these particles the coarse grain boundaries offer any easy propagation path. Each of these factors will influence failure of the devices and should one contributing factor be resolved improved device performance could be achieved.
- The 0.5Y devices are capable of consistent expansion to 4mm and have a radial force of greater than 1N/mm at their nominal diameter. These devices exhibit comparable mechanical performance to current BVS technologies available. Consequently, of the two alloys investigated in this work the Mg-4Li-0.5Y alloy is recommended for application in the manufacture of the novel BVS device under investigation. Devices manufactured from the Mg-4Li-0.5Y alloy should be investigated further through in *vivo* studies where the biocompatibility and degradation profile of the alloy/device can be better understood.

6.2 Recommendations

This work has demonstrated that the two alloy wires under investigation have similar mechanical properties to current Mg alloy wires being developed for bioresorbable medical

devices. BVS devices manufactured from the 0.5Y alloy wire are shown to meet the required performance criteria set out at the start of the project. The investigations both answered many questions and revealed interesting avenues for future work, both in terms of device development and material investigation. The key packages of future work are described below. They are broken into alloy and device development, though of course alloy development will directly impact device performance.

6.2.1 Alloy Development

- Considering the high density of secondary phase particles in the 2Y alloy wire it would be beneficial to investigate the prior processing of the cold drawn alloy wires to understand at which stage these particles are developed. If this could be identified the processing could be appropriately altered to reduce the precipitation of Y-rich secondary phase particles. Two potential benefits of this are improved strengthening and reduced early fractures of the final device. Firstly, it was shown that despite the high density of these particles in the 2Y alloy wire, in its cold drawn state and when annealed for optimal ductility, it exhibits similar strength to the respective 0.5Y alloy wires. Thus, these particles provided little, to no strengthening effect. Y is known to be one of the most effective solid solution strengtheners in Mg alloys, meaning if increased Y could be maintained in solution, it may lead to strengthening of the alloy wire. Further, cracking was identified initiating close to these secondary phase particles in the final device, whilst large coarse particles were observed in the microstructure that left voids. It follows that if a reduced number of particles were present, as in the 0.5Y alloy wire, cracking (and hence early failure) in the final device would be reduced.
- The work identified that a weaker basal texture was developed in the 2Y alloy wire compared to the 0.5Y alloy. Considering the literature, it would be of interest to investigate an alloy with an Y content closer to the limiting range for texture weakening (≈0.6wt%). Although the alloys investigated in this work contain less Y than the widely applied WE43 alloy there is still preference for bioresorbable metals to have as little REE content as possible. Though weakening of the texture was not shown to be beneficial in this work, it is expected that weakened texture may improve the 2Y alloy wire's performance in the final device if the other factors limiting its application could be improved. Therefore, if weakening of the texture could be achieved with lower Y

content, the performance of the wire in the final device may be improved whilst the REE content will be minimised.

- It would be of benefit to investigate the effects of increasing the Li content to close to 5.5wt%. It is expected that increasing the Li content will improve ductility but reduce strength. With the alloy wires exhibiting relatively high strength there may be some benefit in increasing the Li content to achieve ductility enhancement if the trade off in strength is not substantial. It is recommended to not go beyond 5.5wt% Li as above this threshold a Li rich phase will develop that is generally associated with decreased corrosion resistance despite offering improved ductility.
- Characterisation of the alloy wires supplied with a final annealing step post cold drawing, that are used in the manufacture of the final devices, were shown to have a layer of coarse grains about their outer diameter. Steps should be taken to investigate the origin of this layer. As was demonstrated with the annealing studies conducted in this work, a process can be developed where this layer is not formed. As coarse grains and inhomogeneous microstructures are associated with increased likelihood of cracking it may lead to improved device performance should this layer be removed.
- Finally, this work optimised an annealing procedure for each cold drawn alloy wire and characterised their microstructures. Key microstructural differences were observed between the annealed alloy wires produced as part of this work and those supplied from the manufacturer. Limitations in the bespoke furnace setup meant that a sufficient length of cold drawn wire could not be annealed in the vacuum tube furnace to manufacture a complete device. If this could be achieved it would be of benefit to apply the alloy wires, post annealing in the vacuum tube furnace, in the manufacture of the BVS device. If this were conducted it would be expected that devices could be produced without a layer of coarse grains about the wire surface, potentially leading to improved device performance.

6.2.2 Device

- Repeat radial force testing should be conducted to ensure the repeatability of the tests conducted.
- It was demonstrated that the 0.5Y devices could be repeatedly expanded to 4mm from an ID of 1.5mm. Although suitable for progressing the design towards pre-clinical animal trials it would be beneficial to investigate the minimum diameter these devices could be

crimped to and achieve consistent expansion as minimising the crossing profile of devices will improve deliverability.

- The texture developed along the ID of the alloy wires was attributed to recrystallisation being dominated by grains nucleated from tensile twins, maintaining their orientation. It would be of interest to confirm this through investigation of the deformed microstructure to identify if deformation was dominated by tensile twinning.
- The texture developed along the ID of the devices is expected to be less favourable for ductility and consequently device performance. Methods should be investigated to prevent this texture developing along the ID of the final device. One method would be to investigate manufacturing the devices at elevated temperatures. It is known that the CRSS of deformation twinning is independent of temperature whereas slip is thermally activated. Therefore, if the devices were manufactured at elevated temperatures, deformation via slip would increase and consequently reduce the activation of deformation twinning.
- Owing to the pulsatile nature of the arteries, where BVS devices will be deployed, a study into the fatigue life of these devices should be conducted. As BVS devices are temporary in nature, they are not required to remain in situ for the remainder of a patient's life as with permanent stents. However, a fatigue study on the final device should be run to understand the response of the device to the cyclic loading expected in *vivo* to ensure it can maintain structural integrity post deployment.
- Within the alloying limits investigated in this work these alloys are assumed to be safe in *vivo* however biocompatibility testing should be conducted to ensure this is the case. This could first begin with in *vitro* cytotoxicity tests and progress through to small animal studies to better understand the in *vivo* response of these alloy wires. These tests could initially be run on the individual alloy wires. The final progression would be to advance the final BVS device towards a pre-clinical animal trial, preferably in a porcine model, to best understand the biocompatibility of the device. From this study information will also be gained on the corrosion rate and mechanical response of the final device in *vivo* and help provide the necessary data to progress to first-in-man clinical trials.
- This work has demonstrated that devices manufactured from the 0.5Y alloy wire exhibit similar mechanical performance to comparable devices. Therefore, the next stage of device development should investigate the biocompatibility and in *vivo* corrosion response of this alloy through a pre-clinical animal trial. The 2Y alloy wire should also be

investigated as, if the limitations identified in this work can be resolved, through the above recommendations, it may demonstrate improved corrosion resistance compared to the 0.5Y alloy wire.

References

1. Roth GA, Mensah GA, Johnson CO, et al. Global Burden of Cardiovascular Diseases and Risk Factors, 1990-2019: Update From the GBD 2019 Study. *J Am Coll Cardiol*. 2020; 76: 2982-3021.
2. Mohebi R, Chen C, Ibrahim NE, et al. Cardiovascular Disease Projections in the United States Based on the 2020 Census Estimates. *Journal of the American College of Cardiology*. 2022; 80: 565-78.
3. Khera R, Valero-Elizondo J and Nasir K. Financial toxicity in atherosclerotic cardiovascular disease in the united states: Current state and future directions. *J Am Heart Assoc*. 2020; 9: e017793-e.
4. Frostegård J. Immunity, atherosclerosis and cardiovascular disease. *BMC Med*. 2013; 11: 117-.
5. Plutzky J. The vascular biology of atherosclerosis. *Am J Med*. 2003; 115: 55-61.
6. Crowther MA. Pathogenesis of atherosclerosis. *Hematology Am Soc Hematol Educ Program*. 2005; 2005: 436-41.
7. Strong JP, Malcom GT, McMahan CA, et al. Prevalence and Extent of Atherosclerosis in Adolescents and Young Adults: Implications for Prevention From the Pathobiological Determinants of Atherosclerosis in Youth Study. *JAMA*. 1999; 281: 727-35.
8. Warboys CM, Amini N, De Luca A and Evans PC. The role of blood flow in determining the sites of atherosclerotic plaques. *F1000 Med Rep*. 2011; 3: 5.
9. Smedby O. Geometric risk factors for atherosclerosis in the aortic bifurcation: A digitized angiography study. *Ann Biomed Eng*. 1996; 24: 481-8.
10. Singh RB, Mengi SA, Xu Y-J, Arneja AS and Dhalla NS. Pathogenesis of atherosclerosis: A multifactorial process. *Exp Clin Cardiol*. 2002; 7: 40-53.
11. Insull WMD. The Pathology of Atherosclerosis: Plaque Development and Plaque Responses to Medical Treatment. *Am J Med*. 2009; 122: S3-S14.
12. Napoli C, Crudele V, Soricelli A, et al. Primary prevention of atherosclerosis: A clinical challenge for the reversal of epigenetic mechanisms? *Circulation*. 2012; 125: 2363-73.
13. Canfield J and Totary-Jain H. 40 years of percutaneous coronary intervention: History and future directions. *J Pers Med*. 2018; 8: 33.
14. Barton M, University of Zürich S, barton@access.uzh.ch, et al. Balloon Angioplasty – The Legacy of Andreas Grüntzig, M.D. (1939–1985). *Frontiers in Cardiovascular Medicine*. 2014; 1.
15. Iqbal J, Gunn J and Serruys PW. Coronary stents: historical development, current status and future directions. *British Medical Bulletin*. 2013; 106: 193-211.
16. Sigwart U, Puel J, Mirkovitch V, Joffre F and Kappenberger L. Intravascular stents to prevent occlusion and restenosis after transluminal angioplasty. *N Engl J Med*. 1987; 316: 701-6.
17. Serruys PW, Strauss BH, Beatt KJ, et al. Angiographic Follow-up after Placement of a Self-Expanding Coronary-Artery Stent. *N Engl J Med*. 1991; 324: 13-7.
18. Moore WS, Ahn SS and Elsevier. *Endovascular surgery*. 4th edition ed. Philadelphia: Philadelphia : Elsevier/Saunders, 2011.
19. Hassan S, Ali MN and Ghafoor B. Evolutionary perspective of drug eluting stents: from thick polymer to polymer free approach. *J Cardiothorac Surg*. 2022; 17: 65-.
20. Caixeta A, Leon MB, Lansky AJ, et al. 5-Year Clinical Outcomes After Sirolimus-Eluting Stent Implantation. Insights From a Patient-Level Pooled Analysis of 4 Randomized Trials

Comparing Sirolimus-Eluting Stents With Bare-Metal Stents. *J Am Coll Cardiol*. 2009; 54: 894-902.
21. Bangalore S, Toklu B, Amoroso N, et al. Bare metal stents, durable polymer drug eluting stents, and biodegradable polymer drug eluting stents for coronary artery disease: mixed treatment comparison meta-analysis. *BMJ*. 2013; 347: f6625-f.
22. Bangalore S, Toklu B, Patel N, Feit F and Stone GW. Newer-Generation Ultrathin Strut Drug-Eluting Stents Versus Older Second-Generation Thicker Strut Drug-Eluting Stents for Coronary Artery Disease: Meta-Analysis of Randomized Trials. *Circulation (New York, NY)*. 2018; 138: 2216-26.
23. Leone A, Simonetti F, Avvedimento M, et al. Ultrathin Struts Drug-Eluting Stents: A State-of-the-Art Review. *Journal of personalized medicine*. 2022; 12: 1378.
24. Sarno G, Lagerqvist B, Fröbert O, et al. Lower risk of stent thrombosis and restenosis with unrestricted use of 'new-generation' drug-eluting stents: A report from the nationwide Swedish Coronary Angiography and Angioplasty Registry (SCAAR). *Eur Heart J*. 2012; 33: 606-13.
25. Matsuoka EK, Hasebe T, Ishii R, Miyazaki N, Soejima K and Iwasaki K. Comparative performance analysis of interventional devices for the treatment of ischemic disease in below-the-knee lesions: a systematic review and meta-analysis. *Cardiovasc Interv and Ther*. 2021; 37: 145-57.
26. Liu X, Zheng G and Wen S. Drug-eluting stents versus control therapy in the infrapopliteal disease: A meta-analysis of eight randomized controlled trials and two cohort studies. *Int J Surg*. 2017; 44: 166-75.
27. Peige Song P, Diana Rudan MD, Yajie Zhu P, et al. Global, regional, and national prevalence and risk factors for peripheral artery disease in 2015: an updated systematic review and analysis. *The Lancet global health*. 2019; 7: e1020-e30.
28. Fowkes FGRP, Rudan DMD, Rudan IP, et al. Comparison of global estimates of prevalence and risk factors for peripheral artery disease in 2000 and 2010: a systematic review and analysis. *Lancet*. 2013; 382: 1329-40.
29. Beard JD. ABC of arterial and venous disease. Chronic lower limb ischaemia. *BMJ British medical journal (International ed)*. 2000; 320: 854-7.
30. Wolf YG, Kobzantsev Z and Zelmanovich L. Size of normal and aneurysmal popliteal arteries: A duplex ultrasound study. *J Vasc Surg*. 2006; 43: 488-92.
31. Lorbeer R, Grotz A, Dörr M, et al. Reference values of vessel diameters, stenosis prevalence, and arterial variations of the lower limb arteries in a male population sample using contrast-enhanced MR angiography. *PLoS One*. 2018; 13: e0197559-e.
32. Fok P-W and Lanzer P. Media sclerosis drives and localizes atherosclerosis in peripheral arteries. *PloS one*. 2018; 13: e0205599-e.
33. Rym El K, Marianne B and Peter AS. Progress on developing an effective below-the-knee drug-coated balloon. *Reviews in cardiovascular medicine*. 2021; 22: 585-95.
34. Konijn LCD, Wakkie T, Spreen MI, et al. 10-Year Paclitaxel Dose-Related Outcomes of Drug-Eluting Stents Treated Below the Knee in Patients with Chronic Limb-Threatening Ischemia (The PADI Trial). *Cardiovasc Intervent Radiol*. 2020; 43: 1881-8.
35. Randomized Controlled Trial of Acotec Drug-eluting Balloon Versus Plain Balloon for Below-the-knee Angioplasty. *Obesity, fitness, & wellness week*. 2020: 5047.
36. Data on Vascular Diseases and Conditions Described by Researchers at University of Colorado (Drug-eluting Balloons and Drug-eluting Stents In the Treatment of Peripheral Vascular Disease). 2019: 94.
37. Linn YL, Choke ETC, Yap CJQ, Tan RY, Patel A and Tang TY. Utility of sirolimus coated balloons in the peripheral vasculature – a review of the current literature. *CVIR Endovasc*. 2022; 5: 29-.

38. Nugraha HG, Hilman S, Santiana L, et al. Drug-Coated Balloon Versus Drug-Eluting Stent in Patients With Femoropopliteal Artery Disease: A Systematic Review and Meta-Analysis. *Vasc Endovascular Surg*. 2022; 56: 385-92.
39. Kim TI and Schneider PA. New Innovations and Devices in the Management of Chronic Limb-Threatening Ischemia. *J Endovasc Ther*. 2020; 27: 524-39.
40. Vanderland M, Ooi YS and Gray WA. Device profile of the tack endovascular system® for the treatment of peripheral arterial disease: overview of safety and efficacy. *Expert review of medical devices*. 2021; 18: 717-26.
41. Xiang P, Wenbo Q, Ying J, Yani W, Bo Y and Jinwei T. Bioresorbable Scaffolds: Contemporary Status and Future Directions. *Frontiers in cardiovascular medicine*. 2020; 7.
42. Kereiakes DJ, Onuma Y, Serruys P and Stone GW. Bioresorbable Vascular Scaffolds for Coronary Revascularization. *Circulation*. 2016; 134: 168-82.
43. Shibbani KK, Bagno LDLeSLDLeS, Poulin M-FM-F, et al. Pre-Clinical Comparative Assessment of a Dedicated Pediatric PLLA based Bioresorbable Scaffold with a Low Profile Bare Metal Stent. *Catheterization and cardiovascular interventions*. 2020; 96: 878-88.
44. Wright J, Nguyen A, D'Souza N, et al. Bioresorbable stent to manage congenital heart defects in children. *Materialia (Oxf)*. 2021; 16: 101078.
45. Shibbani K, Kenny D, McElhinney D, Hijazi ZM and Moran T. Identifying Gaps in Technology for Congenital Interventions: Analysis of a Needs Survey from Congenital Interventional Cardiologists. *Pediatr Cardiol*. 2016; 37: 925-31.
46. Jinnouchi H, Torii S, Sakamoto A, Kolodgie FD, Virmani R and Finn AV. Fully bioresorbable vascular scaffolds: lessons learned and future directions. *Nat Rev Cardiol*. 2019; 16: 286-304.
47. Ellis SG, Kereiakes DJ, Metzger DC, et al. Everolimus-Eluting Bioresorbable Scaffolds for Coronary Artery Disease. *N Engl J Med*. 2015; 373: 1905-15.
48. Haude M, Ince H, Kische S, et al. Sustained safety and clinical performance of a drug-eluting absorbable metal scaffold up to 24 months: pooled outcomes of BIOSOLVE-II and BIOSOLVE-III. *EuroIntervention*. 2017; 13: 432.
49. Pappalardo D, Mathisen Tr and Finne-Wistrand A. Biocompatibility of Resorbable Polymers: A Historical Perspective and Framework for the Future. *BIOMACROMOLECULES*. 2019; 20: 1465-77.
50. Ulery BD, Nair LS and Laurencin CT. Biomedical applications of biodegradable polymers. *J Polym Sci B Polym Phys*. 2011; 49: 832-64.
51. Ang HY, Bulluck H, Wong P, Venkatraman SS, Huang Y and Foin N. Bioresorbable Stents: Current and Upcoming Bioresorbable Technologies. *Int J Cardiol*. 2016; 228: 931-9.
52. Toong DWY, Toh HW, Ng JCK, et al. Bioresorbable polymeric scaffold in cardiovascular applications. *Int J Mol Sci*. 2020; 21: 3444.
53. Peng X, Qu W, Jia Y, Wang Y, Yu B and Tian J. Bioresorbable Scaffolds: Contemporary Status and Future Directions. *Front Cardiovasc Med*. 2020; 7: 589571.
54. McMahon S, Bertollo N, Cearbhaill EDO, et al. Bio-resorbable polymer stents: a review of material progress and prospects. *Progress in polymer science*. 2018; 83: 79-96.
55. Onuma Y, Dudek D, Thuesen L, et al. Five-year clinical and functional multislice computed tomography angiographic results after coronary implantation of the fully resorbable polymeric everolimus-eluting scaffold in patients with de novo coronary artery disease: The absorb cohort a trial. *JACC Cardiovasc Interv*. 2013; 6: 999-1009.
56. Serruys P, Ormiston J, van Geuns RJ, et al. A Polylactide Bioresorbable Scaffold Eluting Everolimus for Treatment of Coronary Stenosis 5-Year Follow-Up. *J Am Coll Cardiol*. 2016; 67: 766-76.

57. Ali ZA, Serruys PW, Kimura T, et al. 2-year outcomes with the Absorb bioresorbable scaffold for treatment of coronary artery disease: a systematic review and meta-analysis of seven randomised trials with an individual patient data substudy. *Lancet*. 2017; 390: 760-72.
58. Lafont A and Mennuni MG. What Happened to the Bioresorbable Scaffold Concept: Black Tide or Chernobyl? *Circ Cardiovasc Interv*. 2018; 11: e006283-e.
59. Kereiakes DJ, Ellis SG, Metzger DC, et al. Clinical Outcomes Before and After Complete Everolimus-Eluting Bioresorbable Scaffold Resorption: Five-Year Follow-Up From the ABSORB III Trial. *Circulation (New York, NY)*. 2019; 140: 1895-903.
60. Wu X, Wu S, Kawashima H, et al. Current perspectives on bioresorbable scaffolds in coronary intervention and other fields. *Expert review of medical devices*. 2021; 18: 351-66.
61. Ang HY, Huang YY, Lim ST, Wong P, Joner M and Foin N. Mechanical behavior of polymer-based vs. metallic-based bioresorbable stents. *Journal of thoracic disease*. 2017; 9: S923-S34.
62. Dandan X, Fan Y, Yufeng Z, Yunsong L and Yongsheng Z. Research status of biodegradable metals designed for oral and maxillofacial applications: A review. *Bioactive materials*. 2021; 6: 4186-208.
63. Peuster M, Wohlsein P, Brügmann M, et al. A novel approach to temporary stenting: degradable cardiovascular stents produced from corrodible metal—results 6–18 months after implantation into New Zealand white rabbits. *Heart*. 2001; 86: 563-9.
64. Zheng J-F, Xi Z-W, Li Y, et al. Long-term safety and absorption assessment of a novel bioresorbable nitrided iron scaffold in porcine coronary artery. *Bioact Mater*. 2022; 17: 496-505.
65. Carluccio D, Xu C, Venezuela J, et al. Additively manufactured iron-manganese for biodegradable porous load-bearing bone scaffold applications. *Acta Biomater*. 2020; 103: 346-60.
66. Salama M, Vaz MF, Colaço R, Santos C and Carmezim M. Biodegradable Iron and Porous Iron: Mechanical Properties, Degradation Behaviour, Manufacturing Routes and Biomedical Applications. *Journal of functional biomaterials*. 2022; 13: 72.
67. Gąsior G, Szczepański J and Radtke A. Biodegradable iron-based materials—what was done and what more can be done? *Materials*. 2021; 14: 3381.
68. Witte F. The history of biodegradable magnesium implants: A review. *Acta Biomater*. 2010; 6: 1680-92.
69. Zhang T, Wang W, Liu J, Wang L, Tang Y and Wang K. A review on magnesium alloys for biomedical applications. *Frontiers in bioengineering and biotechnology*. 2022; 10: 953344-.
70. Herber V, Okutan B, Antonoglou G, G Sommer N and Payer M. Bioresorbable Magnesium-Based Alloys as Novel Biomaterials in Oral Bone Regeneration: General Review and Clinical Perspectives. *J Clin Med*. 2021; 10: 1842.
71. Shukufe A and Masoud M. Biodegradable magnesium-based biomaterials: An overview of challenges and opportunities. *MedComm (2020)*. 2021; 2: 123-44.
72. Liu J, Liu B, Min S, et al. Biodegradable magnesium alloy WE43 porous scaffolds fabricated by laser powder bed fusion for orthopedic applications: Process optimization, in vitro and in vivo investigation. *Bioact Mater*. 2022; 16: 301-19.
73. Dambatta MS, Kurniawan D, Izman S, Yahaya B and Hermawan H. Review on Zn-Based Alloys as Potential Biodegradable Medical Devices Materials. *Applied Mechanics and Materials*. 2015; 776: 277-81.
74. Levy GK, Goldman J and Aghion E. The prospects of zinc as a structural material for biodegradable implants—a review paper. *Metals (Basel)*. 2017; 7: 402.

75. Mostaed E, Sikora-Jasinska M, Drelich JW and Vedani M. Zinc-based alloys for degradable vascular stent applications. *Acta Biomater*. 2018; 71: 1-23.
76. Venezuela J and Dargusch MS. The influence of alloying and fabrication techniques on the mechanical properties, biodegradability and biocompatibility of zinc: A comprehensive review. *ACTA BIOMATER*. 2019; 87: 1-40.
77. Hernández-Escobar D, Champagne S, Yilmazer H, Dikici B, Boehlert CJ and Hermawan H. Current status and perspectives of zinc-based absorbable alloys for biomedical applications. *ACTA BIOMATER*. 2019; 97: 1-22.
78. Li G, Yang H, Zheng Y, et al. Challenges in the use of zinc and its alloys as biodegradable metals: Perspective from biomechanical compatibility. *Acta Biomater*. 2019; 97: 23-45.
79. Jin H, Zhao S, Guillory R, et al. Novel high-strength, low-alloys Zn-Mg (<0.1wt% Mg) and their arterial biodegradation. *Mater Sci Eng C Mater Biol Appl*. 2018; 84: 67-79.
80. Drelich AJ, Zhao S, Guillory RJ, Drelich JW and Goldman J. Long-term surveillance of zinc implant in murine artery: Surprisingly steady biocorrosion rate. *Acta Biomater*. 2017; 58: 539-49.
81. Li HF, Xie XH, Zheng YF, et al. Development of biodegradable Zn-1X binary alloys with nutrient alloying elements Mg, Ca and Sr. *Sci Rep*. 2015; 5: 10719.
82. Hehrlein C, Schorch B, Kress N, et al. Zn-alloy provides a novel platform for mechanically stable bioresorbable vascular stents. *PLOS ONE*. 2019; 14: e0209111-e.
83. Peeters P, Bosiers M, Verbist J, Deloose K and Heublein B. Preliminary Results after Application of Absorbable Metal Stents in Patients with Critical Limb Ischemia. *J Endovasc Ther*. 2005; 12: 1-5.
84. Schranz D, Zartner P, Michel-Behnke I and Akintürk H. Bioabsorbable metal stents for percutaneous treatment of critical recoarctation of the aorta in a newborn. *Catheter Cardiovasc Interv*. 2006; 67: 671-3.
85. McMahon CJ, Oslizlok P and Walsh KP. Early restenosis following biodegradable stent implantation in an aortopulmonary collateral of a patient with pulmonary atresia and hypoplastic pulmonary arteries. *Catheter Cardiovasc Interv*. 2007; 69: 735-8.
86. Cerrato E, Barbero U, Gil Romero JA, et al. Magmaris™ resorbable magnesium scaffold: state-of-art review. *Future cardiology*. 2019; 15: 267-79.
87. Bennett J, De Hemptinne Q and McCutcheon K. Magmaris resorbable magnesium scaffold for the treatment of coronary heart disease: overview of its safety and efficacy. *Expert Rev Med Devices*. 2019; 16: 757-69.
88. Haude MP, Ince HP, Abizaid AMD, et al. Safety and performance of the second-generation drug-eluting absorbable metal scaffold in patients with de-novo coronary artery lesions (BIOSOLVE-II): 6 month results of a prospective, multicentre, non-randomised, first-in-man trial. *Lancet*. 2016; 387: 31-9.
89. Menze R and Wittchow E. In vitro and in vivo evaluation of a novel bioresorbable magnesium scaffold with different surface modifications. *J Biomed Mater Res B Appl Biomater*. 2021; 109: 1292-302.
90. Boeder NF, Dörr O, Koepp T, et al. Acute Mechanical Performance of Magmaris vs. DESolve Bioresorbable Scaffolds in a Real-World Scenario. *Frontiers in cardiovascular medicine*. 2021; 8: 696287-.
91. Gutiérrez-Barrios A, Gheorghe LL, Camacho Freire S, et al. Long-term clinical, angiographic, and optical coherence tomography findings of Mg-based bioresorbable scaffold in patients with acute coronary syndrome. *Catheter Cardiovasc Interv*. 2021; 98: E69-E77.
92. Hideo-Kajita A, Wopperer S, Seleme VB, Ribeiro MH and Campos CM. The development of magnesium-based resorbable and iron-based biocorrodible metal scaffold

technology and biomedical applications in coronary artery disease patients. *Applied sciences*. 2019; 9: 3527.
93. Haude M, Wlodarczak A, van der Schaaf RJ, et al. Safety and performance of the third-generation drug-eluting resorbable coronary magnesium scaffold system in the treatment of subjects with de novo coronary artery lesions: 6-month results of the prospective, multicenter BIOMAG-I first-in-human study. *EClinicalMedicine*. 2023; 59: 101940-.
94. Michael Haude AW, René J van der Schaaf, Jan Torzewski, Bert Ferdinande, Javier Escaned, Juan F Iglesias, Johan Bennett, Gabor G. Toth, Michael Joner, Ralph Toelg, Marcus Wiemer, Göran Olivecrano, Paul Vermeersch, Hector M. Garcia-Garcia, Ron Waksman. A new resorbable magnesium scaffold for de novo coronary lesions (DREAMS 3): one-year results of the BIOMAG-1 first-in-human study. *EuroPCR 2023*. Paris, France2023.
95. Zhou R, Roy A and Silberschmidt VV. A crystal-plasticity model of extruded AM30 magnesium alloy. *Computational materials science*. 2019; 170: 109140.
96. Agnew SR. *Deformation mechanisms of magnesium alloys-2*. Elsevier Ltd, 2012, p.63-104.
97. Hutchinson WB and Barnett MR. Effective values of critical resolved shear stress for slip in polycrystalline magnesium and other hcp metals. *Scripta materialia*. 2010; 63: 737-40.
98. Mises RV. Mechanik der plastischen Formänderung von Kristallen. *Z angew Math Mech*. 1928; 8: 161-85.
99. Martin G, Sinclair CW and Lebensohn RA. Microscale plastic strain heterogeneity in slip dominated deformation of magnesium alloy containing rare earth. *Materials Science & Engineering A*. 2014; 603: 37-51.
100. Martin G, Sinclair CW and Schmitt J-H. Plastic strain heterogeneities in an Mg–1Zn–0.5Nd alloy. *Scripta materialia*. 2013; 68: 695-8.
101. Orozco-Caballero A, Lunt D, Robson JD and Quinta da Fonseca J. How magnesium accommodates local deformation incompatibility: A high-resolution digital image correlation study. *Acta materialia*. 2017; 133: 367-79.
102. Ma Z-C, Tang X-Z, Mao Y and Guo Y-F. The plastic deformation mechanisms of hcp single crystals with different orientations: Molecular dynamics simulations. *Materials (Basel)*. 2021; 14: 1-16.
103. Becerra A and Pekguleryuz M. Effects of lithium, indium, and zinc on the lattice parameters of magnesium. *Journal of Materials Research*. 2008; 23: 3379-86.
104. Zeng Y, Jiang B, Yang QR, et al. Effect of Li content on microstructure, texture and mechanical behaviors of the as- extruded Mg- Li sheets. *Materials Science and Engineering A*. 2017; 700: 59-65.
105. Agnew SR, Horton JA and Yoo MH. Transmission electron microscopy investigation of ⟨c+a⟩ dislocations in Mg and α-solid solution Mg-Li alloys. *Metall and Mat Trans A*. 2002; 33: 851-8.
106. Barnett MR. 3 - Twinning and its role in wrought magnesium alloys. Elsevier Ltd, 2012, p. 105-43.
107. Nie JF, Shin KS and Zeng ZR. Microstructure, Deformation, and Property of Wrought Magnesium Alloys. *Metall Mater Trans A*. 2020; 51: 6045-109.
108. Zhang K, Zheng J-H, Huang Y, Pruncu C and Jiang J. Evolution of twinning and shear bands in magnesium alloys during rolling at room and cryogenic temperature. *Materials & design*. 2020; 193: 108793.

109. Jäger A, Habr S and Tesař K. Twinning-detwinning assisted reversible plasticity in thin magnesium wires prepared by one-step direct extrusion. *Materials & design*. 2016; 110: 895-902.
110. Sandlöbes S, Zaefferer S, Schestakow I, Yi S and Gonzalez-Martinez R. On the role of non-basal deformation mechanisms for the ductility of Mg and Mg– Y alloys. *Acta Materialia*. 2011; 59: 429-39.
111. Schestakow I, Chen JQ, Sandlöbes S, et al. The Relation between Shear Banding, Microstructure and Mechanical Properties in Mg and Mg-Y Alloys. *Materials science forum*. 2011; 690: 202-5.
112. Sun L, Bai J, Xue F, Tao L, Chu C and Meng J. Exceptional texture evolution induced by multi-pass cold drawing of magnesium alloy. *MATER DESIGN*. 2017; 135: 267-74.
113. Wu L, Agnew SR, Ren Y, et al. The effects of texture and extension twinning on the low-cycle fatigue behavior of a rolled magnesium alloy, AZ31B. *Materials science & engineering A, Structural materials : properties, microstructure and processing*. 2010; 527: 7057-67.
114. Kaibyshev R. 5 - Dynamic recrystallization in magnesium alloys. 2012: 186-225.
115. Kim YJ, Lee JU, Kim YM and Park SH. Microstructural evolution and grain growth mechanism of pre-twinned magnesium alloy during annealing. *Journal of magnesium and alloys*. 2021; 9: 1233-45.
116. Miller VM, Nie J-F and Pollock TM. Nucleation of recrystallization in magnesium alloy grains of varied orientation and the impacts on texture evolution. *Journal of magnesium and alloys*. 2022; 10: 3041-53.
117. Basu I and Al-Samman T. Triggering rare earth texture modification in magnesium alloys by addition of zinc and zirconium. *Acta Materialia*. 2014; 67: 116-33.
118. Guan D, Rainforth WM, Ma L, Wynne B and Gao J. Twin recrystallization mechanisms and exceptional contribution to texture evolution during annealing in a magnesium alloy. *Acta materialia*. 2017; 126: 132-44.
119. Martin É, Mishra RK and Jonas JJ. Effect of twinning on recrystallisation textures in deformed magnesium alloy AZ31. *Philosophical magazine (Abingdon, England)*. 2011; 91: 3613-26.
120. Li X, Yang P, Wang LN, Meng L and Cui F. Orientational analysis of static recrystallization at compression twins in a magnesium alloy AZ31. *Materials science & engineering A, Structural materials : properties, microstructure and processing*. 2009; 517: 160-9.
121. Zeng ZR, Zhu YM, Xu SW, et al. Texture evolution during static recrystallization of cold-rolled magnesium alloys. *Acta materialia*. 2016; 105: 479-94.
122. Levinson A, Mishra RK, Doherty RD and Kalidindi SR. Influence of deformation twinning on static annealing of AZ31 Mg alloy. *Acta materialia*. 2013; 61: 5966-78.
123. Xin Y, Zhou H, Wu G, Yu H, Chapuis A and Liu Q. A twin size effect on thermally activated twin boundary migration in a Mg–3Al–1Zn alloy. *Materials science & engineering A, Structural materials : properties, microstructure and processing*. 2015; 639: 534-9.
124. Basu I, Al-Samman T and Gottstein G. Shear band- related recrystallization and grain growth in two rolled magnesium- rare earth alloys. *Materials Science & Engineering A*. 2013; 579: 50-6.
125. Griffiths D. Explaining texture weakening and improved formability in magnesium rare earth alloys. Taylor & Francis, 2015, p. 10-24.
126. Guan D, Rainforth WM, Gao J, Ma L and Wynne B. Individual effect of recrystallisation nucleation sites on texture weakening in a magnesium alloy: Part 2- shear bands. *Acta Materialia*. 2018; 145: 399-412.
127. Robson JD, Henry DT and Davis B. Particle effects on recrystallization in magnesium–manganese alloys: Particle-stimulated nucleation. *Acta Materialia*. 2009; 57: 2739-47.

128. Huppmann M, Gall S, Müller S and Reimers W. Changes of the texture and the mechanical properties of the extruded Mg alloy ME21 as a function of the process parameters. *Materials science & engineering A, Structural materials : properties, microstructure and processing*. 2010; 528: 342-54.
129. Al-Samman T and Li X. Sheet texture modification in magnesium-based alloys by selective rare earth alloying. *Materials science & engineering A, Structural materials : properties, microstructure and processing*. 2011; 528: 3809-22.
130. Al-Samman T. Modification of texture and microstructure of magnesium alloy extrusions by particle-stimulated recrystallization. *Materials science & engineering A, Structural materials : properties, microstructure and processing*. 2013; 560: 561-6.
131. Luo AA. Recent magnesium alloy development for elevated temperature applications. *International materials reviews*. 2004; 49: 13-30.
132. Gao L, Chen RS and Han EH. Solid solution strengthening behaviors in binary Mg–Y single phase alloys. *Journal of Alloys and Compounds*. 2009; 472: 234-40.
133. Gao L, Chen RS and Han EH. Effects of rare-earth elements Gd and Y on the solid solution strengthening of Mg alloys. *Journal of Alloys and Compounds*. 2009; 481: 379-84.
134. Sandlöbes S, Pei Z, Friák M, et al. Ductility improvement of Mg alloys by solid solution: Ab initio modeling, synthesis and mechanical properties. *Acta materialia*. 2014; 70: 92-104.
135. Sandlöbes S, Friák M, Neugebauer J and Raabe D. Basal and non-basal dislocation slip in Mg–Y. *Materials science & engineering A, Structural materials : properties, microstructure and processing*. 2013; 576: 61-8.
136. Imandoust A, Barrett CD, Al-Samman T, Inal KA and El Kadiri H. A review on the effect of rare- earth elements on texture evolution during processing of magnesium alloys.(Review). *Journal of Materials Science*. 2017; 52: 1.
137. Ball EA and Prangnell PB. Tensile-compressive yield asymmetries in high strength wrought magnesium alloys. *Scripta metallurgica et materialia*. 1994; 31: 111-6.
138. Bohlen J, Nürnberg MR, Senn JW, Letzig D and Agnew SR. The texture and anisotropy of magnesium– zinc– rare earth alloy sheets. *Acta Materialia*. 2007; 55: 2101-12.
139. Stanford N and Barnett MR. The origin of " rare earth" texture development in extruded Mg- based alloys and its effect on tensile ductility. *Materials Science and Engineering A*. 2008; 496: 399-408.
140. Guan D, Rainforth WM, Gao J, Sharp J, Wynne B and Ma L. Individual effect of recrystallisation nucleation sites on texture weakening in a magnesium alloy: Part 1- double twins. *Acta Materialia*. 2017; 135: 14-24.
141. Tang W, Zhou G, Shao Y, Li D, Peng Y and Wang H. On the role of yttrium in microstructure evolution and texture modification during magnesium alloy extrusion. *Materials characterization*. 2020; 162: 110189.
142. Basu I, Al-Samman T and Gottstein G. Shear band-related recrystallization and grain growth in two rolled magnesium-rare earth alloys. *Materials science & engineering A, Structural materials : properties, microstructure and processing*. 2013; 579: 50-6.
143. Wu BL, Zhao YH, Du XH, Zhang YD, Wagner F and Esling C. Ductility enhancement of extruded magnesium via yttrium addition. *Materials science & engineering A, Structural materials : properties, microstructure and processing*. 2010; 527: 4334-40.
144. Stanford N, Atwell D and Barnett MR. The effect of Gd on the recrystallisation, texture and deformation behaviour of magnesium-based alloys. *Acta materialia*. 2010; 58: 6773-83.
145. Hantzsche K, Bohlen J, Wendt J, Kainer KU, Yi SB and Letzig D. Effect of rare earth additions on microstructure and texture development of magnesium alloy sheets. *Scripta Materialia*. 2010; 63: 725-30.

146. Mahjoub R and Stanford N. The electronic origins of the “rare earth” texture effect in magnesium alloys. *Sci Rep*. 2021; 11: 14159-.
147. Guan D, Liu X, Gao J, Ma L, Wynne BP and Rainforth WM. Exploring the mechanism of “Rare Earth” texture evolution in a lean Mg–Zn–Ca alloy. *SCI REP-UK*. 2019; 9: 7152-.
148. Sanjari M, Farzadfar A, Kabir ASH, et al. Promotion of texture weakening in magnesium by alloying and thermomechanical processing: (I) alloying.(Author abstract). 2014; 49: 1408.
149. Barnett MR, Nave MD and Bettles CJ. Deformation microstructures and textures of some cold rolled Mg alloys. *Materials Science & Engineering A*. 2004; 386: 205-11.
150. Robson JD, Haigh SJ, Davis B and Griffiths D. Grain Boundary Segregation of Rare- Earth Elements in Magnesium Alloys.(Report). 2016; 47: 522.
151. Basu I, Pradeep KG, Mießen C, Barrales-Mora LA and Al-Samman T. The role of atomic scale segregation in designing highly ductile magnesium alloys. *Acta Materialia*. 2016; 116: 77-94.
152. Robson JD. Effect of rare- earth additions on the texture of wrought magnesium alloys: The role of grain boundary segregation. 2014, p. 3205-12.
153. Hadorn JP, Sasaki TT, Nakata T, Ohkubo T, Kamado S and Hono K. Solute clustering and grain boundary segregation in extruded dilute Mg–Gd alloys. *Scripta materialia*. 2014; 93: 28-31.
154. Stanford N, Sha G, Xia JH, Ringer SP and Barnett MR. Solute segregation and texture modification in an extruded magnesium alloy containing gadolinium. *Scripta Materialia*. 2011; 65: 919-21.
155. Stanford N. The effect of calcium on the texture, microstructure and mechanical properties of extruded Mg–Mn–Ca alloys. *Materials science & engineering A, Structural materials : properties, microstructure and processing*. 2010; 528: 314-22.
156. Kim DW, Suh BC, Shim MS, Bae JH, Kim DH and Kim NJ. Texture Evolution in Mg-Zn-Ca Alloy Sheets. *Metall Mater Trans A*. 2013; 44: 2950-61.
157. Heinz Mueller PU, Joerg Loeffler. Magnesium-Zinc-Calcium Alloy And Method For Producing Implants Containing The Same. US-11499214-B2 (Patent). Biotronik AG, 2019, p. 1964.
158. Maier P, Griebel A, Jahn M, et al. Corrosion Bending Fatigue of RESOLOY® and WE43 Magnesium Alloy Wires. 2019, p. 175-81.
159. Nienaber M, Braatz M, Ben Khalifa N and Bohlen J. Property profile development during wire extrusion and wire drawing of magnesium alloys AZ31 and ZX10. *Materials & design*. 2022; 224: 111355.
160. Nie JF and Muddle BC. Characterisation of strengthening precipitate phases in a Mg–Y–Nd alloy. *Acta materialia*. 2000; 48: 1691-703.
161. Izumi S, Yamasaki M and Kawamura Y. Relation between corrosion behavior and microstructure of Mg– Zn– Y alloys prepared by rapid solidification at various cooling rates. *Corrosion Science*. 2009; 51: 395-402.
162. Milkereit B, Burgschat L, Kemsies RH, Springer A, Schick C and Kessler O. In situ differential scanning calorimetry analysis of dissolution and precipitation kinetics in Mg–Y–RE alloy WE43. *Journal of magnesium and alloys*. 2019; 7: 1-14.
163. Argade GR, Panigrahi SK and Mishra RS. Aging response on the stress corrosion cracking behavior of wrought precipitation-hardened magnesium alloy. *J Mater Sci*. 2020; 55: 1216-30.
164. Yang L, Huang Y, Peng Q, et al. Mechanical and corrosion properties of binary Mg–Dy alloys for medical applications. *Materials Science & Engineering B*. 2011; 176: 1827-34.

165. Maier P, Steinacker A, Clausius B and Hort N. Influence of Solution Heat Treatment on the Microstructure, Hardness and Stress Corrosion Behavior of Extruded Resoloy ®. *JOM*. 2020; 72: 1870-9.
166. Huang P, Li J, Zhang S, et al. Effects of lanthanum, cerium, and neodymium on the nuclei and mitochondria of hepatocytes: Accumulation and oxidative damage. *Environ Toxicol Pharmacol*. 2010; 31: 25-32.
167. Dziuba D, Meyer-Lindenberg A, Seitz JM, Waizy H, Angrisani N and Reifenrath J. Long-term in vivo degradation behaviour and biocompatibility of the magnesium alloy ZEK100 for use as a biodegradable bone implant. *Acta Biomater*. 2013; 9: 8548-60.
168. Hofstetter J, Becker M, Martinelli E, et al. High-Strength Low-Alloy (HSLA) Mg–Zn–Ca Alloys with Excellent Biodegradation Performance. *JOM*. 2014; 66: 566-72.
169. Bakhsheshi-Rad HR, Abdul-Kadir MR, Idris MH and Farahany S. Relationship between the corrosion behavior and the thermal characteristics and microstructure of Mg–0.5Ca–xZn alloys. *Corrosion science*. 2012; 64: 184-97.
170. Koike J, Kobayashi T, Mukai T, et al. The activity of non- basal slip systems and dynamic recovery at room temperature in fine- grained AZ31B magnesium alloys. *Acta Materialia*. 2003; 51: 2055-65.
171. Cha P-R, Han H-S, Yang G-F, et al. Biodegradability engineering of biodegradable Mg alloys: tailoring the electrochemical properties and microstructure of constituent phases. *Sci Rep*. 2013; 3: 2367-.
172. Jafari S, Raman RKS, Davies CHJ, Hofstetter J, Uggowitzer PJ and Löffler JF. Stress corrosion cracking and corrosion fatigue characterisation of MgZn1Ca0.3 (ZX10) in a simulated physiological environment. *J Mech Behav Biomed Mater*. 2017; 65: 634-43.
173. Hofstetter J, Rüedi S, Baumgartner I, et al. Processing and microstructure–property relations of high-strength low-alloy (HSLA) Mg–Zn–Ca alloys. *Acta materialia*. 2015; 98: 423-32.
174. Yu X, Jiang B, He J, Liu B and Pan F. Oxidation resistance of Mg-Y alloys at elevated temperatures and the protection performance of the oxide films. *Journal of alloys and compounds*. 2018; 749: 1054-62.
175. Fan JF, Yang CL, Han G, Fang S, Yang WD and Xu BS. Oxidation behavior of ignition-proof magnesium alloys with rare earth addition. *Journal of alloys and compounds*. 2011; 509: 2137-42.
176. Sun H-f, Chao H-y and Wang E-d. Microstructure stability of cold drawn AZ31 magnesium alloy during annealing process. *Transactions of Nonferrous Metals Society of China*. 2011; 21: s215-s21.
177. Han W and Fang F. Fundamental aspects and recent developments in electropolishing. *International journal of machine tools & manufacture*. 2019; 139: 1-23.
178. Raval A, Choubey A, Engineer C and Kothwala D. Surface Conditioning of 316LVM Slotted Tube Cardiovascular Stents. *J Biomater Appl*. 2005; 19: 197-213.
179. Yang G, Wang B, Tawfiq K, Wei H, Zhou S and Chen G. Electropolishing of surfaces: theory and applications. *Surface engineering*. 2017; 33: 149-66.
180. Eliaz N and Nissan O. Innovative processes for electropolishing of medical devices made of stainless steels. *J Biomed Mater Res A*. 2007; 83A: 546-57.
181. ASTM. ASTM Standard E1558 09, "Standard Guide for Electrolytic Polishing of Metallographic Specimens", ASTM International, West Conshohocken, PA, 2003, DOI:10.1520/E1558-09R14. 2014.
182. Lee S-J, Chen Y-H and Hung J-C. The investigation of surface morphology forming mechanisms in electropolishing process. *International journal of electrochemical science*. 2012; 7: 12495-506.

183. Chatterton M, Robson J and Henry D. Texture Evolution during Wire Drawing of Mg-RE Alloy. Hoboken, NJ, USA: Hoboken, NJ, USA: John Wiley & Sons, Inc, 2014, p. 251-6.
184. Chunlei G, Xiaohui L, Deng N, Xiang Z, Kaihong Z and Zhenghua H. Microstructure evolution and mechanical properties of biomedical Mg- Zn- Gd alloy wires. *17TH IUMRS INTERNATIONAL CONFERENCE IN ASIA*2017, p. <xocs:firstpage xmlns:xocs=""/>.
185. Xue J, Griebel AJ, Zhang Y, et al. Influence of Thermal Processing on Resoloy Wire Microstructure and Properties. *Advanced engineering materials*. 2021; 23: n/a.
186. Chapuis A and Driver JH. Temperature dependency of slip and twinning in plane strain compressed magnesium single crystals. *Acta materialia*. 2011; 59: 1986-94.
187. Jing Bai Lingling Yin Ye Lu Yiwei Gan Feng Xue Chenglin Chu Jingli Yan Kai Yan Xiaofeng Wan Zhejun T. Preparation, microstructure and degradation performance of biomedical magnesium alloy fine wires. *Progress in Natural Science*. 2014; 24: 523-30.
188. Sun L, Bai J, Yin L, et al. Effect of annealing on the microstructures and properties of cold drawn Mg alloy wires. *Materials science & engineering A, Structural materials : properties, microstructure and processing*. 2015; 645: 181-7.
189. Griebel AJ, Schaffer JE, Hopkins TM, et al. An in vitro and in vivo characterization of fine WE43B magnesium wire with varied thermomechanical processing conditions. *J Biomed Mater Res B Appl Biomater*. 2018; 106: 1987-97.
190. Dexue L, Donglin Y, Xinling L and Shiwen H. Mechanical properties, corrosion resistance and biocompatibilities of degradable Mg-RE alloys: A review. *Journal of materials research and technology*. 2019; 8: 1538-49.
191. Xia D, Liu Y, Wang S, et al. In vitro and in vivo investigation on biodegradable Mg-Li-Ca alloys for bone implant application. *Sci China Mater*. 2018; 62: 256-72.
192. BS ISO 7802:2013: Metallic materials. Wire. Wrapping test. British Standards Institute, 2013.
193. Lee S-K, Lee I-K, Lee S-M and Lee S-Y. Prediction of Effective Strain Distribution in Two-Pass Drawn Wire. *MATERIALS*. 2019; 12: 3923.
194. Barrett CD, Imandoust A and El Kadiri H. The effect of rare earth element segregation on grain boundary energy and mobility in magnesium and ensuing texture weakening. *Scripta Materialia*. 2018; 146: 46-50.
195. Zhang J, Mao C, Long CG, et al. Phase stability, elastic properties and electronic structures of Mg–Y intermetallics from first-principles calculations. *J MAGNES ALLOY*. 2015; 3: 127-33.
196. Xu L, Liu X, Sun K, Fu R and Wang G. Corrosion Behavior in Magnesium-Based Alloys for Biomedical Applications. *MATERIALS*. 2022; 15: 2613.
197. Korgiopoulos K and Pekguleryuz M. The significant effect of trace yttrium level on the mechanical properties of cast Mg–6Al alloy through a refinement mechanism. *Materials science & engineering A, Structural materials : properties, microstructure and processing*. 2020; 775: 138966.
198. Jinghuai Z, Shujuan L, Ruizhi W, Legan H and Milin Z. Recent developments in high-strength Mg-RE-based alloys: Focusing on Mg-Gd and Mg-Y systems. *Journal of magnesium and alloys*. 2018; 6: 277-91.
199. Guan D, Nutter J, Sharp J, Gao J and Mark Rainforth W. Direct observation of precipitation along twin boundaries and dissolution in a magnesium alloy annealing at high temperature. *Scripta materialia*. 2017; 138: 39-43.
200. Huang K, Marthinsen K, Zhao Q and Logé RE. The double-edge effect of second-phase particles on the recrystallization behaviour and associated mechanical properties of metallic materials. *Progress in materials science*. 2018; 92: 284-359.
201. Nienaber M, Yi S, Kainer KU, Letzig D and Bohlen J. On the direct extrusion of magnesium wires from mg-al-zn series alloys. *Metals (Basel)*. 2020; 10: 1-16.

202. Tan HC and Ananthakrishna R. A review of bioresorbable scaffolds: hype or hope? *Singapore Med J*. 2017, p. 512-5.
203. Jeżewski MP, Kubisa MJ, Eyileten C, et al. Bioresorbable Vascular Scaffolds-Dead End or Still a Rough Diamond? *J Clin Med*. 2019; 8: 2167.
204. Rapetto C and Leoncini M. Magmaris: A new generation metallic sirolimus-eluting fully bioresorbable scaffold: Present status and future perspectives. *J Thorac Dis*. 2017; 9: S903-S13.
205. Bossard M, Madanchi M, Avdijaj D, et al. Long-Term Outcomes After Implantation of Magnesium-Based Bioresorbable Scaffolds-Insights From an All-Comer Registry. *Front Cardiovasc Med*. 2022; 9: 856930-.
206. Tovar Forero M, Zandvoort L, Masdjedi K, et al. Serial invasive imaging follow-up of the first clinical experience with the Magmaris magnesium bioresorbable scaffold. *Catheter Cardiovasc Interv*. 2020; 95: 226-31.
207. Barkholt TØ, Neghabat O, Holck EN, Andreasen LN, Christiansen EH and Holm NR. Bioresorbable magnesium scaffold in the treatment of simple coronary bifurcation lesions: The BIFSORB pilot II study. *Catheter Cardiovasc Interv*. 2021.
208. Biotronik. BIOMAG-I Clinical Trial Reaches Primary Endpoint at Six Month for Unique Next Generation Resorbable Magnesium Scaffold. 2022.
209. Ng J, Foin N, Ang HY, et al. Over- expansion capacity and stent design model: An update with contemporary DES platforms. *International Journal of Cardiology*. 2016; 221: 171-9.
210. Barkholt TØ, Webber B, Holm NR and Ormiston JA. Mechanical properties of the drug-eluting bioresorbable magnesium scaffold compared with polymeric scaffolds and a permanent metallic drug-eluting stent. *Catheter Cardiovasc Interv*. 2020; 96: E674-E82.
211. Foin N, Lee R, Bourantas C, et al. Bioresorbable vascular scaffold radial expansion and conformation compared to a metallic platform: Insights from in vitro expansion in a coronary artery lesion model. *EuroIntervention*. 2016; 12: 834-44.
212. ASTM. ASTM Standard F3067−14 "Standard Guide for Radial Loading of Balloon-Expandable and Self-Expanding Vascular Stents" ASTM International, West Conshohocken, PA, 2003, DOI:10.1520/F3067-14R21. 2021.
213. John H, Gregory SR and Anthony R. Chapter 7 - Recrystallization of Single-Phase Alloys. Third Edition ed.: Elsevier Ltd, 2017, p. 245-304.
214. Koike J. Enhanced deformation mechanisms by anisotropic plasticity in polycrystalline Mg alloys at room temperature. *Metallurgical and materials transactions A, Physical metallurgy and materials science*. 2005; 36: 1689-96.
215. Yuan W, Panigrahi SK, Su JQ and Mishra RS. Influence of grain size and texture on Hall–Petch relationship for a magnesium alloy. *Scripta materialia*. 2011; 65: 994-7.
216. Xing Z, Fan H and Kang G. Interaction between crack and grain boundary in magnesium. *Engineering fracture mechanics*. 2022; 275: 108866.
217. Tian J, Deng J-f, Chang Y, Shi Q-x, Liang W and Ma J. A study of unstable fracture of a magnesium alloy caused by uneven microstructure. *Materials letters*. 2022; 314: 131799.
218. della Ventura NM, Sharma A, Cayron C, et al. Response of magnesium microcrystals to c-axis compression and contraction loadings at low and high strain rates. *Acta materialia*. 2023; 248.
219. Nie J-F. Precipitation and Hardening in Magnesium Alloys. *Metall Mater Trans A*. 2012; 43: 3891-939.
220. Cui X, Yu Z, Liu F, Du Z and Bai P. Influence of secondary phases on crack initiation and propagation during fracture process of as-cast Mg-Al-Zn-Nd alloy. *Materials science &*

engineering A, Structural materials : properties, microstructure and processing. 2019; 759: 708-14.